Naphthalimide Luminogens: Structure-Property Relationships and Sensing Applications

A Dissertation Submitted for the Degree of

Doctor of Philosophy

By

Niranjan Meher

Roll No. 146122018

Department of Chemistry

Indian Institute of Technology Guwahati

March, 2019

Department of Chemistry
IIT Guwahati

PhD Thesis

Naphthalimide Luminogens: Structure-Property Relationships and Sensing Applications

By

Niranjan Meher

Supervisor

Prof. Parameswar Krishnan Iyer

March, 2019

PhD Thesis

Naphthalimide Luminogens: Structure-Property Relationships and Sensing Applications

Niranjan Meher

Dedicated to My Maa…

Indian Institute of Technology Guwahati
Department of Chemistry

Certificate

This is to certify that the work contained in the thesis entitled "**Naphthalimide Luminogens: Structure-Property Relationships and Sensing Applications**" by **Niranjan Meher**, a student of Department of Chemistry, Indian Institute of Technology Guwahati, for the award of the degree of Doctor of Philosophy has been carried out under my supervision. This work has not been submitted elsewhere for any degree.

March 2019
IIT Guwahati

Parameswar Krishnan Iyer
Thesis Supervisor
Department of Chemistry
IIT Guwahati
Guwahati-781039, Assam, India.

Indian Institute of Technology Guwahati
Department of Chemistry

Statement

I do hereby declare that the work contained in the thesis entitled "**Naphthalimide Luminogens: Structure-Property Relationships and Sensing Applications**" is the results of investigations carried out by me in the department of chemistry, Indian Institute of Technology Guwahati under the supervision of Prof. Parameswar Krishnan Iyer. This work has not been submitted elsewhere for the award of any degree.

In keeping with the general practice of reporting my observations, due acknowledgements have been made wherever the work described is based on the findings of my collaborators.

March, 2019
IIT Guwahati

Niranjan Meher

Acknowledgments

It has been incredibly fascinating and rewarding for me to thank several personages who have contributed to this thesis in many ways:

To commence with, I feel a deep sense of gratitude to my parents and sisters who formed part of my vision and provide persistent inspiration in each and every situation in my life. Words may prove a meagre means to write down my feelings for my *Maa*, the endless and unconditional love with moral strength, thanks *Maa* just for everything!!! I dedicate this Ph.D. Thesis to you and always believe in having your divine presence and spiritual support throughout.

I express my sincere gratitude to the person who made the biggest difference in my life, my supervisor, Prof. Parameswar Krishnan Iyer. He has been there, in front of my eyes for the last five years, motivating and inspiring every bit of me towards new possibilities in life. His attitude of making serendipitous observations and converting them to new possibilities, correlating ideas, and understanding the obvious has helped me come a long way and will always guide me in the future. He made me realized what I had only heard, “When the going gets tough, the tough get going.” I will never find words to tell what I owe to him.

I owe my sincere gratitude to my doctoral committee members, Prof. Aditya Narayan Panda, Prof. Bhisma Kumar Patel, Dr. Subhas Chandra Pan, Dr. Vishal Trivedi, Dr. Sachin Kumar, and Dr. Kalyan Raidongia for their precious time and suggestions to improve my research works.

One of my good decisions was to start learning with one of my hard-working senior Dr. Sayan Roy Chowdhury. He is the person who made me learn basic experimental works and instruments handling. Although, I preferred to work on aggregation later, I really grateful to him for guiding me in my early phase of research work and really enjoyed a lot working with his company.

My special words of thanks should also go to Sameer Bhaiya, Akhtar Bhaiya, Adil Bhaiya, and Anamika Di for guiding me during my initial phase of research work. I really appreciate the plenty of scientific discussions with them, which helped me to learn and analyze many experimental and theoretical studies. Besides, I am also grateful to have a big pool of

brilliant labmates from different backgrounds who helped me to learn and improve my research work time-to-time through discussions. I also express my heartfelt gratitude to Iyer Sir for conducting regular group meetings, which always provide an excellent platform to learn a lot.

I thank Dr. Swagatika Panda and Dr. Sachin Kumar from BSBE department, IITG for their help in the biological works presented in Chapter 4. I really appreciate the effort of Swagatika Di to finish the work faster than the stipulated time. I also thank Anil Parsram Bidkar and Prof. Siddhartha Sankar Ghosh from BSBE department, IITG for helping me in the biological studies of one of my ongoing project.

My acknowledgment will never be complete without the special mention of all my lab seniors who have taught me the lab culture and have lived by example to make me understand the hard facts of life. I would like to acknowledge Dr. Muthuraj Balakrishnan, Dr. Radhakrishna Ratha, Dr. Suresh Vasimalla, Dr. T. Bhim Raju, Dr. Sameer Hussain, Dr. Anamika Dey, Dr. Anamika Kalita, Dr. Ashish Singh, Dr. Akhtar Hussain Malik, Dr. Arvin Sain Tanwar, Dr. Dipjyoti Das, Dr. Sayan Roy Chowdhury, Dr. P. Gopikrishna, and M. Adil Afroz for all their constant support and motivation during the last five years of my stay in the lab.

My heartfelt thanks to my fellow labmates, Rahul Anna, Raman Ji, Subrata, Maimur, Ramesh Ji, Indrani, Debasish, Rabindra, Nehal, Ritesh, Paromita, Retwik, Nasima, Biki Ji, Anwesha, Kabita, Anita, Rajdixit, Priyam, Debika and the postdoctoral fellows, Dr. Priyanka, Dr. Ekta, Dr. Himani and Dr. Muzafar for being there always and bearing with me the good and bad times during my wonderful days of Ph.D. The discussion and suggestions from all of them were always valuable to me.

I owe my special thanks to my special friends for their moral support and motivation, which drives me to give my best. Ritesh, Madhu, Dhananjaya da, Ahwan Da, Sanket, Harekrushna Da, Sashi Da, Biswajit, Dillip Da, Balaram Da, Prakash, Himadree, Aneeta Di, Tushar and Swarup Da.....thanks to one and all for being with me in thicks and thins of my life.

I sincerely admire the special contribution of my friends Dillip Da, Biswajit, Himadree, and Utsab in many experimental studies like TRPL, single crystal XRD, and FESEM.

I would like to acknowledge all the teachers I learned from since my childhood with a special mention of Dibakara Sir, Akash Sir, and Sananda Sir, I would not have been here without their guidance, blessing, and support.

I am grateful to all my friends from SU and IITG who have been a source of moral support to me and have extended their helping hands without fail. I would also like to thank all my colleague from the Department of Chemistry, IITG, for all the support that they have showered upon me. I could not have asked for more than what I got from them.

I acknowledge the Department of Science and Technology (DST), India; the Department of Electronics & Information Technology (DeitY), India; and the DST-Max Planck Society, Germany for providing the required funding and fellowship to pursue research at IITG. Last but not least, the Department of Chemistry, Centre for Nanotechnology and the Central Instruments Facility, IIT Guwahati are acknowledged for instrument facilities.

Niranjan Meher

Synopsis

Naphthalimides are well-known conventional dyes that have been explored extensively in various real-world applications. However, in the development of versatile fluorescent materials, a notorious photophysical phenomenon called aggregation caused quenching (ACQ) frequently comes into the fore and restricts their potential applications. As the naphthalimides are planar aromatic core with strong electron withdrawing nature, the intermolecular π-π stacking interactions are highly prominent in their condensed state. In contrast to the nature of intermolecular interactions in the well-known propeller-shaped luminogens like tetraphenyle ethylene (TPE) or silole derivatives, the planar naphthalimide derivatives often undergo detrimental face-to-face π-π stacking interactions in their condensed state that lead to significant reduction in their fluorescence emission. However, in 2011 Chang and co-workers reported the first aggregation induced enhanced emission (AIEE)-active naphthalimide derivatives by extending the π-conjugation by core substitution with rigid aromatic units that formed fluorescent nanoparticles in water. The idea was to weaken or distort the detrimental face-to-face π-π stacking interactions among the naphthalimide cores by converting them into V-shaped nonplanar and flexible molecules that restrict the formation of non-fluorescent H-aggregates. This example demonstrated that conventional ACQphoric molecules could also be converted into strong condensed state emitters by judicious structural perturbation. In other words, the condensed state emission in luminogenic systems is primarily dependent on the nature of intermolecular interactions. Besides, the strong intermolecular π-π stacking interactions among naphthalimide core could be easily tuned and controlled by their structural perturbation at the molecular level which in turn can be used to generate finely tuned supramolecular self-assembly with distinct photophysical properties. In recent years, the design of spontaneously self-assembled molecular systems into multifunctional micro and nano-architectures has secured a special place among the scientific community. In particular, spontaneously self-assembled fluorescent systems with precisely controlled uniform size and shape of supramolecules have provided fascinating applications in the field of optoelectronic and biomedical applications.

In this thesis, various strategies of structural manipulations in ACQphoric organic small molecules have been unveiled as an effective yet simple tool to generate and systematically tune supramolecular self-assembly and condensed state emission properties. Interestingly,

unlike the electronic influence in the molecularly dispersed state, the condensed state photophysical and morphological properties of small molecules were found to be dictated by their distinct intermolecular π-π stacking interaction of the planar aromatic core. Besides, the highly fluorescent nanoaggregate dispersion of the AIE/AIEE active naphthalimide congeners with specific receptor site have been used to detect various environmentally toxic and biologically active analytes in aqueous media. Overall, the thesis work focuses on the exploration of the structure-property relationships of the naphthalimide derivatives with sensing applications on multiple platforms.

The content of this thesis report entitled "**Naphthalimide Luminogens: Structure-Property Relationships and Sensing Applications**" has been divided into five chapters as summarized below:

Chapter 1 commences with a brief essay on the need and discovery of condensed state emission. Guided by the mechanistic aspects of condensed state emission, this chapter summarizes the importance, applications and structural manipulation in naphthalimide luminogens along with a concluding remark on this thesis work.

Chapter 2 demonstrates the influence of non-conjugated pendant chains on the supramolecular self-assembly and solid-state emission of the quinolone substituted naphthalimide luminogens. This chapter also includes the detection and unfolding of multi-functional nonheme protein ferritin under physiological conditions, which serves as a well-known inflammatory marker for various diseases.

Chapter 3 provides a conceptual insight on functional group assisted fine-tuning of supramolecular self-assembly and condensed state luminescence in naphthalimides, where the intermolecular packing arrangements dominate their condensed state properties over the electronic influence of the attached functional groups at the molecular level.

Chapter 4 demonstrates the formyl group driven ultra-detection of hydrazine on multiple platforms, which includes the fabrication of simple and portable Whatman paper strips for the cost-effective on-site detection of hydrazine vapors. The detection mechanism involved a reaction-based spontaneous formation of a non-fluorescent hydrazone Schiff base derivative via intramolecular charge transfer process.

Chapter 5 demonstrates the spontaneous formation of long alkyl chain incited fluorescent naphthalimide nanosheets. Along with the mechanistic aspect of condensed state emission in these ACQphoric naphthalimide congeners, sensitive detection of organic volatile

contaminants in water via acceptor excited photoinduced electron transfer (*a*-PET) has been unveiled.

The thesis concludes with a brief future prospective on the developed strategies and materials with tunable condensed state properties that could extend the applications of small molecule based classical fluorophores towards many unexplored possibilities.

Chapter 1: Introduction

Recent developments and mechanistic perspective on condensed state emission of organic fluorophores have been discussed in this chapter. Along with the diverse potential applications of classical fluorophores, the need of condensed state emissive materials has been highlighted in this section. Besides the different types of condensed state emission in chromophoric systems, the diverse technological applications of naphthalimide luminogens, easy synthetic manipulations on the naphthalimide core to achieve condensed state emission, and a concluding remark on this thesis work has been included in this chapter.

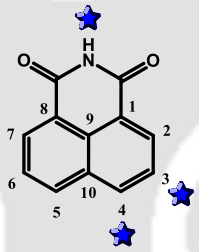

Figure S1. Structure of naphthalimide core indicating the reactive site, where wide variety of structural manipulation can be perceived to achieve condensed state emission this classical fluorophore.

Chapter 2: Pendant Chain Engineering to Fine-Tune the Nanomorphologies and Solid State Luminescence: Ultra-Detection of Ferritin in Aqueous Media

Strategically, a series of five angular "V" shaped naphthalimide AIEEgens with varying pendant chains (butyl, hexyl, octyl, cyclohexyl and methylcyclohexyl) have been synthesized to fine-tune their nanomorphological and photophysical properties. With similar aromatic cores and electronic states, unexpected tuning of the condensed state emission colors and nanomorphologies of naphthalimides have been achieved for the first time simply by judicious choice of the non-conjugated pendant chain. Conclusive analysis by various spectroscopic techniques and computational studies confirmed the full control of the pendant chain (in terms of bulkiness around the naphthalimide core, which restricts the ease

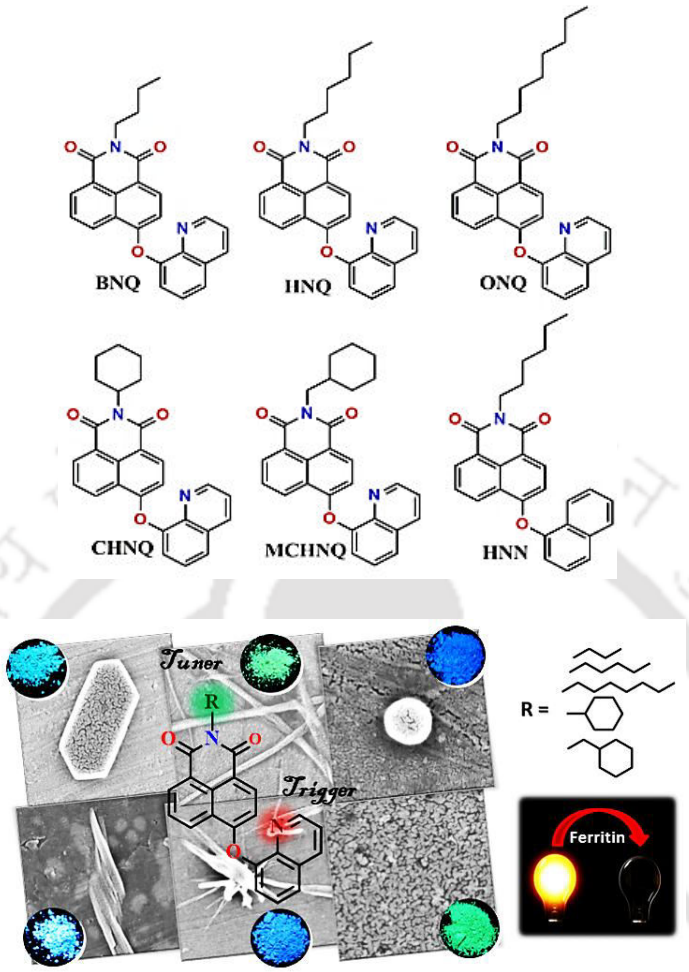

Figure S2. Chemical structures used and the schematic of pendant chain engineering in naphthalimides to fine-tune the nanomorphologies and solid state emission color. Detection of multi-functional nonheme protein ferritin at nanomolar level has also been achieved.

of intermolecular π–π interactions) over the nanoaggregate morphology and solid state emissive properties of the AIEEgens; this method can be rationalized to all aggregation-prone systems. Thus, considering the prime role of the active layer nanomorphology in all organic optoelectronic devices, this methodology may emerge as a promising tool to improve device performance. Besides, the **HNQ** nanoribbons with higher surface area in aqueous media were employed for the sensitive detection of multi-functional nonheme protein ferritin (K_{sv} = 0.83 × 10^{7} M^{-1}) with a limit of detection 67.25 × 10^{-11} M (0.33 ng mL^{-1}) under physiological conditions, which serves as a well-known inflammatory marker for various diseases. The fluorescent nanoribbons were also found to modify the *α*-helix content of ferritin, thereby inducing conformational changes in their secondary structure.

Chapter 3: Functional Group Engineering to Fine-Tune the Supramolecular Self-Assembly and Condensed State Luminescence

Engineering well-defined supramolecular fluorescent nano-architectures based on organic small molecules has been an important scientific challenge. In this chapter, a library of naphthalimide congeners (**1-15**) have been strategically designed that provides a conceptual insight of functional group controlled aggregation-induced emission (AIE) in conventional strong aggregation-caused quenching (ACQ) active fluorophores. Along with the regulation of ACQ-to-AIE transformation and tailoring of condensed state emission, the simple yet potential design strategy of functional groups engineering has been demonstrated for the

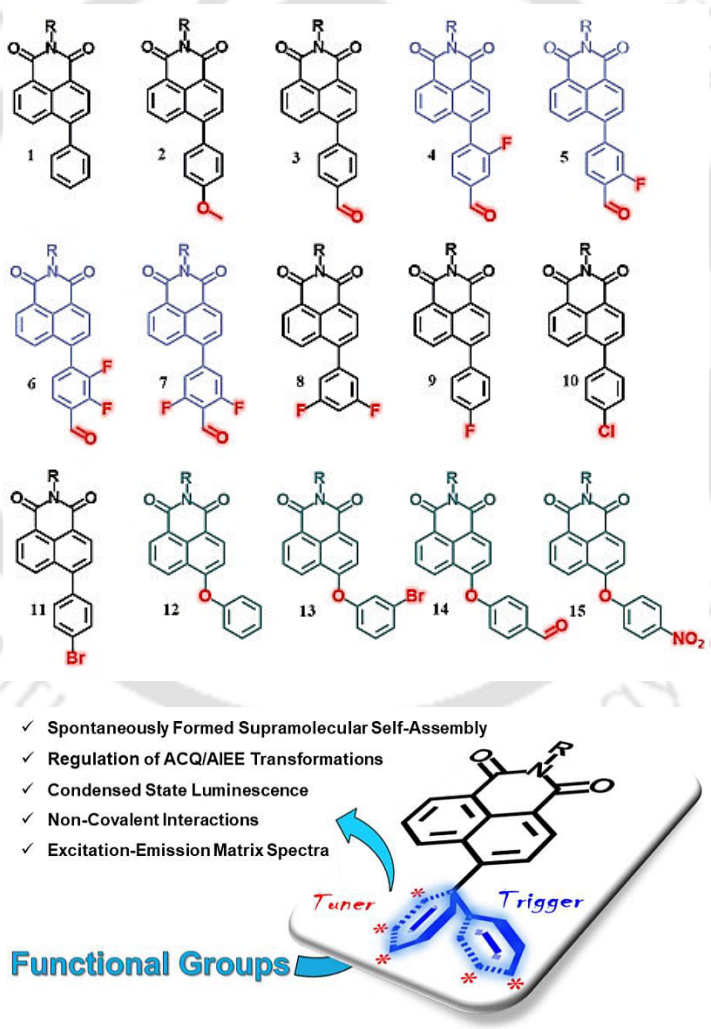

Figure S3. Structures of naphthalimide congeners used to demonstrated the functional group incited fine-tune of condensed state photophysical and supramolecular self-assembly properties without the electronic influence of the attached functional groups.

first time to spontaneously generate and systematically tailor the supramolecular self-assembly of organic small molecules into well-defined nano-architectures. Single-crystal XRD analysis of six congeners unveiled that, unlike the electronic effect of the functional groups, the tuning of condensed state photophysical and morphological properties are dictated by their distinct magnitude of the steric effect exerted around the planar aromatic core and are also supported by their excitation-emission matrix (EEM) spectra recorded at different concentrations. Considering the crucial role of the active layer nanomorphology in biology as well as various organic optoelectronic devices, this simple yet potential design strategy is a promising tool to improve device performance such as light emitting, photovoltaics and sensing applications.

Chapter 4: Formyl Group Driven Ultra-Detection of Hydrazine on Multiple Platforms

The designed naphthalimide AIEEgen (NIBD) with formyl group as receptor site accomplished ultrasensitive detection of hydrazine at parts per trillion level (LOD/81 ppt) in aqueous media with high selectivity and an enormous improvement over the existing state-of the art. An exceptional sensitivity is also achieved in the vapor phase (LOD/0.003%) using a Whatman paper strip based portable device for simple and cost-effective on-site detection. The detection mechanism involved a reaction-based spontaneous formation of a non-fluorescent hydrazone Schiff base derivative (NIBDH). The *in vitro* potential of the AIEEgenic probe was also demonstrated in two mammalian cell lines i.e. HeLa (human cervical cancer cell line) and HEK293T (Human embryonic kidney cell line that expresses a mutant version of the SV40 large T antigen). Owing to the highly selective formation of the hydrazone Schiff base complex with hydrazine, NIBD responds to the existence of hydrazine in both these cell lines without any interference from other biologically rich metal ions and

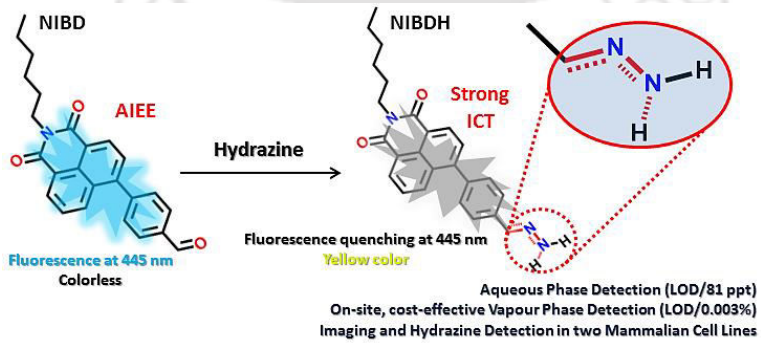

Figure S4. Schematic of formyl group driven ultra-detection of hydrazine on multiple platforms via formation of a non-fluorescent hydrazone Schiff base derivative as a result of intramolecular charge transfer process.

amino acids. These outcomes could initiate a much wider use of formyl group triggered hydrazone Schiff base complexation for probing and manipulating hydrazine biology associated with several metabolic activities.

Chapter 5: Spontaneously Self-Assembled Naphthalimide Nanosheets: Condensed State Emission and Unveiling *a*-PET for Sensitive Detection of Organic Volatile Contaminants in Water

A simple design strategy of long alkyl chain substitution was formulated to block the detrimental π–π interaction that potentially transforms the aggregation-caused quenching (ACQ) chromophores into aggregation-induced emission (AIE) active smart nanomaterials. The long octadecyl pendant chain substituted naphthalimide (NI) derivatives self-assembled into fluorescent nanosheets (NS)-like structures that spontaneously have surfaces coated with NI cores in water. The fluorescent NS were subsequently used to recognize the organic volatile contaminants (OVCs) at ppb levels via an acceptor-excited photoinduced electron transfer (*a*-PET) mechanism, unveiled as the first representative example. A new design strategy is thereby provided to detect toxic xylene derivatives in water using smart nanomaterials.

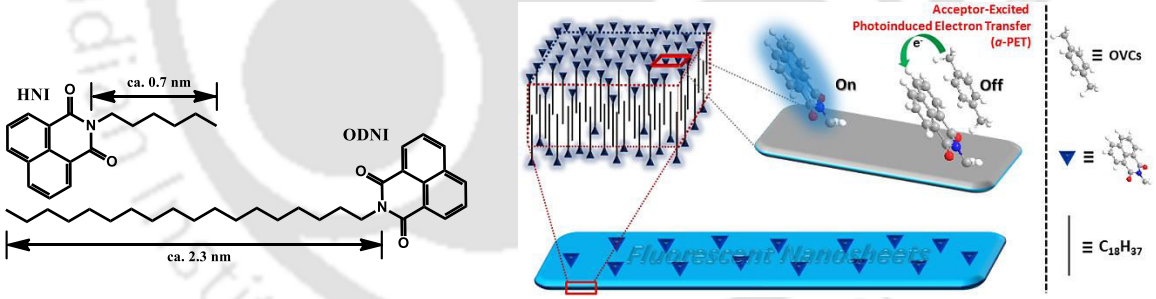

Figure S5. Chemical structures of naphthalimide congeners used for the study and the schematic of long alkyl chain assisted condensed state emission along with their application for OVCs detection via *a*-PET mechanism in water.

Future Aspect and Thesis Overview

Naphthalimide (NI) compounds are imide-group-containing well-known acceptors and their derivatives have been developed to realize multiple applications over the past several decades. Because of their accepting capacity and high PL quantum yields, NIs have received considerable attention among the scientific community. The AIE activity in NIs opens a new class of AIE-active materials with immense possibilities for various real-world applications

like bio- and chemosensors, organic light-emitting diodes, stimuli response materials, in vitro and in vivo imaging, and as biogenic molecules. Because of the good biocompatibility, photostability, and high condensed-state emission behavior, NIs are promising for in-depth and long-term bioimaging and tracking applications. Multiple research groups have devoted careful efforts to expand the scope of this core as a possible alternative to existing systems. The highly electron withdrawing and asymmetric NI cores have been realized to have unique structure–property relationships. Because of the strong tendency of the NI cores toward intermolecular π-π stacking interactions, the structural conformation of the asymmetric NI core could be easily tweaked to extend their applications toward many unexplored possibilities.

In this context, this research work focused to develop new strategies to control the ACQ/AIE phenomenon in NI derivatives. In particular, the research work of this thesis includes the construction and systematic tuning of condensed state properties of the NIs by simple structural perturbation. Different approaches have been unveiled to tune the supramolecular

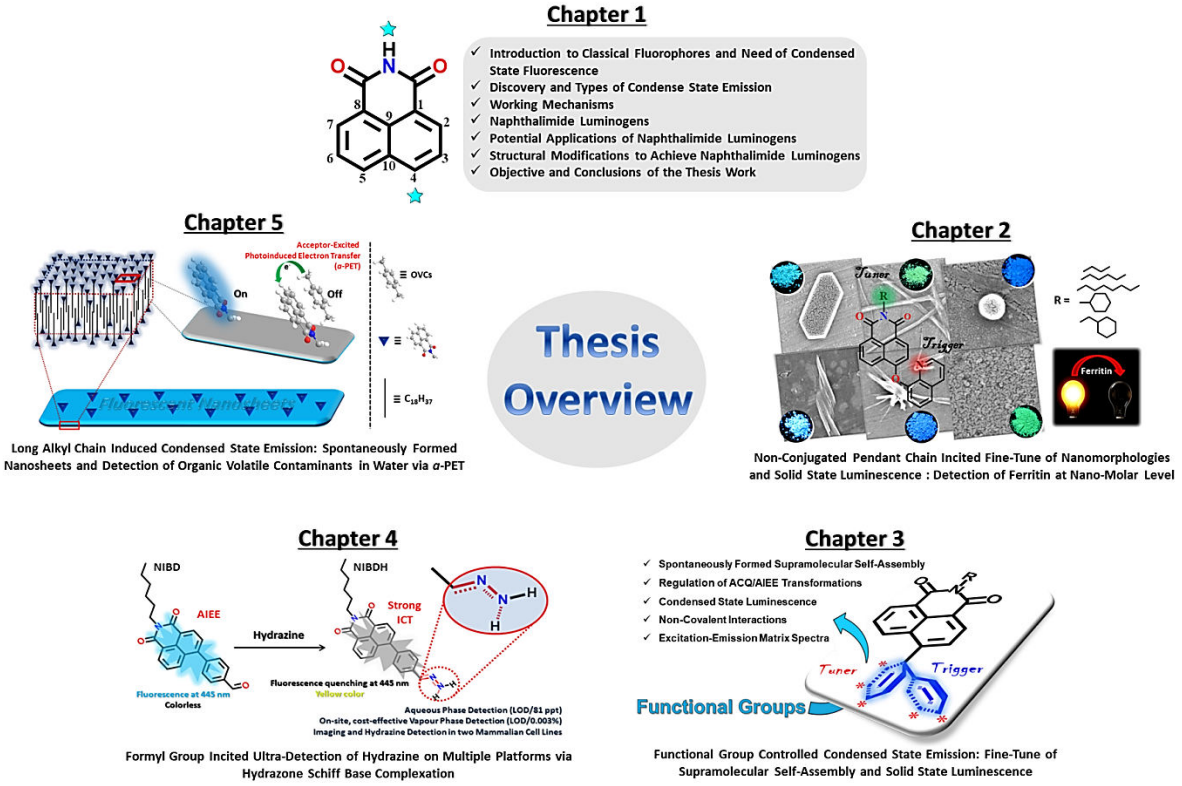

Figure S6. Development of new strategies to generate condensed state emission in classical fluorophores with systematic tuning of supramolecular self-assembly and solid state emission. Besides, the spontaneously formed fluorescent supramolecules were used to detect biologically active and environmentally active analytes in aqueous media.

self-assembly in NIs by judicious simple structural manipulations. Since the intermolecular packing arrangement plays a significant role in the supramolecular self-assembly and photophysical properties of the NIs over the electronic influence of the attached motifs, it could hugely benefit their utility to evaluate their biomedical applications as distinct supramolecular assembly spontaneously generated from electronically similar molecular species. Apart from the different strategies developed to generate and tailor the condensed state photophysical and self-assembly properties of the NIs, the spontaneously formed fluorescent supramolecular assembly of the NIs have been employed for the detection of various environmentally toxic and biologically active analytes in physiological conditions.

Contents

Chapter 1.	Introduction		01
	1.1	Classical Fluorophores and Need of Condensed State Emitters	03
	1.2	Discovery and Types of Condense State Emission	04
		1.2.1. Aggregation Induced Emission	05
		1.2.2. Aggregation Induced Emission Enhancement	05
		1.2.3. Dual-State Emission	06
		1.2.4. Crystallization Induced Emission	06
	1.3	Working Mechanisms	06
	1.4	Naphthalimide Luminogens	08
	1.5	Potential Applications of Naphthalimide Luminogens	09
	1.6	Structural Modifications to Achieve Naphthalimide Luminogens	10
	1.7	Objective and Conclusions of the Thesis Work	11
		References	14
Chapter 2.	Pendant Chain Engineering to Fine-Tune the Nanomorphologies and Solid State Luminescence: Ultra-Detection of Ferritin in Aqueous Media		17
		Abstract	19
	2.1	Introduction	20
	2.2	Experimental Section	22
		2.2.1. Materials and Instrumentations	22
		2.2.2. Sensing studies	22
		2.2.3. Calculation of Detection Limit	23
		2.2.4. Theoretical Studies	23
		2.2.5. Quantum Yield Calculations	23
		2.2.6. Synthesis of Compounds	23
	2.3	Results and Discussion	26
		2.3.1. Design, Synthesis and Characterization	26
		2.3.2. AIEE Studies	27
		2.3.3. Study of Solid State Fluorescence Tuning	28
		2.3.4. XRD Analysis	30
		2.3.5. Self-Assembly Analysis	31

2.3.6. Detection of Ferritin 32
2.3.7. Evaluation of Detection Mechanism 34
2.4 Conclusion 35
References 36
Appendix 39

Chapter 3. Functional Group Engineering to Fine-Tune the Supramolecular Self-Assembly and Condensed State Luminescence 57
Abstract 59
3.1 Introduction 60
3.2 Experimental Section 61
3.2.1. Materials and Instrumentations 61
3.2.2. Preparation of the Test Solution 62
3.2.3. Preparation of FESEM Samples 62
3.2.4. Theoretical Studies 62
3.2.5. Quantum Yield Calculations 63
3.2.6. Crystallographic Details 63
3.2.7. Synthetic Procedures 63
3.3 Results and Discussion 68
3.3.1. Design, Synthesis and Characterization 68
3.3.2. Tuning of Condensed State Luminescence without the Electronic Influence of Functional Groups 69
3.3.3. Functional Groups Controlled ACQ-to-AIEE Transformations 71
3.3.4. Concentration Dependent Excitation-Emission Matrix (EEM) Spectra and Assessment of Multifluorophoric Systems 73
3.3.5. Functional Group Controlled Spontaneously Formed Supramolecular Nano-Architectures 74
3.3.6. Orderliness of Supramolecular Assembly Reflecting Condensed State Luminescence 77
3.3.7. XRD Analysis of the Supramolecular Interactions in Naphthalimides 78
3.3.8. Elucidation of Dark State in 15 81
3.4 Conclusion 83
References 83

Appendix 86

Chapter 4. Formyl Group Driven Ultra-Detection of Hydrazine on Multiple Platforms 121

Abstract 123

4.1 Introduction 124

4.2 Experimental Section 125

4.2.1. Materials and Instrumentations 125

4.2.2. Cell Culture and Imaging 125

4.2.3. Sensing Studies 126

4.2.4. Calculation of Detection Limit 126

4.2.5. Synthesis of Compounds 126

4.2.6. Theoretical Studies 126

4.2.7. Calculation of Stern–Völmer Quenching Constant and Limit of Detection 127

4.3 Results and Discussion 127

4.3.1. Design, Synthesis and Characterization 127

4.3.2. Detection Hydrazine in Aqueous Medium 128

4.3.3. Selectivity Study 128

4.3.4. Elucidation of the Detection Mechanism 129

4.3.5. Detection of Hydrazine Vapour Cost-Effective Paper Strips 131

4.3.6. In Vitro Detection of Hydrazine in Two Mammalian Cells 133

4.4 Conclusion 135

References 135

Appendix 137

Chapter 5. Spontaneously Self-Assembled Naphthalimide Nanosheets: Condensed State Emission and Unveiling *a*-PET for Sensitive Detection of Organic Volatile Contaminants in Water 143

Abstract 145

5.1 Introduction 146

5.2 Experimental Section 147

5.2.1. Materials and Instrumentations 147

5.2.2. Synthetic Procedure of ODNI and HNI 148

5.2.3. Preparation of ODNI Nanosheets 148
5.2.4. Preparation of FESEM and AFM Samples 148
5.2.5. Preparation of Samples for PXRD Study 149
5.2.6. Calculation of Detection Limit 149
5.2.7. Theoretical Studies 149
5.2.8. Calculation of Stern–Völmer quenching constant and Limit of Detection 149
5.3 Results and Discussion 150
5.3.1. Design, Synthesis and Characterization 150
5.3.2. Aggregation Study 151
5.3.3. Morphological Analysis 152
5.3.4. XRD Analysis 152
5.3.5. Detection of Organic Volatile Contaminants 154
5.3.6. Evaluation of Detection Mechanism 155
5.4 Conclusion 157
References 157
Appendix 160

Future Aspect and Thesis Overview 171
Publications 175
Patents 176
Awards 176
Conferences 177
Vitae 178

Chapter 1

Introduction

Gopikrishna; P.; **Meher, N.**; Iyer, P. K. *ACS Appl. Mater. Interfaces* **2018**, *10*, 12081−12111.

1.1. Classical Fluorophores and Need of Condensed State Emitters

The advancement of organic luminescent materials with high-tech innovations has immensely benefited the whole world and has unlocked several avenues in modern technological developments by gaining deeper insight into their light-emitting processes. Research on luminescent materials remains a key focus and hot topic in the scientific community and can be witnessed by the Nobel awarded work in the year 2008 for the development of green fluorescent proteins (GFP), which enabled to gain extraordinary insights into biological pathways by visualizing the biochemical structures and processes.[1] Theoretical prospect of the luminescent materials suggest that it can be applied in all physical states, i.e., solid, liquid, and gaseous. However, in contrast to the bright fluorescence emission in the dilute solution state, most of these conventional fluorophores exhibit reduced emission or complete emission quenching in their condensed state.[2-5] As depicted in the Figure 1.1,[6] the molecularly dissolved solution of fluorescein in water emits intensely. With gradual increase in the fraction of poor solvent (e.g., acetone), the bright emission gets decreased progressively and becomes almost non-fluorescent. This is due to the increase in the local concentration of fluorescein as a result of its poor miscibility in acetone and the fluorescence quenching becomes clearly visible above 60 vol % of acetone. With increasing acetone fraction, the fluorescence emission of fluorescein disappears owing to severe aggregates formation. The planar aromatic core of fluorescein enables its molecules to undergo strong intermolecular π–π stacking interaction and forms the non-fluorescent nanoaggregates. Besides, fluorescein does not emit light at all in its powder form, which could be the enhanced π–π stacking interaction in its solid state. This kind of fluorescence reduction of conventional fluorophores are termed as aggregation-caused quenching (ACQ) and has been well-documented for many decades since the discovery of concentration quenching (CQ) effect by Förster in 1954.[7] In this notorious photophysical behavior CQ, the fluorescent dyes in solution state are often quenched with increase in their concentration as a result of aggregates formation and has been well-summarized by Birks in his classic book on Photophysics of Aromatic Molecules.[8] However the aggregates formation is highly prominent in the poor solvent even at low concentrations and in solid state as well and can quench the fluorescent properties of the fluorophores completely.

The vast majority of the real-world applications including optoelectronics applications in organic light-emitting diodes (OLEDs) and organic field-effect transistors (OFETs) deal with

materials in their condensed state, where luminogenic materials are employed as thin solid powder or films or crystals.[1] Besides, organic fluorophoric materials have huge applications in the field of biomedical science and are applied in aqueous media or physiological environments. Despite the incorporation of polar functional groups like carboxylic and sulfonic acid groups for water solubility, the strong hydrophobicity of the aromatic cores of the fluorophores are highly prone to aggregates formation and could reduce the fluorescence efficiency significantly. Despite very important technological applications of the conventional dyes, the appearance of such detrimental ACQ phenomenon serves as a serious negative optical effect preventing their wide and versatile application as light emitting materials (Figure 1.1 and 1.2).[1,9-11] Thus, the development of materials that can emit intensely in their condensed state are of huge significance and impactful that could unlock many avenues to an array of possibilities with great potential for high-tech innovations.

1.2. Discovery and Types of Condense State Emission

It was all started with the overwhelming discovery of the concept of aggregation-induced emission (AIE) by Tang and Co-workers in 2001 that changed the way of thinking on aggregating materials.[12] In contrast to the non-fluorescent properties of the conventional dyes in their condensed state, the propeller-shaped non-emissive hexaphenylsilole (HPS) derivative, which is the first discovered AIEgen, in its molecularly dissolved solution states were found to emit intensely under appropriate conditions (e.g. aggregated or in solid state). These kinds of new generation unconventional fluorescence emitters were termed as

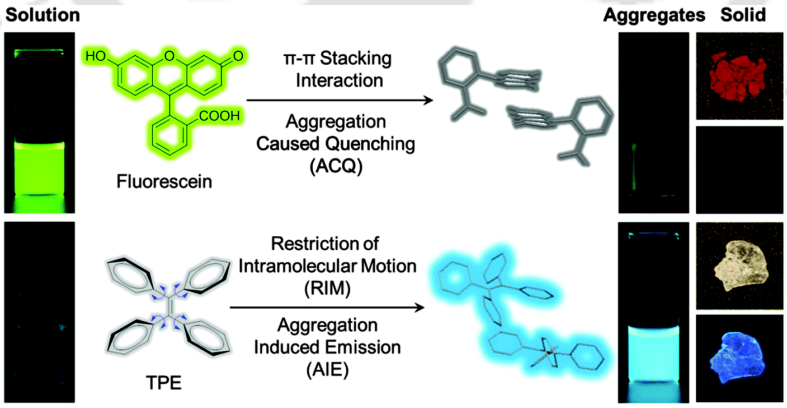

Figure 1.1. Most of the widely used fluorophores such as fluorescein are strong emitters in the solution state. However, the emission is quenched in the aggregate state or solid state due to the π-π stacking interaction. The propeller-shaped AIE luminogen, tetraphenylethene (TPE) turns on its emission upon aggregation. The solid state of TPE is highly emissive. Reproduced from Ref. 6 with permission from The Royal Society of Chemistry.

luminogens. In the case of these AIEgens, the aggregates (together) are more luminescent than the solution (individual), whereas in the ACQ system the reverse is true—the individuals are more luminescent than together. Few of well-known strong condensed state emitters have been presented in Figure 1.2.[1,9] Depending upon the nature of fluorescence property of the luminogens at different states, the condensed state phenomenon of the luminogens can be divided into many categories and have been discussed subsequently.

1.2.1. Aggregation-Induced Emission

As depicted in Figure 1.1, the well-explored fluorescein dye emits intensely in their dilute solutions, whereas suffers from an almost complete fluorescent reduction in poor solvent.[1,9] However, the propeller-shaped tetraphenylethylene (TPE) derivative are found to have exactly opposite photophysical properties to that of fluorescein and exhibits strong emission in their poor solvent owing to the formation of homogeneously dispersed nanoaggregates. This kind of phenomenon where the completely non-fluorescent property of molecules in its solution is induced to exhibit strong fluorescence upon the formation of nanoaggregates is termed as aggregation-induced emission (AIE).

1.2.2. Aggregation Induced Emission Enhancement

Following the discovery, Park et al. in 2002 introduced another phenomenon called as aggregation induced emission enhancement (AIEE), a subgroup of AIE.[1,13] AIEEactive molecules exhibit emission in both solution and aggregated state. The materials falling in this column could emit reasonably in its solution state (in good solvent) but undergo steady decrease in its fluorescence emission with increasing fraction of poor solvent. However, the strong emission of these materials tunes back strongly due to the formation of highly

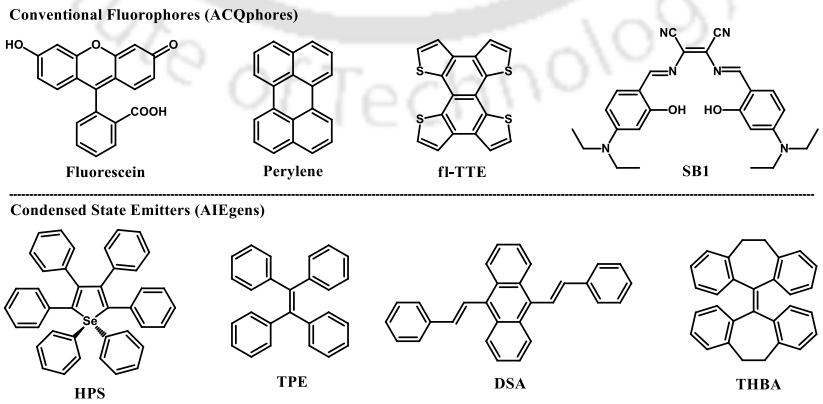

Figure 1.2. Molecular structures of some conventional ACQphoric fluorophores and few of well-explored condensed state emitter.

emissive nanoaggregates as a result of the synergetic effect of intramolecular planarization and J-aggregation. The emissive nature of these kinds of AIEE-active materials is of huge importance due to their applicability in both solution and condensed state.

1.2.3. Dual-State Emission

Apart from the concept of AIE and AIEE, another interesting phenomenon of dual state emission (DSE) has also been introduced by Tang et al., wherein the luminogens emit efficiently in both solution as well as the condensed state.[14] As seen in AIEEgenic materials, where the fluorescence emission decreases with increasing fraction of poor solvent, the DSE-active materials show intense emission in all possible composition of solvent with different polarity. However, development of dual state emitting materials is still at its preliminary stage.[15,16] Luminogens with dual state emission properties have been designed by taking advantage of both inherent ACQ and AIE dyes that emit intensely in both solution, aggregated and solid states. These dual state luminogens have added few special advantages compared to ACQ, AIE, and AIEE luminogens.

1.2.4. Crystallization Induced Emission

Another concept of crystallization-induced emission (CIE) appears to be a potential finding added to the field of condensed state luminescent materials.[17,18] In contrary to the AIE, AIEE and DSE active, where the materials are intensely emissive in their solid powder form or in aggregated form, these CIE active materials emit faintly in their solid amorphous state. However, crystallization of molecules induces significant enhancements in its fluorescence efficiency as compared to both its molecular solutions and amorphous powders. This remarkable CIE effect enables ready modulation of the light emission of luminogens between dark and bright states by simple external stimuli such as heating, cooling, and fuming processes. Thus, by modulating the solid state between the amorphous and crystalline phase, CIE dyes could find an array of novel applications in environmental protection, chemosensors, rewritable optical media, and optical displays.

1.3. Working Mechanisms

To get into the mechanistic insight of this interesting phenomenon of condensed state emission, many research groups hypothesized several mechanistic pathways including J-aggregate formation, conformational planarization, twisted intramolecular charge transfer (TICT), excited state intramolecular proton transfer (ESIPT) and E/Z isomerization.[1,9]

However, none of these mechanisms could be universalized because of their inapplicability to all the reported luminogenic systems. In 2014, Tang and co-workers once again tried to generalize its working mechanism and drew a strong aspect regarding the condensed state emission process.[1,9] In that review article, with solid theoretical and experimental proof, restriction of intramolecular motions (RIM) was hypothesized to be the most reliable and effective working mechanism for the condensed state emission. Applying fundamental physics, upon excitation, the organic molecules having rigid rotators could consume the maximum amount of energy through dynamic intramolecular rotation and vibrations. Because of this, they became less emissive or nonemissive in the solution state. Whereas, in aggregated or solid state, the molecules interlock themselves that restrict the intramolecular rotation (RIR) and vibration (RIV) and relax through radiative pathways. It is also noteworthy to mention that the face-to-face strong π–π stacking interactions are primarily responsible for the ACQ phenomenon that subsequently lead to the radiationless relaxations with bathochromic shifts as frequently seen in the crystals of the conventional luminophores. Considering these prospects, the well-known AIEgens (TPE, HPS, etc.) were designed in such a way that their propeller-shaped molecular conformations restrict intermolecular face-to-face π–π stacking interaction and make them highly emissive in their condensed state (Figure 1.1). This general concept can be applied to any planar ACQ system to induce AIE properties through structural manipulation by disturbing their planarity or preventing the planar core from strong π–π stacking interactions. Thus, research groups are constantly trying to develop new strategies, which can be applied to the existing inherent conventional dyes for the generation of condensed state emission to unlock their wide versatile applications.

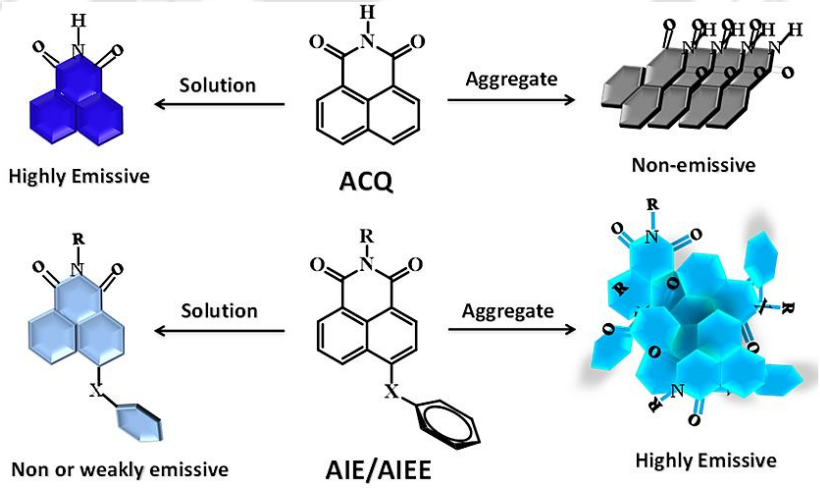

Figure 1.3. Graphical representation of ACQ NI and AIE/AIEE active NI in solution and aggregated state.

1.4. Naphthalimide Luminogens

To date, a wide variety of cores with the AIE or AIEE properties have been reported. Primarily, the TPE and silole cores have been extensively explored. Apart from these well-known condensed state emitters, research groups are constantly trying to explore either new AIE/AIEE active cores or to structurally manipulate the well-known conventional dyes to unlock their many restricted areas of applications caused due to the detrimental ACQ property.[1,9] Many conventional strong ACQphoric dyes like fluorescein, perylene have been successfully transformed into strong condensed state emitters and found to have huge significance in the field of optoelectronic to biomedical applications.[1]

Naphthalimide (NI) core is considered as one of the most versatile fluorophore unit owing to its unique photophysical properties.[19] Its UV–visible absorption and fluorescence emission energy falls within the visible region and can be tuned up to the near-IR region which could provide an excellent platform to probe the microenvironment of biological systems. Besides, the NI dyes have been used in the construction of novel therapeutics and in the dye industry as a powerful absorber for colorful dyes.[20] The NIs and its derivatives have immense potential in the area of optoelectronic materials, fluorescent sensors, laser dyes, bioimaging, etc., because of their extraordinary thermal and chemical stability with high fluorescence quantum yields.[19,21] The NIs are also known to have high antitumor activity toward various murine and human cells.[22] Again, the extension of the aromatic ring with thiazole and polythiazole groups have been manipulated in the construction of several photonucleases and anticancer bleomycin related antibiotics.[23] Sulfonated NI derivatives were also reported to have antiviral activity with selective in vitro activity toward the human immune deficiency virus (HIV-1).[24] Brominated NIs at the third and fourth place could act as the photochemotherapeutic inhibitory materials in the blood (Figure 1.4).[25] NI derivatives are also powerful photoreagents and can be photoactivated to kill tumor cells.[26] This unlocks their wide probable applications toward phototherapy. The NI core could also be extended for anticancer agents and DNA-binding motifs.

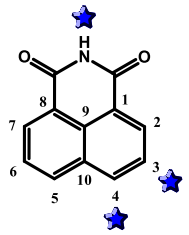

Figure 1.4. Representation of NI core indicating the most reactive positions (red star).

In the past decades, although naphthalimide (NI) cores have been widely used as a classical fluorophores, their ACQ properties screen their potential applications. To the best of our knowledge, in 2011 Chang and co-workers reported AIEEactive NIs for the first time by extending the π-conjugation by core substitution with rigid aromatic units.[27] These V-shaped nonplanar and flexible NIs were reported to form fluorescent organic nanoparticles with AIEE characteristics. As shown in Figure 1.3, the highly fluorescent planar NI molecules (in solution state) were extensively affected by dense face-to-face packing and got quenched in the aggregated state through H-aggregation. However, their core substitution with rigid aromatic core restricts their H-type aggregation (nonfluorescent or weakly fluorescent in solution state because of dynamic rotation and vibration) and became highly fluorescent in aggregated and solid state (Figure 1.3). This example established that an ACQ fluorophore can be easily transformed into an AIE-active material by breaking its planarity through rigid aromatic core substitution. There are also some other methods, such as appending ACQ units on a polymeric chain to synthesize AIEgens. The basic aim of such structural transformation is to restrict or weaken the detrimental face-to-face π–π stacking interactions of the aromatic cores in their condensed state.[28]

1.5. Potential Applications of Naphthalimide Luminogens

Subsequently, this ACQ hurdle was potentially resolved by well-designed structural modifications by various research groups. To date, plenty of NI derivatives have been reported with high fluorescence quantum yields in the solid or aggregated state by

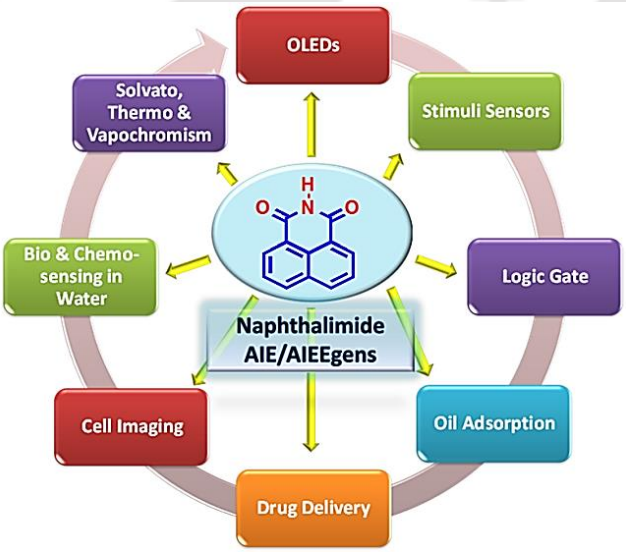

Figure 1.5. Possible technological applications of the AIE/AIEE active NIs.

introducing different organic moieties at the fourth position or by N-functionalization, and opened up various restricted areas with potential applications (Figure 1.5).[28] These transformed luminogens have been efficiently employed in OLEDs and can also stain living cells effectively. Most of the luminogens are usually insoluble in aqueous media that lead to the formation of highly stable fluorescent organic nanoaggregates. These nanoaggregates with the higher surface area along with their inherent molecular properties have been applied for various biological/biomedical activities both in vitro and in vivo. Thus, it is evident that the NI derivatives have found wide applications in the past few years and many outstanding examples of NI based AIE/AIEEgens have been reported, that demonstrate the huge versatility of this NI core by integrating them with the young concept of AIE/AIEE.[28]

1.6. Structural Modifications to Achieve Naphthalimide Luminogens

Because of the easy N-functionalization of the 1,8-naphthalic anhydride precursor via simple Gabriel phthalimide synthesis, most literature has reported substituting the nonpolar alkyl amine groups to form imide linkages that enhanced the solubility in organic solvents. However, most of the naphthalimides with N-functionalization have appeared to be less efficient in term of their magnitude of condensed state fluorescence due to the possibility of $\pi-\pi$ stacking interactions between the planar naphthalimide cores. It has been observed that the strong stacking interaction between the naphthalimide cores has been successfully overcome by functionalizing at the alternative reactive position of the aromatic core (Figure 1.4).

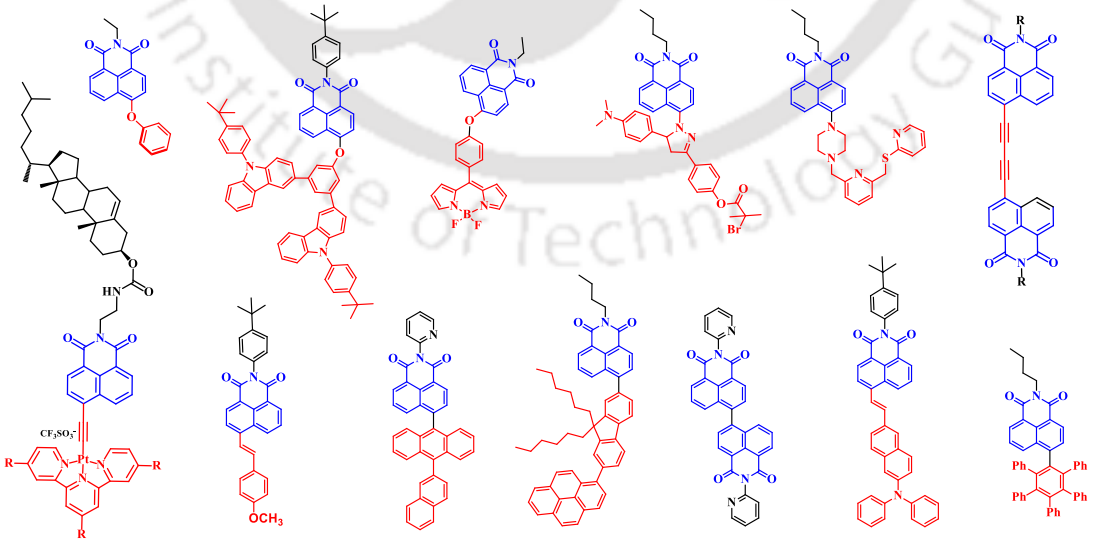

Figure 1.6. The chemical structures of few of the well explored core functionalized naphthalimide AIE/AIEE luminogens employed in diverse technological applications.[28]

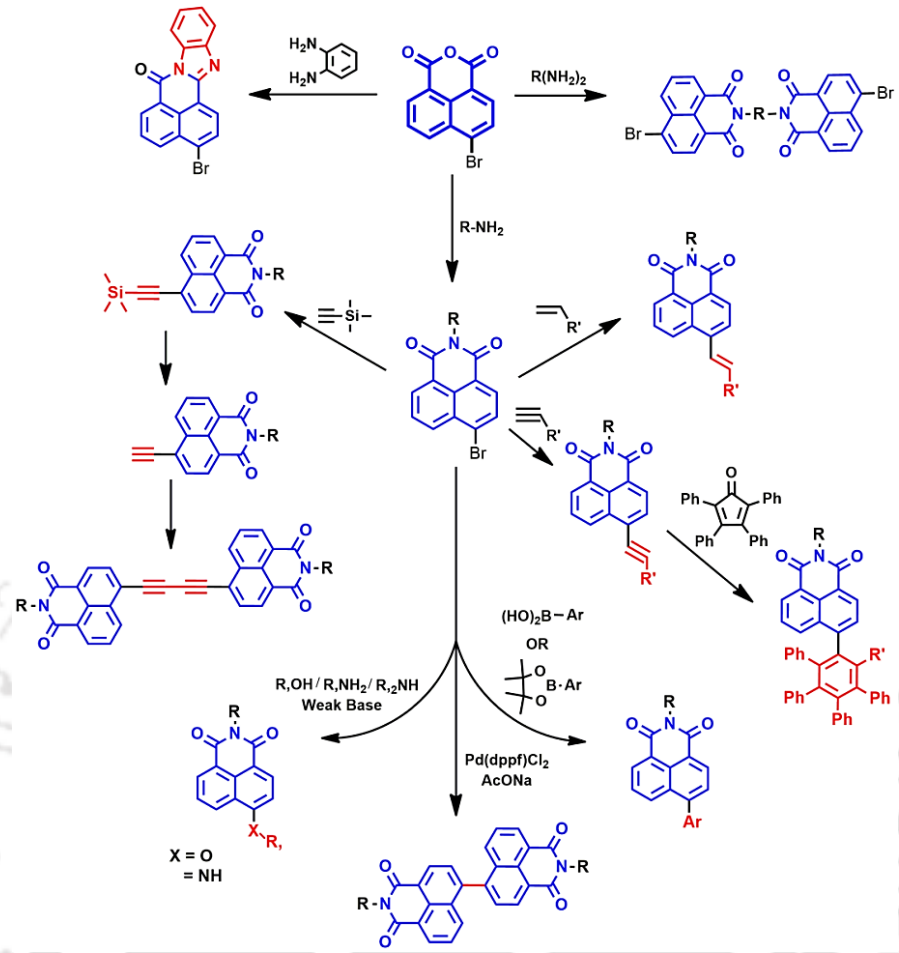

Scheme 1.1. Possible Synthetic Routes for Producing the AIE/AIEE Active NIs.

The 4th position of the core was realized to be highly susceptible and has been effectively tweaked through a variety of synthetic routes and has successfully generated strong condensed state emission properties in conventional naphthalimide core. The various facile synthetic routes that have evolved in past decades are summarized in Scheme 1.1.[28] In particular; the substitution of rigid aromatic core in the 4th position of the naphthalimide core has appeared to be the most efficient naphthalimide AIE/AIEE luminogens. The chemical structures of few of the well explored core functionalized naphthalimide AIE/AIEE luminogens employed in diverse technological applications have been summarized in Figure 1.6.[28]

1.7. Objective and Conclusions of the Thesis Work

Naphthalimides are well-known conventional dyes that have been explored extensively in various real-world applications. However, in the development of versatile fluorescent

materials, a notorious photophysical phenomenon called ACQ frequently comes into the fore and restricts their potential applications. As the naphthalimides are planar aromatic core with strong electron withdrawing nature, the intermolecular *π-π* stacking interactions are highly prominent in their condensed state. In contrast to the nature of intermolecular interactions in the well-known propeller-shaped luminogens like TPE or silole derivatives, the planar naphthalimide derivatives often undergo detrimental face-to-face *π-π* stacking interactions in their condensed state that lead to significant reduction in their fluorescence emission. However, in 2011 Chang and co-workers reported the first AIEE-active naphthalimide derivatives by extending the *π*-conjugation by core substitution with rigid aromatic units that formed fluorescent nanoparticles in water.[27] The idea was to weaken or distort the detrimental face-to-face *π-π* stacking interactions among the naphthalimide cores by converting them into V-shaped nonplanar and flexible molecules that restrict the formation of non-fluorescent H-aggregates. This example demonstrated that conventional ACQphoric molecules could also be converted into strong condensed state emitters by judicious structural perturbation. In other words, the condensed state emission in luminogenic systems is primarily dependent on their nature of intermolecular interactions. Besides, the strong intermolecular *π-π* stacking interactions among naphthalimide core could be easily tuned and controlled by their structural perturbation at the molecular level which in turn can be used to generate finely tuned supramolecular self-assembly with distinct photophysical properties. In recent years, the design of spontaneously self-assembled molecular systems into multifunctional micro and nano-architectures has secured a special place among the scientific community. In particular, spontaneously self-assembled fluorescent systems with precisely controlled uniform size and shape of supramolecules have fascinating applications in the field of optoelectronic and biomedical applications.

In this thesis work, various strategies of structural manipulations in ACQphoric organic small molecules have been unveiled as an effective yet simple tool to generate and systematically tune supramolecular self-assembly and condensed state emission properties. Interestingly, unlike the electronic influence in the molecularly dispersed state, the condensed state photophysical and morphological properties of small molecules were found to be dictated by their distinct intermolecular *π-π* stacking interaction of the planar aromatic core. Besides, the highly fluorescent nanoaggregate dispersion of the AIE/AIEE active naphthalimide congeners with specific receptor site has been used to detect various environmentally toxic and biologically active analytes in aqueous media. Overall, the thesis

work focuses on the exploration of the structure-property relationships of the naphthalimide derivatives with sensing applications on multiple platforms.

The complete thesis has been divided into five chapters as summarized below:

Chapter 1 commences with a brief essay on the need and discovery of condensed state emission. Guided by the mechanistic aspects of condensed state emission, this chapter summarizes the importance, applications and structural manipulation in naphthalimide luminogens along with a concluding remark on this thesis work.

Chapter 2 demonstrates the influence of non-conjugated pendant chains on the supramolecular self-assembly and solid-state emission of the quinolone substituted naphthalimide luminogens. This chapter also includes the detection and unfolding of multi-functional nonheme protein ferritin under physiological conditions, which serves as a well-known inflammatory marker for various diseases.

Chapter 3 provides a conceptual insight on functional group assisted fine-tuning of supramolecular self-assembly and condensed state luminescence in naphthalimides, where the intermolecular packing arrangements dominates their condensed state properties over the electronic influence of the attached functional groups at the molecular level.

Chapter 4 demonstrates the formyl group driven ultra-detection of hydrazine on multiple platforms, which includes the fabrication of simple and portable Whatman paper strips for the cost-effective on-site detection of hydrazine vapor. The detection mechanism involved a reaction-based spontaneous formation of a non-fluorescent hydrazone Schiff base derivative via intramolecular charge transfer process.

Chapter 5 demonstrates the spontaneous formation of long alkyl chain incited fluorescent naphthalimide nanosheets. Along with the mechanistic aspect of condensed state emission in these ACQphoric naphthalimide congeners, sensitive detection of organic volatile contaminants in water via acceptor excited photoinduced electron transfer (*a*-PET) has been unveiled.

Reference

(1) Mei, J.; Leung, N. L. C.; Kwok, R. T. K.; Lam, J. W. Y.; Tang, B. Z. *Chem. Rev.* **2015**, *115*, 11718−11940.

(2) Photonic Research Systems, http://www.prsbio.com/html/general_faq.html#q4; retrieved on May 15, **2014**.

(3) Thomas III, S. W.; Joly, G. D.; Swager, T. M. *Chem. Rev.* **2007**, *107*, 1339-1386.

(4) Hoeben, F. J. M.; Jonkheijm, P.; Meijer, E. W.; Schenning, A. P. H. J. *Chem. Rev.* **2005**, 105, 1491-1546.

(5) Bunz, U. H. F. *Chem. Rev.* **2000**, *100*, 1605-1644.

(6) Chen, S.; Wang, H.; Hong, Y.; Tang, B. Z. *Mater. Horiz.* **2016**, *3*, 283-293.

(7) Förster, T.; Kasper, K. Ein Konzentrationsumschlag der Fluoreszenz. *Z. Phys. Chem. (Muenchen, Ger.)* **1954**, *1*, 275−277.

(8) Photophysics of Aromatic Molecules; Birks, J. B., Ed.; Wiley: London, **1970**.

(9) Mei, J.; Hong, Y.; Lam, J. W. Y.; Qin, A.; Tang, Y.; Tang, B. Z. *Adv. Mater.* **2014**, *26*, 5429−5479.

(10) Ma, X.; Sun, R.; Cheng, J.; Liu, J.; Gou, F.; Xiang, H.; Zhou, X. *J. Chem. Educ.* **2016**, *93*, 345−350.

(11) Viglianti, L.; Leung, N. L. C.; Xie, N.; Gu, X.; Sung, H. H. Y.; Miao, Q.; Williams, I. D.; Licandro, E.; Tang, B. Z. *Chem. Sci.* **2017**, *8*, 2629-2639.

(12) Luo, J. D.; Xie, Z. L.; Lam, J. W. Y.; Cheng, L.; Chen, H. Y.; Qiu, C. F.; Kwok, H. S.; Zhan, X. W.; Liu, Y. Q.; Zhu, D. B.; Tang, B. Z. *Chem. Commun.* **2001**, 1740−1741.

(13) An, B. K.; Kwon, S. K.; Jung, S. D.; Park, S. Y. *J. Am. Chem. Soc.* **2002**, *124*, 14410−14415.

(14) Chen, G.; Li, W.; Zhou, T.; Peng, Q.; Zhai, D.; Li, H.; Yuan, W. Z.; Zhang, Y.; Tang, B. Z. *Adv. Mater.* **2015**, *27*, 4496−4501.

(15) Li, W. J.; Liu, D. D.; Shen, F. Z.; Ma, D. G.; Wang, Z. M.; Feng, T.; Xu, Y. X.; Yang, B.; Ma, Y. G. *Adv. Funct. Mater.* **2012**, *22*, 2797−2803.

(16) Liu, Y. W.; Zhang, Y.; Wu, X. H.; Lan, Q.; Chen, C. S.; Liu, S. W.; Chi, Z. G.; Jiang, L.; Chen, X. D.; Xu, J. R. *J. Mater. Chem. C* **2014**, *2*, 1068−1075.

(17) Dong, Y.; Lam, J. W. Y.; Qin, A.; Sun, J.; Liu, J.; Li, Z.; Sun, J.; Sung, H. H. Y.; Williams, I. D.; Kwok, H.-S.; Tang, B. Z. *Chem. Commun.* **2007**, 3255−3257.

(18) Dong, Y.; Lam, J. W. Y.; Qin, A.; Li, Z.; Sun, J.; Sung, H. H. Y.; Williams, I. D.; Tang, B. Z. *Chem. Commun.* **2007**, 40−42.

(19) Banerjee, S.; Veale, E. B.; Phelan, C. M.; Murphy, S. A.; Tocci, G. M.; Gillespie, L. J.; Frimannsson, D. O.; Kelly, J. M.; Gunnlaugsson, T. *Chem. Soc. Rev.* **2013**, *42*, 1601–1618.

(20) Duke, R. M.; Veale, E. B.; Pfeffer, F. M.; Kruger, P. E.; Gunnlaugsson, T. *Chem. Soc. Rev.* **2010**, *39*, 3936–3953.

(21) Chen, X. Q.; Wang, F.; Hyun, J. Y.; Wei, T. W.; Qiang, J.; Ren, X. T.; Shin, I.; Yoon, J. *Chem. Soc. Rev.* **2016**, *45*, 2976–3016.

(22) Brana, M. F.; Castellano, J. M.; Moran, M. *Anti-Cancer Drug Des.* **1993**, *8*, 257– 268.

(23) M207. Brana, F.; Berlanga, J. M. C.; Roldan, C. M. DE patent 2318136 A1, **1973**.

(24) Rideout, D.; Schinazi, R.; Pauza, C. D.; Lovelace, K.; Chiang, L. C.; Calogeropoulou, T.; Mccarthy, M.; Elder, J. H. *J. Cell. Biochem.* **1993**, *51*, 446–457.

(25) Chanh, T. C.; Lewis, D. E.; Allan, J. S.; Sogandaresbernal, F.; Judy, M. M.; Utecht, R. E.; Matthews, J. L. *AIDS Res. Hum. Retroviruses* **1993**, *9*, 891–896.

(26) Bailly, C.; Brana, M.; Waring, M. J. *Eur. J. Biochem.* **1996**, *240*, 195–208.

(27) Lin, H. H.; Chan, Y. C.; Chen, J. W.; Chang, C. C. *J. Mater. Chem.* **2011**, *21*, 3170–3177.

(28) Gopikrishna, P.; Meher, N.; Iyer, P. K. *ACS Appl. Mater. Interfaces* **2018**, *10*, 12081–12111.

Chapter 2

Pendant Chain Engineering to Fine-Tune the Nanomorphologies and Solid State Luminescence: Ultra-Detection of Ferritin in Aqueous Media

Meher, N.; Chowdhury, S. R.; Iyer, P. K. *J. Mater. Chem. B*, **2016**, *4*, 6023–6031.

Meher, N.; Iyer, P. K. *Nanoscale*, **2017**, *9*, 7674–7685.

Abstract

Strategically, a series of five angular "V" shaped naphthalimide AIEEgens with varying pendant chains (butyl, hexyl, octyl, cyclohexyl and methylcyclohexyl) have been synthesized to fine-tune their nanomorphological and photophysical properties. With similar aromatic cores and electronic states, unexpected tuning of the condensed state emission colors and nanomorphologies of naphthalimides has been achieved for the first time simply by judicious choice of the non-conjugated pendant chain. Conclusive analysis by various spectroscopic techniques and computational studies confirmed the full control of the pendant chain (in terms of bulkiness around the naphthalimide core, which restricts the ease of intermolecular π–π interactions) over the nanoaggregate morphology and solid state emissive properties of the AIEEgens; this method can be rationalized to all aggregation-prone systems. Thus, considering the prime role of the active layer nanomorphology in all organic optoelectronic devices, this methodology may emerge as a promising tool to improve device performance. Besides, the **HNQ** nanoribbons with higher surface area in aqueous media were employed for the sensitive detection of the multi-functional nonheme protein ferritin (K_{sv} = 0.83 × 10^{7} M^{-1}) with a limit of detection 67.25 × 10^{-11} M (0.33 ng mL^{-1}) under physiological conditions, which serves as a well-known inflammatory marker for various diseases. The fluorescent nanoribbons were also found to modify the α-helix content of ferritin, thereby inducing conformational changes in their secondary structure.

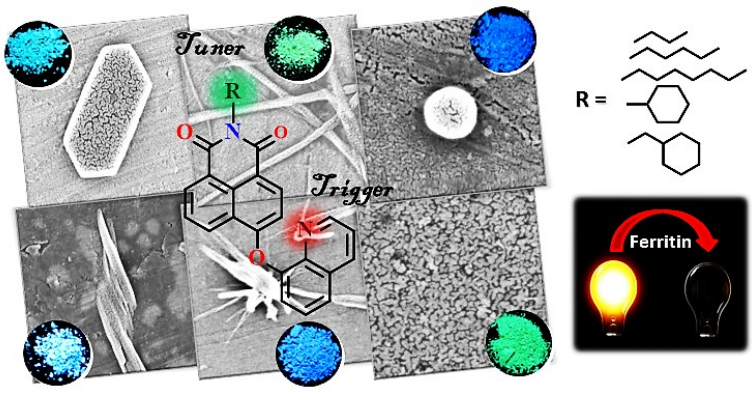

2.1. Introduction

Recently, the young field of solid-state luminescence has gained considerable attention due to its broad range of applications in the fields of optoelectronic devices, bio/chemosensors, cancer theranostics, DNA visualization and many more.[1-3] In various systems, low molecular weight small molecules are favored over polymer systems due to their ease of synthesis, structural modification and device fabrication processes involving vapor deposition.[4-6] Among the commonly encountered small fluorescent units, owing to their various potential applications, 1,8-napthalimide derivatives have been established as a flexible class of luminogens.[7,8] Due to their strong tendencies to undergo intermolecular π–π stacking, these derivatives are appropriate candidates for optoelectronic and semiconductor applications. Because π–π stacking plays a vital role in the intermolecular packing of naphthalimides, which controls the photophysical properties of the molecules, the extent of π–π stacking has been systematically modulated without perturbing the electronic environments of the naphthalimides. In this work, precise variation of the pendant chain as an effective tool to modulate the intermolecular π–π interactions of naphthalimides has been carefully studied. Perturbation of the intermolecular π–π interactions affects the solid state luminescence directly and causes drastic changes in the morphology of the nanoaggregates. Although several strategies, such as doping, piezochromism, and cocrystals, have been explored, systematic changes at the molecular level through facile synthetic methods can serve as an easier and more effective tool to control the condensed state luminescence and the nanomorphology of these compounds.[9-11]

Hence, bearing in mind both the fundamental and real-world significance, new molecular systems that can self-assemble spontaneously and reproducibly into multifunctional nanostructures and microstructures are of enormous interest.[12-14] In recent years, considerable efforts have been devoted to explore supramolecular self-assembly, which can provide a fascinating platform for developing functional materials with large surface-to-volume ratios that can have applications in various fields.[12-14] Previously, blue emitting conjugated polymer appended with an 8-hydroxyquinoline moiety has been demonstrated to show high sensitivity towards iron and iron containing metalloproteins, where a 4 : 1 THF/water solvent system was used considering its solubility issues which probably hinders its practical application.[15] Furthermore, it has also been reported that an AIE-active fluorophore has sensitivity up to 0.78 ng mL^{-1} towards ferritin.[16] Few other promising reports on ferritin detection have also appeared recently.[17-23] The multi-functional protein

ferritin is a well-known inflammatory marker with possible roles in proliferation, immunosuppression, iron delivery, angiogenesis, and several other diseases.[24] A higher level of ferritin in the sera indicates the growth of cancer tumor cells and is highly expressed in tumor-associated macrophages.[25] Thus the down regulation of ferritin could be used as an attractive target for cancer therapy and can disrupt the tumor microenvironment, thereby killing cancer cells, and enhance its sensitivity to chemotherapy.[25]

Herein, highly fluorescent AIEE-active probe (**HNQ**) was employed for the detection of metalloproteins, especially nonheme protein ferritin, and the fluorescent nanoribbons of the small molecule was found to have a limit of detection (LOD) up to 0.33 ng mL^{-1} under physiological conditions. Again, this newly reported AIEEgen can also induce conformational changes in its secondary structure that offers valuable insights to elucidate the role of the protein involved in iron metabolism.[26,27] All these studies were carried out under physiological conditions (pH = 7.4) in water using a green emitting AIEEgen, which is more suitable for practical applications.

In recent examples, the role of a single nitrogen atom in the photophysical and morphological properties of the V-shaped naphthalimides involving *J*-aggregate formation through intermolecular π–π interactions has been established.[28] The naphthalimide core was functionalized with 8-hydroxy quinoline/α-naphthol at the 4^{th} position, where the N-atom of the quinoline moiety has been used as a triggering unit. As shown in Figure 2.1, to tune its morphological and optical properties, the naphthalimide core was precisely alkylated with different pendant chains, viz. butyl (**BNQ**), hexyl (**HNQ**), octyl (**ONQ**), cyclohexyl (**CHNQ**) and methylcyclohexyl (**MCHNQ**). The presence of the N-atom is highly crucial in the formation of nanoaggregates because its presence increases the molecular dipole moment, which triggers intermolecular π–π interactions (Figure A2.1).[29] To affirm the triggering effect of the N-atom, a model compound without the N-atom (**HNN**) at the quinoline moiety was also included in these studies.

The overall objective was to understand and explore the conceptual hurdles in fine-tuning and controlling the nanomorphologies of nanoaggregates and the solid-state luminescence of aggregation-prone fluorescent systems via a simple and effective methodology without disturbing the aromatic core. Besides, the spontaneously self-assembled **HNQ** nanoribbons with higher volume-to-surface ratio can detect nonheme protein ferritin at the nanomolar level and can induce conformational changes in the protein microenvironment under physiological conditions.

2.2. Experimental Section

2.2.1. Materials and Instrumentations

All starting materials, reagents, and analytes (4-bromo-1,8-naphthalene anhydride, 8-hydroxyquinoline, α-naphthol, alkylamines, protein analytes, deuterated solvents) were purchased from Sigma Aldrich (INDIA). HPLC grade solvents and potassium carbonate were purchased from Zenith India and Northeast Chemicals. The chemicals purchased were of reagent grade and used without additional purification. NMR (^{1}H, ^{13}C) spectra were recorded with a Bruker Avance 600 MHz NMR spectrometer by taking residual solvent signal as an internal reference. Electrospray ionization mass (ESI-MS) spectra were recorded on a Waters (Micro mass MS-Technologies) Q-Tof MS Analyzer spectrometer. Perkin-Elmer Model Lambda-35 spectrophotometer and Horiba Fluoromax-4 spectrofluorometer have been used to record UV/vis and PL spectra respectively in a 3 ml quartz cuvettes of path length 1 cm at 298 K. Fluorescence quantum yields in solutions were calculated by standard methods using Quinine sulfate (Φ_F = 0.577 in 0.1 M H_2SO_4, λ_{ex} = 350 nm). Solid state absorbance and emission were recorded with Fluoromax-4 fluorescence spectrophotometer equipped with a Quanta-ϕ integrating sphere to get solid state fluorescence quantum yield. Hydrodynamic diameters of the nanoaggregates were obtained in a Malvern Zetasizer instrument. Single crystal data were obtained with a Bruker SMART APEX diffractometer equipped with a CCD area detector. The data integration and reduction were processed with SAINT. SHELXL-97 was used for the structure solutions via direct method and refined by full-matrix least-squares on F^2. Atomic force microscopy images were recorded on an Agilent 5500-AFM/STM instrument. FE-SEM images were obtained on Sigma Carl ZEISS field emission scanning electron microscope by drop casting the aqueous solution on aluminium foil and were left for drying at room temperature. CD spectra were recorded on a JASCO, J–815 CD Spectrometer, model no. J–815–150S. Changes in the secondary structure of metalloproteins were recorded in the far UV region (190 – 240 nm) using 0.4 cm path length cells and 20 nm min^{-1} scan speed.

2.2.2. Sensing studies

The monomer **HNQ** (4.2 mg) stock solution was prepared at a concentration of 10 mM in 1 mL DMF. This was diluted to 20 μM for each titration in a 1 mL cuvette. The stock solutions of metalloproteins and non-metalloproteins (ferritin concentration taken was 0.1 mM, rest

ware of 1mM) were introduced in portions and the fluorescence intensity changes were recorded at pH 7.4 at room temperature (excitation wavelength: 360 nm) in Tris-buffer.

2.2.3. Calculation of Detection Limit

For calculating detection limit, different samples of **HNQ** (20 μM) each containing Ferritin (0 nM, 10 nM, 20 nM, 30 nM, and 40 nM) were prepared separately and fluorescence spectrum was then recorded for each sample by exciting at 360 nm. The detection limit plot for Ferritin was obtained by plotting change in the fluorescence intensity vs I_0/I of Ferritin. The curve shows a linear relationship and the correlation coefficient (R^2) via linear regression analysis was calculated to be 0.9966. The limit of detection (LOD) was then calculated using the equation $3\sigma/K$, where σ represents the standard deviation for the intensity of **HNQ** in the absence of Ferritin and K symbolizes slope of the equation. The ferritin used was from horse spleen having molecular weight more than 5 lakhs.[30]

2.2.4. Theoretical Studies

Ground state geometric optimizations were done by density functional theory (DFT) with the B3LYP functional as implemented in Gaussian 03 software package using the 6-31G basis set. Absolute energies are given in hartrees or eV without additional corrections. Dipole moments were calculated by single point calculations (B3LYP/6-31G) using the optimized structures.

2.2.5. Quantum Yield Calculations

PL quantum yields (Φ_s) of naphthalimides were calculated by taking quinine sulfate (Φ_s = 0.57 in 0.1 M H_2SO_4) as standard and using the equation shown below:

$$\Phi_s = \Phi_r (A_r F_s / A_s F_r) (\eta_s^2 / \eta_r^2)$$

Where, s and r represent sample and reference, Φ signifies the quantum yield, A denotes absorbance, F signifies relative integrated fluorescence intensity, and η represents the refractive index of the medium.

2.2.6. Synthesis of Compounds

Alkylation: To a suspension of 4-bromonaphthalene anhydride (554.2 mg, 2 mmol) in ethanol, butylamine (146.28 mg, 2 mmol) was added dropwise at room temperature. The temperature was increased and stirred for 8 hours at 85 °C. The mixture was cooled and the

solvent was evaporated under reduced pressure. The solid residue was dissolved in chloroform and washed with water for two times. The organic layer was concentrated after drying over anhydrous Na_2SO_4. Finally, column purification was performed to obtain the pure product (**BN**).

Similar procedures were followed by taking equal equivalents of respective alkyl or cycloalkylamines to get the other Alkylated 4-bromonaphthalimides derivatives (**HN**, **ON**, **CHN** and **MCHN**) as mentioned in **Scheme 1**.

BN: Light grey solid (595 mg, 89% yield); M.p. 100-102 ^oC; HRMS (*m/z*): calcd for $C_{16}H_{14}BrNO_2$ 331.0208; found 332.0280 $[M+H]^+$; ^1H NMR (600 MHz, $CDCl_3$, δ ppm) 8.44 (d, 1H), 8.34 (d, 1H), 8.20 (d, 1H), 7.82 (d, 1H), 7.63 (t, 1H), 3.97 (t, 2H) 1.52 (m, 2H), 1.26 (m, 2H), 0. 78 (t, 3H); ^{13}C NMR (150.00 MHz, $CDCl_3$, δ ppm) 163.79, 133.35, 132.16, 131.36, 131.25, 130.77, 130.34, 129.14, 128.24, 123.32, 122.46, 40.57, 30.35, 20.56, 14.02.

HN: Light green solid (615 mg, 85% yield); M.p. 92-93 ^oC; HRMS (*m/z*): calcd for $C_{18}H_{18}BrNO_2$ 359.0521; found 360.0600 $[M+H]^+$; ^1H NMR (600 MHz, $CDCl_3$, δ ppm) 8.57 (d, 1H), 8.46 (d, 1H), 8.32 (d, 1H), 7.94 (d, 1H), 7.77 (t, 1H), 4.12 (t, 3H) 1.70 (m, 2H), 1.31 (m, 6H), 0.87 (t, 3H); ^{13}C NMR (150.00 MHz, $CDCl_3$, δ ppm) 163.63, 163.60, 133.22, 132.06, 131.25, 131.16, 130.61, 130.24, 128.98, 128.15, 123.21, 122.34, 40.78, 31.71, 28.18, 26.96, 22.74, 14.25.

ON: Light brown solid (620 mg, 80% yield); M.p. 85-86 ^oC; HRMS (*m/z*): calcd for $C_{20}H_{22}BrNO_2$ 387.083; found 388.0950 $[M+H]^+$; ^1H NMR (600 MHz, $CDCl_3$, δ ppm) 8.64 (d, 1H), 8.54 (d, 1H), 8.39 (d, 1H), 8.02 (d, 1H), 7.83 (t, 1H), 4.15 (t, 2H) 1.71 (m, 2H), 1.34 (m, 10H), 0.87 (t, 3H); ^{13}C NMR (150.00 MHz, $CDCl_3$, δ ppm) 163.73, 133.32, 132.15, 131.34, 131.24, 130.74, 130.32, 129.11, 128.22, 123.31, 122.45, 40.82, 32.00, 29.51, 29.40, 28.27, 27.32, 22.83, 14.28.

CHN: White solid (586 mg, 82% yield); M.p. 82-83 ^oC; HRMS (*m/z*): calcd for $C_{18}H_{16}BrNO_2$ 357.063; found 358.0455 $[M+H]^+$; ^1H NMR (600 MHz, $CDCl_3$, δ ppm) 8.62 (d, 1H), 8.52 (d, 1H), 8.37 (d, 1H), 8.01 (d, 1H), 7.83 (t, 1H), 4.15 (m, 1H) 2.54 (m, 2H) 1.90 (m, 2H), 1.74 (m, 2H), 1.45 (m, 2H), 0.87 (m, 2H); ^{13}C NMR (150.00 MHz, $CDCl_3$, δ ppm) 164.02, 163.98, 132.82, 131.88, 131.85, 131.10, 131.06, 130.40, 129.67, 128.96, 123.64, 122.78, 54.11, 29.71, 29.08, 26.49, 25.42, 22.83.

MCHN: White solid (645 mg, 86% yield); M.p. 72-74 ^oC; HRMS (*m/z*): calcd for $C_{18}H_{16}BrNO_2$ 371.053; found 372.0633 $[M+H]^+$; ^1H NMR (600 MHz, $CDCl_3$, δ ppm) 8.63 (d,

1H), 8.53 (d, 1H), 8.38 (d, 1H), 8.01 (d, 1H), 7.82 (t, 1H), 4.04 (d, 2H) 1.88 (m, 1H) 1.67 (m, 5H), 1.17 (m, 5H); ^{13}C NMR (150.00 MHz, $CDCl_3$, δ ppm) 164.12, 133.35, 132.28, 131.48, 131.26, 130.79, 130.34, 129.21, 128.26, 123.29, 122.43, 46.34, 36.88, 32.11, 31.14, 29.89, 26.53, 26.06.

Post functionalization: To different round bottom flasks, each containing the solution of **BN**, **HN**, **ON**, **CHN** and **MCHN** (0.5 mmol) in dry DMF (5 mL), 1 mmol of 8-hydroxyquinoline (for **HNN**, α-naphthol was taken) and 200 mg of K_2CO_3 were added to them separately and were refluxed for 15 hours. The solvents were vaporized under vacuum and the residues were extracted with chloroform (30×3 mL). The organic layers were washed with H_2O several times followed by washing with brine and dried over anhydrous Na_2SO_4. The crude products were concentrated and purified through column chromatography over silica gel to get the final products (**BNQ**, **HNQ**, **ONQ**, **CHNQ**, **MCHNQ,** and **HNN**) respectively.

BNQ: Light yellow solid (164 mg, 82 % yield); M.p. 177-179 ^{o}C; HRMS (*m/z*): calcd for $C_{25}H_{20}N_2O_3$ 396.147; found 397.1581 $[M+H]^+$; ^{1}H NMR (600 MHz, $CDCl_3$, δ ppm) 8.87 (m, 2H), 8.67 (d, 1H), 8.39 (d, 1H), 8.27 (d, 1H), 7.79 (m, 2H), 07.58 (d, 1H), 7.49 (d, 1H), 7.46 (d, 1H), 6.75 (d, 1H), 4.18 (t, 2H), 1.72 (m, 2H), 1.45 (m, 2H), 0.98 (t, 3H), ^{13}C NMR (150.00 MHz, $CDCl_3$, δ ppm) 164.71, 164.06, 160.58, 151.30, 150.99, 141.41, 136.48, 132.90, 132.05, 129.24, 129.18, 129.05, 126.95, 126.71, 126.65, 125.64, 124.06, 122.36, 120.28, 116.84, 111.57 40.53, 30.45, 20.60, 14.05.

HNQ: Yellow solid (155 mg, 73 % yield); M.p. 168-170 ^{o}C; HRMS (*m/z*): calcd for $C_{27}H_{24}N_2O_3$ 424.1787; found 425.1894 $[M+H]^+$; ^{1}H NMR (600 MHz, $CDCl_3$, δ ppm) 8.85 (d, 2H), 8.64 (d, 1H), 8.37 (d, 1H), 8.24 (d, 1H), 7.76-7.79 (m, 2H), 07.57 (t, 1H), 7.46 (d, 2H), 6.72(d, 1H), 4.14 (t, 2H), 1.70 (m, 2H), 1.32 (m, 6H), 86 (t, 3H), ^{13}C NMR (150.00 MHz, $CDCl_3$, δ ppm) 164.58, 163.93, 160.51, 151.11, 150.91, 141.31, 136.42, 132.84, 131.95, 130.24, 129.81, 129.16, 126.89, 126.62, 125.63, 123.91, 122.72, 122.29, 120.32, 116.84, 111.39, 40.53, 31.72, 28.25, 26.97, 22.73, 14.25.

ONQ: White solid (182 mg, 80 % yield); M.p. 150-153 ^{o}C; HRMS (*m/z*): calcd for $C_{29}H_{28}N_2O_3$ 452.210; found 453.2165 $[M+H]_+$; ^{1}H NMR (600 MHz, $CDCl_3$, δ ppm) 8.86 (d, 2H), 8.66 (d, 1H), 8.39 (d, 1H), 8.26 (d, 1H), 7. 79 (d, 2H), 07.59 (t, 1H), 7.48 (m, 2H), 6.74(d, 1H), 4.16 (t, 2H), 1.72 (m, 2H), 1.25-1.43 (m, 10H), 0.87 (t, 3H), ^{13}C NMR (150.00 MHz, $CDCl_3$, δ ppm) 164.69, 164.04, 160.56, 151.30, 150.98, 141.41, 136.51, 132.89, 132.04,

130.35, 129.94, 129.22, 126.96, 126.69, 125.65, 123.89, 122.76, 122.37, 120.30, 116.94, 111.35, 40.62, 32.02, 29.55, 29.43, 28.37, 27.37, 22.83, 14.28.

CHNQ: Light pink solid (170 mg, 80.5 % yield); M.p. 167-169 ^{o}C; HRMS (*m/z*): calcd for $C_{27}H_{22}N_2O_3$ 422.163; found 423.1719 $[M+H]^+$; ^{1}H NMR (600 MHz, $CDCl_3$, δ ppm) 8.87 (d, 1H), 8.84 (d, 1H), 8.64 (d, 1H), 8.37 (d, 1H), 8.26 (d, 1H), 7.78 (m, 2H), 7.58 (t, 1H), 7.44 (d, 1H), 7.43 (d, 1H), 6.75(d, 1H), 5.02 (m, 1H), 2.55 (m, 2H), 1.87 (m, 2H), 1.72 (m, 3H), 0.88 (m, 3H), ^{13}C NMR (150.00 MHz, $CDCl_3$, δ ppm) 165.11, 164.49, 160.24, 151.45, 150.95, 141.38, 136.47, 132.76, 131.92, 130.33, 129.91, 128.91, 126.93, 126.71, 125.50, 123.94, 122.73, 122.53, 120.08, 116.92, 111.79, 53.84, 29.89, 29.34, 26.78, 25.69, 22.88.

MCHNQ: Yellow solid (162 mg, 74 % yield); M.p. 189-191 ^{o}C; HRMS (*m/z*): calcd for $C_{28}H_{24}N_2O_3$ 436.178; found 437.1878 $[M+H]^+$; ^{1}H NMR (600 MHz, $CDCl_3$, δ ppm) 8.87 (m, 2H), 8.66 (d, 1H), 8.39 (d, 1H), 8.27 (d, 1H), 7.80 (m, 2H), 7.59 (d, 1H), 7.46 (d, 1H), 7.45 (d, 1H), 6.75(d, 1H), 4.05 (d, 2H), 1.72 (m, 1H), 1.63 (m, 2H), 1.22 (m, 4H), 0.88 (m, 3H), ^{13}C NMR (150.00 MHz, $CDCl_3$, δ ppm) 165.03, 164.39, 160.54, 151.30, 150.98, 141.39, 136.51, 133.00, 132.15, 130.34, 129.97, 129.22, 126.96, 126.70, 125.64, 123.99, 122.70, 122.37, 120.28, 116.95, 111.58, 46.23, 36.96, 32.12, 31.19, 29.89, 26.59, 26.11.

HNN: Light grey solid (189 mg, 89 % yield); M.p. 112-114 ^{o}C; HRMS (*m/z*): calcd for $C_{28}H_{25}NO_3$ 423.183; found 424.1926 $[M+H]^+$; ^{1}H NMR (600 MHz, $CDCl_3$, δ ppm) 8.88 (dd, 1H), 8.70 (dd, 1H), 8.38 (d, 1H), 7.93 (m, 2H), 7.83 (m, 2H), 7.54 (m, 2H), 7.28 (t, 1H), 6.77(d, 1H), 4.16 (t, 2H), 1.72 (m, 2H), 1.62 (m, 2H), 1.32 (m, 5H), 0.88 (t, 3H), ^{13}C NMR (150.00 MHz, $CDCl_3$, δ ppm) 164.41, 163.73, 160.19, 150.36, 135.21, 132.91, 131.91, 129.71, 128.47, 128.24, 126.99, 126.75, 126.73, 126.63, 125.91, 125.90, 123.54, 122.74, 121.44, 116.90, 116.61, 110.31, 40.42, 31.58, 28.09, 26.82, 22.59, 14.10.

2.3. Results and Discussion

2.3.1. Design, Synthesis and Characterization

Inspired by the proven applications of the 8-hydroxyquinoline moiety in various biosensing and therapeutics arenas,[28,31] the naphthalimide core was functionalized with 8-hydroxyquinoline and specific pendant hydrocarbon alkyl chains or rings. The core functionalized V-shaped naphthalimides were prepared in two steps, starting from commercially accessible 4-bromo-1,8-naphthalic anhydride (Scheme A2.1). The alkylation steps were first performed in each case before functionalization at the 4th position of the 1,8-

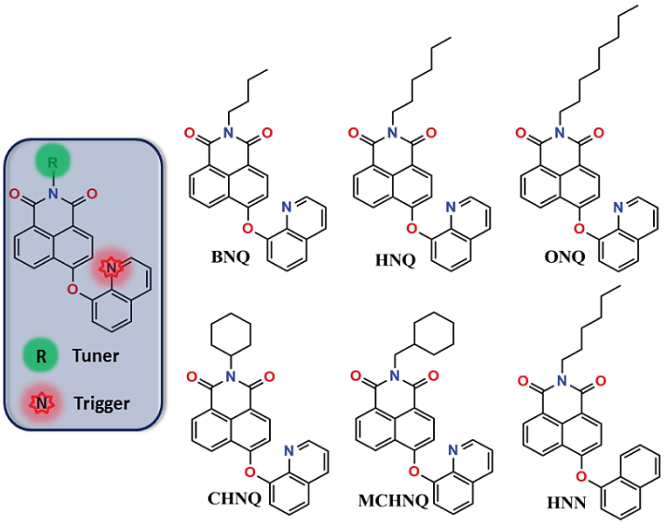

Figure 2.1. Chemical structures of the naphthalimide luminogens.

naphthalic anhydride core in consideration of solubility issues during purification and characterization. 4-Bromo-1,8-naphthalic anhydride and the respective alkyl or cycloalkylamines were refluxed in ethanol for 8 hours, leading to the formation of 4-bromo-N-alkylnaphthalimide precursors through condensation reactions (Scheme A2.1). The alkylated precursors were next functionalized with 8-hydroxyquinoline or α-naphthol by weak base assisted nucleophilic phenoxide substitution. All the congeners were well characterized by different techniques, such as ^{1}H and ^{13}C NMR spectroscopy, IR spectroscopy and HRMS; these can be found in the appendix.

2.3.2. AIEE Studies

DFT computational studies were performed for all the congeners using the 6-31G(d) basis set and the B3LYP hybrid functional incorporated in the Gaussian 09 package. The almost identical electronic states, dipole moments and dihedral angles for all the congeners signified the inertness of the pendant chains towards their photoluminescence (PL) properties (Figure A2.1). To confirm the above assumption, UV-Vis and fluorescence spectra of the congeners were recorded in DMF; these spectra clearly depicted almost analogous photophysical properties of the congeners in the solution state (λ_{abs} = 361 to 363 nm, λ_{emi} = 436 to 438 nm; for **HNN**, λ_{emi} = 412 nm) (Figure 2.2a). In contrast to the classical fluorophores, the emission intensities of the naphthalimides in the pure solution state decreased with increasing concentration, indicating the AIEE behavior of the congeners.[32-34] Having obtained this clue, the AIEE properties of the congeners at different f_w values in DMF were further investigated. To our delight, the fluorescence emission along with the

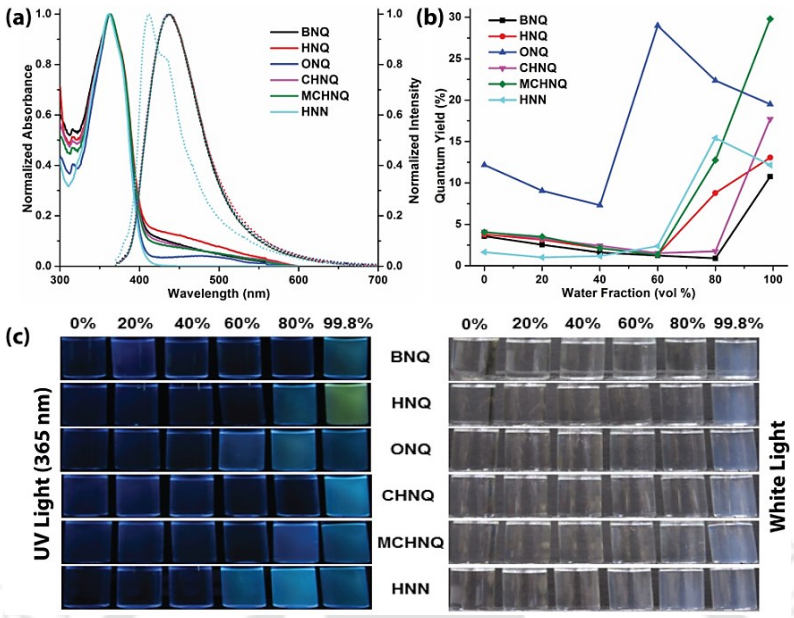

Figure 2.2. (a) Absorption (solid lines) and emission (dotted lines) spectra of all congeners at 20 μM concentrations in DMF (λ_{ex} = 360 nm). (b) Quantum yields of all congeners at different f_w values in DMF (20 μM). (c) Photographs of the naphthalimides at different f_w values in DMF under UV light (365 nm irradiation) and white light.

fluorescence quantum yields of the congeners increased (1.5 to 7 fold) at higher f_w values, although the naphthalimides are completely insoluble in water (Figure 2.2b, A2.2–A2.7, and Table A2.1). The increasing baselines with red-shifted absorption spectra and the turbidities of the solutions at higher f_w reflect nanoaggregate formation in each case (Figure 2.2 and A2.2–A2.7). Nanoaggregate formation is the prime factor in the enhanced red shifted emission of the fluorophores, where the well-known RIR (restriction in intramolecular rotation) phenomenon operates. In this series of naphthalimides, although the aromatic cores were similar, great differences were observed in the emission spectra of the compounds with varying pendant chains in the aggregated state (Figure A2.8). The distinct photophysical properties of the congeners with similar naphthalimide aromatic cores in their aggregated states (in contrast to their similar photophysical properties in their monomeric/solution states) substantiates the rare diversity of the intermolecular packing, which is fully controlled and directed by the pendant chains.

2.3.3. Study of Solid State Fluorescence Tuning

As intermolecular interactions are more prominent in the solid state than in the aggregated state, the solid state emission spectra of the congeners were carefully recorded. In contrast to the solution state, each of the congeners emitted distinctly in the solid state, with red-

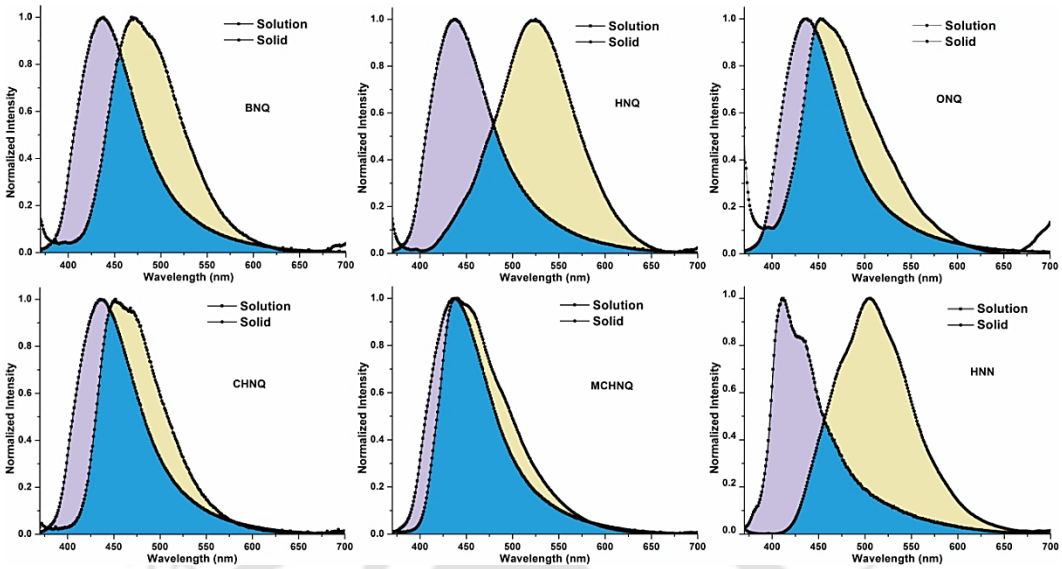

Figure 2.3. Solid-state emission spectra of the naphthalimide congeners (λ_{ex} = 360 nm) compared to their solution state (λ_{ex} = 360 nm, 20 μM DMF solutions) emissions.

shifts of nearly 2 to 100 nm in their emission maximum bands while moving from **MCHNQ** to **HNQ** (Figure 2.3 and 2.4a); this indicates transitions in their emission properties from the monomeric (solution) to the condensed state. The solution and solid-state emission spectra were plotted together in order to enable a convenient comparison (Figure 2.3). The achievement of this distinct red-shift in each of the congeners varying only in their side chains is conceptually very significant and can be attributed to the interruption of the pendant chain in the intermolecular packing energized by π–π interactions, which reduces the effective cumulative band gap in the condensed state. Thus, the visual appearances of the naphthalimides in the solid state under UV irradiation are greatly affected, with a distinct change in color from blue to light green (Figure 2.4b); this confirms the prominent role of the pendant chains. The ground state optimized structures showed that the pendant chains in **CHNQ** and **MCHNQ** increased the bulk around the naphthalimide core, which can restrict the aromatic planes closer to each other (Figure A2.1). Thus, **MCHNQ** and **CHNQ** showed very small red shifts in solid state luminescence from their corresponding solution state emissions (2 nm and 16 nm respectively) (Figure 2.3). Accordingly, the bulkiness of the pendant chain around the aromatic core can precisely control the intermolecular packing in each of the naphthalimides, thereby tuning their condensed state optical properties. As further support to this assumption, the solid state φ_F values for MC**HNQ** and C**HNQ** were found to be the highest (27.0 ± 0.9 and 26.1 ± 1.1, respectively) within the series, reflecting their weaker intermolecular interactions in the condensed state compared to the other congeners.[28,35,36] In contrast, the comparatively lower solid state φ_F of **HNQ** (9.4 ± 0.6) may

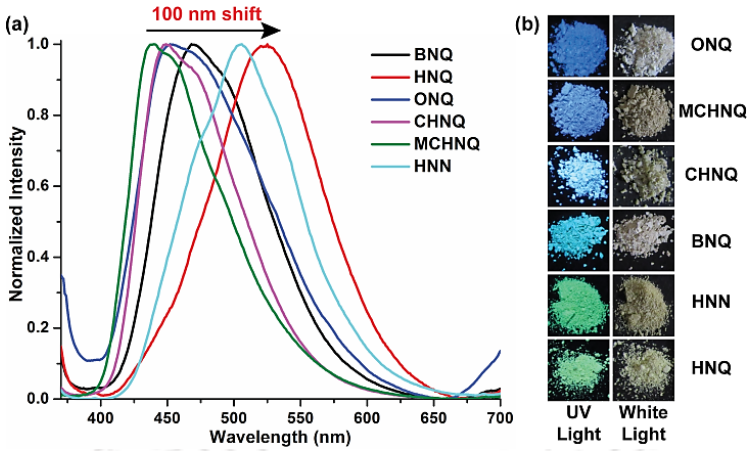

Figure 2.4. (a) Solid-state emission spectra of the compounds (λ_{ex} = 360 nm). (b) Digital photographs of the compounds under UV light (365 nm) illumination and white light illumination

be due to the strong coupling of electronic states between adjacent molecules, which facilitates non-radiative relaxation pathways (Table A2.1).[29,35,36].

2.3.4. XRD Analysis

To obtain further insight into their intermolecular interactions, we attempted to obtain single crystals of the naphthalimides. Unfortunately, even after several attempts, except for **HNQ** (CCDC 1452816), the quality of the single crystals we obtained for **BNQ** and **HNN** were inappropriate for X-ray crystallography studies, whereas the single crystals of the remaining derivatives were also inferior. In **HNQ**, the involvement of strong intermolecular multiple π–π interactions (3.596 to 3.773 Å considering the centroid-to-centroid distance, 3.346 to 3.526 Å considering the shortest distance) along with multiple CH–X bonds, where, X = N, O, or π (2.449 to 3.561 Å), led to the formation of highly ordered *J*-aggregates in the condensed state, with a maximum red-shifted emission band (Figure 2.5a). Powder X-ray diffraction (PXRD) measurements were performed in order to obtain information about the intermolecular π–π interactions in the other congeners. The PXRD patterns of the naphthalimides were compared with the simulated PXRD pattern generated from the SC-XRD data of **HNQ** (Figure 2.5b). None of the congeners except **HNQ** showed sharp multiple peaks between 2θ angles of 19 to 27°, corresponding to the *d*-spacing of 4.667 to 3.299 Å between the aromatic planes; this reflected the presence of comparatively weak intermolecular interactions.[27-39] The broad peaks in this region symbolize the distorted packing of aromatic cores with varying *d*-spacing. Thus, from both the PXRD and SC-XRD data analysis, it can be concluded that the geometry and bulkiness of the pendant chain

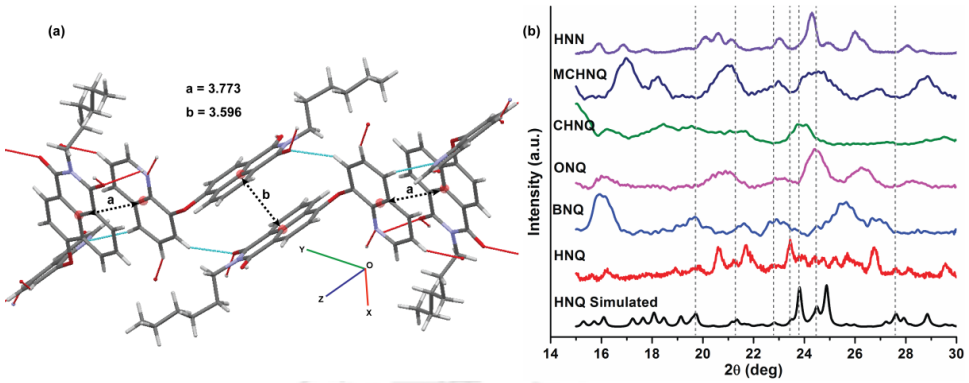

Figure 2.5. (a) Crystal packing diagram of HNQ showing multiple intermolecular π–π and CH–X (X = N, O, π) interactions. (Values are given in Å.) (b) Wide-angle X-ray diffractograms of bulk solids compared with the simulated powder-XRD pattern of HNQ determined from its single crystal results.

controls the packing orientation and coupling of electronic states between neighboring molecules via intermolecular π–π interactions.

2.3.5. Self-Assembly Analysis

Striking variations in the aggregation, solid state emission and powder XRD patterns of these quinolone-functionalized naphthalimide AIEEgens evidenced a profound pendant chain effect; if these implicit suppositions are accurate, this effect could be exploited to tune the morphologies of the aggregates. Dynamic light scattering (DLS) studies of the naphthalimide aggregates (20 μM) were carried out in aqueous media and confirmed the presence of stable and monodispersed nanoaggregates of different sizes from 166 to 281 nm (Figure A2.9–A2.10). This clearly indicates the pendant chain-dependent formation of nanoaggregates in each of the congeners. To comprehend their morphologies, FESEM images of the naphthalimide aggregates were obtained. It was observed that under precisely similar conditions, the AIEEgens formed distinctive nanostructures and microstructures depending upon the respective pendant chain attached to the naphthalimide core (Figure 2.6). **BNQ** formed elongated square bipyramidal-like structures of various sizes, whereas **ONQ** formed symmetrical nanospheres with diameters of nearly 250 nm. **CHNQ** and **MCHNQ** formed microfiber and nanorod-like morphologies, respectively, while **HNQ** showed a highly regular nanoribbon-like morphology. Although the derivatives have similar electronic environments (evidenced from DFT computational studies), they have enormous morphological disparities in their aggregated states (Figure A2.1). This tuning of their nanomorphologies can be attributed to the variation of the pendant chains and established its control of the intermolecular packing in terms of bulkiness. For example, **HNQ** and **ONQ**

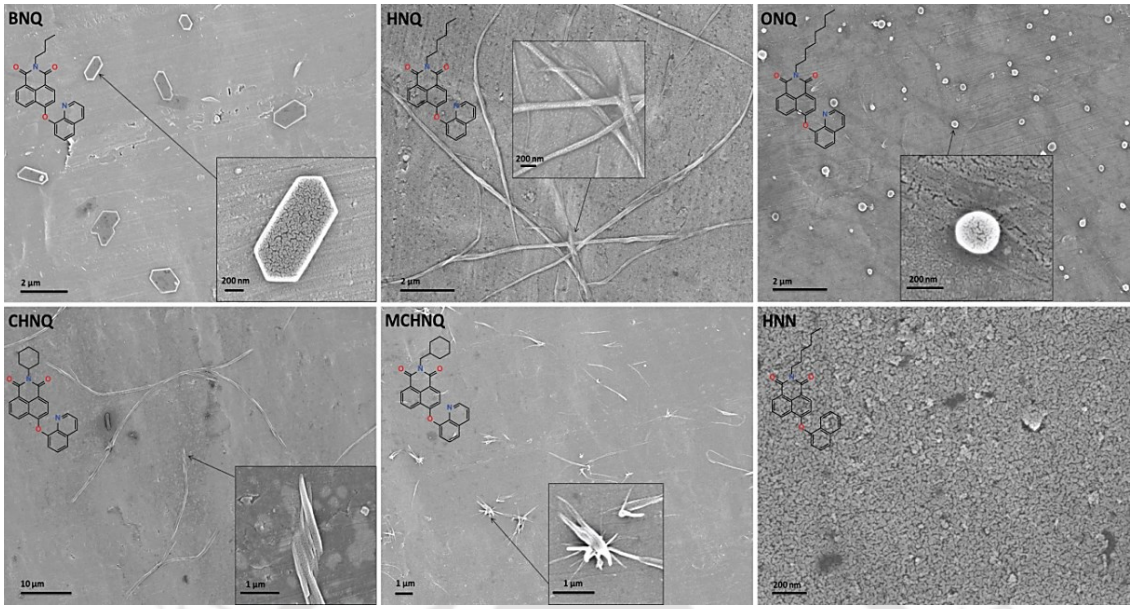

Figure 2.6. FESEM images of the nano and microstructures of the luminogens formed in 99.9% f_w (10 μM) by a simple dropcasting technique. The insets show the corresponding chemical structures (left) and magnified images (right).

have nearly identical band gaps (3.787 eV and 3.794 eV, respectively) and dipole moments (7.883 d and 7.889 d, respectively); however, an enormous variation exists in their nanomorphologies owing to their distinct intermolecular arrangements in the aggregated state. Despite also having very similar molecular structures, **HNN** formed distorted nanoparticles while **HNQ** formed well-organized nanoribbon-like structures; this clearly demonstrates the triggering nature of the single N-atom of the quinoline ring in the aggregated and solid states (Figure 2.6). These morphological variations strengthened the proposition that even when using the same aromatic core with analogous platforms and conditions, the nanoaggregate morphologies can be tuned efficiently by careful choice of the pendant chains.

2.3.6. Detection of Ferritin

Considering the higher surface area, the green emitting nanoribbons of 8-hydroxyquinoline substituted naphthalimide (**HNQ**) at 20 mM concentration were employed to interact with iron containing heme and non-heme metalloproteins in aqueous media. The elevated levels, localization and accumulation of these metalloproteins in the brain lead to many neurodegenerative diseases, such as Alzheimer's disease, Parkinson's disease, amyotrophic lateral sclerosis, prion disease and Huntington's disease.[15,40] The metalloproteins used in this

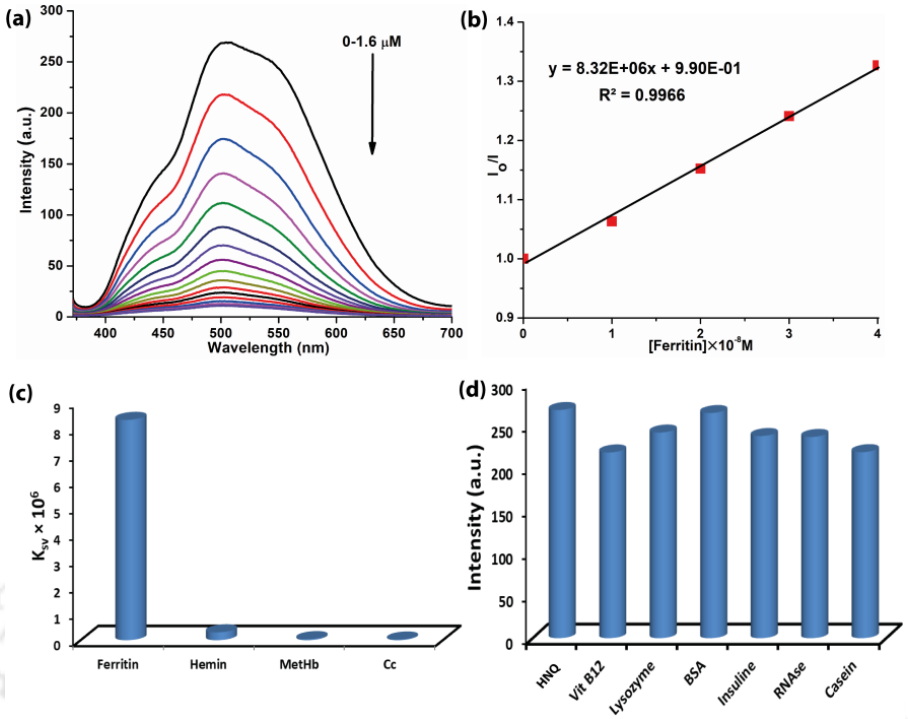

Figure 2.7. Fluorescence response of **HNQ** (20 μM) toward proteins and hemin was checked at pH 7.4 in Tris-HCl solution (a) ferritin was added up to a concentration of 1.6 μM, (b) Stern–Volmer plot for ferritin. (c) Bar diagram depicting the changes observed in K_{sv}. (d) Bar diagram depicting the changes observed in the fluorescence intensity of **HNQ** in the presence of various proteins up to 20 μM.

study comprise ferritin, MetHb, Cc, insulin, Vit B12 and nonmetalloproteins, such as lysozyme, BSA and casein along with protoporphyrin IX hemin. It was observed that the fluorescent nanoribbons are highly sensitive towards ferritin (K_{sv} = 0.83 × 10^7 M^{-1}, R^2 = 0.9966) with a LOD of 0.33 ng mL^{-1} (67.25 × 10^{-11} M) at pH 7.4 in Tris-HCl buffer (Figure 2.7a–c and A2.11, also see the appendix for the calculation of the detection limit). Other iron containing metalloproteins studied here showed very low sensitivity with a K_{sv} value of 0.29 × 10^6 M^{-1} for hemin, 0.04 × 10^6 M^{-1} for MetHb and 0.02 × 10^6 M^{-1} for Cc (Figure 2.7c and A2.12–A2.13). Conclusively, **HNQ**-nanoribbons were found to be highly sensitive towards non-heme metalloproteins. Since the heme group consists of a porphyrin ring in which iron ion is coordinated by four pyrrole moieties, there is a possibility of some competition between **HNQ**-nanoribbons and the porphyrin ring to bind iron. The interaction of **HNQ**-nanoribbons with metalloproteins Vit-B12 and insulin (containing metal ions other than Fe^{2+} or Fe^{3+}) along with nonmetalloproteins BSA, lysozyme, casein and RNAse was also studied (Figure 2.7d and A2.14–A2.15). However, the fluorescence of **HNQ**-nanoribbons was barely affected by these metalloproteins, even at higher concentrations (30 μM) as compared to ferritin (1.6 μM).

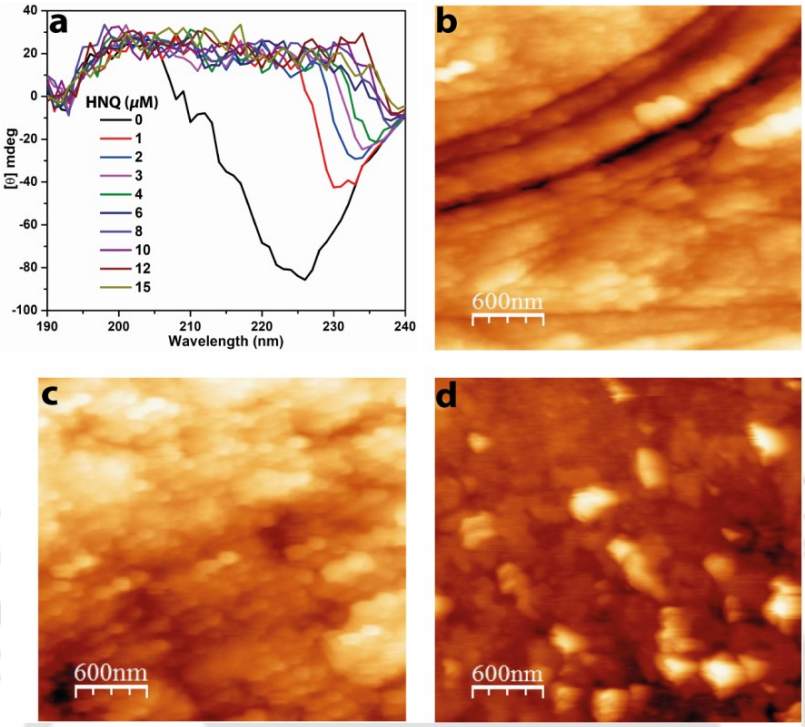

Figure 2.8. (a) Far-UV circular dichorism spectra of 10 μM ferritin measured in the presence of different concentrations of **HNQ**. AFM topography images of 10 μM of **HNQ** in the presence of 0.3 μM (b), 0.7 μM (c), and 1.3 μM (d) of ferritin formed from the evaporation of a 99.9% H_2O–0.1% DMF mixture on a glass slide at 37 ^oC.

2.3.7. Evaluation of Detection Mechanism

Furthermore, to explore the impact of **HNQ**-nanoribbons on the microenvironment of non-heme protein ferritin, circular dichroism (CD) spectra were recorded to monitor the structural transformations in the protein secondary structure (Figure 2.8a). The far-UV region extending from 180 to 250 nm reveals information about the peptide bond asymmetric environment, the secondary structure of proteins and can predict the conformational changes in it.[26,27] Ferritin (10 μM) in Tris-HCl buffer gave a characteristic peak at 225 nm, assigned to the percentage of the α-helix, turn and random structures present in the protein. Addition of a very small amount of **HNQ** (1 μM) was found to modify the random conformation of ferritin completely, but affect the α-helix content slightly. Steady addition of **HNQ** probe up to 15 μM concentration showed that the α-helix content was diminished completely (Figure 2.8 and Table A2.3). From the observed CD data, it was concluded that the α-helix content of ferritin could be unfolded effectively by using the

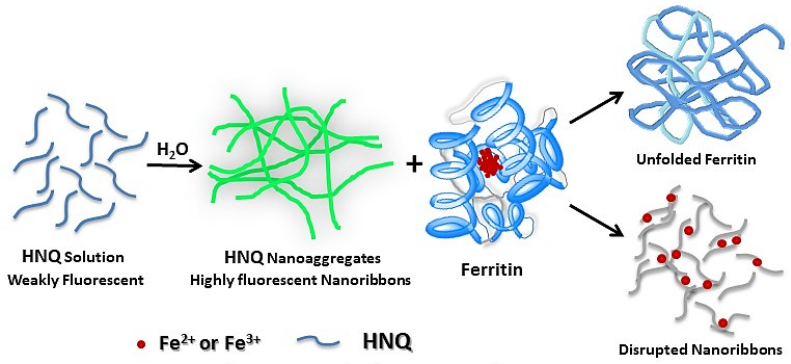

Figure 2.9. Illustration of the mechanism of protein unfolding and nanoribbon disruption using a fluorescent probe under physiological conditions with AIEE characteristics.

AIEE-active nanoribbons, thereby bringing conformational alterations in the microenvironment of metalloprotein that have therapeutic potential toward tumor progression and therapy resistance.[24,25,41,42] These results also confirm that the activity of proteins can be controlled efficiently by using **HNQ**-nanoribbons.[26] Again the amendment in the **HNQ**-nanoribbons, which leads to quenching in its fluorescence intensity, was confirmed through the AFM topography study (Figure 2.8b-2.8d). AFM images of 10 μM of **HNQ** with varying concentrations of ferritin were obtained, which give a clear idea of nanoribbon disruption. Addition of only 0.3 μM of ferritin (Figure 2.8b) significantly disrupted the nanoribbon morphology, and upon further addition of up to 1.3 μM of ferritin (Figure 2.8d) a complete change in AFM topography was observed. The disruption of nanoribbons (sensing mechanism) along with the unfolding in the ferritin secondary structure can be correlated with the presence of an 8-hydroxyquinoline moiety, which selectively binds with Fe^{2+} and Fe^{3+} ions,[15] within the available iron pool of ferritin and confirmed the path of protein unfolding. To confirm the fluorescence response of **HNQ** (20 μM) towards Fe^{2+} and Fe^{3+} ions the fluorescence spectra were recorded in Tris-HCl buffer under physiological conditions (Figure A2.16). It was confirmed that **HNQ** nanoribbons were more sensitive towards Fe^{3+} (K_{sv} = 54122 M^{-1}) than to Fe^{2+} (K_{sv} = 40314 M^{-1}). Thus, binding of metal ions with the quinoline moieties could be the primary reason that deteriorates the intermolecular head-to-tail π–π interactions, thereby disrupting the fluorescent nanoribbons into non-fluorescent co-aggregates (Figure 2.9).

2.4. Conclusion

In summary, a series of quinolone-substituted structurally similar naphthalimide AIEEgens were investigated; for the first time, the significant effects of apparently related pendant

chains were demonstrated in controlling the solid-state emissions and supramolecular self-assembly properties of these organic small molecules. The fine tuning of their aggregate morphologies and solid state luminescence properties was correlated with their variance in intermolecular packing. Finally, highly fluorescent nanoaggregates of **HNQ** with higher surface area formed in water were employed to detect multi-functional nonheme protein ferritin with a LOD of 67.25 × 10^{-11} M (0.33 ng mL^{-1}), which is the best observation in the literature using an AIEEgen under physiological conditions. Besides, the **HNQ** nanoribbons ensure its potential to induce conformational modification in the secondary structure of ferritin with an extremely controlled unfolding of the α-helix was achieved by varying the concentration of **HNQ** that can have potential applications to study structurally transformed protein intermediates and may be obliging for clinical therapeutic purposes for cancer therapy and several neurodegenerative diseases. Therefore, apart from the highly sensitive detection of ferritin in physiological conditions, the performed study provides a conceptually unique yet simple and effective tool to tune supramolecular self-assembly of organic small molecules for optoelectronic application.

References

(1) Mei, J.; Hong, Y.; Lam, J. W. Y.; Qin, A.; Tang, Y.; Tang, B. Z. *Adv. Mater.* **2014**, *26*, 5429–5479.

(2) Ding, D. Li, K.; Liu, B.; Tang, B. Z. *Acc. Chem. Res.* **2013**, *46*, 2441–2453.

(3) Yuan, Y.; Feng, G.; Qin, W.; Tang, B. Z.; Liu, B. *Chem. Commun.* **2014**, *50*, 8757–8760.

(4) Mas-Torrent, M.; Rovira, C. *Chem. Soc. Rev.* **2008**, *37*, 827–838.

(5) Walker, B.; Kim, C.; Nguyen, T.-Q. *Chem. Mater.* **2011**, *23*, 470–482.

(6) Lin, Y.; Li, Y.; Zhan, X. *Chem. Soc. Rev.* **2012**, *41*, 4245–4272.

(7) Zhang, C.; Liu, Z.; Li, Y.; He, W.; Gao, X.; Guo, Z. *Chem. Commun.* **2013**, *49*, 11430–11432.

(8) Lee, M. H.; Han, J. H.; Lee, J.-H.; Choi, H. G.; Kang, C.; Kim, J. S. *J. Am. Chem. Soc.* **2012**, *134*, 17314–17319.

(9) Dong, Y.; Xu, B.; Zhang, J.; Tan, X.; Wang, L.; Chen, J.; Lu, H.; Wen, S.; Li, B.; Ye, L.; Zou, B.; Tan, W. *Angew. Chem., Int. Ed.* **2012**, *51*, 10782–10785.

(10) Yan, D.; Delori, A.; Llyod, G. O.; Friscic, T.; Day, G. M.; Jones, W.; Lu, J.; Wei, M.; Evans, D. G.; Duan, X. *Angew. Chem., Int. Ed.* **2011**, *50*, 12483–12486.

(11) Bolton, O.; Lee, K.; Kim, H.-J.; Lin, K. Y.; Kim, J. *Nat. Chem.* **2011**, *3*, 205–210.

(12) Hochbaum, A. I.; Yang, P. *Chem. Rev.* **2010**, *110*, 527–546.

(13) Palmer, L. C.; Stupp, S. I. *Acc. Chem. Res.* **2008**, *41*, 1674–1684.

(14) Hasegawa, M.; Iyoda, M. *Chem. Soc. Rev.* **2010**, *39*, 2420–2427.

(15) Muthuraj, B.; Hussain, S.; Iyer, P. K. *Polym. Chem.* **2013**, *4*, 5096–5107.

(16) Wang, F.; Wen, J.; Huang, L.; Huanga, J.; Ouyang, J. *Chem. Commun.* **2012**, *48*, 7395–7397.

(17) Fan, J.; Ding, L.; Bo, Y.; Fang, Y. *ACS Appl. Mater. Interfaces* **2015**, *7*, 22487–22496.

(18) Dwivedi, A. K.; Iyer, P. K. *Macromol. Biosci.* **2014**, *14*, 508–514.

(19) Wang, L.; Liu, Y.; Yang, J.-X.; Tao, X.; Liu, Z. *Chem. Commun.* **2012**, *48*, 5742–5744.

(20) Miranda, O. R.; Chen, H.-T.; You, C.-C.; Mortenson, D. E.; Yang, X.-C.; Bunz, U. H. F.; Rotello, V. M. *J. Am. Chem. Soc.* **2010**, *132*, 5285–5289.

(21) Jiwpanich, S.; Sandanaraj, B. S.; Thayumanavan, S. *Chem. Commun.* **2009**, 806–808.

(22) Sandanaraj, B. S.; Demont, R.; Thayumanavan, S. *J. Am. Chem. Soc.* **2007**, *129*, 3506–3507.

(23) Sandanaraj, B. S.; Demont, R.; Aathimanikandan, S. V.; Savariar, E. N.; Thayumanavan, S. *J. Am. Chem. Soc.* **2006**, *128*, 10686–10687.

(24) Kell, D. B.; Pretorius, E. *Metallomics* **2014**, *6*, 748–773.

(25) Alkhateeb, A. A.; Connor, J. R. *Biochim. Biophys. Acta* **2013**, *1836*, 245–254.

(26) Dwivedi, A. K.; Prasad, K. M.; Trivedi, V.; Iyer, P. K. *ACS Appl. Mater. Interfaces* **2012**, *4*, 6371–6377.

(27) Divsalar, A.; Bagheri, M. J.; Saboury, A. A.; Torshizi, H. M.; Amani, M. *J. Phys. Chem. B* **2009**, *113*, 14035–14042.

(28) Meher, N.; Chowdhury, S. R.; Iyer, P. K. *J. Mater. Chem. B* **2016**, *4*, 6023–6031.

(29) Yang, Y.; Su, X.; Carroll, C. N.; Aprahamian, I. *Chem. Sci.* **2012**, *3*, 610–613.

(30) Fankuchen, I. *J. Biol. Chem.* **1943**, *150*, 57-59.

(31) Chowdhury, S. R.; Agarwal, M.; Meher, N.; Muthuraj, B.; Iyer, P. K. *ACS Appl. Mater. Interfaces* **2016**, *8*, 13309–13319.

(32) Sylvia, J. M.; Janni, J. A.; Klein, J. D.; Spencer, K. M. *Anal. Chem.* **2000**, *72*, 5834–5840.

(33) Hodyss, R.; Beauchamp, J. L. *Anal. Chem.* **2005**, *77*, 3607–3610.

(34) Popov, A.; Chen, H.; Kharybin, O. N.; Nikolaev, E. N.; Cooks, R. G. *Chem. Commun.* **2005**, 1953–1955.

(35) Yan, D.; Evans, D. G. *Mater. Horiz.* **2014**, *1*, 46–57.

(36) Varughese, S. *J. Mater. Chem. C* **2014**, *2*, 3499–3516.

(37) Vasimalla, S.; Senanayak, S. P.; Sharma, M.; Narayan, K. S.; Iyer, P. K. *Chem. Mater.* **2014**, *26*, 4030–4037.

(38) Shin, S.; Gihm, S. H.; Park, C. R.; Kim, S.; Park, S. Y. *Chem. Mater.* **2013**, *25*, 3288–3295.

(39) Mandal, J.; Prasad, S. K.; Rao, D. S. S.; Ramakrishnan, S. *J. Am. Chem. Soc.* **2014**, *136*, 2538–2545.

(40) Sayre, L. M.; Perry, G.; Smith, M. A. *Curr. Opin. Chem. Biol.* **1999**, *3*, 220–225.

(41) Heegaard, N. H. H.; Rovatti, L.; Nissen, M. H.; Hamdan, M. J. *J. Chromatogr. A* **2003**, *1004*, 51–59.

(42) Jorgensen, C. S.; Ryder, L. R.; Steino, A.; Hojrup, P.; Hansen, J.; Beyer, N. H.; Heegaard, N. H. H.; Houen, G. *Eur. J. Biochem.* **2003**, *270*, 4140–4148.

Appendix

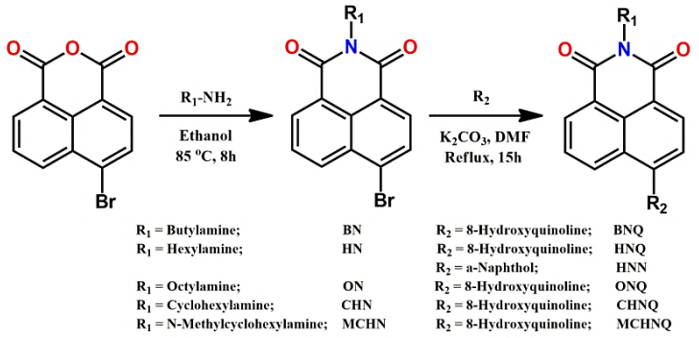

Scheme A2.1: Synthetic route to **naphthalimides**.

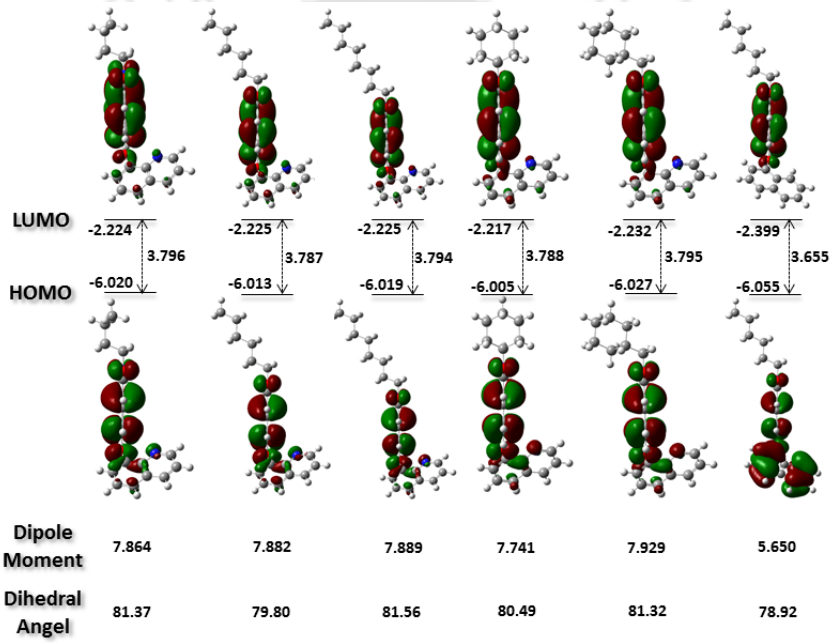

Figure A2.1. Optimized structures in electronic ground state with electron density of HOMO and LUMO (Gaussian 03, DFT B3LYP 6-31G basis set). Energy of HOMO, LUMO and band gaps are in eV, dipole moments are in debye and dihedral angels are in "o" with respect to naphthalimide and quinoline/naphthalene plane. (Left to Right: **BNQ, HNQ, ONQ, CHNQ, MCHNQ** and **HNN**).

Table A2.1. Photophysical properties of Naphthalimide AIEgens with various f_w (0%-99%) in DMF at 20 μM concentration.

Compound	f_w in DMF	$\lambda_{abs.\,max}$ [nm]	ε^a [$M^{-1}cm^{-1}$]	$\lambda_{em.\,max}{}^b$ [nm]	Stokes shift $\Delta\lambda$/nm	Φ_{FL} [%]^c	Φ_{FL} (%) (solid)
BNQ	0%	363	2882.525	435	72	3.57	16.9±1.2
	20%	365	3103.35	438	73	2.53	
	40%	365	2913.575	442	77	1.60	
	60%	369	2247.975	443	74	1.23	
	80%	371	2028.475	444	73	0.89	
	99.8%	374	2466.625	474	100	10.77	

HNQ	0%	362	3125.425	435	73	3.76	9.4±0.6
	20%	365	2971.475	439	74	3.15	
	40%	368	2816.45	457	89	2.11	
	60%	391	2755	493	102	1.31	
	80%	389	2530.775	494	105	8.78	
	99.8%	390	2879.6	494	104	13.06	
ONQ	0%	363	3100	438	75	12.17	21.3±0.8
	20%	365	3204.575	441	76	9.05	
	40%	366	2325.25	445	79	7.30	
	60%	368	2206.45	447	79	28.98	
	80%	369	2959.25	448	79	22.37	
	99.8%	370	3074.1	457	87	19.51	
CHNQ	0%	363	2808.95	436	73	4.10	26.1±1.1
	20%	365	3233.3	443	78	3.25	
	40%	366	2485.075	443	77	2.41	
	60%	367	2216.225	447	80	1.52	
	80%	368	2206.675	438	70	1.73	
	99.8%	389	2959.9	464	75	17.70	
MCHNQ	0%	363	2721.125	438	75	4.05	27.0±0.9
	20%	365	2652.25	444	79	3.50	
	40%	366	2310.225	444	78	2.13	
	60%	368	2474.075	442	74	1.32	
	80%	365	1940.35	444	79	1.27	
	99.8%	373	2601.45	457	84	29.79	
HNN	0%	362	3400.925	412	50	1.64	11.7±0.8
	20%	364	3457.475	411	47	1.01	
	40%	366	3404.375	429	63	1.16	
	60%	368	3069.7	429	61	2.36	
	80%	370	3601.175	482	112	15.42	
	99.8%	383	3915.85	481	98	12.16	

[a]Measured at each absorption maximum. [b]Excited at 360 nm for all compounds. [c]Quantum yields were calculated by using quinine sulfate (0.1 M H_2SO_4, λ_{ex} = 350 nm, Φ_{FL} = 57.7%) solution as reference together with the following formula: $\Phi_{FL}=\Phi_{FL}(I/I_R)(A_R/A)(\eta^2/\eta_R^2)$, where Φ = quantum yield, I = Intensity of emission, A = absorbance at λ_{ex}, η = refractive index of solvent, R = reference. (20 μM)

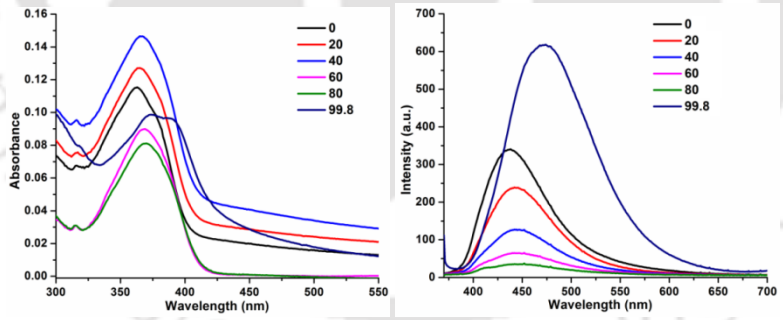

Figure A2.2. Absorption (left) and emission spectra (right) of **BNQ** (at 25 °C, 20 μM, λ_{ex} = 360 nm).

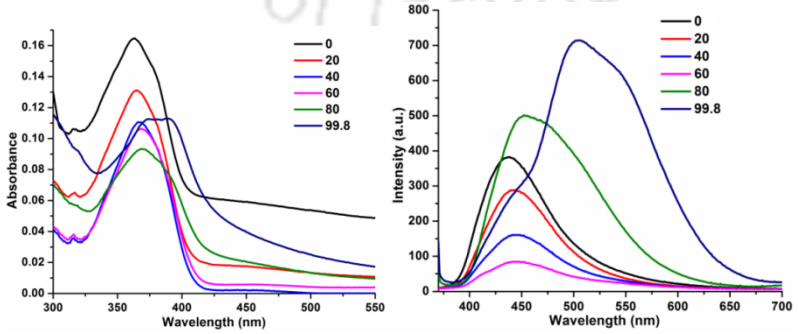

Figure A2.3. Absorption (left) and emission spectra (right) of **HNQ** (at 25 °C, 20 μM, λ_{ex} = 360 nm).

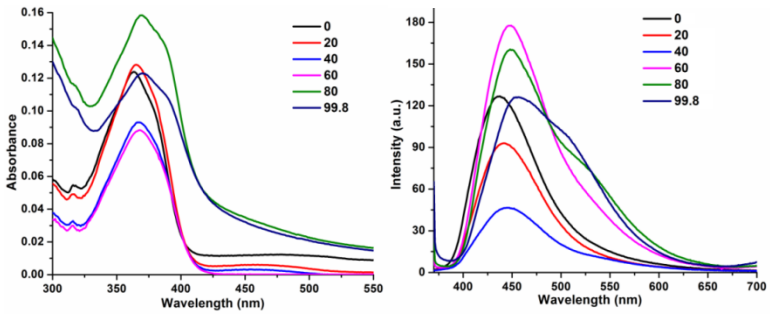

Figure A2.4. Absorption (left) and emission spectra (right) of **ONQ** (at 25 °C, 20 μM, λ_{ex} = 360 nm)**.**

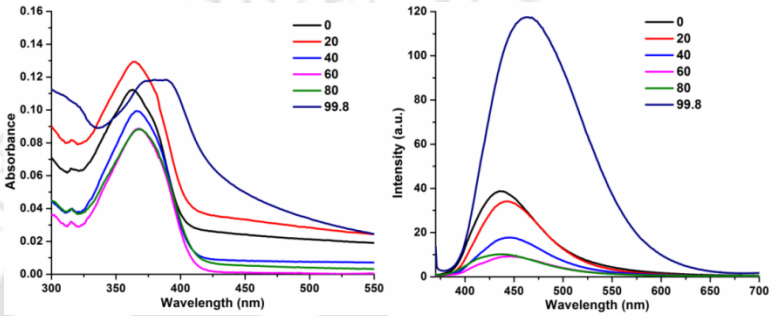

Figure A2.5. Absorption (left) and emission spectra (right) of **CHNQ** (at 25 °C, 20 μM, λ_{ex} = 360 nm)**.**

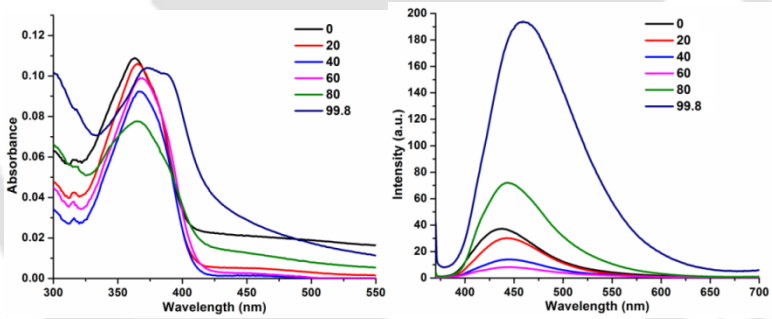

Figure A2.6. Absorption (left) and emission spectra (right) of **MCHNQ** (at 25 °C, 20 μM, λ_{ex} = 360 nm)**.**

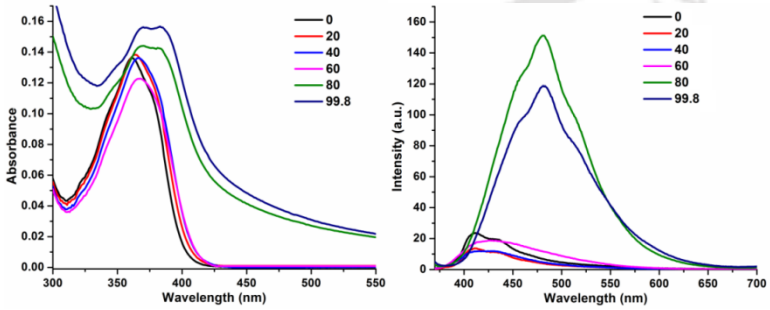

Figure A2.7. Absorption (left) and emission spectra (right) of **HNN** (at 25 °C, 20 μM, λ_{ex} = 360 nm)**.**

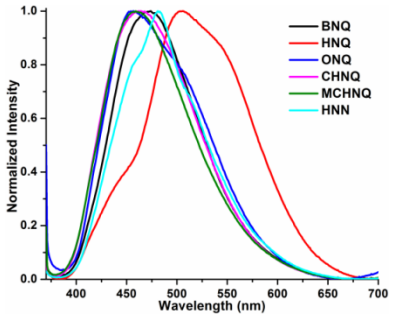

Figure A2.8. Emission spectra in 99.8% water-0.2% DMF. (20 μM, λ_{ex} 360 nm)

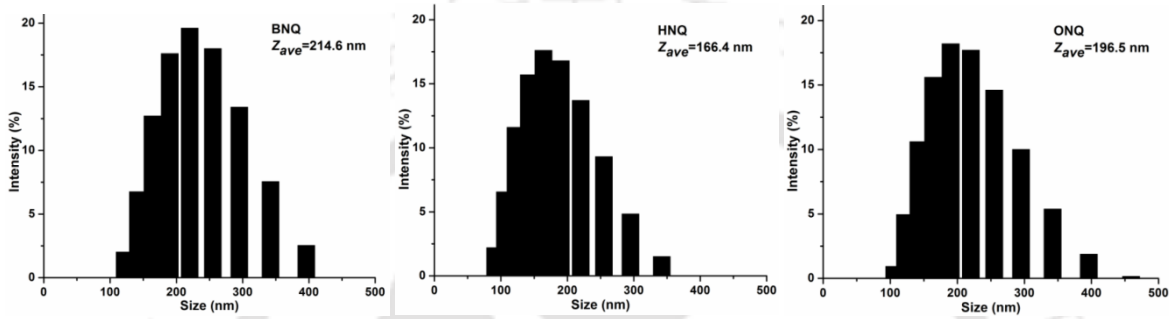

Figure A2.9. Size distribution by DLS of **BNQ**, **HNQ** and **ONQ** aggregate respectively (99.8% Water-0.2% DMF mixture solution at 25 °C, 20 μM).

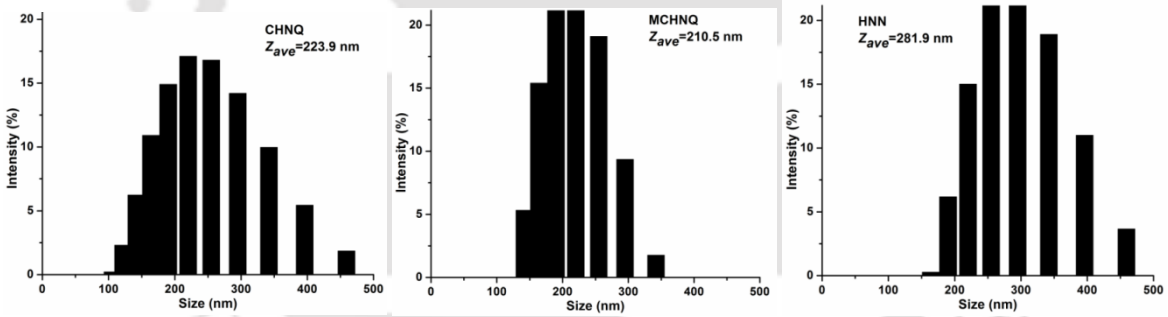

Figure A2.10. Size distribution by DLS of **CHNQ**, **MCHNQ** and **HNN** aggregate respectively (99.8% Water-0.2% DMF mixture solution at 25 °C, 20 μM).

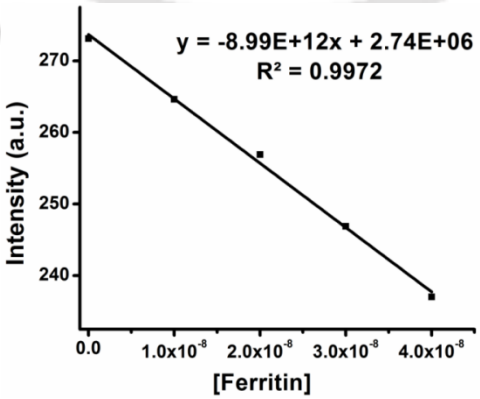

Figure A2.11 Fluorescence response of **HNQ** (20 μM) taken in aqueous solution (at pH 7.4) as a function of Ferritin concentration.

LOD = 3 × S.D. / k

LOD = 3 × 2015.279 / 8.99×10^{12}

= 67.25×10^{-11} M (0.33 ng/μL)

Table A2.2. A comparative study of the K_{sv} and detection limit along with material and medium used for Ferritin detection of some representative reports.

Publication	Material Used	K_{sv} (M^{-1})	Detection Limit	Medium Used
Present Manuscript	**AIEEgen**	**0.83×10^7**	**67.25×10^{-11} M (0.33 ng μL^{-1})**	**Buffer (pH=7.4)**
Chem. Commun. **2012**, 48, 7395–7397	AIEgen	---	0.78 ng μL^{-1}	BSPSA staining
ACS Appl. Mater. Interfaces **2015**, 7, 22487–22496	Bispyrene Surfactant Assembly	1.71×10^7	---	HEPES
Macromol. Biosci. **2014**, 14, 508–514	Polymer	0.37×10^7	---	Buffer (pH=7.4)
Polym. Chem. **2013**,4, 5096-5107	Polymer	0.84×10^7	---	THF:Water v/v=4:1
Chem. Commun. **2012**, 48, 5742–5744	Microparticle	0.057×10^7	---	Buffer (pH 7.4)
J. Am. Chem. Soc., **2010**, *132, 5285–5289*	β-Gal/AuNP	---	100×10^{-11} M	Buffer
Chem. Commun. **2009**, 806–808	Dendrimers	0.20×10^7	---	Buffer
J. Am. Chem. Soc. **2007**, 129, 3506–3507	Polymer-Dye" complex	0.10×10^7	---	Water
J. Am. Chem. Soc. **2006**, 128, 10686-10687	Polymer	0.10×10^7	---	Water

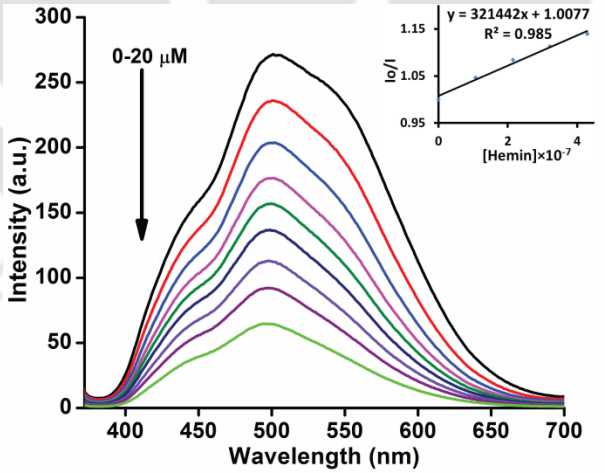

Figure A2.12. Effect of increasing concentration of Hemin on the fluorescence spectra of **HNQ** (20 μM at pH 7.4) at room temperature. Inset is the Stern–Volmer plots for the fluorescence quenching of **HNQ** by hemin.

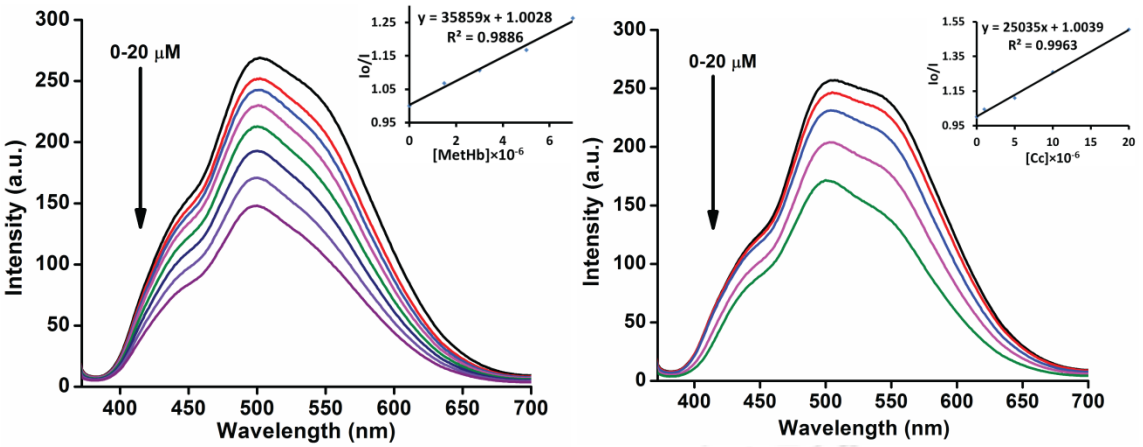

Figure A2.13. Effect of increasing concentration of MetHb and Cc on the fluorescence spectra of **HNQ** (20 μM at pH 7.4) at room temperature. Inset is the respective Stern–Volmer plots for the fluorescence quenching of **HNQ** by MetHb and Cc.

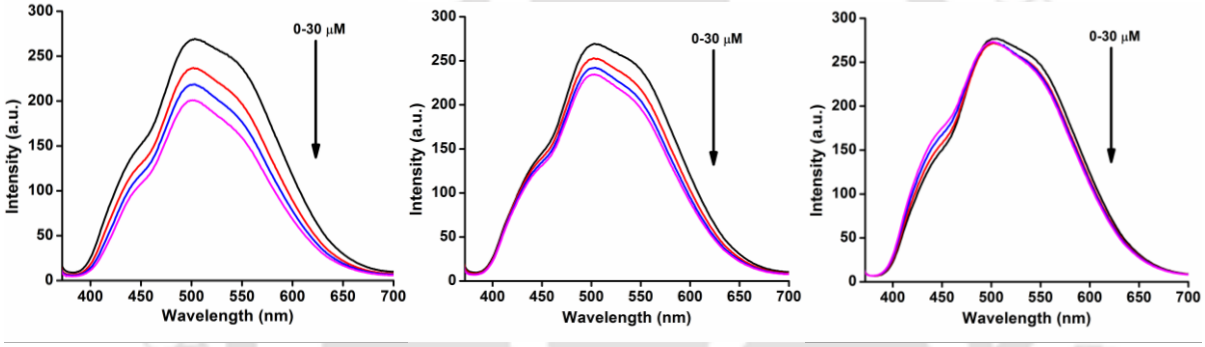

Figure A2.14. Effect of increasing concentration of Vit B_{12}, Lysozyme and BSA on the fluorescence spectra of **HNQ** (20 μM at pH 7.4) at room temperature (From left to right respectively).

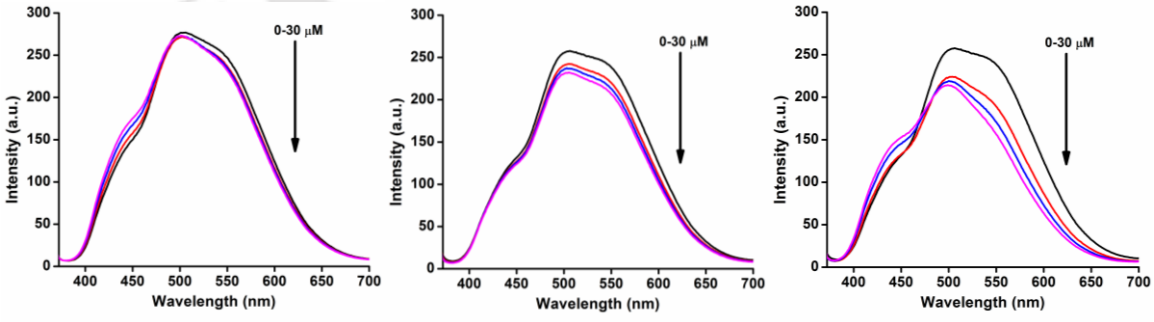

Figure A2.15. Effect of increasing concentration of Insuline, RNAse and Casein on the fluorescence spectra of **HNQ** (20 μM at pH 7.4) at room temperature (from left to right respectively).

Table A2.3. Changes in the secondary structure of ferritin upon interaction with **HNQ**-nanoribbons at different concentration.

[HNQ] in μM	% α-helix	% turn	% random coil
0	32	34.8	33.2
1	35.9	64.1	0
2	34.2	65.6	0
3	30.5	69.5	0
4	25.8	74.2	0
6	24.5	75.5	0
8	18.2	81.8	0
10	15	85	0
12	4.7	95.3	0
15	0	100	0

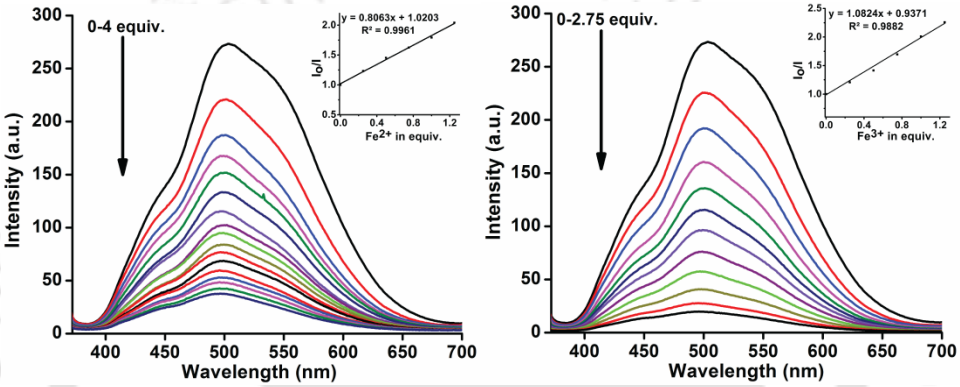

Figure A2.16. Fluorescence response of **HNQ** (20 μM at pH 7.4) in presence of various concentrations of Fe^{2+} (left) and Fe^{3+} (right) at room temperature.

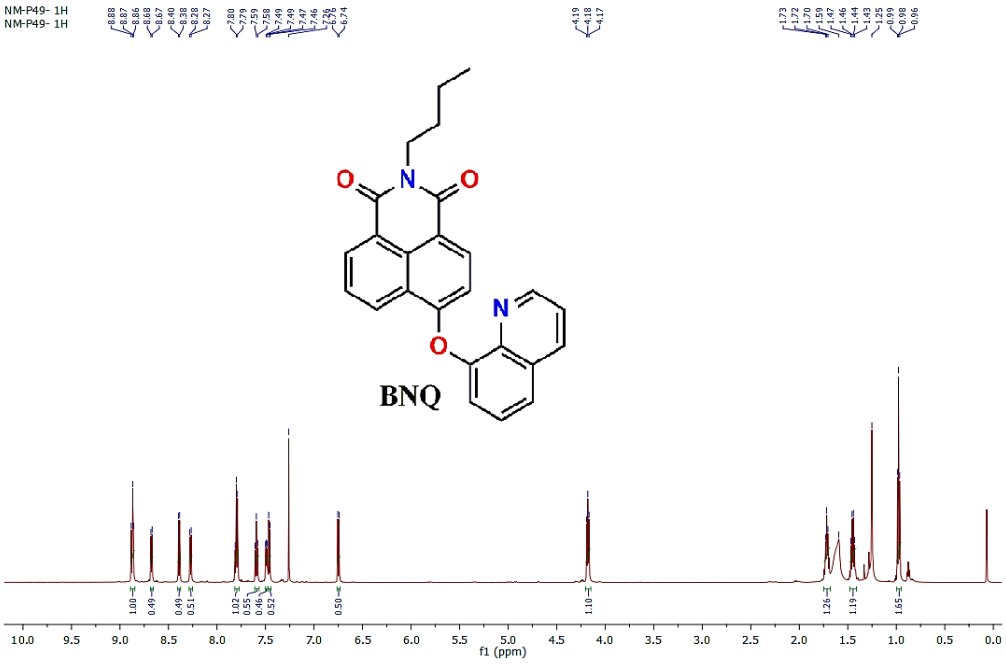

^{1}H spectra of **BNQ**

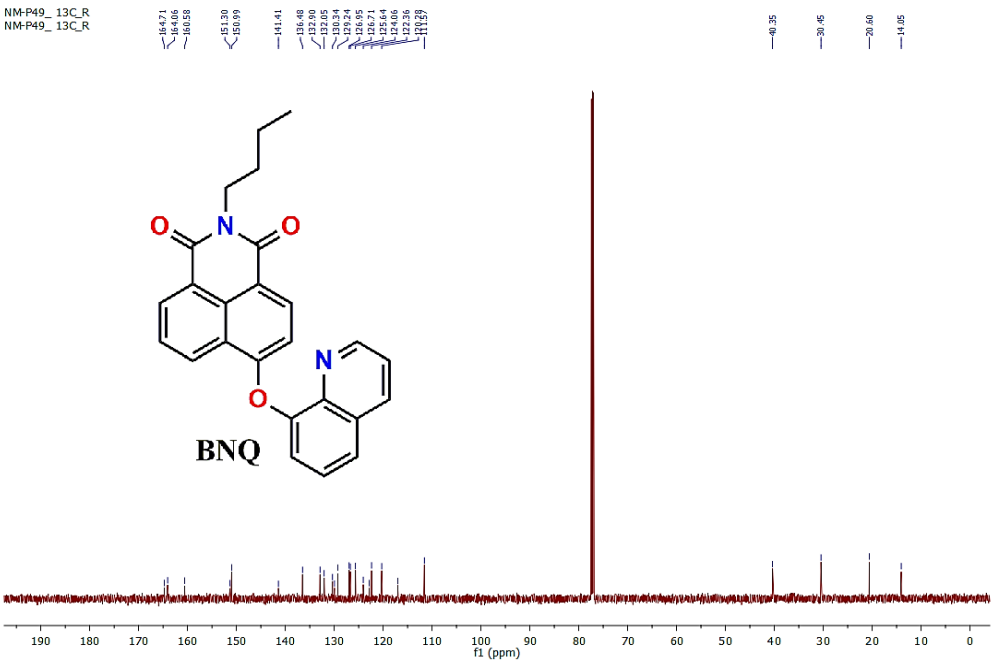

^{13}C spectra of **BNQ**

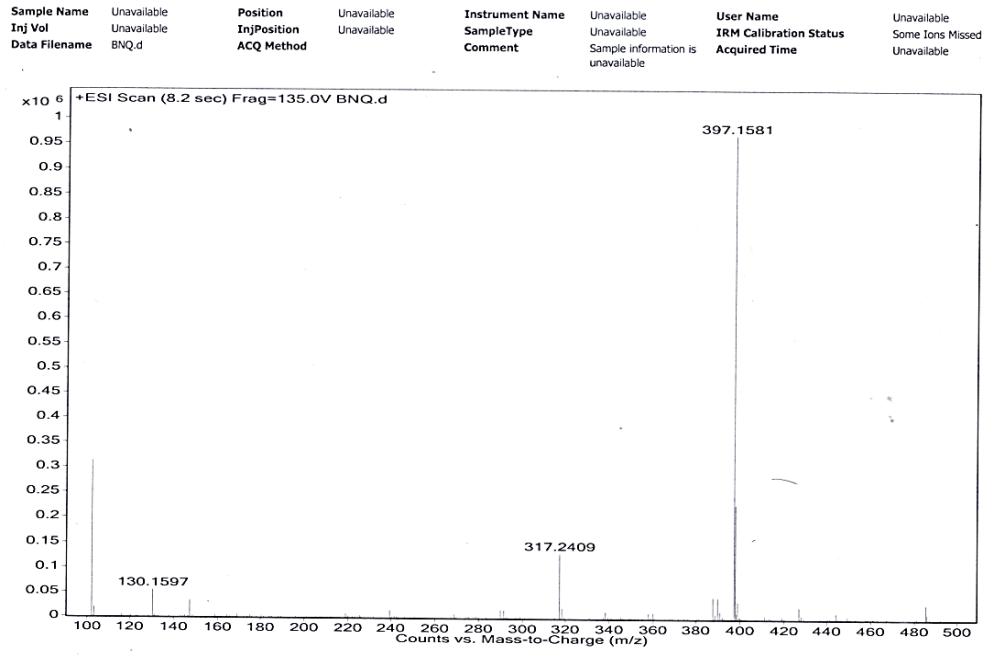

Mass spectra oh **BNQ**

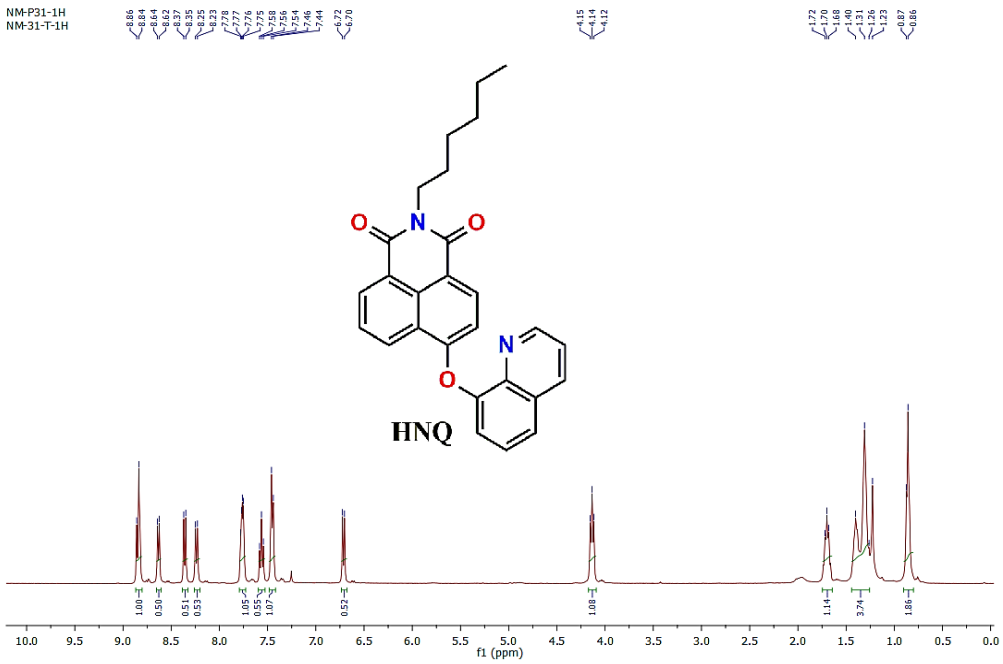

^{1}H spectra of HNQ

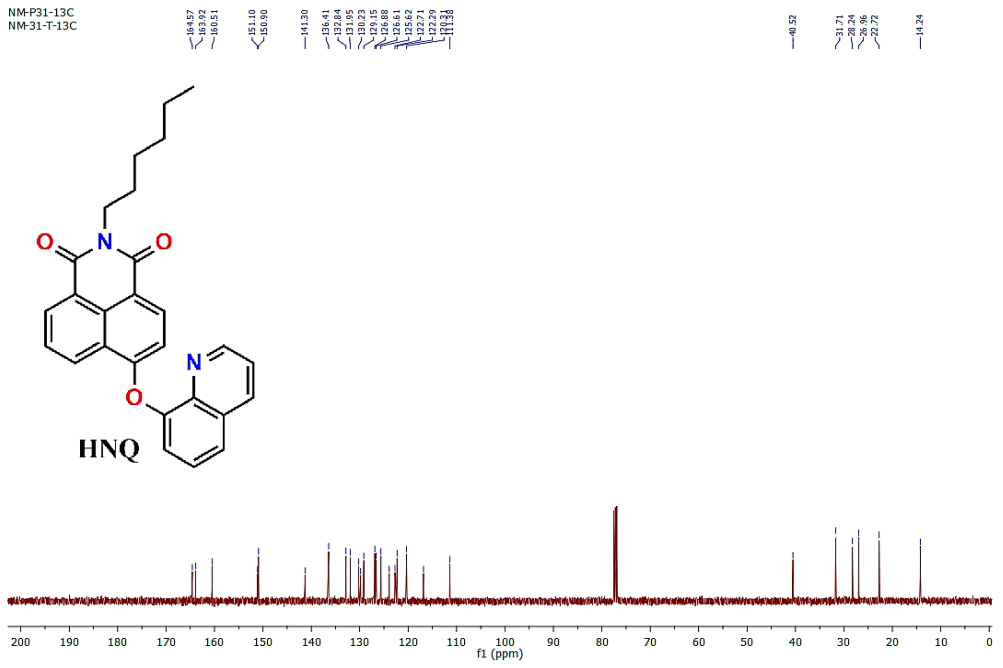

^{13}C spectra of HNQ

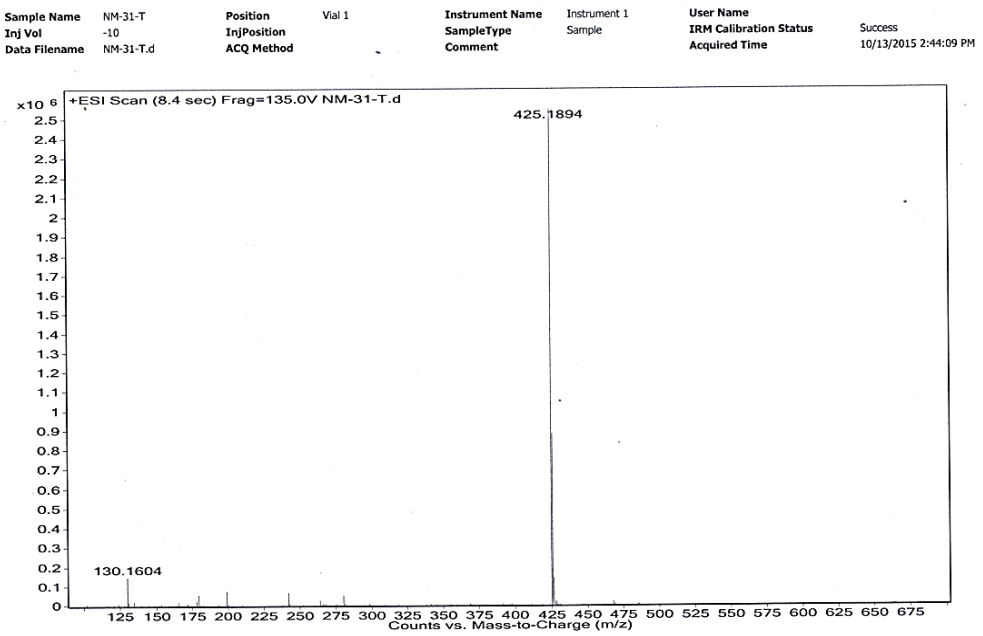

Mass spectra of **HNQ**

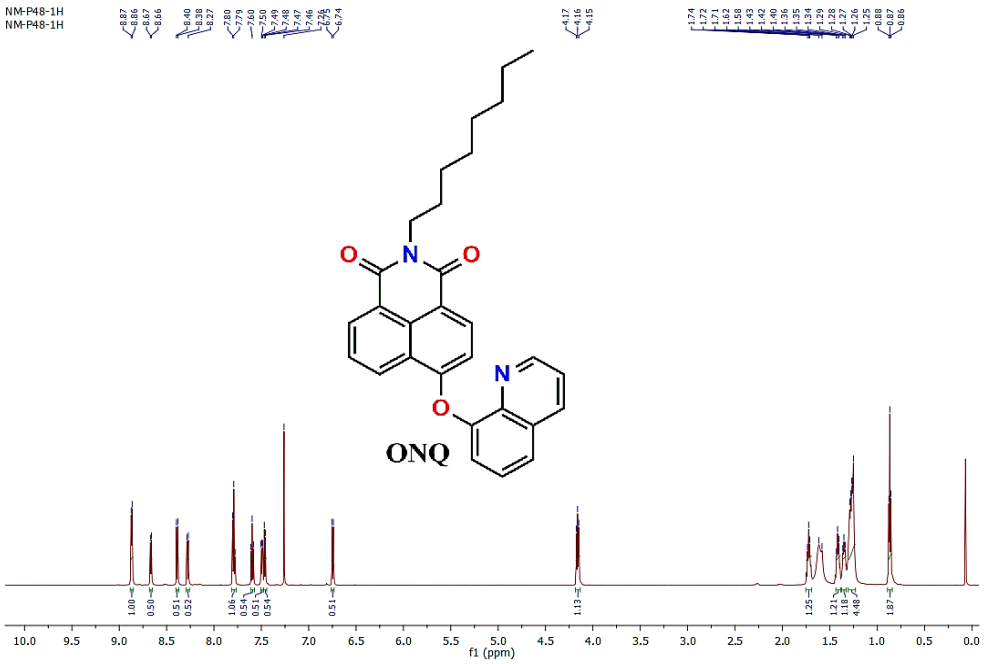

^{1}H spectra of **ONQ**

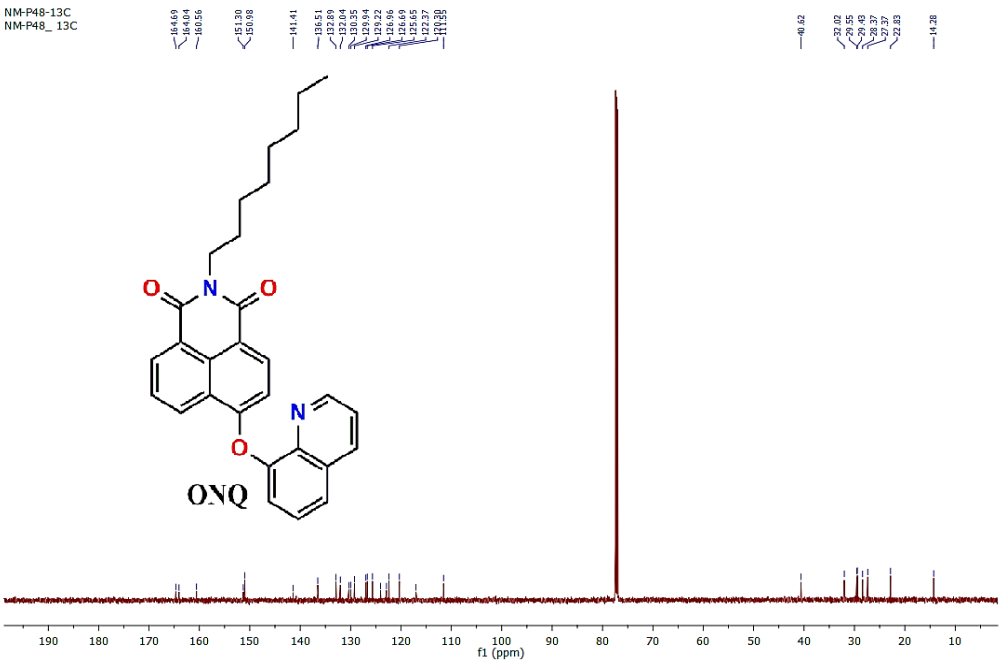

^{13}C spectra of **ONQ**

Sample Name	Unavailable	**Position**	Unavailable	**Instrument Name**	Unavailable	**User Name**	Unavailable
Inj Vol	Unavailable	**InjPosition**	Unavailable	**SampleType**	Unavailable	**IRM Calibration Status**	All Ions Missed
Data Filename	ONQ.d	**ACQ Method**		**Comment**	Sample information is unavailable	**Acquired Time**	Unavailable

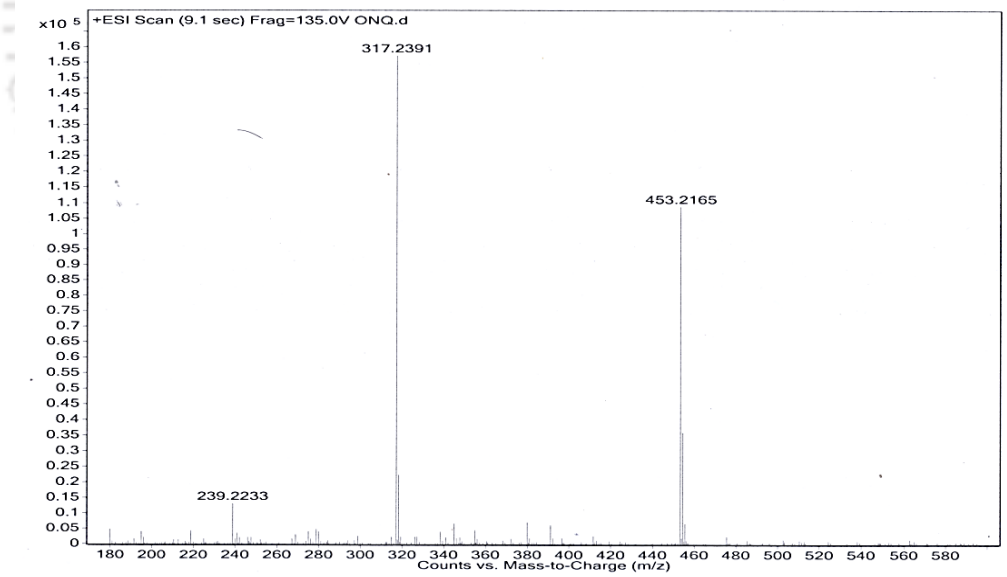

Mass spectra of **ONQ**

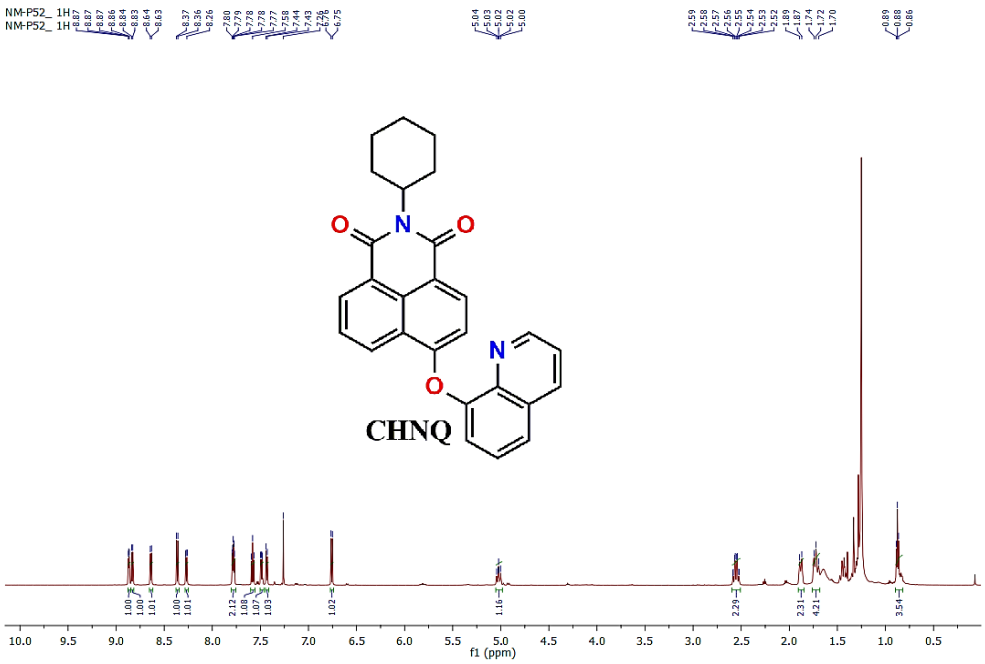

^{1}H spectra of **CHNQ**

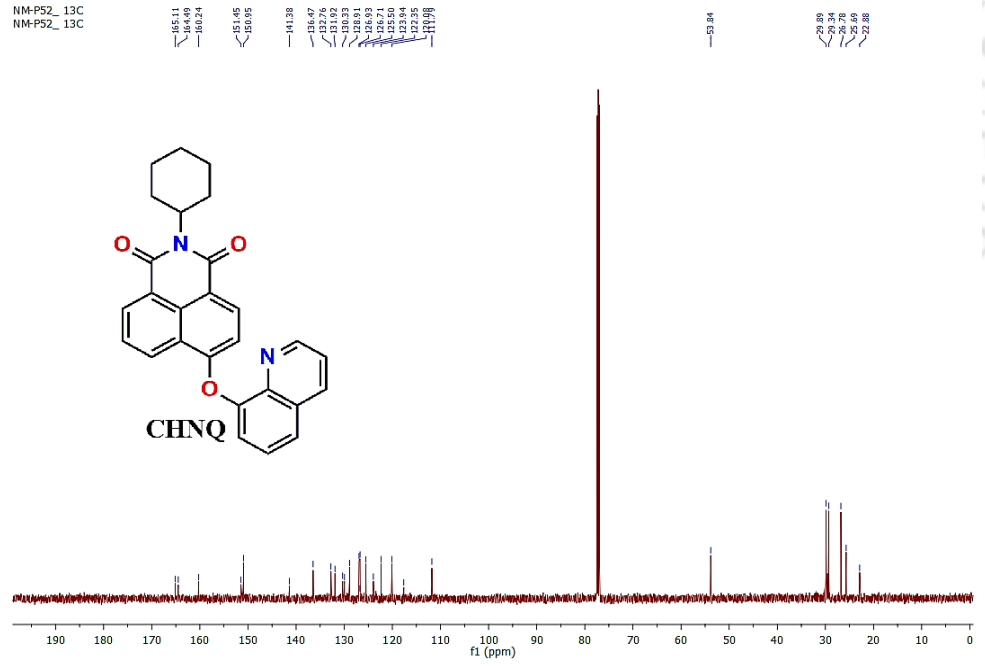

^{13}C spectra of **CHNQ**

Sample Name	Unavailable	**Position**	Unavailable	**Instrument Name**	Unavailable	**User Name**	Unavailable
Inj Vol	Unavailable	**InjPosition**	Unavailable	**SampleType**	Unavailable	**IRM Calibration Status**	Some Ions Missed
Data Filename	CHNQ.d	**ACQ Method**		**Comment**	Sample information is unavailable	**Acquired Time**	Unavailable

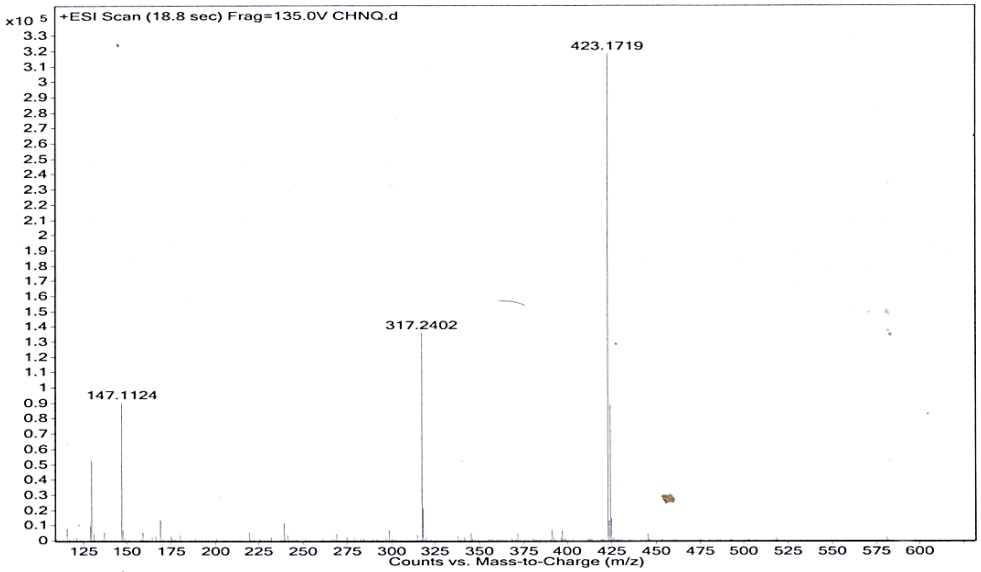

Mass spectra of **CHNQ**

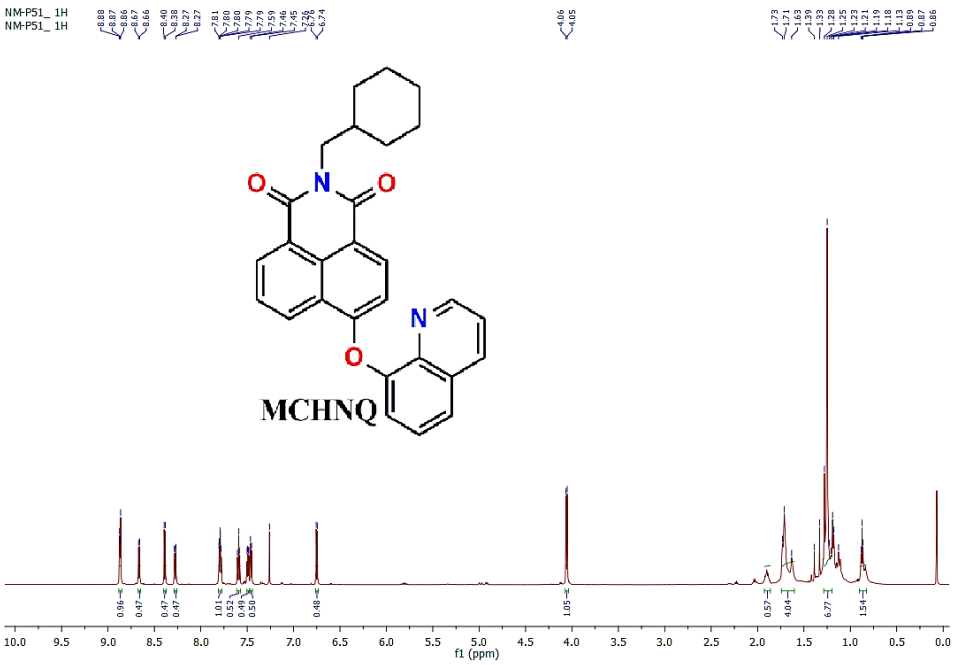

^{1}H spectra of **MCHNQ**

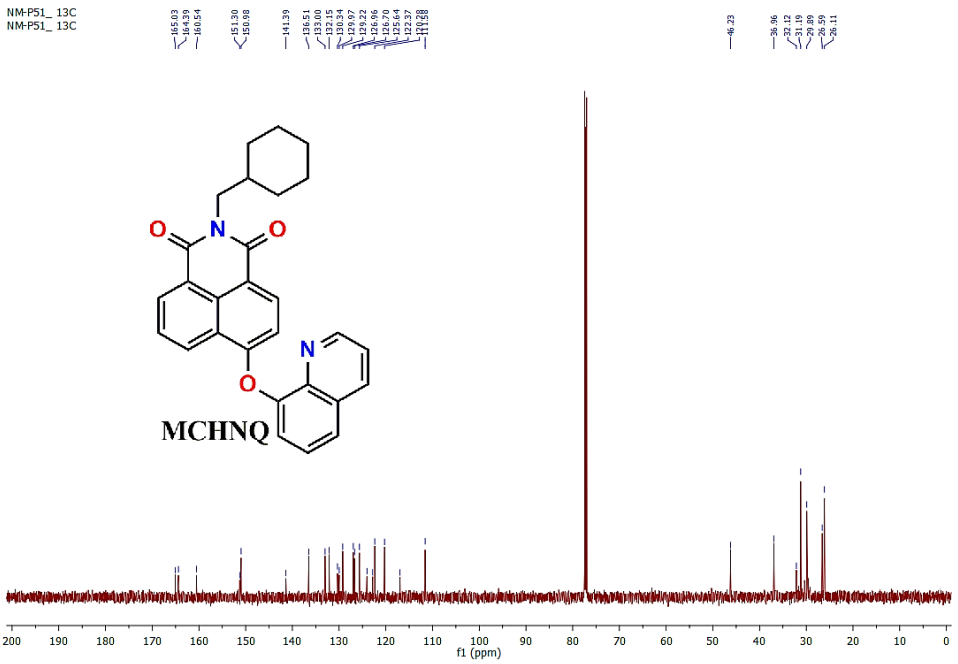

^{13}C spectra of **MCHNQ**

Sample Name	Unavailable	**Position**	Unavailable	**Instrument Name**	Unavailable	**User Name**	Unavailable
Inj Vol	Unavailable	**InjPosition**	Unavailable	**SampleType**	Unavailable	**IRM Calibration Status**	Some Ions Missed
Data Filename	MCHNQ.d	**ACQ Method**		**Comment**	Sample information is unavailable	**Acquired Time**	Unavailable

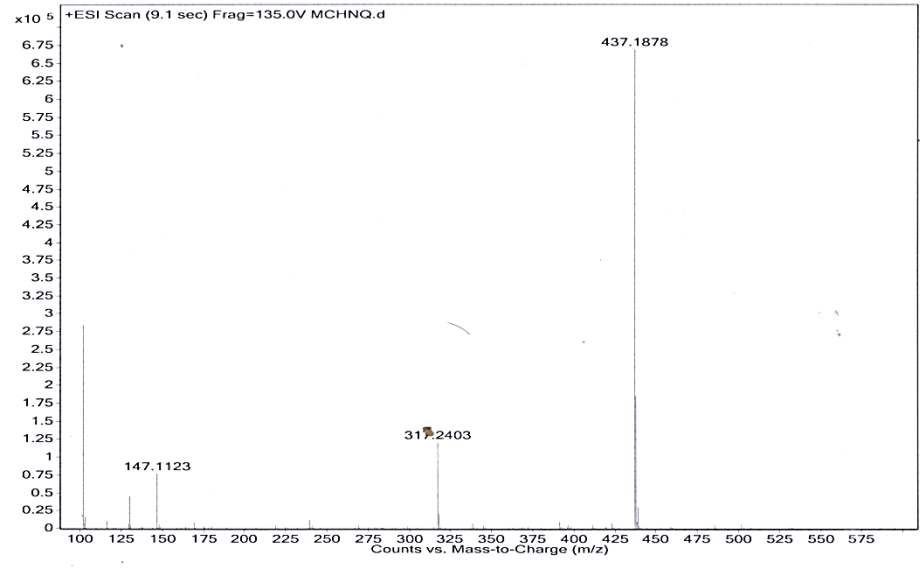

Mass spectra of **MCHNQ**

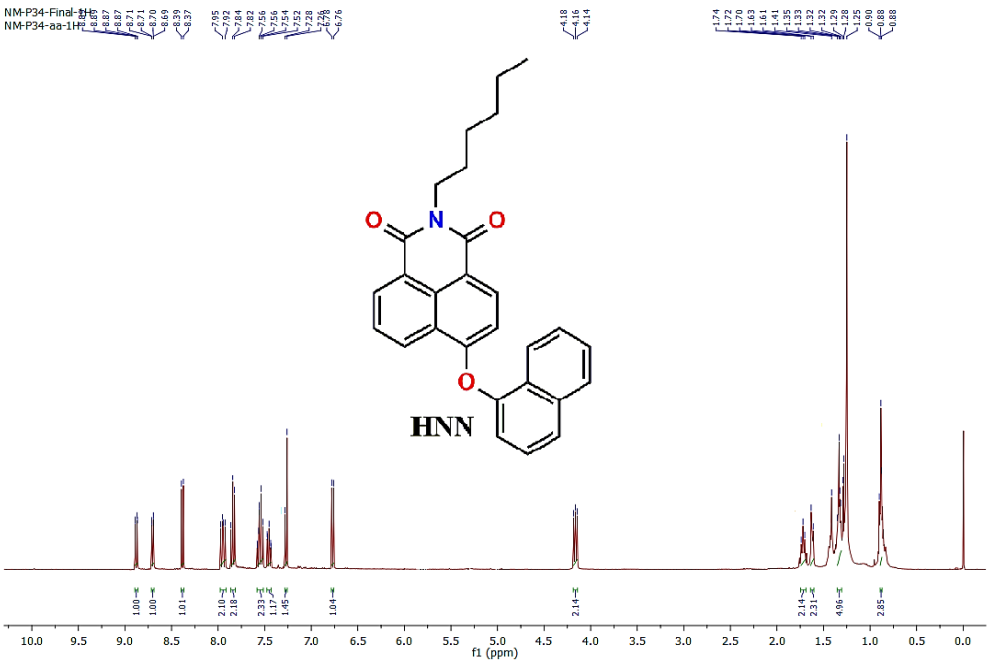

^{1}H spectra of HNN

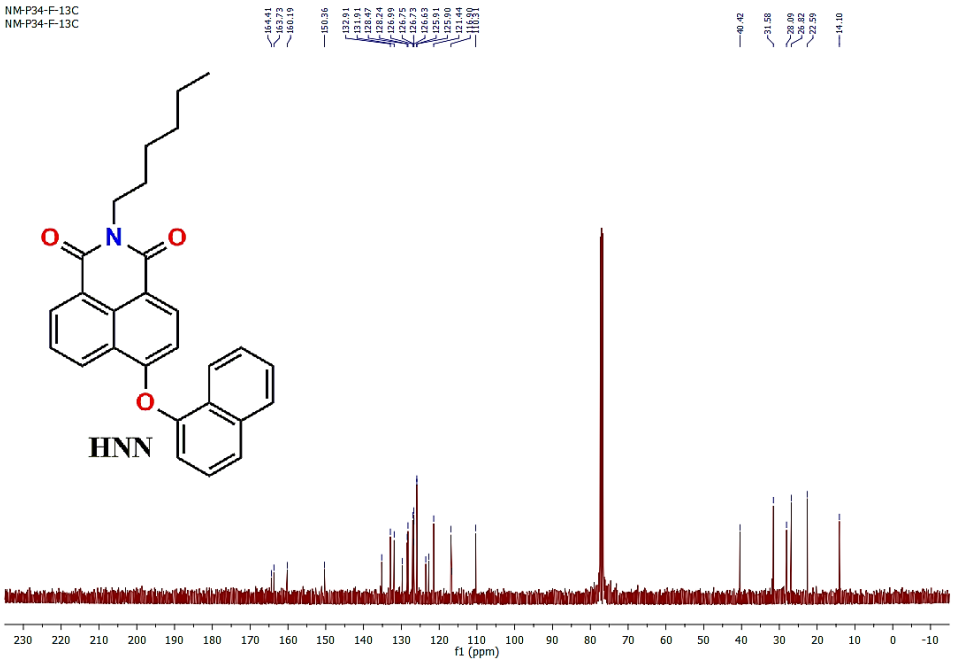

^{13}C spectra of HNN

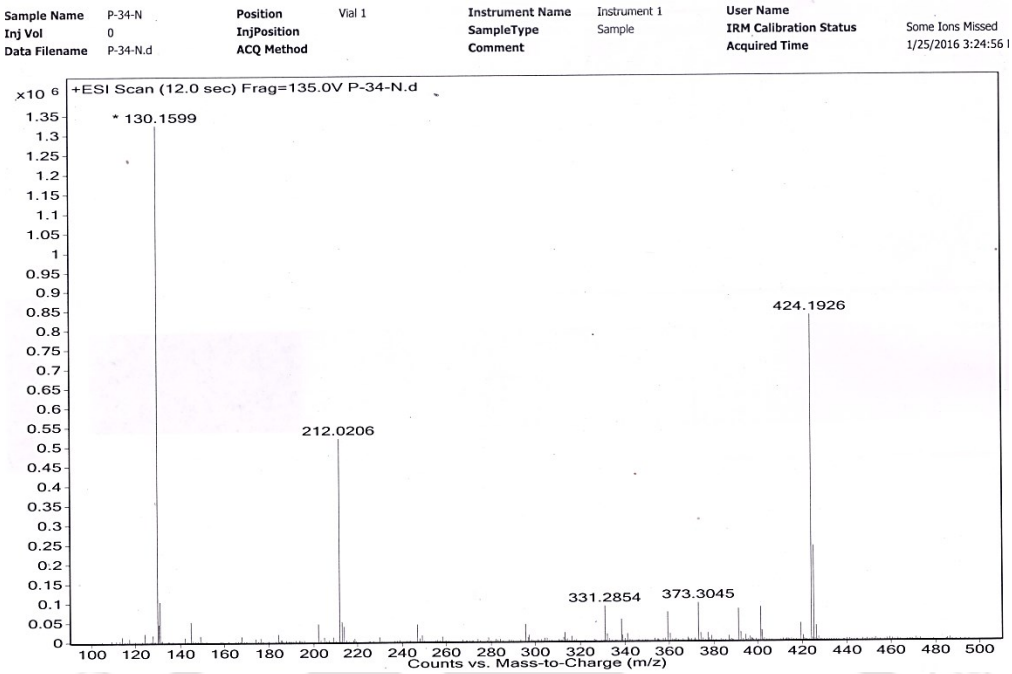

Mass spectra of **HNN**

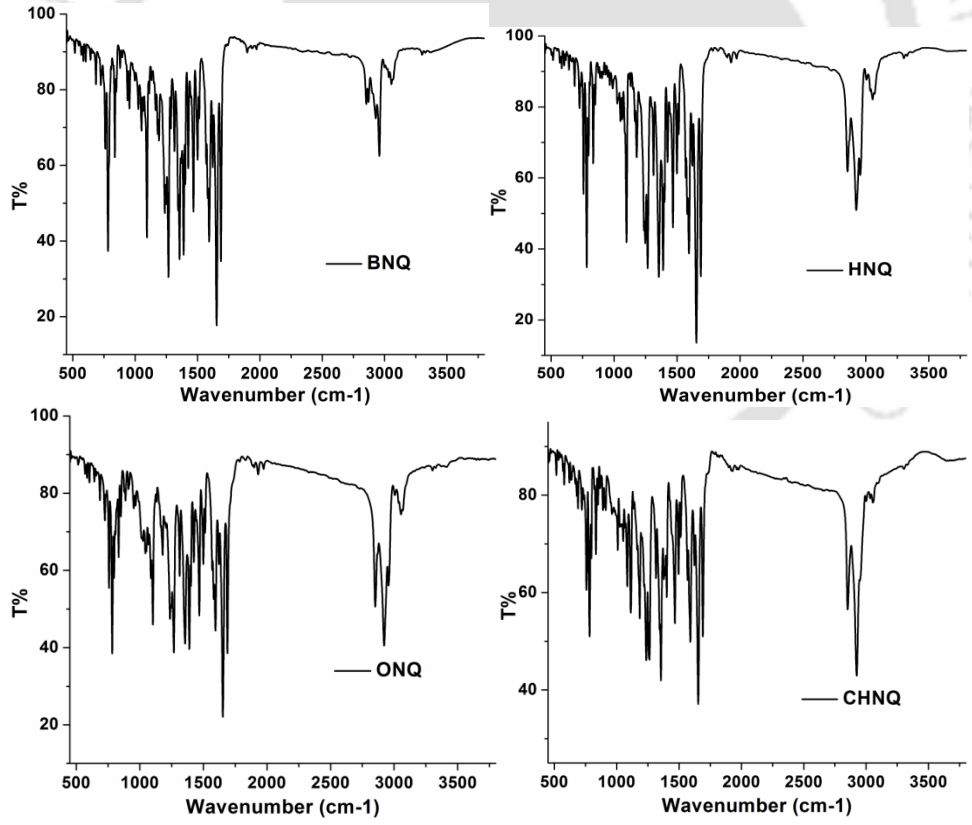

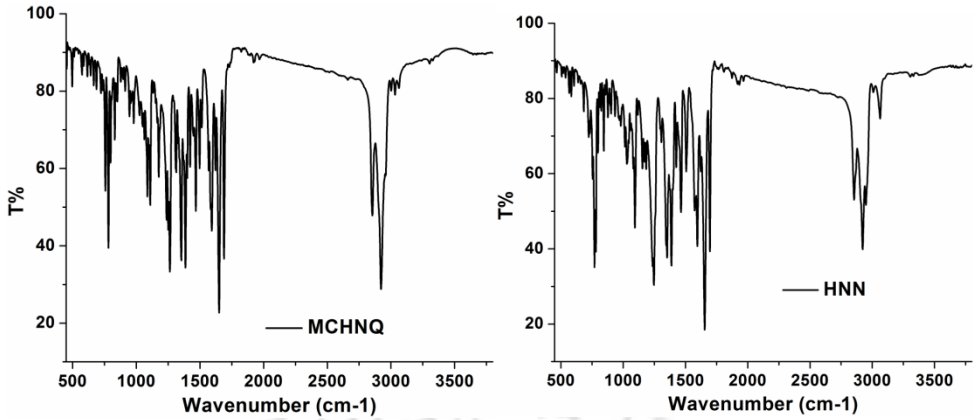

IR Spectra of the **Naphthalimide Congeners**

Chapter 3

Functional Group Engineering to Fine-Tune the Supramolecular Self-Assembly and Condensed State Luminescence

Meher, N.; Iyer, P. K.* *Nanoscale*, **2019**, *11*, 13233-13242.

Meher, N.; Iyer, P. K. Functional Group Engineering in Naphthalimides to Fine-Tune the Supramolecular Self-Assembly and Condensed State Luminescence, Ref No. 201931020811, App. Number: TEMP/E-1/21902/2019-KOL, (21/01/2019).

Abstract

Engineering well-defined supramolecular fluorescent nano-architectures based on simple organic small conjugated molecules has been an essential scientific challenge. Herein, a library of naphthalimide congeners (1-15) has been strategically designed that unveils a conceptual insight of functional group controlled condensed state emission and aggregation-induced emission (AIE) in conventional strong aggregation-caused quenching (ACQ) active fluorophores. Along with the regulation of ACQ-to-AIE transformation and tailoring condensed state emission, the simple yet potential design strategy of functional groups engineering has been established for the first time to spontaneously generate and systematically tailor the supramolecular self-assembly of organic small molecules into highly defined nano-architectures. Single-crystal XRD analysis of six congeners revealed that, unlike the well-established electronic contribution of the functional groups in the molecularly dispersed state, the condensed state photophysical and morphological properties are dictated by the distinct intermolecular π-π stacking interaction of the planar aromatic core. This research work demonstrated a novel and potential design strategy that emerges as a promising route to build fluorescent supramolecular nanoassembly from non-fluorescent conjugated molecules for a variety of future applications.

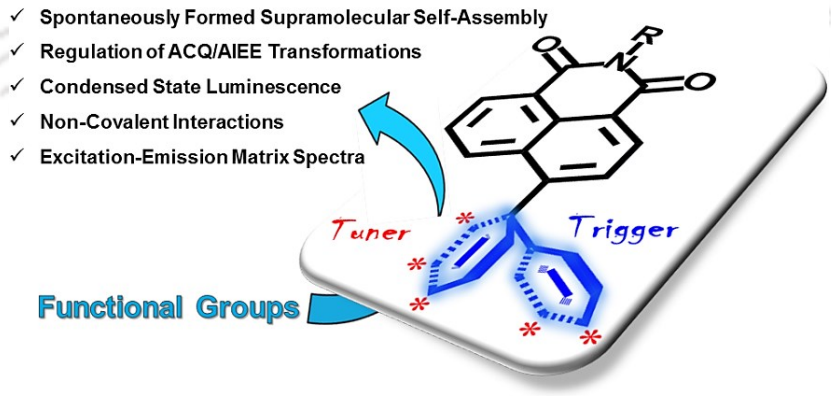

3.1. Introduction

Among the diverse fields of supramolecular chemistry, the bottom-up methodology has emerged as a powerful tool to construct various micro and nano-architectures.[1-5] In recent years, the design of spontaneously self-assembled molecular systems into multifunctional micro and nano-architectures have secured a special place among the scientific community.[6] In particular, spontaneously self-assembled and responsive molecular systems with fluorescence property are of unique research interest.[7,8] The depth and breadth of their scope could be evidenced by the advancement towards a variety of applications benefiting from the precisely controlled uniform size and shape of supramolecules and thus remains as one of the most important parameters for their diverse real-world application.[9-12] However, owing to the detrimental π-π stacking interactions between the aromatic planes, the conventional fluorophores habitually undergo the unwanted ACQ effect in their aggregated/self-assembled state.[9,13,14] In 2001, the concept of AIE with principally opposite photophysical property to that of the ACQ was introduced which has altered the approach about chromophore aggregation in terms of their fluorescence property.[15] These fluorophores, so-called luminogens, are dimly luminescent in dilute solution but furnish bright luminescence in their condensed state and thus open up their practical applications toward many restricted arrays as compared to the conventional fluorophores.[16-18]

With huge exponential progress of the AIEgenic materials in various real-world applications such as optoelectronics, theranostics, and bioimaging,[16-18] research groups are now continuously exploring new strategies to create and manipulate new AIEgenic luminogens. Apart from the concept of restriction of intra-molecular motion (RIM), several new strategies have been developed where the condensed-state emission could be manipulated by anion–π+ interactions, ionization or space conjugation.[19-21] Besides, by decorating with inherent AIE active chromophores, various types of organic-framework (OF) were also designed with high condensed state quantum yields.[22–24] While recognizing the eminence of AIEgenic materials, the job to strategically develop new design that can potentially transform a conventional ACQphore into an efficient AIEgen is far from trivial. Recently, simple long chain alkylation has been formulated to induce AIEgenic property in strong ACQ-active naphthalimide cores.[9] In another report, formyl group was shown to participate in the ACQ-to-AIE transformation process by modulating the intermolecular interaction and

their self-assembly property as well.[25] In the present work, the conceptual insight of functional group induced ACQ-to-AIE transformation has been evaluated by designing a library of naphthalimide congeners decorated with different types of functional groups thus providing an alternative approach for realizing optically active molecules.

In our previous report, we could demonstrate that altering simple non-conjugated alkyl chain in naphthalimides could also be used to tune their condensed state photophysical and morphological property.[26] The alkyl chains of different size /structure were established to exert different extent of steric hindrance around the naphthalimide core leading to different modes of supramolecular self-assembly. In the current work, along with the tuning of condensed state emission property (~100 nm) and regulation of ACQ-to-AIE transformation phenomenon, the simple strategy of functional groups engineering has been explored to generate and systematically tune the supramolecular nano-assembly formation through simple and cost-effective methodology that may lead to huge technological advancement in the field of organic optoelectronic device fabrications based on small molecules (Figure 3.1a). In contrast to the existing literature on the tuning of condensed state morphological property, where sophisticated techniques have been developed to generate and tailor the self-assembly,[27,28] the conceptually unique functional group engineering has been developed as a simple and highly feasible method to generate and fine-tune fluorescent supramolecular self-assembly. Besides, owing to the highly responsive nature in presence of few functional groups, the supramolecular self-assembly of the molecules could also be tuned by minor modification of the solvent composition in the dispersion medium and can reflect their aggregated state fluorescence behavior. It has been unveiled that, the functional groups could influence the intermolecular non-covalent interactions and packing arrangements of the congeners significantly in the condensed state (as confirmed from single crystal analysis), thus resulting in the drastic perturbation and responses of their spontaneously formed self-assembly and condensed state photophysical property.

3.2. Experimental Section

3.2.1. Materials and Instrumentations

All starting materials and reagents (viz: 1,8-naphthalic anhydride, 4-bromo-1,8-naphthalic anhydride, hexylamine, and phenylboronic acid derivatives) were purchased from Sigma Aldrich (INDIA) and were of reagent grade. HPLC grade solvents used in this study were purchased from Fisher Scientific Ltd. and RANKEM. NMR (^{1}H, ^{13}C) spectra were recorded

with a Bruker Avance 600 MHz spectrometer. All solutions for ^{1}H and ^{13}C spectra were obtained taking residual solvent signal as an internal reference. Electrospray ionization mass spectrometry (ESI-MS) was recorded on a Waters (Micro mass MS-Technologies) Q-Tof MS Analyzer spectrometer. UV/vis and PL spectra were recorded on a Perkin-Elmer Model Lambda-750 spectrophotometer and a Horiba Fluoromax-4 spectrofluorometer respectively using 4 mm quartz cuvettes at 298 K. Lifetime measurements were performed using a time-correlated single photon counting set up from Horiba. The laser diode 375 (DeltaDiode-375) was used as a source with an excitation wavelength of 375 nm. Malvern Zetasizer instrument was used to measure the hydrodynamic diameter of the compounds. Field emission scanning electron microscopy (FESEM) images were obtained on Sigma Carl ZEISS field emission scanning electron microscope. X-ray diffraction (XRD) measurements were performed using Bruker D2 PHASER X-ray diffractometer (10 mA, 30 kV) equipped with Ni-filtered Cu Kα radiation, at a wavelength of 0.154 nm. The samples were scanned in the 2θ range of 5–50° at a scan rate of 1.2° min^{-1}. Single crystal data were obtained with a Bruker SMART APEX diffractometer equipped with a CCD area detector.

3.2.2. Preparation of the Test Solution

Stock solutions of probes **1-15** and **HNI** (1×10^{-5} M) were prepared in DMF, while stock solutions of various test species (1×10^{-5} M) were prepared by dissolving an appropriate amount of the testing species in methanol. The test solutions of the probes (10 μM) were prepared at different water fraction in DMF for aggregation study. The probe (10 μM) nanoaggregate suspension in 99.9% water was prepared for the titration study with various analytes. The resulting solution was shaken well at room temperature before recording the spectra.

3.2.3. Preparation of FESEM Samples

The morphological analysis of the supramolecular self-assembly was carried out by FE-SEM. As pictured in Figure 3.5q, the simple methodology was performed to prepare the samples. The dilute suspension of the naphthalimide congeners (10 μM) in 99.9% water-0.1% DMF were drop casted on aluminium foil coated glass surface and were dried in room temperature overnight before analysis

3.2.4. Theoretical Studies

To investigate the non-fluorescent nature of **15** in both solution and condensed state, the electronic properties of all the congeners along with various other small molecules were

calculated using density functional theory (DFT). The ground state and excited state optimized geometries along with HOMO/LUMO electron density and energy were calculated using B3LYP hybrid functional incorporated in the Gaussian 09 package.[1,2] The 6-31G basis set for all the atoms has been used in all calculations, which offers high-quality outcomes at a reasonable time.

3.2.5. Quantum Yield Calculations

Fluorescence quantum yields (Φ_s) of the naphthalimides were calculated by taking quinine sulfate (Φ_r = 0.57 in 0.1 M H_2SO_4) as standard and using the equation shown below:

$$\Phi_s = \Phi_r (A_r F_s / A_s F_r) (\eta s^2 / \eta r^2)$$

Where, s and r represent sample and reference, Φ signifies the quantum yield, A denotes absorbance, F signifies relative integrated fluorescence intensity, and η represents the refractive index of the medium.

3.2.6. Crystallographic Details

Concentrated solutions of the congeners in DMF were prepared by heating at 60 ^oC and then were filtered off to leave behind the undissolved compound or any dust particles. After about 1-3 weeks, different shaped crystals for **2**, **8**, **9, 10** and **12** suitable for X-ray structure analysis were obtained. However, several attempts to obtain crystals for other congeners in various solvents and their mixture failed or very thin/small crystals were obtained that were not suitable for single crystal analysis. For the control study, the crystal data for HNI was obtained from the Cambridge Crystallographic Data Centre where the crystals of HNI were generated by slow diffusion of n-hexane into a solution of dichloromethane containing HNI.[3] Nevertheless, we also obtained the HNI crystal in DMF and were found to have exactly the same intermolecular packing arrangement to that of the HNI single crystal obtained from CCDC which shows the non-polymorphic nature of HNI.

3.2.7. Synthetic Procedures

HNI and HNIBr: 1,8-naphthalic anhydride (5 m.mol) was taken in ethanol (20 mL) and hexylamine (5.2 m.mol) was added to it dropwise at room temperature. The suspension was heated at 85 ^oC with vigorous stirring for 12h. Then the mixture was cooled to room temperature and then kept at 5 ^oC for 1 h to recrystallize **HNI**. The solvent was filtered out and the HNI residue was washed with ethanol to get the pure light brown crystalline solid of

HNI (84% yield). Similar synthetic procedure was followed for **HNIBr** (4-bromo-1,8-naphthalic anhydride was taken in place 1,8-naphthalic anhydride) yielding a light green color solid with 81% yield.

Characterization data of HNI: ^{1}H NMR (600 MHz, $CDCl_3$, δ ppm) 0.91 (t, 3H), 1.35 (m, 4H), 1.44 (m, 2H), 1.75 (m, 2H), 4.19 (t, 2H), 7.77 (t, 2H), 8.22 (d, 2H), 8.61 (d, 2H). ^{13}C NMR (150.00 MHz, $CDCl_3$, δ ppm) 14.22, 22.71, 26.94, 28.20, 31.70, 40.63, 122.85, 127.04, 128.24, 131.29, 131.67, 133.96, 164.32. HRMS (+ESI): Calculated for $C_{18}H_{19}NO_2$ 281.1416 $[M]^+$, Found 282.1371 $[M+1]^+$.

Characterization data of HNIBr: ^{1}H NMR (600 MHz, $CDCl_3$, δ ppm) 0.87 (t, 3H), 1.32 (m, 6H), 1.70 (m, 2H), 4.12 (t, 2H) 7.77 (t, 1H), 7.95 (d, 1H), 8.32 (d, 1H), 8.46 (d, 1H), 8.57 (d, 1H). ^{13}C NMR (150.00 MHz, $CDCl_3$, δ ppm) 14.18, 22.68, 26.89, 28.11, 31.64, 40.71, 122.28, 123.14, 128.09, 128.91, 130.17, 130.54, 131.09, 131.18, 131.99, 133.15, 163.54, 163.56. HRMS (+ESI): Calculated for $C_{18}H_{18}BrNO_2$ 359.0521 $[M]^+$, 361.0500$[M+2]^+$, Found 360.0600 $[M+H]^+$, 362.0581 $[M+H+2]^+$.

Synthetic Procedure for 1 to 11: Compound **HNIBr** (0.5 m.mol) and the respective boronic acid (1 m.mol) were dissolved into 6 mL of THF in 50 ml round bottom flask, and then 2 mL of 2.0 M potassium carbonate solution was added to the flask. The mixture solutions was degassed with nitrogen for 15 min and then 5 mg of catalyst $Pd(PPh_3)_4$ was added to them. The mixtures were stirred at 85 °C under nitrogen atmosphere and the progress of reactions was monitored by taking TLC. After 15 h, the solutions were cooled and extracted with $CHCl_3$. The organic layers were dried over anhydrous sodium sulfate. The solvent was removed and were purified by column chromatography.

Characterization data for 1: ^{1}H NMR (600 MHz, $CDCl_3$, δ ppm) 0.90 (t, 3H), 1.34 (m, 4H), 1.45 (m, 2H), 1.75 (m, 2H), 4.20 (t, 2H) 7.53 (m, 5H), 7.70 (m, 2H), 8.26 (d, 1H), 8.64 (t, 2H). ^{13}C NMR (150.00 MHz, $CDCl_3$, δ ppm) 14.22, 22.72, 26.96, 28.23, 31.72, 40.67, 121.94, 123.06, 126.95, 127.97, 128.59, 128.79, 130.01, 130.18, 130.93, 131.28, 132.73, 138.97, 146.97, 164.27, 164.47. HRMS (+ESI): Calculated for $C_{24}H_{23}NO_2$ 357.1729 $[M]^+$, Found 358.1806 $[M+H]^+$.

Characterization data for 2: ^{1}H NMR (600 MHz, $CDCl_3$, δ ppm) 0.89 (t, 3H), 1.35 (m, 4H), 1.44 (m, 2H), 1.75 (m, 2H), 3.92 (s, 3H), 4.20 (t, 2H) 7.08 (d, 2H), 7.45 (d, 2H), 7.68 (m, 2H), 8.30 (d, 1H), 8.62 (d, 2H). ^{13}C NMR (150.00 MHz, $CDCl_3$, δ ppm) 14.22, 22.73, 26.96, 28.23, 31.72, 40.66, 55.59, 114.29, 114.92, 116.15, 121.54, 123.06, 126.82, 127.89,

130.30, 131.00, 131.27, 132.84, 146.80, 160.04, 164.33, 164.53. HRMS (+ESI): Calculated for $C_{25}H_{25}NO_3$ 387.1834 $[M]^+$, Found 388.1963 $[M+H]^+$.

Characterization data for 3: ^{1}H NMR (600 MHz, $CDCl_3$, δ ppm) 0.89 (t, 3H), 1.34 (m, 4H), 1.43 (m, 2H), 1.74 (m, 2H), 4.19 (t, 2H) 7.71 (m, 4H), 8.07 (d, 2H), 8.17 (d, 1H), 8.66 (t, 2H), 10.15 (s, 1H). ^{13}C NMR (150.00 MHz, $CDCl_3$, δ ppm) 14.10, 22.68, 26.91, 28.17, 31.66, 40.69, 122.71, 123.19, 127.37, 127.92, 128.71, 129.77, 129.97, 130.16, 130.60, 130.89, 131.32, 131.57, 132.09, 136.22, 145.04, 145.17, 163.97, 164.18, 191.76. HRMS (+ESI): Calculated for $C_{25}H_{23}NO_3$ 385.1678 $[M]^+$, Found 386.1839 $[M+H]^+$.

Characterization data for 4: ^{1}H NMR (600 MHz, $CDCl_3$, δ ppm) 0.89 (t, 3H), 1.35 (m, 4H), 1.42 (m, 2H), 1.74 (m, 2H), 4.20 (t, 2H) 7.63 (t, 1H), 7.74 (m, 2H), 7.76 (d, 1H), 7.79 (d, 1H), 7.87 (d, 1H), 8.67 (m, 2H), 10.11 (d, 1H). ^{13}C NMR (150.00 MHz, $CDCl_3$, δ ppm) 14.22, 22.72, 26.95, 28.22, 31.70, 40.76, 116.26, 116.41, 123.27, 127.58, 128.70, 130.62, 131.59, 131.76, 132.99, 138.70, 138.74, 139.01, 159.38, 161.04, 163.97, 164.17, 190.43. ^{19}F NMR (564.00 MHz, DMSO-d_6, δ ppm) -112.76. HRMS (+ESI): Calculated for $C_{25}H_{22}FNO_3$ 403.1584 $[M]^+$, Found 404.1640 $[M+H]^+$.

Characterization data for 5: ^{1}H NMR (600 MHz, $CDCl_3$, δ ppm) 0.88 (t, 3H), 1.32 (m, 4H), 1.41 (m, 2H), 1.74 (m, 2H), 4.19 (t, 2H) 7.36 (d, 1H), 7.43 (d, 1H), 7.70 (d, 1H), 7.74 (t, 1H), 8.06 (t, 1H), 8.17 (d, 1H), 8.66 (d, 2H), 10.48 (s, 1H). ^{13}C NMR (150.00 MHz, $CDCl_3$, δ ppm) 14.20, 22.71, 26.93, 28.20, 31.69, 40.77, 118.12, 118.26, 123.32, 127.68, 127.88, 129.18, 129.20, 129.54, 130.70, 131.62, 143.77, 147.33, 147.39, 163.71, 163.90, 164.13, 165.44, 186.70, 186.74. ^{19}F NMR (564.00 MHz, DMSO-d_6, δ ppm) -120.07. HRMS (+ESI): Calculated for $C_{25}H_{22}FNO_3$ 403.1584 $[M]^+$, Found 404.1649 $[M+H]^+$.

Characterization data for 6: ^{1}H NMR (600 MHz, $CDCl_3$, δ ppm) 0.90 (t, 3H), 1.33 (m, 4H), 1.43 (m, 2H), 1.75 (m, 2H), 4.20 (t, 2H) 7.34 (t, 1H), 7.75 (m, 2H), 7.77 (t, 1H), 7.96 (d, 1H), 8.68 (m, 2H), 10.47 (s, 1H). ^{13}C NMR (150.00 MHz, $CDCl_3$, δ ppm) 14.22, 22.72, 26.95, 28.22, 31.70, 40.80, 123.34, 123.37, 123.83, 125.96, 126.00, 126.97, 126.99, 127.83, 128.58, 128.72, 129.76, 130.56, 131.72, 134.51, 137.68, 163.85, 164.07, 185.70. ^{19}F NMR (564.00 MHz, DMSO-d_6, δ ppm) -144.83 (d), -138.63 (d). HRMS (+ESI): Calculated for $C_{25}H_{21}F_2NO_3$ 421.1489 $[M]^+$, Found 422.1563 $[M+H]^+$.

Characterization data for 7: ^{1}H NMR (600 MHz, $CDCl_3$, δ ppm) 0.89 (t, 3H), 1.34 (m, 4H), 1.44 (m, 2H), 1.74 (m, 2H), 4.19 (t, 2H) 7.18 (d, 2H), 7.70 (d, 1H), 7.78 (d, 1H), 8.17 (d, 1H), 8.67 (t, 2H), 10.45 (s, 1H). ^{13}C NMR (150.00 MHz, $CDCl_3$, δ ppm) 14.21, 22.71, 26.93,

28.20, 31.69, 40.82, 114.21, 114.24, 114.35, 114.38, 123.44, 123.61, 127.81, 127.97, 128.74, 129.27, 13.63, 131.20131.76142.54, 147.51, 163.78, 164.03, 184.12. ^{19}F NMR (564.00 MHz, DMSO-d_6, δ ppm) -144.85. (d). HRMS (+ESI): Calculated for $C_{25}H_{21}F_2NO_3$ 421.1489 $[M]^+$, Found 422.5724 $[M+H]^+$.

Characterization data for 8: ^{1}H NMR (600 MHz, $CDCl_3$, δ ppm) 0.89 (t, 3H), 1.34 (m, 4H), 1.44 (m, 2H), 1.74 (m, 2H), 4.19 (t, 2H), 6.98 (t, 1H) 7.04 (d, 2H), 7.68 (d, 1H), 7.75 (t, 1H), 8.20 (d, 1H), 8.65 (t, 2H). ^{13}C NMR (150.00 MHz, $CDCl_3$, δ ppm) 14.22, 22.73, 26.95, 28.22, 31.71, 40.76, 104.20 (d), 113.18 (dd), 122.88, 123.27, 127.52, 127.87, 128.74, 129.74, 130.75, 131.55, 131.85, 142.07, 144.11, 162.34, 164.01, 164.24. ^{19}F NMR (564.00 MHz, DMSO-d_6, δ ppm) -109.10. HRMS (+ESI): Calculated for $C_{24}H_{21}F_2NO_2$ 393.1540 $[M]^+$, Found 394.1611 $[M+H]^+$.

Characterization data for 9: ^{1}H NMR (600 MHz, $CDCl_3$, δ ppm) 0.90 (t, 3H), 1.34 (m, 4H), 1.44 (m, 2H), 1.75 (m, 2H), 4.20 (t, 2H), 7013 (t, 1H) 7.25 (m, 2H), 7.48 (t, 1H), 7.67 (d, 1H), 7.71 (t, 1H), 8.21 (d, 1H), 8.64 (t, 2H). ^{13}C NMR (150.00 MHz, $CDCl_3$, δ ppm) 14.22, 22.73, 26.96, 28.24, 31.73, 40.70, 114.21, 115.75, 115.84, 115.89, 115.98, 123.17, 127.12, 128.05, 130.89, 131.36, 131.67, 131.72, 132.40, 139.43, 145.79, 164.20, 164.40. ^{19}F NMR (564.00 MHz, DMSO-d_6, δ ppm) -113.48. HRMS (+ESI): Calculated for $C_{24}H_{22}FNO_2$ 375.1635 $[M]^+$, Found 376.1726 $[M+H]^+$.

Characterization data for 10: ^{1}H NMR (600 MHz, $CDCl_3$, δ ppm) 0.90 (t, 3H), 1.34 (m, 4H), 1.44 (m, 2H), 1.75 (m, 2H), 4.20 (t, 2H), 7.44 (d, 2H) 7.53 (d, 2H), 7.67 (d, 1H), 7.71 (t, 1H), 8.20 (dd, 1H), 8.64 (d, 2H). ^{13}C NMR (150.00 MHz, $CDCl_3$, δ ppm) 14.22, 22.73, 26.96, 28.23, 31.72, 40.72, 122.31, 123.19, 127.20, 127.95, 129.10, 130.06, 130.88, 131.29, 131.41, 132.28, 134.92, 137.37, 145.54, 164.16, 164.37. HRMS (+ESI): Calculated for $C_{24}H_{22}ClNO_2$ 391.1339 $[M]^+$, Found 391.1594 $[M+H]^+$.

Characterization data for 11: ^{1}H NMR (600 MHz, $CDCl_3$, δ ppm) 0.89 (t, 3H), 1.34 (m, 4H), 1.44 (m, 2H), 1.74 (m, 2H), 4.19 (t, 2H), 7.38 (d, 2H) 7.68 (m, 2H), 8.19 (d, 1H), 8.63 (d, 2H). ^{13}C NMR (150.00 MHz, $CDCl_3$, δ ppm) 14.22, 22.72, 26.95, 28.22, 31.72, 40.71, 114.21, 123.08, 127.20, 127.88, 128.80, 129.97, 13087, 131.41, 131.57, 132.04, 132.26, 137.84, 145.53, 164.15, 164.35. HRMS (+ESI): Calculated for $C_{24}H_{22}BrNO_2$ 435.0834 $[M]^+$, Found 436.0912 $[M+H]^+$.

Synthetic Procedure for 12 to 15: To a solution of **HNIBr** (0.5 mmol) in DMF (10 mL), 0.7 mmol of the respective phenol derivative and K_2CO_3 (300 mg) were added and the

mixture was vigorously stirred and heated at 130 ^{o}C for 15 hours. The solvent was evaporated under vacuum and residue extracted with chloroform (40×5 mL). The organic layer was washed with H_2O several times followed by brine, dried over anhydrous Na_2SO_4 and concentrated under reduced pressure to get the crude product that was purified by silica gel column chromatography increasing the polarity slowly using a mixture of hexane and chloroform to get the pure the products.

Characterization data for 12: ^{1}H NMR (600 MHz, $CDCl_3$, δ ppm) 0.89 (t, 3H), 1.34 (m, 4H), 1.44 (m, 2H), 1.74 (m, 2H), 4.17 (t, 2H), 6.91 (d, 1H), 7.19 (d, 2H), 7.31 (t, 1H), 7.48 (t, 2H), 7.78 (dd, 1H), 8.45 (d, 1H), 8.68 (m, 2H),. ^{13}C NMR (150.00 MHz, $CDCl_3$, δ ppm) 14.22, 22.72, 26.96, 28.25, 31.72, 40.58, 110.76, 116.81, 120.91, 122.83, 124.09, 125.71, 126.63, 128.67, 129.83, 130.54, 132.00, 132.91, 155.00, 159.97, 163.92, 164.54. HRMS (+ESI): Calculated for $C_{24}H_{23}NO_3$ 373.1678 $[M]^+$, Found 394.1768 $[M+H]^+$.

Characterization data for 13: ^{1}H NMR (600 MHz, $CDCl_3$, δ ppm) 0.89 (t, 3H), 1.34 (m, 4H), 1.44 (m, 2H), 1.74 (m, 2H), 4.17 (t, 2H), 6.98 (d, 1H), 7.12 (d, 1H), 7.34 (m, 2H), 7.42 (d, 1H), 7.79 (t, 1H), 8.49 (d, 1H), 8.62 (d, 1H), 8.66 (d, 1H). ^{13}C NMR (150.00 MHz, $CDCl_3$, δ ppm) 14.22, 22.72, 26.95, 28.24, 31.72, 40.62, 111.63, 117.61, 119.29, 122.94, 123.51, 123.98, 124.15, 126.91, 128.42, 128.70, 129.84, 131.58, 132.12, 132.73, 156.01, 158.99, 163.78, 164.43. HRMS (+ESI): Calculated for $C_{24}H_{22}BrNO_3$ 451.0783 $[M]^+$, Found 452.0861 $[M+H]^+$.

Characterization data for 14: ^{1}H NMR (600 MHz, $CDCl_3$, δ ppm) 0.89 (t, 3H), 1.34 (m, 4H), 1.44 (m, 2H), 1.74 (m, 2H), 4.18 (t, 2H), 7.13 (d, 1H), 7.27 (m, 2H), 7.79 (t, 1H), 7.98 (d, 2H), 8.55 (m, 2H), 8.67 (d, 1H), 10.01 (s, 1H). ^{13}C NMR (150.00 MHz, $CDCl_3$, δ ppm) 14.22, 22.73, 26.95, 28.24, 31.71, 40.68, 113.65, 118.61, 119.92, 123.10, 124.63, 127.20, 128.32, 129.95, 132.23, 132.39, 132.53, 133.23, 157.69, 161.04, 163.68, 164.29, 190.70. HRMS (+ESI): Calculated for $C_{24}H_{23}NO_4$ 401.1627 $[M]^+$, Found 402.1759 $[M+H]^+$.

Characterization data for 15: ^{1}H NMR (600 MHz, $CDCl_3$, δ ppm) 0.89 (t, 3H), 1.34 (m, 4H), 1.44 (m, 2H), 1.74 (m, 2H), 4.18 (t, 2H), 7.19 (d, 1H), 7.23 (d, 2H), 7.80 (dd, 1H), 8.32 (d, 2H), 8.49 (d, 1H), 8.56 (d, 1H), 8.68 (t, 1H). ^{13}C NMR (150.00 MHz, $CDCl_3$, δ ppm) 14.21, 22.72, 26.94, 28.23, 32.07, 40.71, 114.34, 119.38, 123.19, 124.66, 126.48, 127.44, 128.08, 129.97, 132.32, 132.40, 139.43, 144.38, 156.97, 161.37, 163.55, 164. HRMS (+ESI): Calculated for $C_{24}H_{22}BrNO_3$ 418.1529 $[M]^+$, Found 419.1665 $[M+H]^+$

3.3. Results and Discussion

3.3.1. Design, Synthesis and Characterization

Strategically, with the goal of exploring the functional group induced supramolecular nano-assembly and condensed state photophysical properties, a library of naphthalimide derivatives (**1-15**) were synthesized via easy and cost-effective synthetic route (Figure 3.1b-c). Inspired by the proven versatility, wide real-world applications and the strong aggregating nature of the naphthalimide core,[18,29-31] 4-bromo-1,8-naphthalic anhydride was chosen as the preferred precursor material and functionalized with different functional groups hosted by phenyl pendants. The phenyl ring was preferred at the 4th position of the naphthalimide core to introduce the concept of AIE via restriction of intramolecular rotation (RIR) and to trigger their condensed state self-assembly.[18,25] Whereas, the hexyl chain was substituted at the amide N-atom to enhance the solubility of the luminogens in common organic solvents for easy synthesis and characterization. Simple cost effective condensation reaction was carried out to get the alkylated naphthalimide derivatives (**HNI** and **BrHNI**) with high yield (81-84% yield, Scheme S1).[18] By taking **BrHNI** as precursor material, Suzuki coupling was carried out with several phenylboronic ester derivatives independently to get **1-**

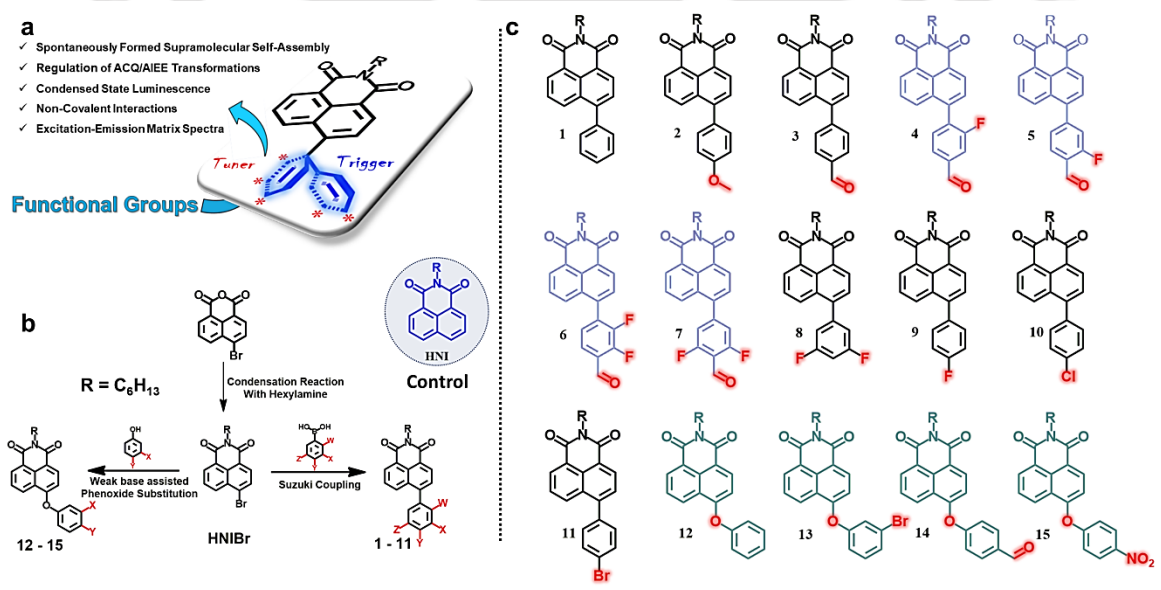

Figure 3.1. (a) Representation of functional group induced fine-tuning of supramolecular self-assembly and condensed state photophysical properties in naphthalimide luminogens. (b) Synthetic route to the naphthalimide congeners. Refer supplementary information for detail synthetic scheme and procedures (Scheme A3.1-A3.3). (c) The chemical structure of the library of synthesized naphthalimide congeners with different functional groups substituted at pendant phenyl rings.

11 in good yield (Figure 3.1b and Scheme A3.2). On the other hand, **12-15** were obtained by weak base assisted phenoxide substitution reaction (Figure 3.1b and Scheme A3.3). All these specific starting materials were selected in accordance to decorate the naphthalimide derivatives with distinct functional groups. Besides, **HNI** without any phenyl core was also included in the library of naphthalimides as a control derivative for the in-depth analysis of the triggerer and tuner activity of the phenyl ring and the functional groups respectively. All the synthesized materials were well characterized by multinuclear NMR spectroscopy (^{1}H, ^{13}C, and ^{19}F), HRMS and FTIR. The detail synthetic procedures along with characterization spectra and data could be found in the electronic supplementary information.

3.3.2. Tuning of Condensed State Luminescence without the Electronic Influence of Functional Groups

Strategically, the highly electron withdrawing naphthalimide core was decorated with different functional groups including both donor- and acceptor-types and a library of structurally identical congeners were designed. Structural architectures suggest that, among all these congeners, **2** with a methoxy functional group could form a favorable donor-acceptor combination and thus relatively red-shifted absorbance (15 nm) and emission maxima (65 nm) to that of other congeners were obtained in the solution state (Figure 3.2a, Figure A3.1-2, and Table A3.1). However, the rest of the congeners (**1, 3-15**) showed nearly identical absorption maxima (within the window of 347-357 nm) with a tuning of emission maxima only up to 25 nm in solution state that corresponds to their molecular photophysical property as a result of π-π electronic transitions (Figure 3.2a). The CIE chromaticity diagram of the emission of naphthalimides in solution state showed that congeners other than **2** and **HNI**, have very insignificant variation in the luminescence color (Figure 3.2b and Table 3.2). Despite having most blue-shifted absorbance (334 nm) and emission (381 nm) spectra in **HNI**, it showed light blue color with CIE coordinates of 0.211 and 0.171 which was due to the eximeric emission of the congener at nearly 540 nm (Figure 3.2a-b and Table S2). By comparing the solution state fluorescence emission of **HNI** and **1**, it can be assumed that the pendant phenyl ring plays a major role by providing an extended conjugation to the naphthalimide core in the solution state. Thus, both the phenyl rings and the functional groups are directly associated with the electronic transitions of the molecules by providing a certain level of donor-acceptor combinations. However, in their solid state, a huge tuning of emission maxima (~100 nm) was observed and the trend of their emission spectra was found to be independent of their donor-acceptor combinations as induced by the pendant

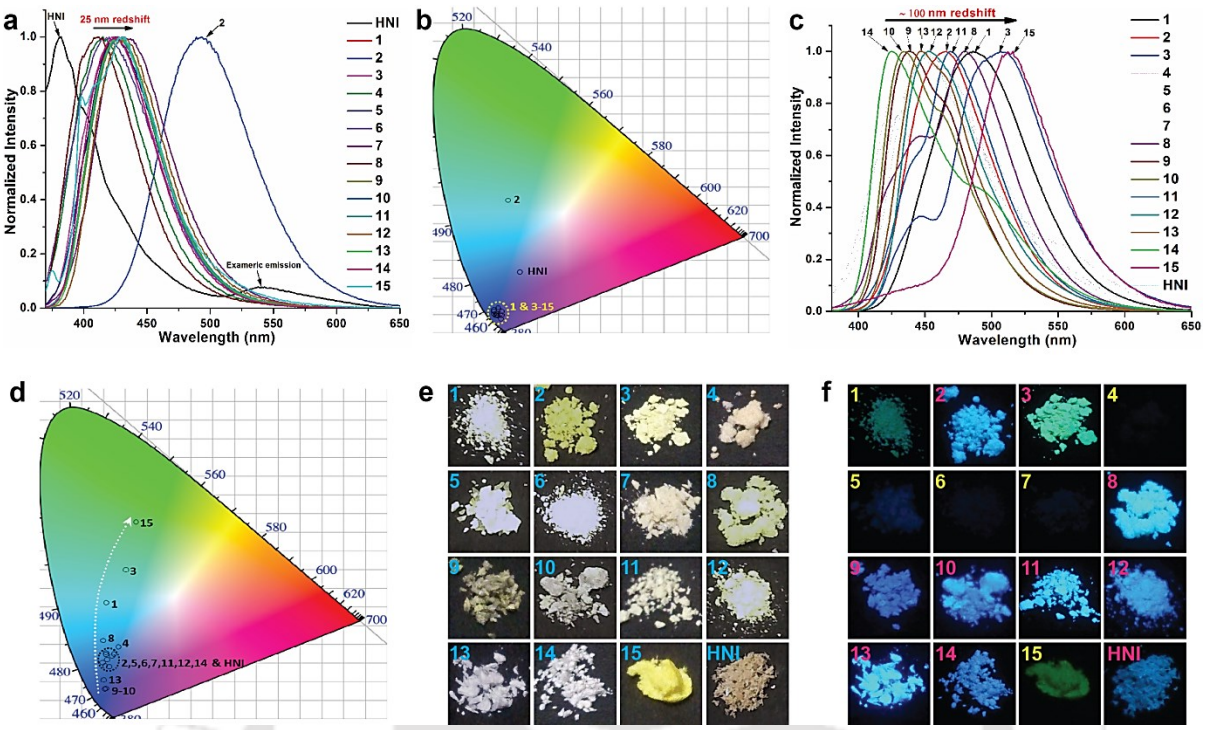

Figure 3.2. (a) Normalized fluorescence spectra of all the congeners in their solution state (in DMF, 10 μM). This represents the monomeric emission of the congeners without any aggregation. (b) CIE chromaticity diagram representing emission color of all the naphthalimide congeners in their dilute solution state. (c) Solid-state fluorescence spectra of the luminogens **1-15** and HNI (λ_{ex} = 355 nm). (d) CIE chromaticity diagram representing solid state emission color of all the naphthalimide congeners. All the respective CIE coordinates were summarized in Table S2, see ESI†. Digital photographs of solid naphthalimides (e) under white light and (f) under UV light (365 nm) illumination.

phenyl rings and the functional groups (Figure 3.2c and Figure A32-3). Huge disparity of their powder color under white light along with the emission color under UV irradiation at 365 nm was observed which matched well with the CIE chromaticity diagram (Figure 3.2d-f and Table A3.2). Few congeners were also witnessed to be very faintly fluorescent in their solid state whereas others showed bright emission indicating their AIE properties confirming the peculiar effect of the functional groups as well (Figure 3.2).[16,17] For instance, **3, 8** and **9** with only formyl group or fluorine moiety were highly fluorescent in their solid powder form, whereas **4-7** containing both the formyl and fluorine groups were almost non-fluorescent (Figure 3.2f). Besides, having the most red-shifted emission spectra in the solution state, congener **2** showed drastic blue-shifted emission spectra to that of **1, 3** and **15** (Figure 3.2). More interestingly, despite the distinct electronegative groups, the fluorescence spectra of the naphthalimides with or without the halides moieties (**1**, **9**, **10** and **11**) coincide with each other in their solution state without any shift in their $\lambda_{emi.max}$ (Figure A3.3, Table

A3.1). This could be due to the presence of the phenyl ring between the naphthalimide core and the functional groups, which reduced their electronic communication effectively. On the other hand, their solid state emission profiles showed huge tuning in their $\lambda_{emi.max}$ and were found to be independent to the order of the electronegativity of the halides (Figure 3.2c). Such deviations suggest that both solutions as well as condensed state photophysical properties of the naphthalimides are hardly influenced by the electronegativity of the functional groups. However, the steric constraints and strength of H-bonding of the functional groups could modulate the intermolecular stacking interaction between the naphthalimide cores in their condensed state effectively which in turn brings a huge perturbation in their luminescence properties.[32,33] The precise role of functional groups in the perturbation of intermolecular stacking interactions have been investigated by the comparative study of single crystals of few congeners.

3.3.3. Functional Groups Controlled ACQ-to-AIEE Transformations

To study the effect of aggregate formation on the fluorescence emission of the congeners, fluorescence spectra of the molecules were recorded at different water fraction (f_w; poor solvent) in DMF (good solvent). Owing to their good solubility in most of the organic solvents, the congeners remain at the molecularly dispersed form in DMF; however, very poor solubility in aqueous media led to the formation of nanoaggregates. The grown-up base line in UV-Visible spectra of the congeners clearly suggested the formation of nanoaggregates at higher f_w (Figure A3.1). Similar to the several disparities observed in their solid state emission property, the congeners with different functional groups exhibited peculiar aggregation based emission behavior in water (Figure 3.3 and Figure A3.4-8). **1** shows ACQphoric nature, however, the presence of the ether group makes **12** an AIEEgenic molecule. Although the solid powder of **4-7** containing both the formyl and fluorine groups were almost non-fluorescent, they showed AIEEgenic nature where an increase in emission with increasing f_w upto 50% was observed. However, the subsequent increase in f_w upto 99.9% caused to decrease the fluorescence emission. Such distinct emissive nature of **4-7** could be due to their distinct intermolecular non-covalent interactions at varying solvent composition and in the solid state. While considering **2**, with increase in f_w from 0-60%, it showed red-shifted emission spectra with decrease in intensity that corresponds to its ICT emission (521 nm). More interestingly, at f_w more than 60%, it started aggregating with blue-shifted enhanced emission at 463 nm (Figure 3.3b and Table A3.1). This signified that the condensed state (both solid state and aggregates in water) is not being influenced by the

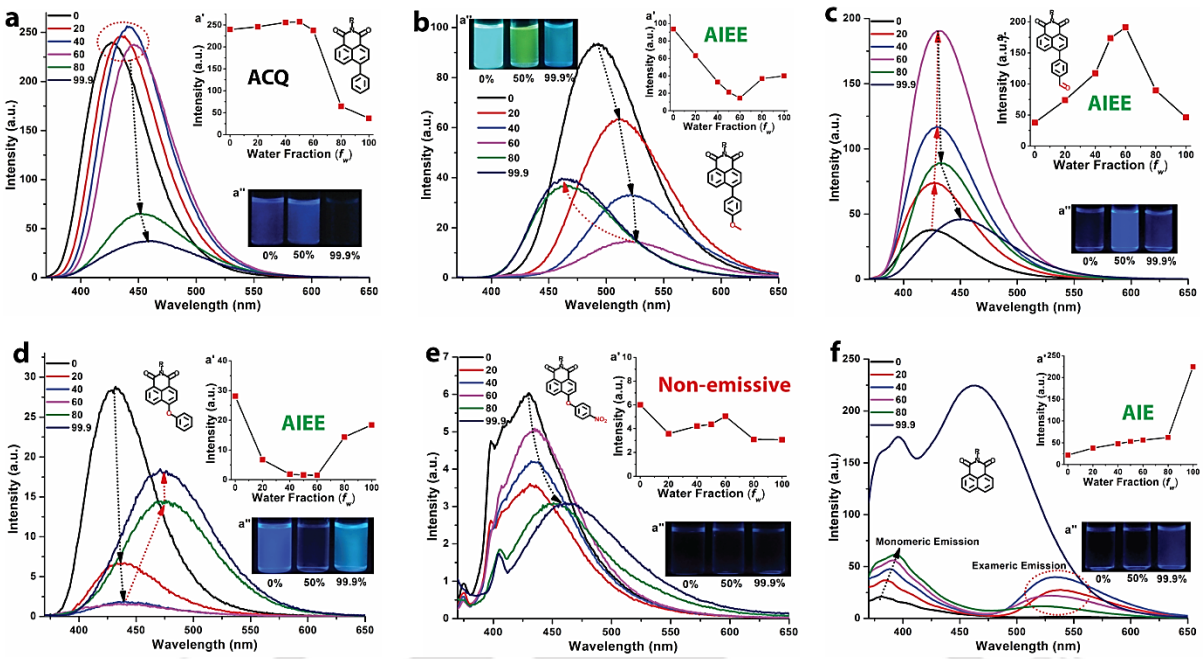

Figure 3.3. Fluorescence spectra of (a) **1**, (b) **2**, (c) **3**, (d) **12**, (e) **15** and (f) **HNI** at various water fractions in DMF (10 μM, excited at 355 nm). Insets: (a') plots of $\lambda_{emi,max}$ along with (a") digital photographs (under 365 nm UV irradiation) of the luminogens at various f_w in DMF. The fluorescence spectra for other congeners at various water fractions in DMF have been presented in the supporting information as Figure A3.4-8.

electronic contribution of the methoxy group. It can be assumed that the intermolecular π-π interactions and packing arrangements of the aromatic core which completely dominate the condensed state emission properties of the congeners is effectively modulated by the functional groups. Again, **1** containing a phenyl pendant that can undergo dynamic rotation in solution state was found to be ACQ in nature, whereas HNI with a single rigid aromatic core exhibited AIEgenic emission (Figure 3.3a and 3.3f). Such experimental observations even in other congeners contradict the most universal mechanism of AIE, i.e. restriction of intramolecular motion (RIM), and thus strengthens the prominent role of the intermolecular π-π interactions and the mode of arrangement between the naphthalimide cores.[16,17] Thus functional group controlled non-covalent intermolecular π-π interactions could efficiently trigger the formation of diverse fluorophoric systems in solution and condensed state which has been investigated by analyzing their excitation-emission matrix (EEM) spectroscopy in the solution state at different concentrations and has been summarized in the following section. Moreover, it was observed that **15** remains completely quenched in both solution and condensed state with a quantum yield below 0.7% (Figure 3.3e and Table A3.1) which was later explored to be caused by photoinduced electron transfer (PET) mechanism.

3.3.4. Concentration-Dependent Excitation-Emission Matrix (EEM) Spectra and Assessment of Multifluorophoric Systems

To obtain more insights into the functional group incited condensed state photophysical properties of the naphthalimide congeners, the excitation-emission matrix (EEM) spectra of their concentrated solution were investigated by comparing with that of the dilute solution.

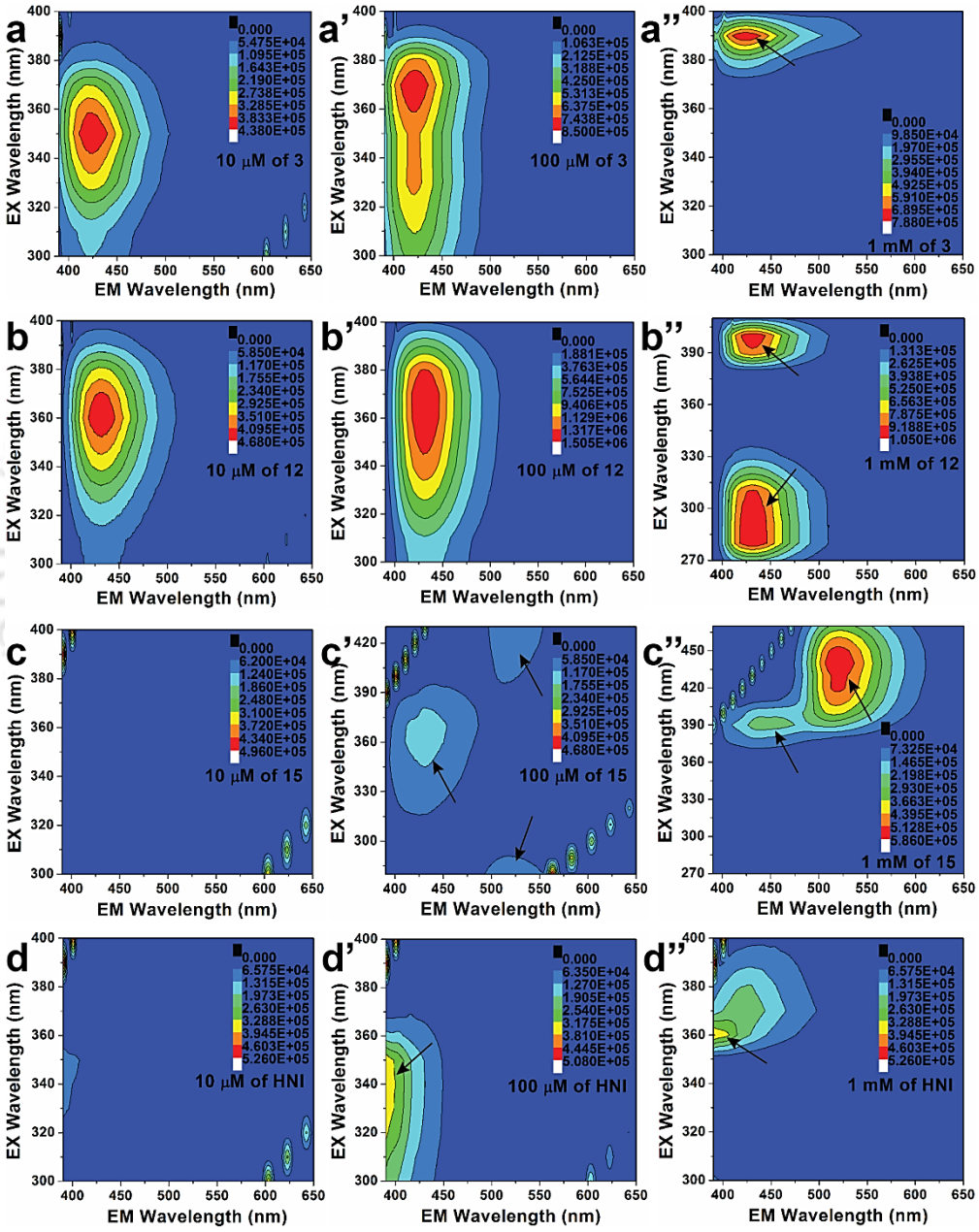

Figure 3.4. EEM spectra (2D contour projections) of the luminogens **3, 12, 15** and **HNI** (a-d, respectively) at different concentration (Left: 10 μM; Middle: 100 μM; Right: 1 mM) in DMF. The Excitation-emission matrix (EEM) spectra for other congeners at different concentrations in DMF have been presented in the supporting information as Figure A3.9.

EEM spectroscopy is recognized to be an effective technique for spectroscopic characterization of multifluorophoric systems.[34] Each EEM could provide the spectral evidence regarding the chemical compositions of a mixture. Since aggregation is a concentration-dependent phenomenon, the EEM spectra of the congeners were recorded in the solution state and a comparative analysis of the spectral evolution at varying concentrations of each congener from 10 μM (diluted) to 1 mM (concentrated) was carried out. The emission spectra of the fluorophores were collected from 390 to 650 nm at room temperature, scanning the excitation wavelength from 300 to 400 nm at 10 nm increments. In Figure 3.4 and Figure A3.9, the emission spectra of the naphthalimides have been presented as 2D contour projections, which will allow perceiving every emission band and its correlation to the appropriate excitation wavelength. At a lower concentration (10 μM), each of the contour projections of **1-14** showed only one symmetric peak centered at its corresponding molecular absorption maxima (within the range of 345-365 nm). With an increase in concentration (at 100 μM), broadening of the contour profiles along the Y-axis (i.e. along excitation wavelength value) was observed that clearly indicated the formation of multifluorophoric components that absorbed a wide range of light, which is not possible for monomeric naphthalimides. However, in most of the congeners, the EEM spectra got split into two different contour profiles in their concentrated solution (1 mM) corresponding to the generation of two well-distinct emissive species: one at longer excitation wavelength and another at shorter excitation wavelengths as compared to their respective monomeric species. This showed the formation of distinct multifluorophoric systems by the naphthalimides at higher concentration. Even in **15** and **HNI**, which were almost non-fluorescent in their solution state, they generated fluorescent species emitting at higher concentration and were centered at red-shifted λ_{ex}. The formation of these new emissive species at different λ_{ex} in the EEM spectra could be directly co-related with their degree of conjugation, i.e. red-shifted contour profile signifies the formation of a new emissive species with higher degree of intermolecular conjugation whereas blue-shifted contour profile could be assigned to the reduction in the conjugation.[34,35] Thus the photophysical properties of the naphthalimides are controlled by their local concentration and confirmed the prominent role of the intermolecular π-π interaction in their condensed state luminescence. Unlike the symmetrical contour profiles for **1-14** at any concentrations, **HNI** (lacking a phenyl ring) showed unsymmetrical EEM spectra at higher concentration which confirmed the triggering property of the pendant phenyl rings in other congeners for enhanced intermolecular interactions.

3.3.5. Functional Group Controlled Spontaneously Formed Supramolecular Nano-Architectures

After realizing the peculiar condensed state luminescence properties in the naphthalimides with an indication of the functional group controlled intermolecular π-π interactions

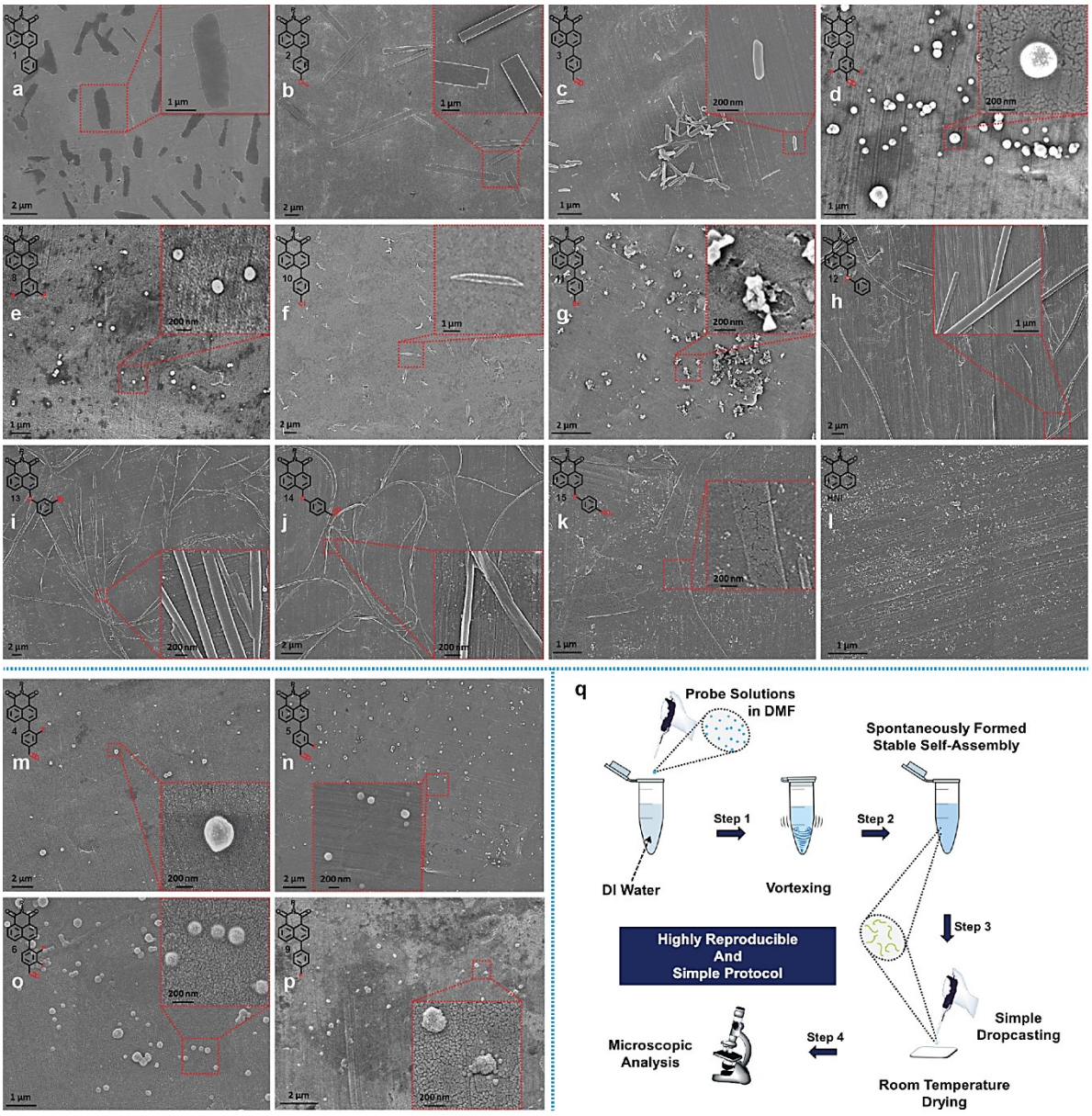

Figure 3.5. (a-p) FESEM images of the nano and micro-assembly of the luminogens formed at 99.9% f_w in DMF (10 μM) spontaneously by simple drop-casting technique followed by room temperature drying as schematically presented in (q). The insets show the corresponding chemical structure of the naphthalimide luminogens (left) and magnified images at selected area (right). (q) Schematic representation of the practically simple, cost-effective and highly reproducible methodology for the preparation of supramolecular nano and micro-assembly from the naphthalimide luminogens.

between naphthalimide cores, the supramolecular self-assembly of the congeners were evaluated by recording Field Emission Scanning Electron Microscopy (FESEM) and Dynamic Light Scattering (DLS) analysis (Figure 3.5 and Figure A3.10). Despite the similar structural skeleton and comparable molecular conformation, DLS studies of the naphthalimide aggregates (10 μM) in aqueous media (with 0.1% DMF) showed a huge disparity in the size of the stable and monodispersed nano-assembly ranging from 170 to 490 nm of Zave (Figure A3.10). FESEM images of the spontaneously self-assembled naphthalimides were obtained by simple drop-casting technique followed by room temperature drying. As schematically presented in Figure 3.5q, the practically simple, cost-effective, and highly reproducible methodology was used for the preparation of the FESEM samples. A fraction of concentrated probe solution in DMF was dispersed in water to get a dispersed probe solution at 10 μM concentration and was well-shaken on a vortex mixer for few seconds. The homogeneously dispersed aqueous solution containing 0.1% DMF was drop-casted on a glass substrate coated with aluminium foil and allowed to dry at room temperature overnight before FESEM analysis. Similar protocols were followed to get all microscopic images for all the congeners.

The FESEM images of spontaneously formed nano-assembly of all the congeners at 99.9% f_w in DMF have been presented in Figure 3.5a-p (insets represent the respective chemical structures). By varying the pendant functional groups in the same naphthalimide skeleton, highly distinct well-defined nano and micro-architectures were generated by simple drop-casting technique under precisely similar conditions. Without any functional groups, **1** self-assembled into micro-aggregates lacking a particular shape and size (Figure 3.5a). However, substitution of a functional group that may be methoxy, formyl, halogen, nitro or ether group, at the phenyl core was found to provide a directional growth to their assembly formation. **2** with methoxy group formed highly regular rectangular shape whereas replacing methoxy with formyl group resulted in the formation of short nano-rod like assembly as observed in **3** (Figure 3.5b-c)**.** The replacement of C-C linkage between naphthalimide and phenyl ring by ether linkage increased the flexibility of the molecules and transformed it into V-shape conformation. This led to the formation of long nano-rods to fibril like morphology (Figure 3.5h-j). Such diverse morphological transformation in the naphthalimides by varying the functional groups confirmed their highly efficient tuning ability. Besides, the formation of unsymmetrical nanoparticles in **HNI** demonstrated the triggering ability of the phenyl core in the supramolecular self-assembly (Figure 3.5l). The formation of spherical nanoparticles in **4-9** demonstrated the dominance of the fluorine moiety over formyl group

owing to its higher electronegative nature and also confirmed the insignificant effect of the attachment position of fluorine moiety (Figure 3.5m-p).

3.3.6. Orderliness of Supramolecular Assembly Reflecting Condensed State Luminescence

Further, the aggregation kinetics of the naphthalimides as a function of f_w in DMF was also studied and correlated to their abnormal aggregation based fluorescence emission in their spontaneously formed supramolecular self-assemblies. Despite the similar molecular skeleton, the naphthalimides showed distinct aggregation based emission enhancement trend. For instance, **3** showed maximum emission intensity at 50% f_w with a steady decline in the emission intensity from 50% to 99.9% f_w in DMF (Figure 3.3c). However, **12** showed the lowest emission intensity at 50% f_w, which increased steadily with the increase in f_w from 50% to 99.9% (Figure 3.3d). To acquire more insight into the aggregation based fluorescence behavior, morphological analysis of the supramolecular assemblies formed at different f_w were carried out (Figure 3.6 and Figure A3.11-13). In sharp contrast to 300-400 nm length of rod-like morphology at 99.9% f_w, **3** formed fine nanoparticles below 20 nm diameter at 50% f_w in DMF (Figure 3.6a). DLS measurements also confirmed the formation of nanoparticles

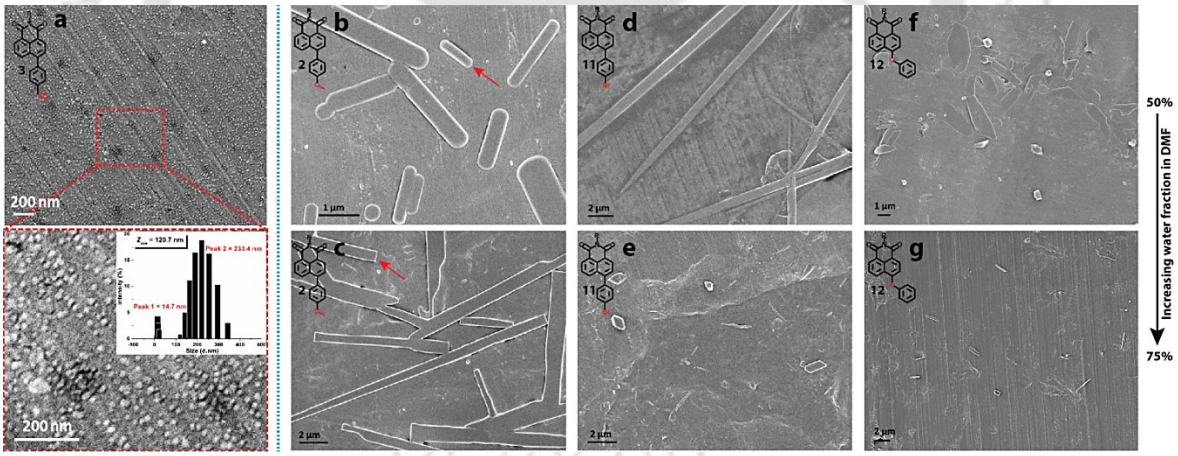

Figure 3.6. (a) FESEM images of the homogeneously dispersed nano-assembly of **3** formed at 50% f_w in DMF along with its magnified image at selected area (10 µM). The insets show the corresponding hydrodynamic diameter of **3** at 50% f_w in DMF (10 µM) where two different size distributions as peak 1 with average size of 14.7 nm and peak 2 with average size of 223.4 nm were observed. (b-g) The morphological transformation in **2, 11** and **12** upon increased f_w in DMF. The critical water content was nearly 50% upto which the molecules remain soluble in the medium. FESEM images of the respective luminogens formed at 50% (b, d and f) and 75% (c, e and g) f_w in DMF respectively. Few more FESEM images of other congeners at different f_w in DMF (10 µM) has been placed in supporting information as Figure A3.11-13, see ESI†. All the FESEM images were obtained by simple drop-casting technique followed by room temperature as schematically presented in Figure 3.5q.

with 14.7 nm of Z_{ave} (inset, Figure 3.6a). Thus, it could be assumed that the formation of very fine and ordered nanoparticles might be responsible for the highest fluorescence emission of **3** at 50% f_w. The FESEM images for few other congeners were obtained at 50% and 75% f_w, which showed drastic perturbation in their nature of self-assembly. As the orderliness of the micro-rods in **2** increased from f_w 50% to 99.9%, the aggregated state emission intensity increased (Figure 3.3b, 3.5b, 3.6b, and 3.6c). Similarly, **11** emitted brighter at 50% f_w in DMF, in which it self-assembled into microneedles like architectures (Figure 3.6d). However, with the increase in f_w the microneedle gradually vanished to form unsymmetrical nanoparticles at 99.9% f_w with steady decay in the fluorescence emission of the aggregates (Figure 3.5g, 3.6e, and A3.7). The lowest fluorescence emission of **12** at 50% f_w and its 8-fold increased emission at 99.9% f_w can also be rationalized with the formation of respective unsymmetrical micro-particles and well-defined nanorods (Figure 3.3d, 3.5h, 3.6f, and 3.6g). Moreover, the commencement of nanorod formation can also be visualized in the FESEM image of **12**-aggregates formed at 75% f_w (Figure 3.6g). Similar results were also obtained in other congeners and thus, the fluorescence emission of the congeners at different f_w in DMF could be readily correlated with the degree of the orderliness of their respective supramolecular self-assembly (Figure 3.4, 3.6 and A3.11-13). Thus, it confirmed the polymorphic nature of the naphthalimide congeners at different f_w leading to distinct spectral as well as morphological perturbation. With the increase in the f_w, the polarity of the medium along with the hydrophobic repulsion between the naphthalimides and the solvent molecule differs which energizes their polymorphic behavior. Additionally, the high responsiveness of the naphthalimides towards solvent composition could be due to the presence of functional groups. Moreover, in few literature, it had been assumed that the decrease of fluorescence emission of AIEgenic materials at higher f_w could be due to the formation of larger agglomeration.[18] However, in this report, we have experimentally demonstrated and correlated the regularity of the supramolecular self-assembly with the fluorescence emission of AIE/AIEEgenic materials.

3.3.7. XRD Analysis of the Supramolecular Interactions in Naphthalimides

To get more insight into the tuner and trigger property of the functional groups and the pendant phenyl cores respectively, the intermolecular interactions along with the packing arrangements of the naphthalimides were analyzed through the single crystal and powder XRD studies. The single crystals of **2, 8, 9, 10** and **12** were obtained by recrystallizing them

from DMF (Figure A3.14 and Table A3.3), whereas the single crystal data of **HNI** was obtained from Cambridge Crystallographic Data Centre (CCDC).[36,37] Nevertheless, we also obtained the **HNI** crystal in DMF and were found to have exactly the same intermolecular packing arrangement to that of the **HNI** single crystal obtained from CCDC (where single crystal had been generated from hexane/DCM solvent system). This confirmed the non-polymorphic nature of **HNI** single crystal formed in different solvent.[38] Unfortunately,

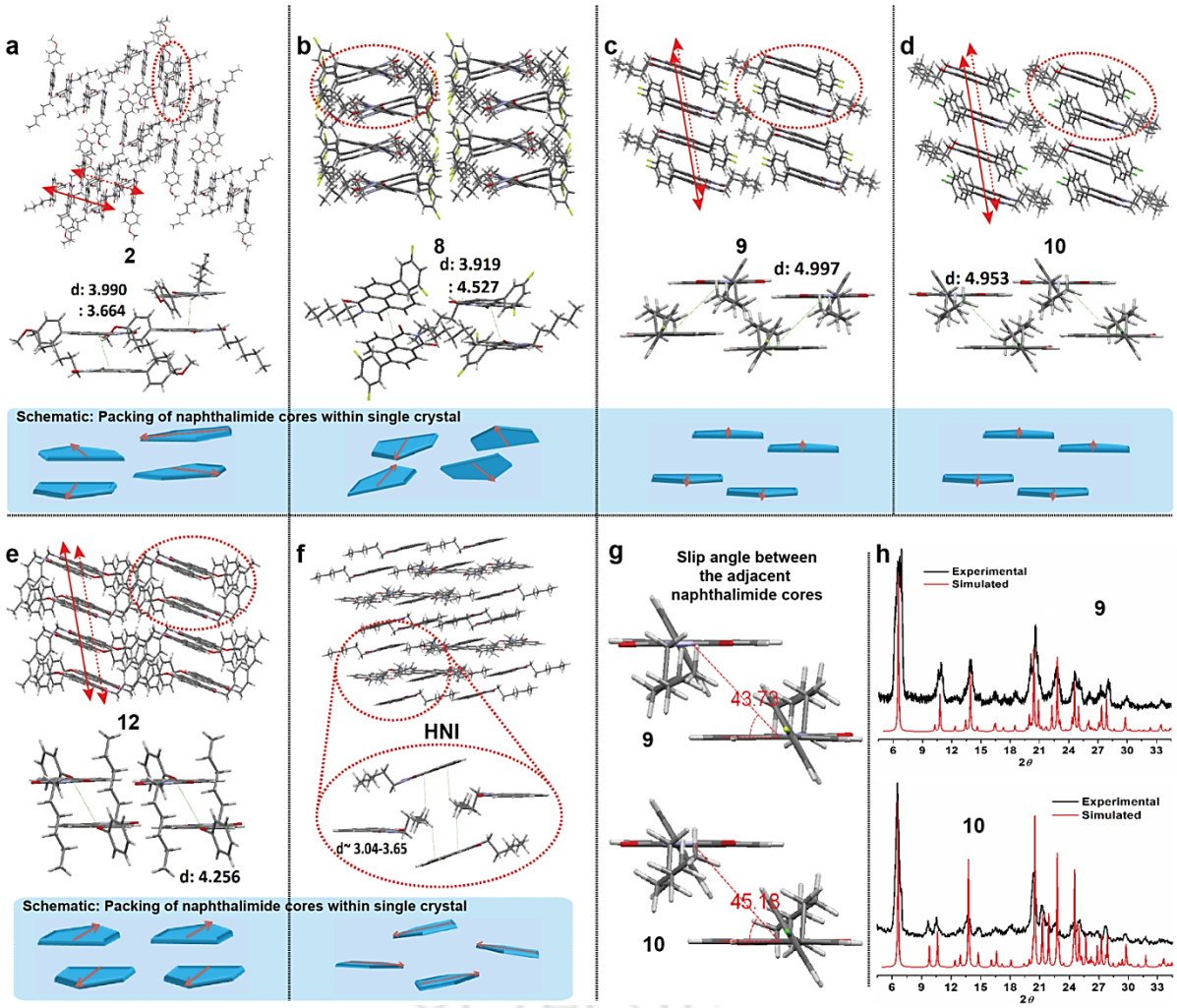

Figure 3.7. (a-f) Single-crystal packing diagram of the bulk along with the packing arrangements of naphthalimide molecules (**2**, **8**, **9**, **10**, **12** and **HNI**) and their corresponding schematic showing π-π stacking interactions among naphthalimide cores. The local packing representations were picked from the portions in circles of corresponding ones, in which the centroid–centroid distances between the naphthalimide cores involved in the π–π stacking interactions have been presented in Å. (g) Intermolecular π-π stacking interactions in **9** and **10** showing the slip angle between the naphthalimide cores. (h) PXRD spectra for **9** and **10** compared with their simulated PXRD pattern as obtained from SCXRD data. The PXRD spectra for other congeners and few more single-crystal packing drawings have been presented in the supporting information as Figure A3.14-18.

despite repeated attempts, the quality of single crystals obtained for few other congeners were inappropriate for X-ray crystallography studies whereas the single crystals of rest of the congeners were too inferior.

As summarized in Figure 3.7, the striking differences in the intermolecular packing arrangements among the naphthalimides were precisely noticeable in their X-ray crystal structure. It is worthy to mention that, although the single crystals of the congeners were obtained from DMF, none of the crystal lattices contained solvent molecules.[38] It can be observed that the CH-π interactions between the naphthalimide core and the alkyl chains are highly dominant in **HNI** (Figure 3.7f), whereas none of the naphthalimide derivatives with pendant phenyl core (**2, 8, 9, 10** and **12**) exhibited CH-π interactions involving naphthalimide cores (Figure 3.7a-e). Such transformation in the crystal packing confirmed the triggering nature of the pendant phenyl ring for dominant π-π stacking interactions among the naphthalimide cores. A huge variation in the nature of intermolecular π-π stacking interactions between the naphthalimide cores were witnessed in these congeners with distinct functional groups attached at the phenyl rings (Figure 3.7a-e and A3.15-17). The schematics as presented in Figure 3.7 give a simplified visualization on the stacking arrangement of the naphthalimide core inside the single crystal and are witness to the fact that without any direct intermolecular interaction of the substituted functional groups with the naphthalimide core, the packing arrangement of the naphthalimide cores had been significantly distorted by minor structural modulation. The subtle difference in their crystal packing could also be correlated with the dihedral angle (θ) between the naphthalimide and phenyl planes (Figure A3.18). It has been well-documented that the electron-withdrawing substituents enhance π–π interactions by decreasing the π-electron density of the π-system, whereas electron-donating substituents weaken the π–π interactions by enhancing the π-electron density of the aromatic core.[39,40] However, a contrary trend was realized in these naphthalimide congeners where, **2** and **12** with the electron-donor functional group (-OMe and -OPh) showed much stronger π–π interactions than other structurally similar congeners with electron withdrawing groups (Figure 3.7a-e). Whereas, despite the significant polarizability difference in -F and -Cl units, a very small deviation in the intermolecular stacking orientations was observed in **9** and **10** leading to almost similar emission spectra with very small shift in their emission maxima (Figure 3.7c, 3.7d, 3.7g). This could be due to the insignificant difference in their magnitude of steric crowding created by -F and -Cl. This confirmed that the condensed state intermolecular π–π interactions in the naphthalimide systems are fully controlled by the steric constraints and are almost independent of the

electronic influence of the functional groups. Thus, the driving forces behind the spontaneously formed distinct and well defined supramolecular assembly could be the finely tailored intermolecular packing arrangements of the naphthalimide cores, which subsequently tuned their condensed state emission properties.[32,33] To rationalize the distinct stacking orientations of the congeners in their stacking interactions, the powder XRD pattern for all the congeners were recorded (Figure 3.7h, A3.19). For few congeners with single crystal XRD data, the experimental PXRD patterns were found to match perfectly with their respective simulated powder XRD patterns (Figure 3.7h, A3.19). Along with the distinct crystallinity in the naphthalimides, the PXRD patterns of most of the congeners showed highly distinct diffraction patterns clearly showing their huge distortion in intermolecular stacking orientations. Whereas, the PXRD pattern of **9** and **10** are highly comparable due to their closely related intermolecular stacking interactions. Thus, the PXRD patterns could also be used secondary tool to gain a relative understanding of the intermolecular stacking distortion in the naphthalimides.

3.3.8. Elucidation of Dark State in 15

Most interestingly, **15** with a nitro functional group remains almost in the dark state in both solution and condensed state with a quantum yield of less than 0.7%, which suggested that the molecule was independent of ACQ or AIE property (Figure 3.3e and Table A3.1). To better understand the fluorescence property of **15** at the molecular level, computational studies for all the congeners were performed by density functional theory (DFT) (Figure A3.20). Unlike in rest of the congeners, **14** and **15** showed complete charge separation, where, the π-electrons over the HOMO and LUMO are localized in their respective donor and acceptor moieties (Figure A3.21). This suggested that, both **14** and **15** could facilitate intramolecular charge transfer (ICT) process via push–pull interactions and could quench the system completely (Figure 3.8a). However, **14** was found to emit intensely in both solution and aggregated state with high quantum yield (Table A3.1). Thus, to better understand, the HOMO/LUMO energy levels of the individual aromatic moieties, which were identical to HNI and various small phenyl derivatives (summarized in Table A3.4, see ESI†), were calculated. The HOMO/LUMO energy levels, as presented in Figure 3.8b, showed a strong probability of donor-excited photoinduced electron transfer (d-PET) process in the HNI/p-nitrophenol system.9,41 However, the PET process is not feasible in HNI/p-hydroxybenzaldehyde system (Figure 3.8b-c).

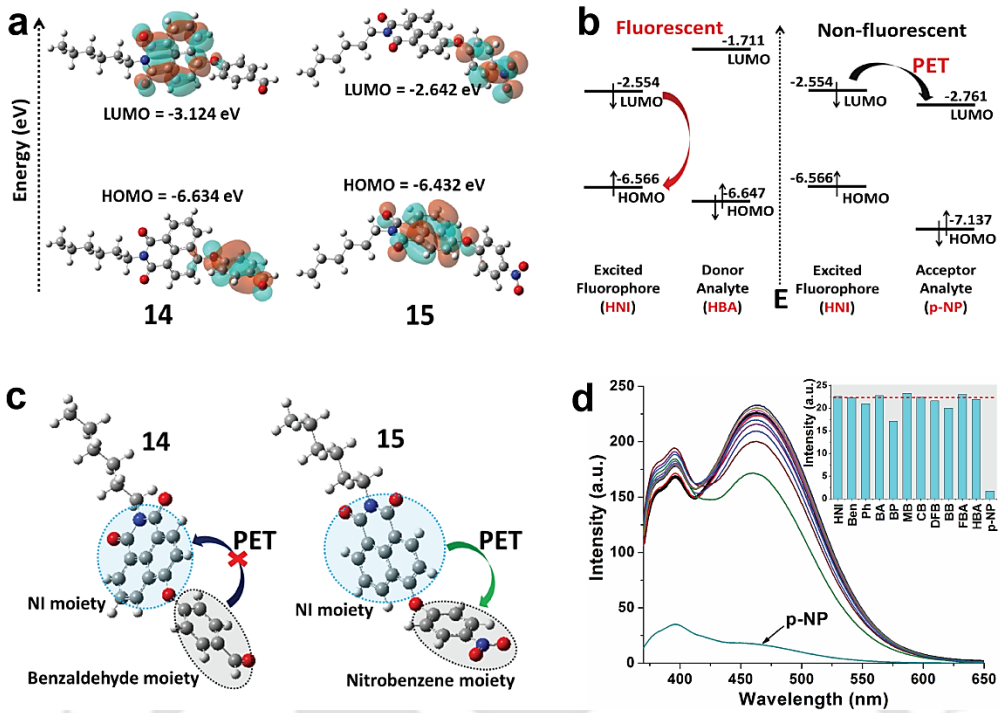

Figure 3.8.. (a) HOMO/LUMO electron distribution in **14** and **15**. (b) Schematic molecular orbital diagram of the fluorescence on/off switch in **HNI** via PET process with p-hydroxybenzaldehyde and p-nitrophenol (values are in eV). (c) Optimized structure of **14** and **15** presenting the co-regulation of response emission by the *d*-PET mechanism. (d) Fluorescence emission spectra of **HNI** (10 μM) in presence of various small molecules (90 μM) in water. Inset: bar diagram showing the fluorescence intensity of HNI and **HNI** + small molecules at 470 nm; left to right: **HNI** only, benzene (Ben), phenol (Ph), benzaldehyde (BA), bromophenol (BP), methoxybenzene (MB), chlorobenzene (CB), difluorobenzene (DFB), bromobenzene (BB), fluorobenzaldehyde (FBA), phydroxybenzaldehyde (HBA), p-nitrophenol (p-NP).

Thus, despite similar electronic distribution to that of 15, 14 emit strongly in both solution and condensed state due to the inhibition of PET process. Besides, the process of PET in 15 was further confirmed experimentally by the fluorescence titration of HNI with various phenyl derivatives likely to be mimics of the pendant phenyl moieties present in 1-15, where significant reduction in fluorescence emission (~90%) was witnessed in presence of p-nitrophenol as compared to other small molecules (Figure 3.8d, A3.21, see ESI†). Thus, the comprehensive study suggested that, although the condensed state fluorescence properties of the naphthalimides are almost independent to the electronic influence of the functional groups, the appearance of PET process can drive the fluorophores completely into the dark state even in their condensed state. Besides, it is not necessary for every nitro-containing chromophore to be non-fluorescent without the feasibility of dynamic electron/energy transfer process, which can be understood by the strong fluorescence in many nitro groups containing proves.[41-43]

3.4. Conclusion

In summary, a library of 15 naphthalimide congeners has been strategically designed and synthesized that demonstrated the unexplored influence of functional groups on the condensed state photophysical and supramolecular self-assembly properties. Along with the tuning of condensed state emission property and regulation of ACQ-to-AIE transformation phenomenon, this simple yet novel strategy generates and systematically tailors the supramolecular assembly via a practically simple protocol. Unlike the electronic dominance of the functional groups in the solution state, the condensed state properties are shown to be regulated by intermolecular packing orientations of the naphthalimide cores, which in turn are controlled by the distinct steric constraint generated by the functional motifs. Therefore, the perturbation of the packing orientation of the naphthalimide congeners provided the required driving force for the spontaneously tailored well defined supramolecular self-assembly, which subsequently alters their condensed state emission properties. Besides, the appearance of PET process has been encountered to completely destroy the fluorescence properties of the fluorophore in both solution and condensed state, which provides vital leads to the strategic design of condensed state emitting materials.

References

(1) Fujita, D.; Ueda, Y.; Sato, S.; Mizuno, N.; Kumasaka, T.; Fujita, M. *Nature* **2016**, *540*, 563-566.

(2) Zhu, R.; Lübben, J.; Dittrich, B.; Clever, G. H.; *Angew. Chem. Int. Ed.* **2015**, *54*, 2796-2800.

(3) Sun, Q.-F.; Iwasa, J.; Ogawa, D.; Ishido, Y.; Sato, S.; Ozeki, T.; Sei, Y.; Yamaguchi, K.; Fujita, M. *Science* **2010**, *328*, 1144-1147.

(4) Hasenknopf, B.; Lehn, J.-M.; Kneisel, B. O.; Baum, G.; Fenske, D. *Angew. Chem. Int. Ed.* **1996**, *35*, 1838-1840.

(5) He, X.; He, Y.; Hsiao, M.-S.; Harniman, R. L.; Pearce, S.; Winnik, M. A.; Manners, I. *J. Am. Chem. Soc.* **2017**, *139*, 9221-9228.

(6) Biedermann, F.; Schneider, H.-J. *Chem. Rev.* **2016**, *116*, 5216-5300.

(7) Sinn, S.; Yang, L.; Biedermann, F.; Wang, D.; Kübel, C.; Cornelissen, J. J. L. M.; Cola, L. D. *J. Am. Chem. Soc.* **2018**, *140*, 2355−2362.

(8) Peebles, C.; Wight, C. D.; Iverson, B. L. *J. Mater. Chem. C* **2015**, *3*, 12156--12163.

(9) Meher, N.; Iyer, P. K. *Angew. Chem. Int. Ed.* **2018**, *57*, 8488-8492.

(10) Shin, S.; Menk, F.; Kim, Y.; Lim, J.; Char, K.; Zentel, R.; Choi, T.-L. *J. Am. Chem. Soc.* **2018**, 140, 6088-6094.

(11) Mal, P.; Breiner, B.; Rissanen, K.; Nitschke, J. R. *Science* **2009**, 324, 1697-1699.

(12) Pluth, M. D.; Bergman, R. G.; Raymond, K. N. *Science* **2007**, 316, 85-88.

(13) Jenekhe, S. A.; Osaheni, J. A. *Science* **1994**, *265*, 765-768.

(14) Martinez, C. R.; Iverson, B. L. *Chem. Sci.* **2012**, *3*, 2191–2201.

(15) Luo, J.; Xie, Z.; Lam, J. W. Y.; Cheng, L.; Chen, H.; Qiu, C.; Kwok, H. S.; Zhan, X.; Liu, Y.; Zhu, D.; Tang, B. Z. *Chem. Commun.* **2001**, 1740-1741.

(16) Mei, J.; Hong, Y.; Lam, J. W. Y.; Qin, A.; Tang, Y.; Tang, B. Z. *Adv. Mater.* **2014**, *26*, 5429-5479.

(17) Mei, J.; Leung, N. L. C.; Kwok, R. T. K.; Lam, J. W. Y.; Tang, B. Z. *Chem. Rev.* **2015**, *115*, 11718-11940.

(18) Gopikrishna, P.; Meher, N.; Iyer, P. K. *ACS Appl. Mater. Interfaces* **2018**, *10*, 12081-12111.

(19) Zhang, H.; Zheng, X.; Xie, N.; He, Z.; Liu, J.; Leung, N. L. C.; Niu, Y.; Huang, X.; Wong, K. S.; Kwok, R. T. K.; Sung, H. H. Y.; Williams, I. D.; Qin, A.; Lam, J. W. Y.; Tang, B. Z. *J. Am. Chem. Soc.* **2017**, *139*, 16264-16272.

(20) Sturala, J.; Etherington, M. K.; Bismillah, A. N.; Higginbotham, H. F.; Trewby, W.; Aguilar, J. A.; Bromley, E. H. C.; Avestro, A.-J.; Monkman, A. P.; McGonigal, P. R. *J. Am. Chem. Soc.* **2017**, *139*, 17882-17889.

(21) Wang, J.; Gu, X.; Zhang, P.; Huang, X.; Zheng, X.; Chen, M.; Feng, H.; Kwok, R. T. K.; Lam, J.W. Y.; Tang, B. Z. *J. Am. Chem. Soc.* **2017**, *139*, 16974-16979.

(22) Moragues, M. E.; Toscani, A.; Sancenon, F.; Martinez-Manez, R.; White, A. J. P.; Wilton-Ely, J. D. E. T. *J. Am. Chem. Soc.* **2014**, *136*, 11930-11933.

(23) Campbell, M. G.; Liu, S. F.; Swager, T. M.; Dinca, M. *J. Am. Chem. Soc.* **2015**, *137*, 13780-13783.

(24) Dong, J.; Zhang, K.; Li, X.; Qian, Y.; Zhu, H.; Yuan, D.; Xu, Q.-H.; Jiang, J.; Zhao, D. *Nat. Commun.* **2017**, *8*, 1142.

(25) Meher, N.; Panda, S.; Kumar, S.; Iyer, P. K. *Chem. Sci.,* **2018**, *9*, 3978-3985.

(26) Meher, N.; Iyer, P. K. *Nanoscale* **2017**, *9*, 7674-7685.

(27) Dong, Y.; Xu, B.; Zhang, J.; Tan, X.; Wang, L.; Chen, J.; Lu, H.; Wen, S.; Li, B.; Ye, L.; Zou, B.; Tan, W. *Angew. Chem., Int. Ed.* **2012**, *51*, 10782-10785.

(28) Yan, D.; Delori, A.; Llyod, G. O.; Friscic, T.; Day, G. M.; Jones, W.; Lu, J.; Wei, M.; Evans, D. G.; Duan, X. *Angew. Chem., Int. Ed.* **2011**, *50*, 12483-12486.

(29) Meher, N.; Chowdhury, S. R.; Iyer, P. K. *J. Mater. Chem. B* **2016**, *4*, 6023-6031.

(30) Duke, R. M.; Veale, E. B.; Pfeffer, F. M.; Kruger, P. E.; Gunnlaugsson, T. *Chem. Soc. Rev.* **2010**, *39*, 3936-3953.

(31) Chen, X. Q.; Wang, F.; Hyun, J. Y.; Wei, T. W.; Qiang, J.; Ren, X. T.; Shin, I.; Yoon, J. *Chem. Soc. Rev.* **2016**, *45*, 2976-3016.

(32) Kasha, M.; Rawls ,H. R.; El-Bayoumi, M. A. *Pure Appl. Chem.* **1965**, *11*, 371.

(33) Davydov, A. S. *Theory of Molecular Excitons*, Plenum Press, New York, **1971**.

(34) Dong, J.; Solntsev, K. M.; Tolbert, L. M. *J. Am. Chem. Soc.* **2009**, *131*, 662-670.

(35) Zhen, G.; Lu, X.; Wang, B.; Zhao, Y.; Chai, X.; Niu, D.; Zhao, A.; Li, Y.; Song, Y.; Cao. X. *Bioresource Technology* **2012**, *124*, 29-36.

(36) Chen, Z.; Wu, D.; Han, X.; Nie, Y.; Yin, J.; Yu, G.-A.; Liu, S. H. **2014**, *CCDC 1014214*: Experimental Crystal Structure Determination, Cambridge Crystallographic Data Centre. http://dx.doi.org/10.5517/cc131cl3.

(37) Chen, Z.; Wu, D.; Han, X.; Nie, Y.; Yin, J.; Yu, G.-A.; Liu, S. H. *RSC Adv.* **2014**, *4*, 63985-63988.

(38) Peebles, C.; Alvey, P. M.; Lynch, V.; Iverson, B. L. *Cryst. Growth Des.* **2014**, *14*, 290–299.

(39) Cozzi, F.; Cinquini, M.; Annuziata, R.; Siegel, J. S. *J. Am. Chem. Soc.* **1993**, *115*, 5330-5331.

(40) Yang, J.; Zhen, X.; Wang, B.; Gao, X.; Ren, Z.; Wang, J.; Xie, Y.; Li, J.; Peng, Q.; Pu, K.; Li, Z. *Nat. Commun.* **2018**, *9*, 840.

(41) Ueno, T.; Urano, Y.; Setsukinai, K.; Takakusa, H.; Kojima, H.; Kikuchi, K.; Ohkubo, K.; Fukuzumi, S.; Nagano, T. *J. Am. Chem. Soc.* **2004**, *126*, 14079–14085.

(42) Zhao, W.; He, Z.; Peng, Q.; Lam, J. W. Y.; Ma, H.; Qiu, Z.; Chen, Y.; Zhao, Z.; Shuai, Z.; Dong, Y.; Tang, B. Z. *Nat. Commun.* **2018**, *9*, 3044.

(43) van der Velde, J. H. M.; Oelerich, J.; Huang, J.; Smit, J. H.; Jazi, A. A.; Galiani, S.; Kolmakov, K.; Gouridis, G.; Eggeling, C.; Herrmann, A.; Roelfes, G.; Cordes, T. *Nat. Commun.* **2016**, *7*, 10144.

Appendix

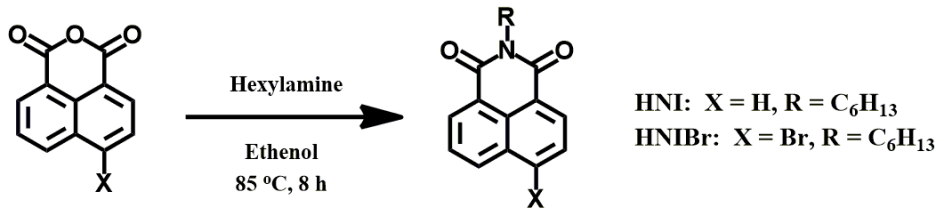

Scheme A3.1. The synthetic procedure used to prepare probe **HNI** and **HNIBr**.

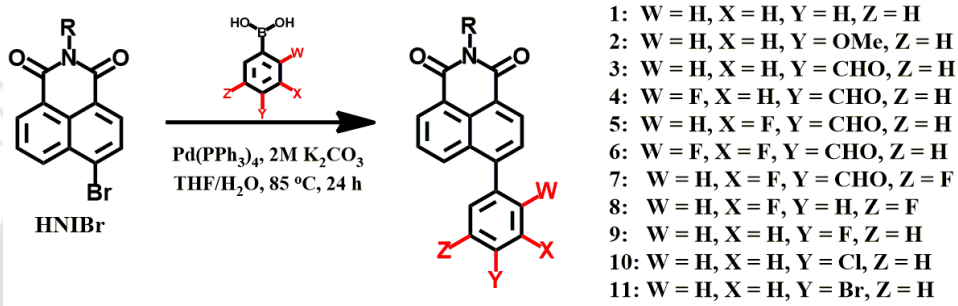

Scheme A3.2. The synthetic procedure used to prepare probe **1** to **11**.

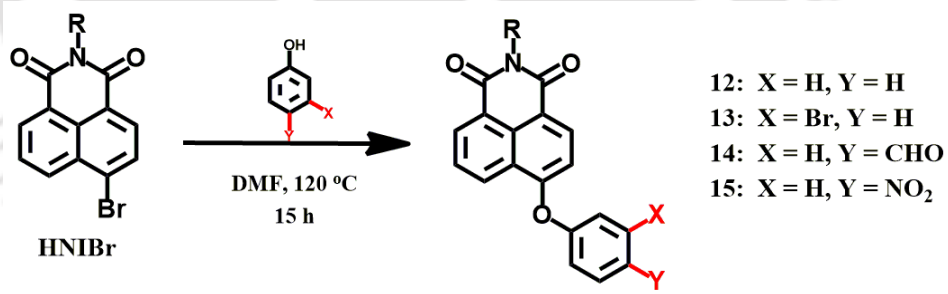

Scheme A3.3. The synthetic procedure used to prepare probe **12** to **15**.

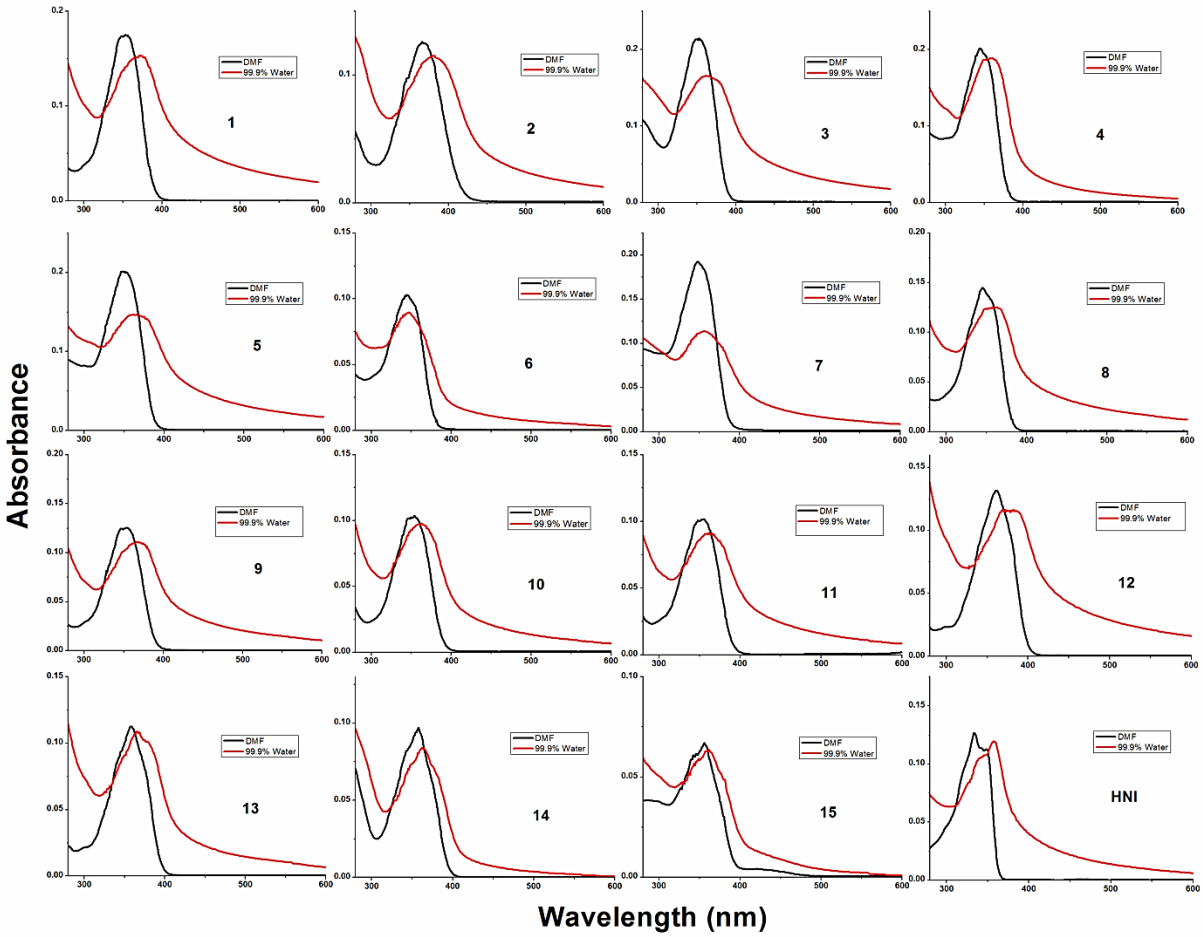

Figure A3.1. Absorption spectra of **1-15** and **HNI** in DMF and at 99.9% water fraction in DMF (at 25 °C, 10 μM).

Table A3.1. Photophysical data for the naphthalimide congeners (**1-15** and **HNI**)

Compound	Solvent[a]	$\lambda_{abs.max}$ (nm)	A	$\lambda_{em.max}$ (nm)	Φ_{FL}[b]
1	0%	353	0.17455	426	0.118
1	50%	359	0.18166	443	0.122
1	99.9%	372	0.15220	460	0.019
2	0%	368	0.11020	491	0.655
2	50%	374	0.13110	521	0.114
2	99.9%	381	0.11543	463	0.304
3	0%	350	0.21420	423	0.028
3	50%	354	0.21704	430	0.088
3	99.9%	362	0.16463	450	0.062
4	0%	347	0.20255	413	0.013
4	50%	352	0.20539	421	0.047

4	99.9%	362	0.18934	433	0.025
5	0%	348	0.20211	423	0.022
5	50%	352	0.20776	431	0.069
5	99.9%	361	0.14708	434	0.047
6	0%	347	0.10352	417	0.031
6	50%	345	0.10855	420	0.072
6	99.9%	347	0.08998	444	0.038
7	0%	349	0.19361	433	0.034
7	50%	350	0.19989	427	0.045
7	99.9%	356	0.11397	432	0.012
8	0%	347	0.14628	410	0.019
8	50%	348	0.14956	424	0.041
8	99.9%	366	0.12658	450	0.019
9	0%	354	0.12579	426	0.796
9	50%	358	0.13033	448	0.927
9	99.9%	366	0.11103	460	0.057
10	0%	354	0.10327	425	0.657
10	50%	354	0.10831	447	0.873
10	99.9%	364	0.09815	459	0.179
11	0%	354	0.10217	426	0.465
11	50%	355	0.10632	444	0.599
11	99.9%	364	0.09043	452	0.183
12	0%	357	0.13058	431	0.130
12	50%	362	0.13412	439	0.010
12	99.9%	385	0.11644	472	0.151
13	0%	356	0.11379	426	0.768
13	50%	359	0.11796	436	0.119
13	99.9%	365	0.10871	468	0.152
14	0%	356	0.09735	424	0.663
14	50%	358	0.09883	436	0.644
14	99.9%	361	0.08361	463	0.233
15	0%	354	0.06762	429	**0.007**
15	50%	354	0.06931	434	**0.005**
15	99.9%	361	0.06317	462	**0.004**
HNI	0%	334	0.12687	381	0.011
HNI	50%	334	0.12780	390	0.034
HNI	99.9%	357	0.12013	462	0.146

[a] Different fraction of water content in DMF. [b] Fluorescence quantum yields calculated using quinine sulfate as the standard (0.1 M H_2SO_4, λ_{ex}=350 nm, Φ_{FL} = 57.7%).

Table A3.2. CIE coordinates for the naphthalimide congeners (**1-15** and **HNI**) in solution and solid state.

Naphthalimidess	Solution		Solid	
	x	y	x	y
1	0.153	0.049	0.164	0.314
2	**0.175**	**0.366**	0.143	0.159
3	0.154	0.053	0.201	0.408
4	0.156	0.046	0.19	0.195
5	0.153	0.055	0.159	0.165
6	0.154	0.054	0.173	0.178
7	0.151	0.066	0.169	0.168
8	0.161	0.048	0.148	0.215
9	0.152	0.053	0.147	0.085
10	0.153	0.051	0.149	0.087
11	0.153	0.055	0.144	0.183
12	0.153	0.061	0.149	0.139
13	0.153	0.052	0.146	0.111
14	0.154	0.048	0.16	0.147
15	0.158	0.073	0.227	0.525
HNI	0.211	0.171	0.151	0.177

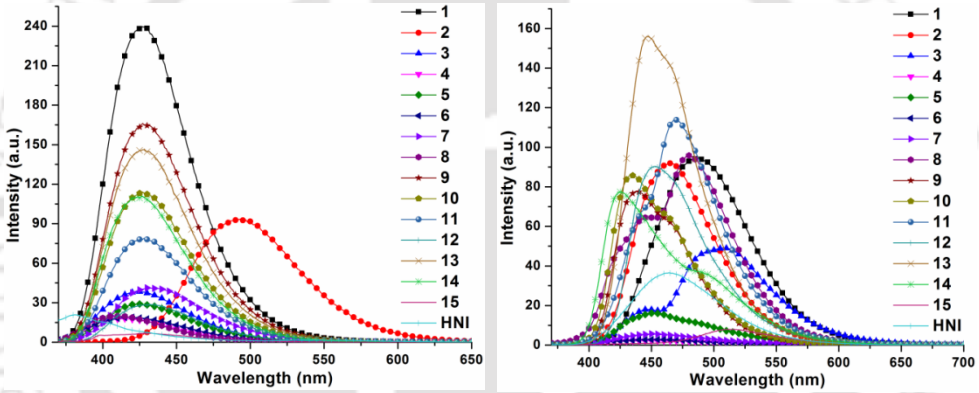

Figure A3.2. (left) Fluorescence spectra of all the congeners in their solution state (in DMF, 10 μM).(right) Solid-state fluorescence spectra of the luminogens. λ_{ex} = 355 nm

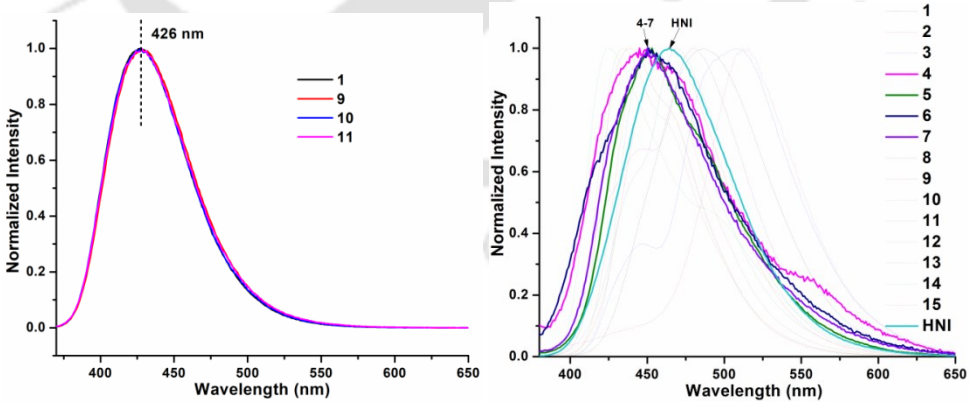

Figure A3.3. (Left) Fluorescence spectra of 1, 9, 10 and 11 in DMF (10 μM, λ_{ex} = 355 nm). (Right) Solid-state fluorescence spectra of the luminogens **1-15** and **HNI** (λ_{ex} = 355 nm).

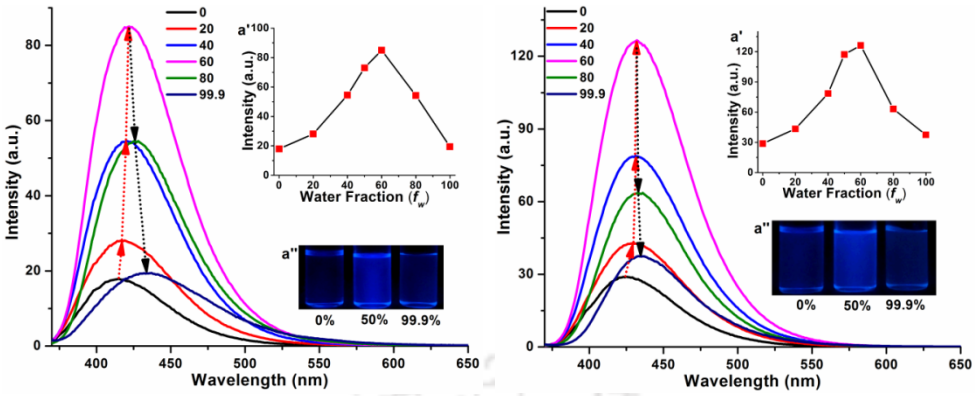

Figure A3.4. Emission spectra of (left) **4** and (right) **5** at different water fraction in DMF (at 25 °C, 10 μM, λ_{ex} = 355 nm). Insets: the respective (a') plot of $\lambda_{emi.max}$ Vs water fraction and (a") digital photographs at different water fraction in DMF under UV irradiation at 365 nm.

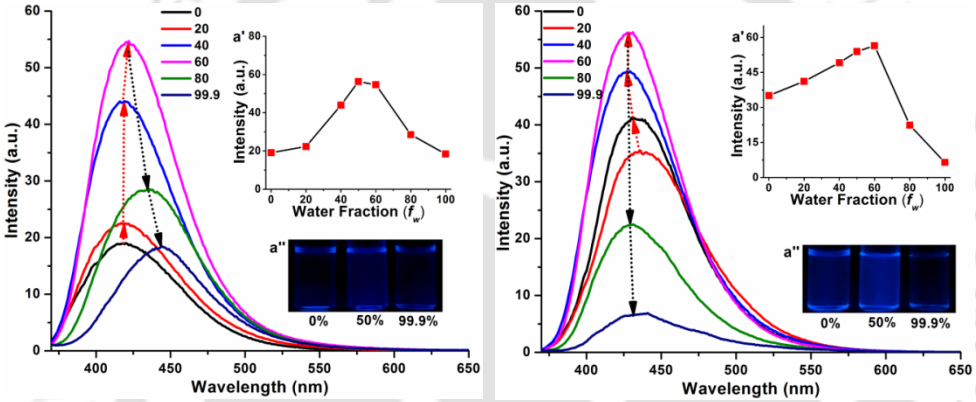

Figure A3.5. Emission spectra of (left) **6** and (right) **7** at different water fraction in DMF (at 25 °C, 10 μM, λ_{ex} = 355 nm). Insets: the respective (a') plot of $\lambda_{emi.max}$ Vs water fraction and (a") digital photographs at different water fraction in DMF under UV irradiation at 365 nm.

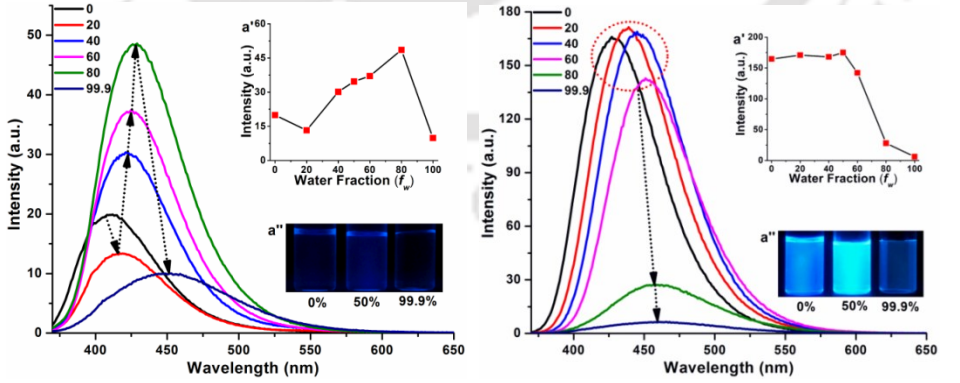

Figure A3.6. Emission spectra of (left) **8** and (right) **9** at different water fraction in DMF (at 25 °C, 10 μM, λ_{ex} = 355 nm). Insets: the respective (a') plot of $\lambda_{emi.max}$ Vs water fraction and (a") digital photographs at different water fraction in DMF under UV irradiation at 365 nm.

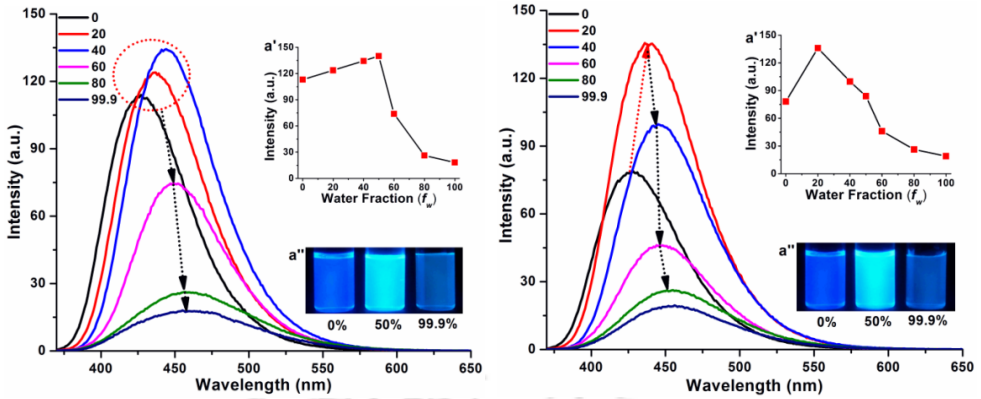

Figure A3.7. Emission spectra of (left) **10** and (right) **11** at different water fraction in DMF (at 25 °C, 10 μM, λ_{ex} = 355 nm). Insets: the respective (a') plot of $\lambda_{emi.max}$ Vs water fraction and (a") digital photographs at different water fraction in DMF under UV irradiation at 365 nm.

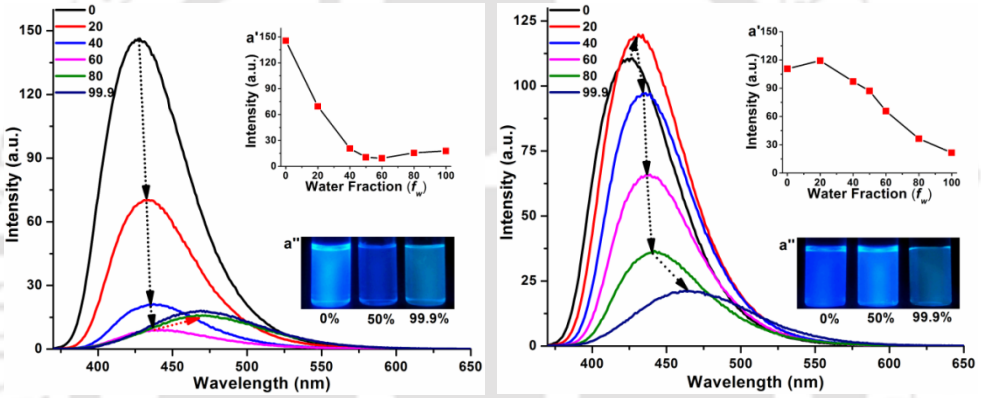

Figure A3.8. Emission spectra of (left) **13** and (right) **14** at different water fraction in DMF (at 25 °C, 10 μM, λ_{ex} = 355 nm). Insets: the respective (a') plot of $\lambda_{emi.max}$ Vs water fraction and (a") digital photographs at different water fraction in DMF under UV irradiation at 365 nm.

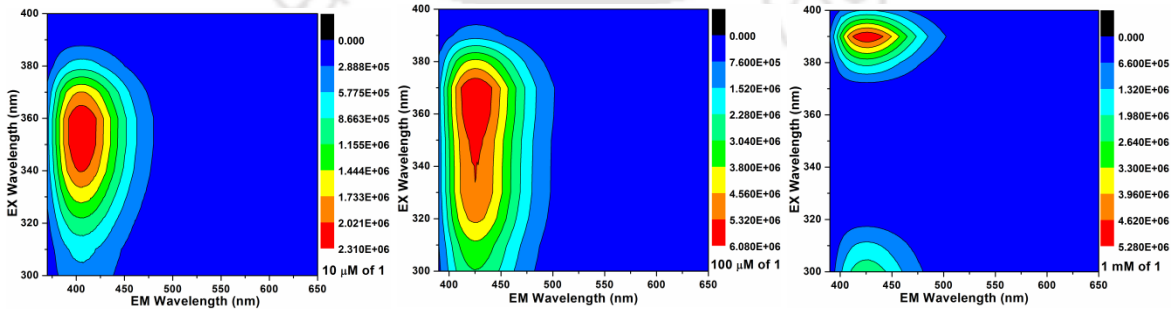

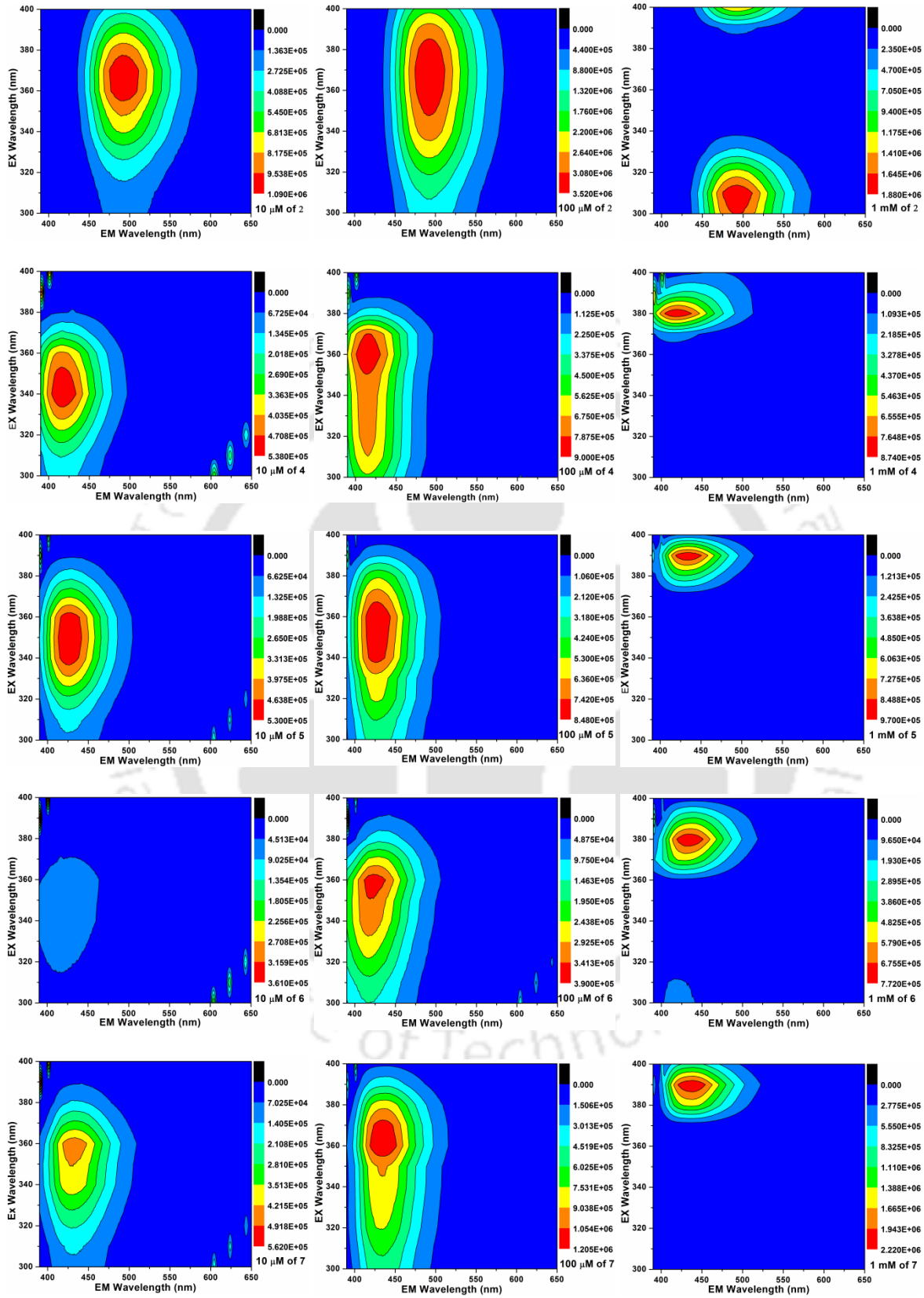

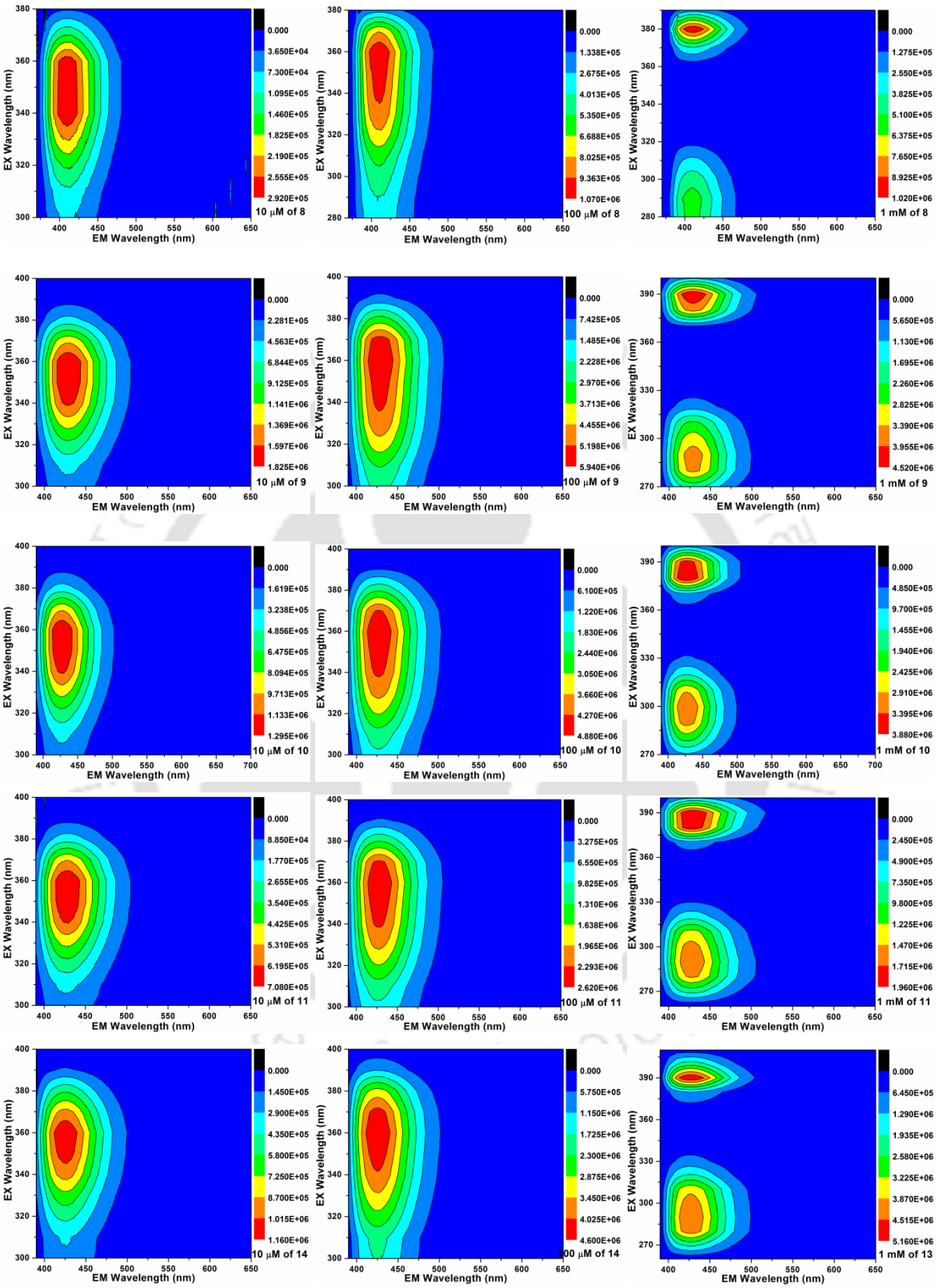

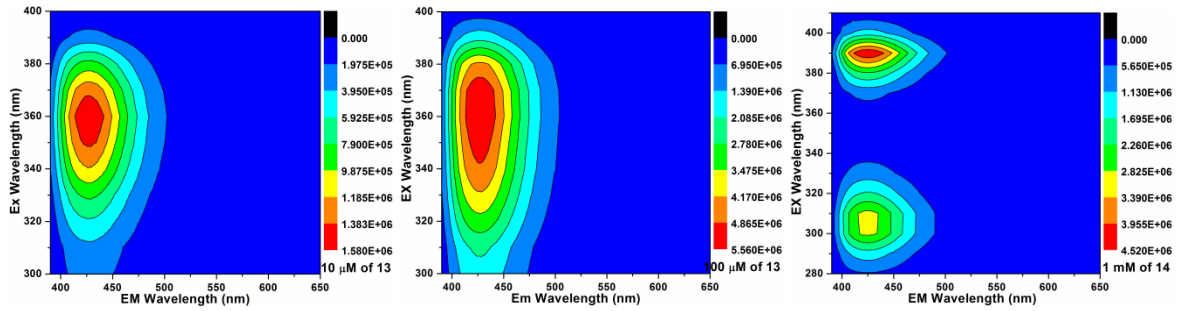

Figure A3.9. Excitation-emission matrix (EEM) spectra (2D contour projections) of **1**, **2**, **4-11**, **13** and **14** in DMF at different probe concentrations at 25 °C. Each row represents the EEM spectra of one congeners with increasing concentrations from left to right.

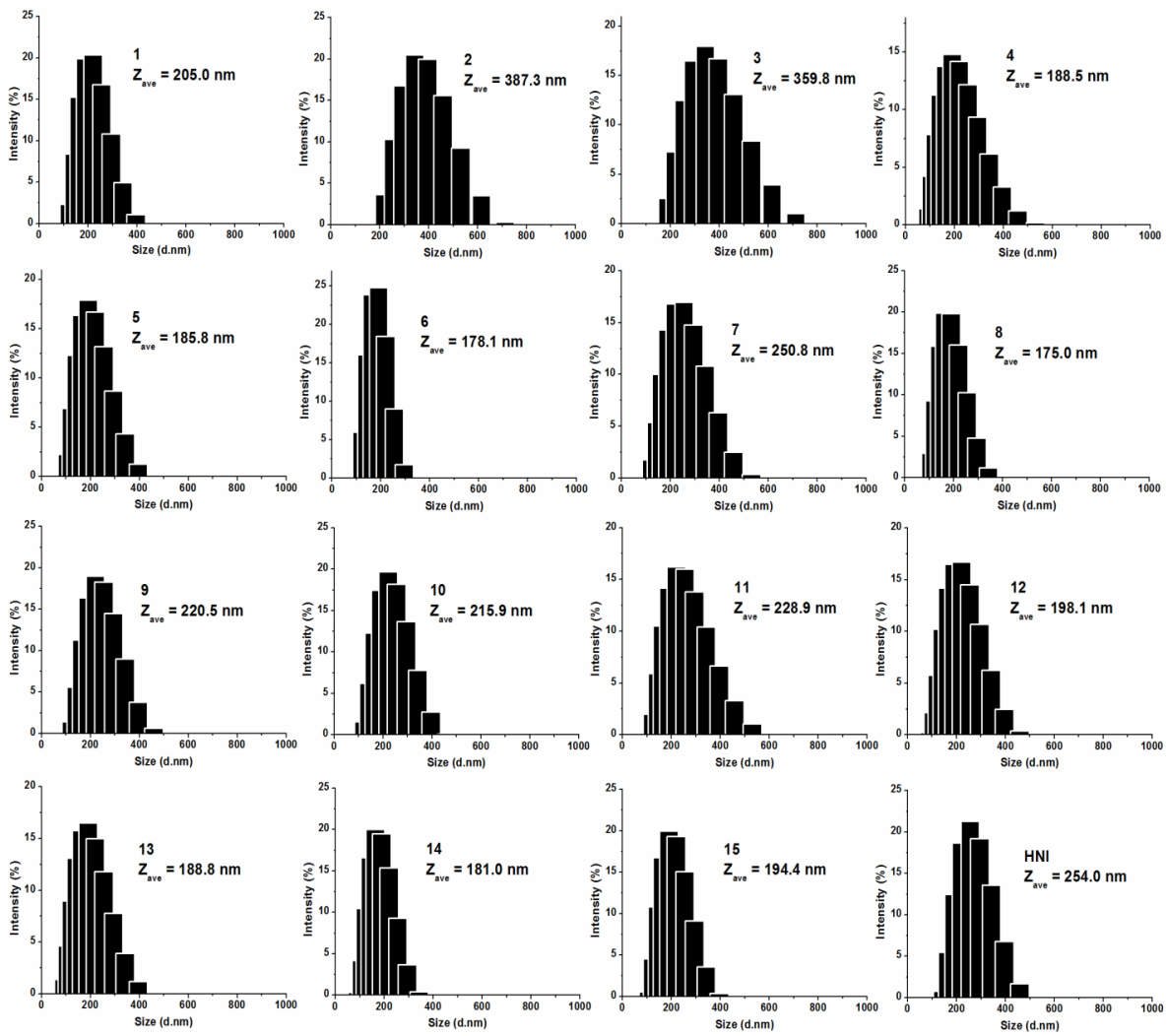

Figure A3.10. Size distribution of **1-15** and **HNI** nanoaggregates (10 μM) by DLS measurements in water at 25 °C.

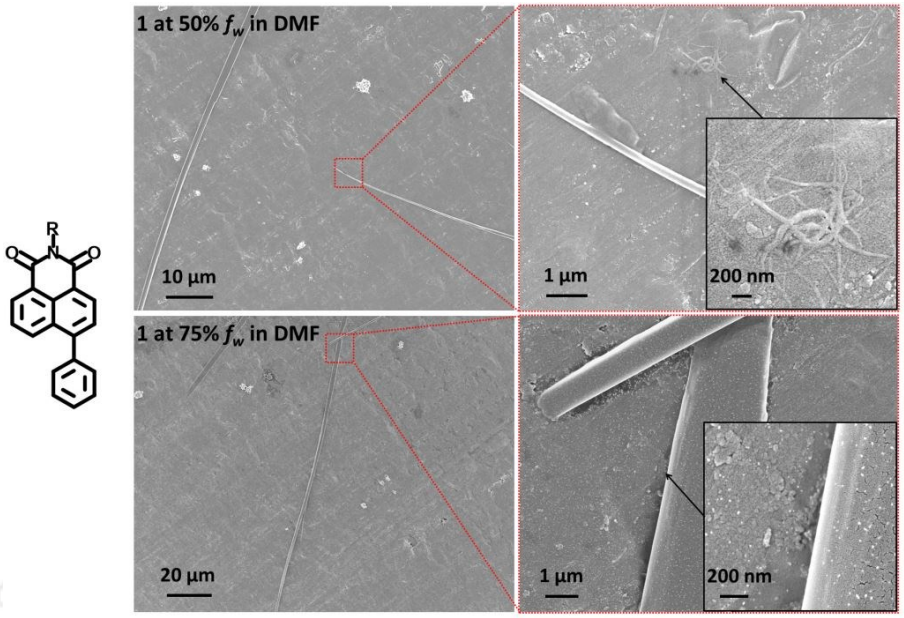

Figure A3.11. FESEM images of the homogeneously dispersed nano-assembly of **1** formed at different f_w in DMF along with its magnified image at selected area (10 µM).

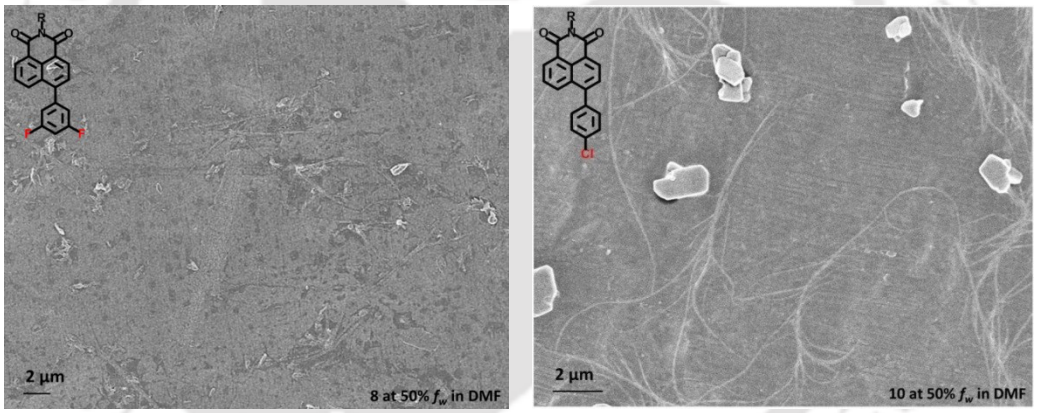

Figure A3.12. FESEM images of the homogeneously dispersed nano-assembly of **8** and **10** formed at 50% f_w in . (10 µM).

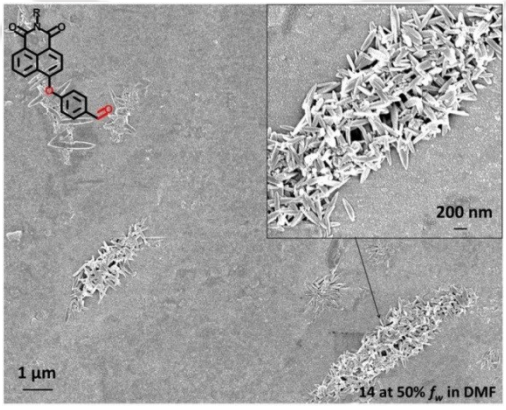

Figure A3.13. FESEM images of the homogeneously dispersed nano-assembly of **14** formed at 50% f_w in DMF (10 µM).

Table A3.3. SC-XRD Data and Parameters for **2**, **8**, **12** and **HNI** crystals.

Compound Code	**2**	**8**	**9**
CCDC	1830094	1830095	1855370
Empirical Formula	$C_{25}H_{25}N_1O_3$	$C_{24}H_{21}F_2N_1O_2$	$C_{24}H_{22}F_1N_1O_2$
Formula Weight	387.47	393.42	375.42
Temperature	298(2) K	298(2) K	298(2) K
Wavelength	0.71073 Å	0.71073 Å	0.71073 Å
Crystal System	monoclinic	monoclinic	triclinic
Space Group	C 12/c1	P 21/c	P -1
Unit Cell Dimension	a = 30.150(3) Å, α= 90° b = 9.1044(5) Å, β = 103.266(3)° c = 14.8046(14) Å, γ = 90°	a = 14.4864(12) Å, α= 90° b = 7.2999(5) Å, β = 92.947(8) ° c = 19.0729(15) Å, γ = 90°	a = 7.9798(6) Å, α= 75.043(7)° b = 8.9908(8) Å, β = 80.201(7)° c = 14.1265(12) Å, γ = 79.756(7)°
Volume	4051.4(6) A^3	2014.3(3) A^3	955.29(14) A^3
Z	8	4	2
Absorption coefficient	0.083 mm^{-1}	0.091 mm^{-1}	0.089 mm^{-1}
F (000)	1648	856	396
Theta range for data collection	2.978 to 24.354°	3.369 to 21.882°	3.369 to 21.882°
Index Range	-27<=h<=26, -6<=k<=10, -13<=l<=14	-17<=h<=19, -9<=k<=8, -23<=l<=23	-10<=h<=10, -11<=k<=11, -18<=l<=15
Reflections Collected/unique	2054/1456 (R_{int} = 0475)	4650/1590 (R_{int} = 0.0521)	4284/1881 (R_{int} = 0.0307)
Goodness-of-fit on F^2	1.085	1.147	1.079
Final R indices [I>2σ(I)]	R1 = 0.0579, ωR2 = 0.1521	R1 = 0.0799, ωR2 = 0.1520	R1 = 0.0667, ωR2 = 0.1396
R indices (all data)	R1 = 0.0786, ωR2 = 0.1740	R1 = 0.2098, ωR2 = 0.2074	R1 = 0.1494, ωR2 = 0.1935
Refinement method	SHELXL	SHELXL	SHELXL
Compound Code	**10**	**12**	**HNI**
CCDC	1882969	1830096	1014214
Empirical Formula	$C_{24}H_{22}Cl_1N_1O_2$	$C_{24}H_{23}N_1O_3$	C_{18} H_{19} N O_2
Formula Weight	391.89	373.44	281.34
Temperature	298(2) K	298(2) K	298(2) K
Wavelength	0.71073 Å	0.71073 Å	0.71073 Å
Crystal System	Triclinic	Triclinic	Monoclinic
Space Group	P -1	P -1	P 21/n
Unit Cell Dimension	a = 7.9984(11) Å, α= 76.64(4) ° b = 9.3801(12) Å, β = 80.682(4) ° c = 13.833(18) Å, γ = 79.49(4)°	a = 7.7872(5) Å, α= 102.882(7) ° b = 8.7869(7) Å, β = 96.881(6) ° c = 15.0163(14) Å, γ = 92.192(6)°	a = 8.2418(14) Å, α= 90° b = 16.336(3) Å, β = 103.266(3)° c = 11.3610(19) Å, γ = 90°
Volume	985.0(2)	992.18(14) A^3	1488.8(4) A^3
Z	2	2	4
Absorption coefficient	0.204 mm^{-1}	0.080 mm^{-1}	0.082 mm^{-1}
F (000)	360	396	600
Theta range for data collection	3.171 to 28.517°	3.593 to 26.097°	2.22 to 25.99°
Index Range	-10<=h<=10, -12<=k<=12, -18<=l<=18	-10<=h<=9, -11<=k<=11, -18<=l<=19	-10<=h<=10, -20<=k<=20, -13<=l<=14
Reflections Collected/unique	4063/1721 (Rint = 0.0909)	4449/2485 (R_{int} = 0.0207)	11160/2930 (R_{int} = 0.0346)
Goodness-of-fit on F^2	0.889	1.035	1.036
Final R indices [I>2σ(I)]	R1 = 0.0509, ωR2 = 0.0950	R1 = 0.0776, ωR2 = 0.2024	R1 = 0.0569, ωR2 = 0.1592
R indices (all data)	R1 = 0.1312, ωR2 = 0.1099	R1 = 0.1252, ωR2 = 0.2433	R1 = 0.0689, ωR2 = 0.1744

Refinement method	SHELXL	SHELXL	SHELXL

The data integration and reduction were processed with SAINT.[4] SHELXL-97 was used for the structure solutions via direct method and refined by full-matrix least-squares on F^2.[5]

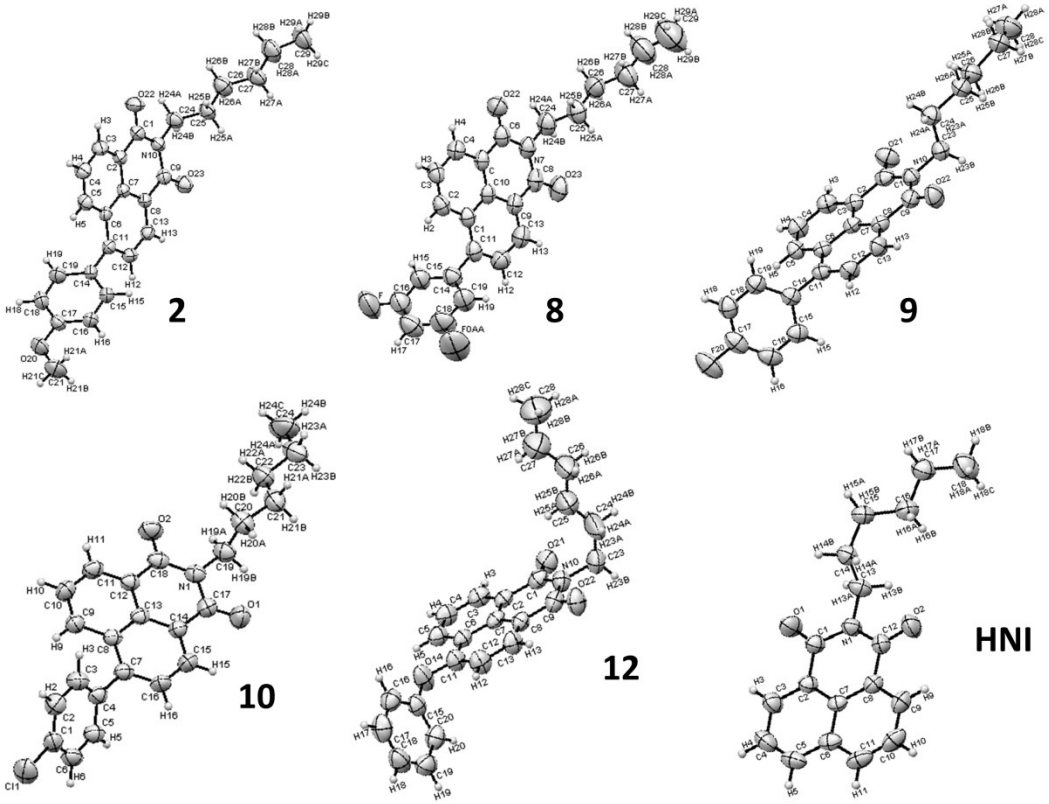

Figure A3.14. Oak Ridge Thermal Ellipsoid Plot (ORTEP) of compounds (**2**, **8**, **9**, **10**, **12** and **HNI**) with the thermal ellipsoids set at 50% probability.

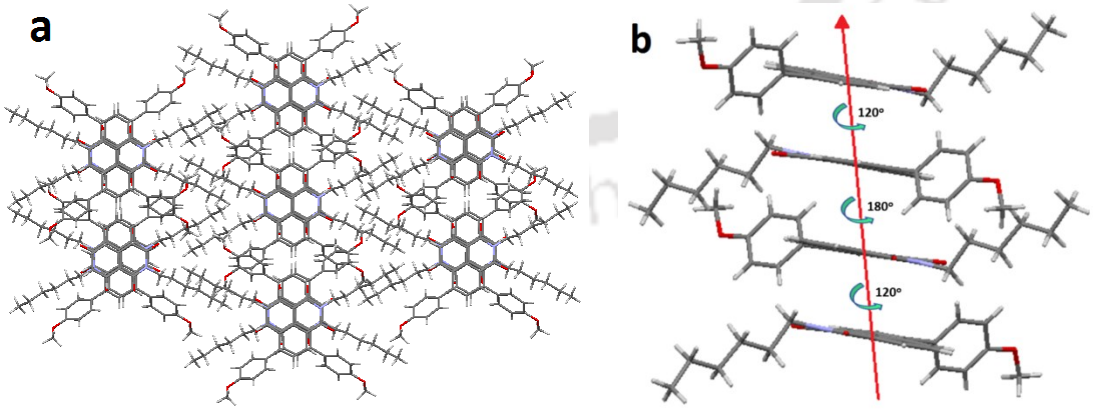

Figure A3.15. (a) Single crystal packing diagram of **2** as viewed down along crystallographic c axis. (b) Face-to-face packing in **2** showing the rotation angle considering the naphthalimide core.

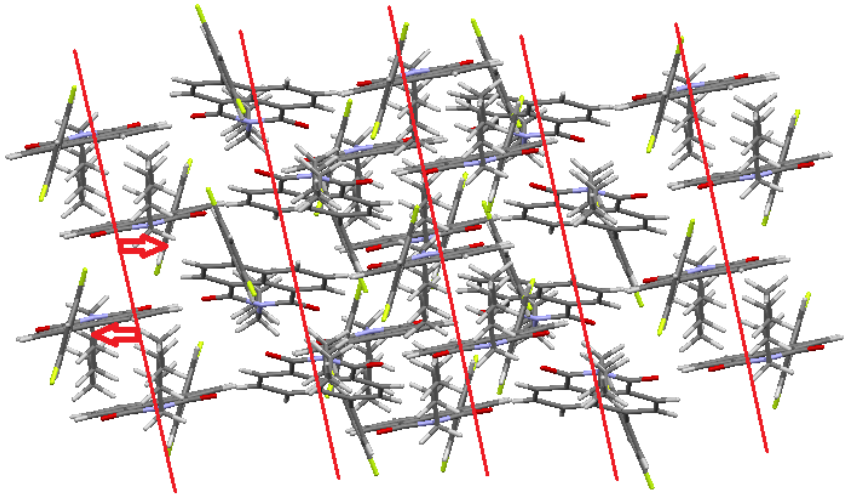

Figure A3.16. Single crystal packing diagram of **8**.

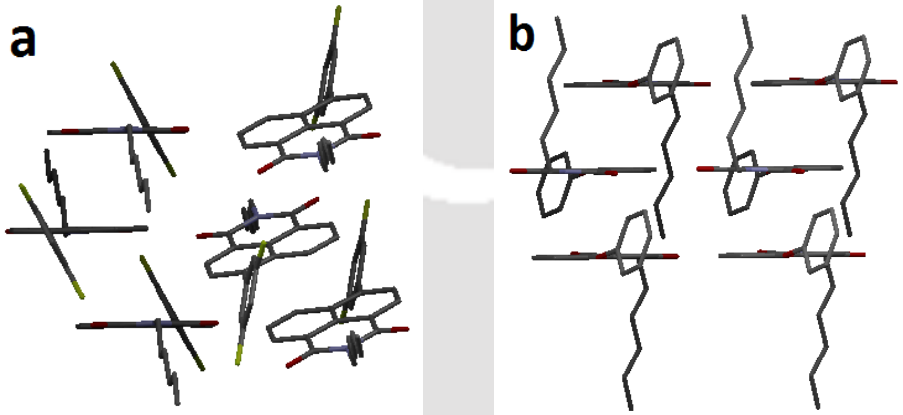

Figure A3.17. Single crystal packing diagram of (a) **8** and (b) **12** showing the arrangement perturbation in the naphthalimide congeners by simple structural modification.

Figure A3.18. Crystal structures of **2**, **8**, **9** and **10** (left to right) showing the dihedral angle between naphthalimide and phenyl planes.

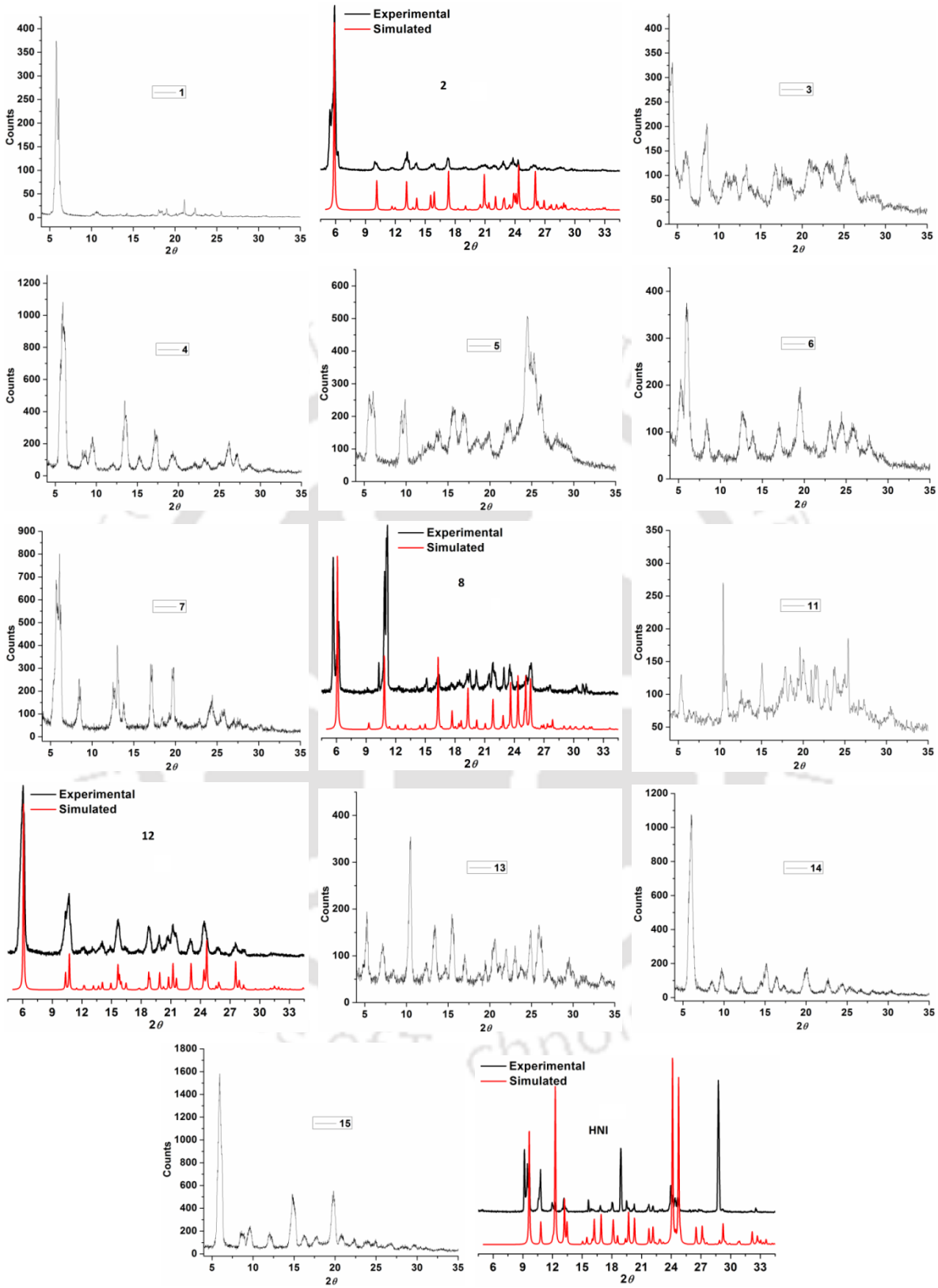

Figure A3.19. PXRD pattern of the congeners. For few compounds with single crystal XRD data, the simulated PXRD patterns have been compared with their respective experimental data.

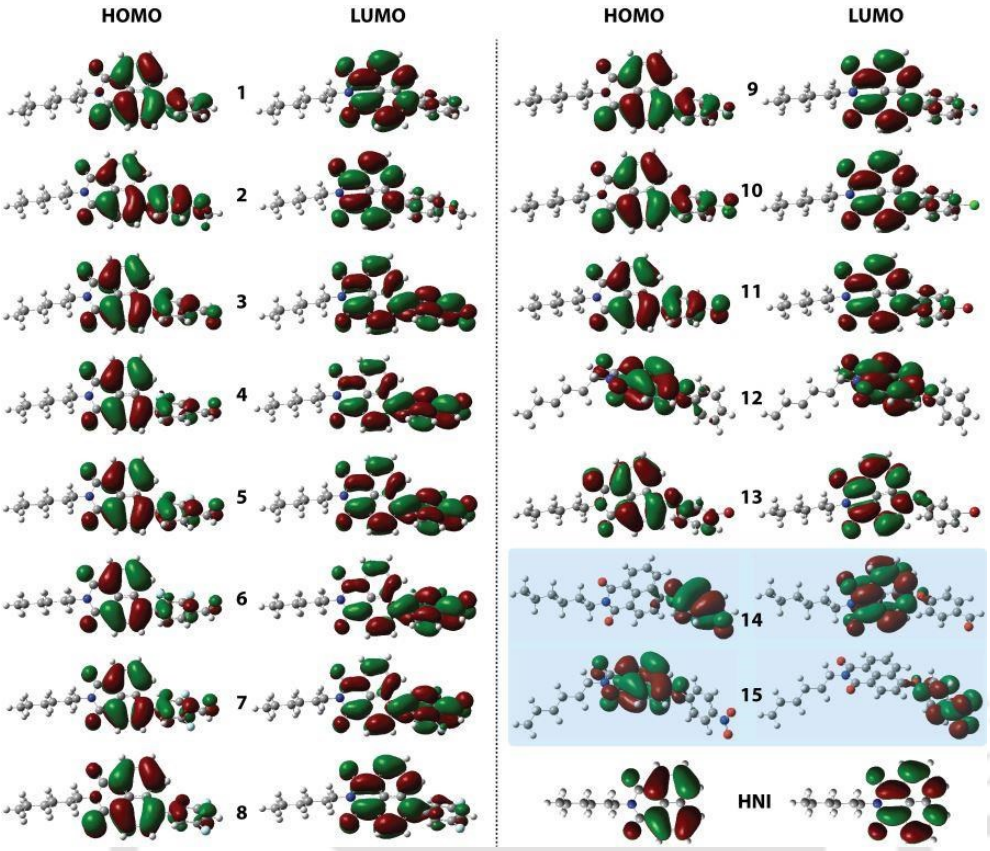

Figure A3.20. Optimized structures and HOMO/LUMO electron density of the congeners in the excited states. Computations were executed using time dependent density functional theory with the B3LYP exchange functional employing 6-31G* basis sets in the Gaussian 09 program.[1,2]

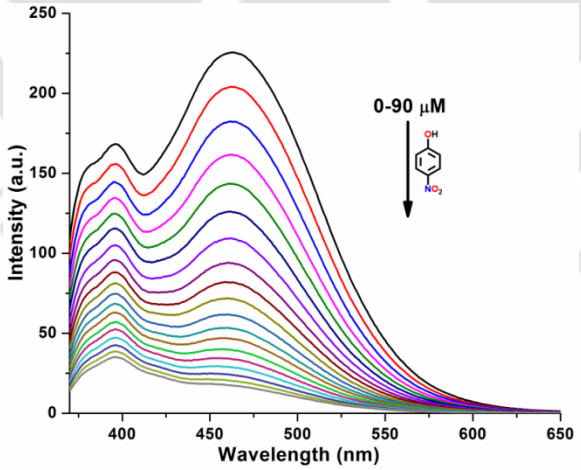

Figure A3.21. Fluorescence response of **HNI** toward p-nitrophenol in water at 25 °C.

Table A3.4. DFT calculated HOMO and LUMO energy levels of **HNI** and other small aromatic analytes.[1,2]

Molecules	HOMO (eV)	LUMO (eV)
HNI	-6.56638	-2.55488
p-nitrophenol	-7.13701	-2.76141
Phenol	-0.12109	5.20799
Bromobenzene	-6.68802	-0.36218
Chlorobenzene	-6.89482	-0.43212
Fluorobenzene	-6.84013	-0.34314
2-fluorobenzaldehyde	-7.01972	-2.08793
3-Bromophenol	-6.40203	-0.42776
3-Fluorobenzaldehyde	-7.28123	-2.22834
4-hydroxybenzaldehyde	-6.64775	-1.7116
1,3-Difluorobenzene	-7.12394	-0.64328
2,3-Difluorobenzaldehyde	-7.28531	-2.38045
2,6-Difluorobenzaldehyde	-7.12013	-2.32521
Benzaldehyde	-6.99306	-1.9018
Benzene	-6.75387	0.102043
PhOMe	-6.50706	-0.02122

^{1}H NMR Spectra

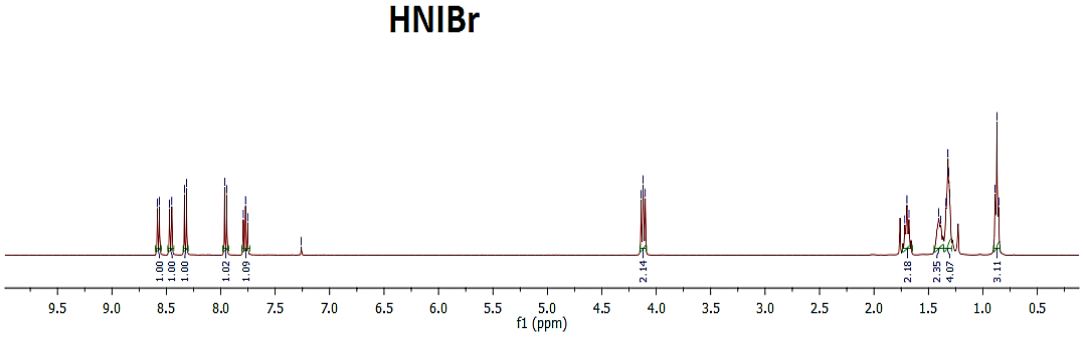

HNI

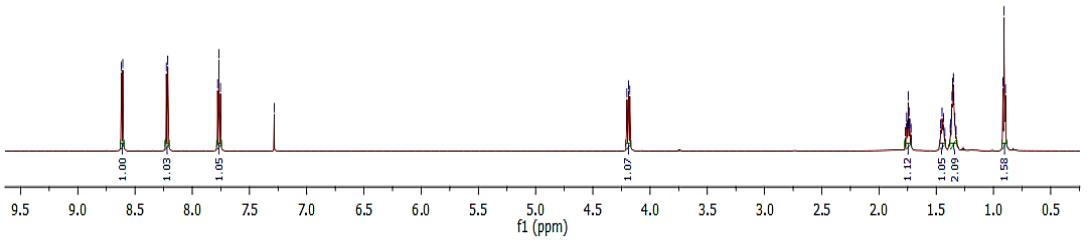

1

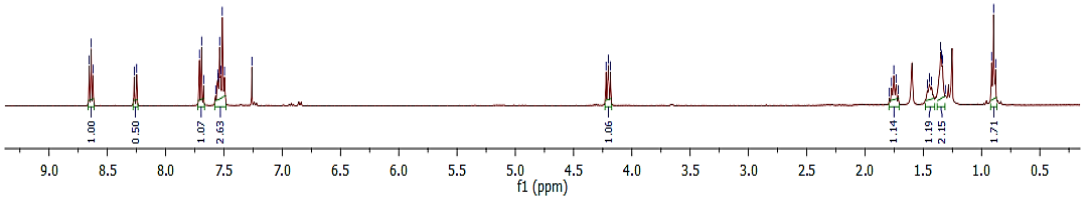

2

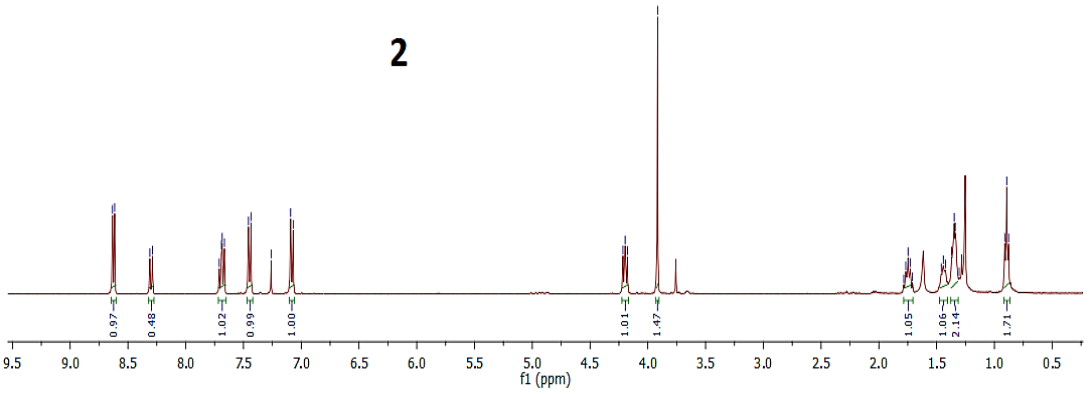

3

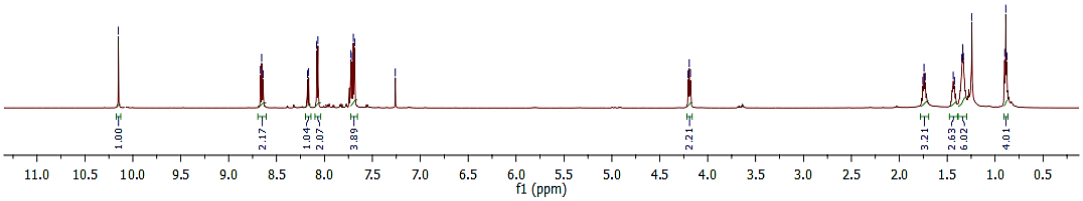

4

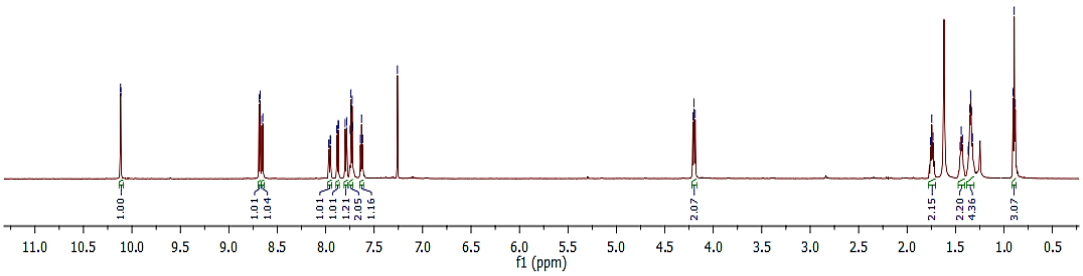

5

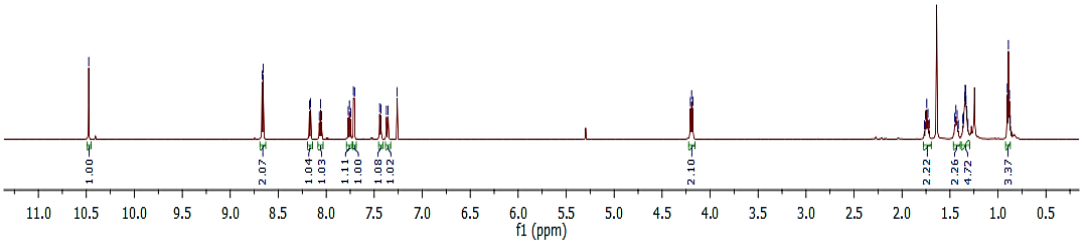

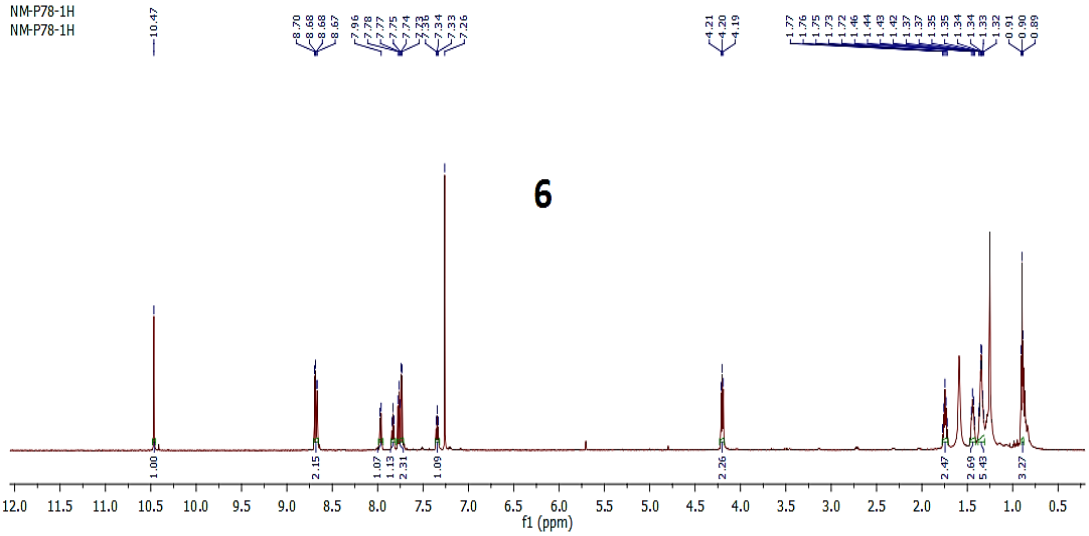

6

7

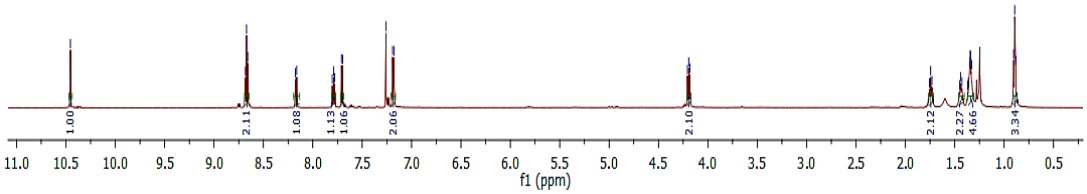

8

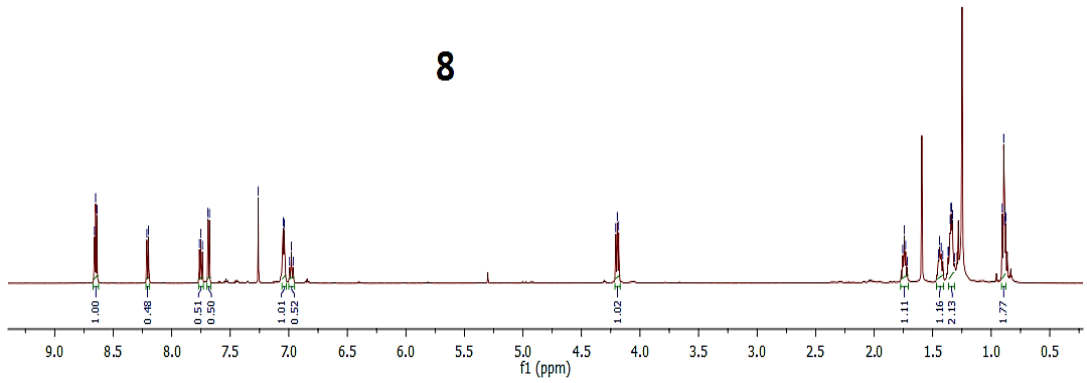

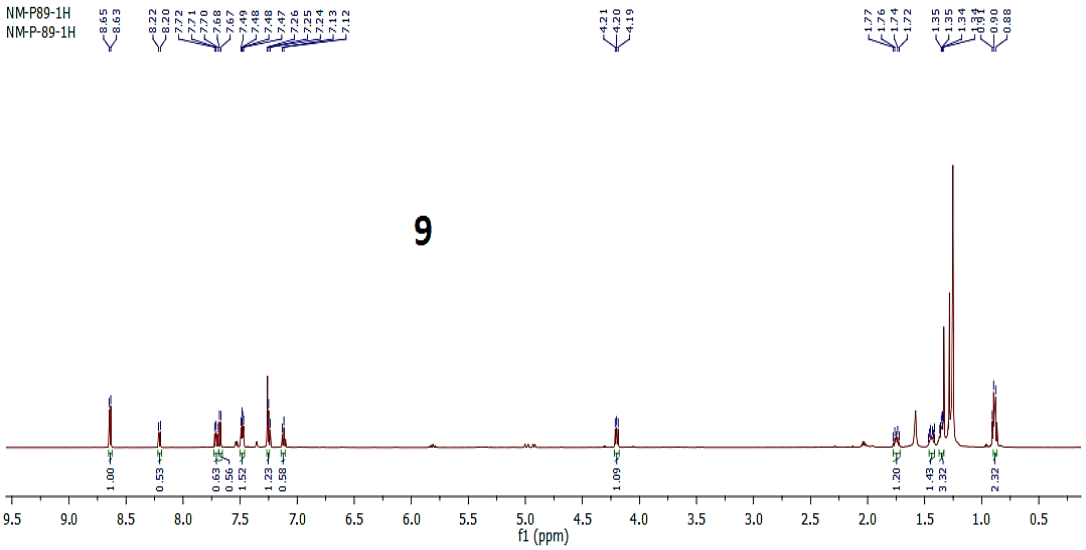

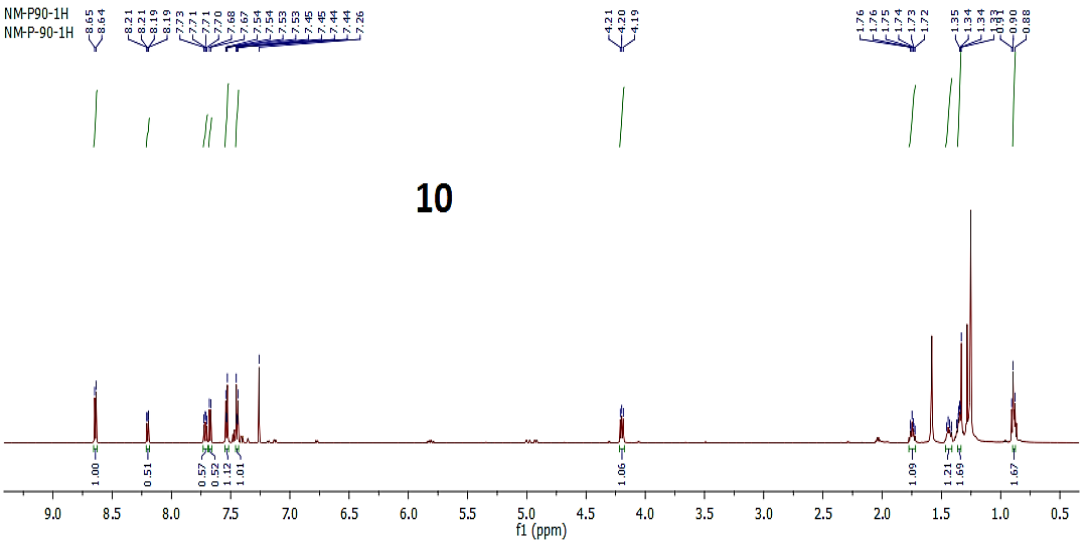

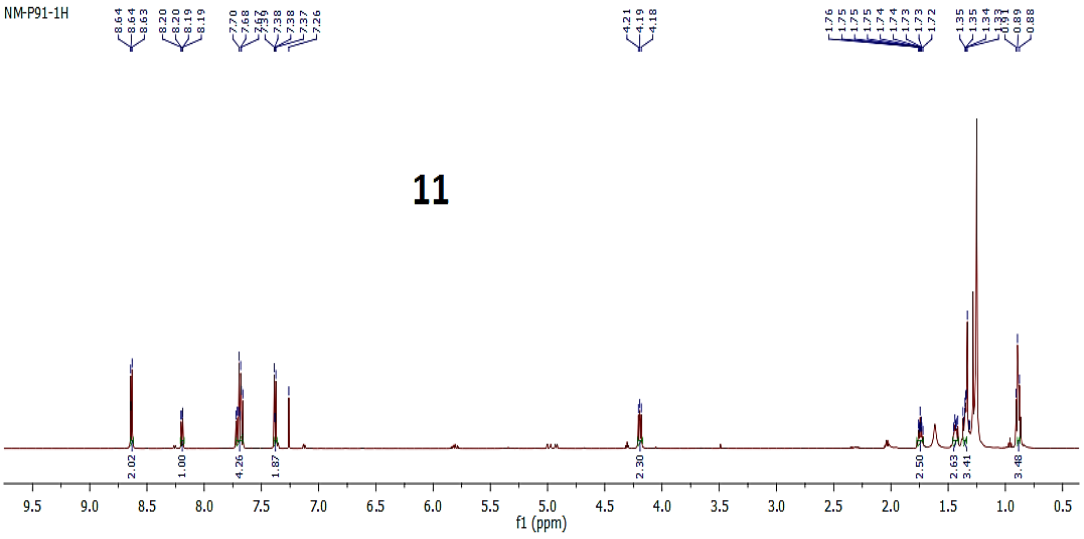

12

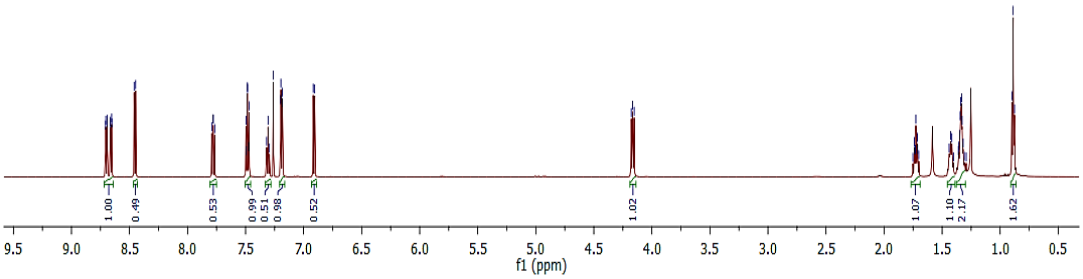

13

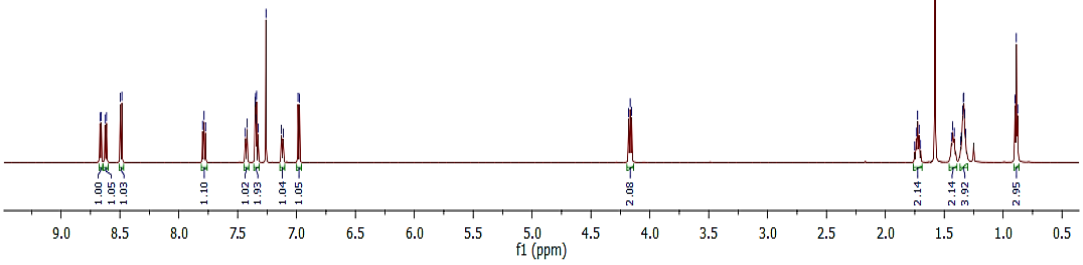

14

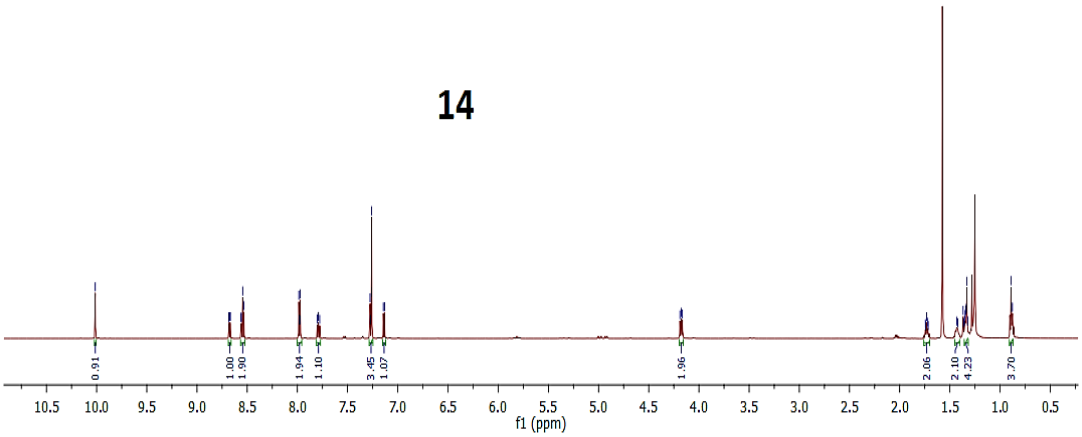

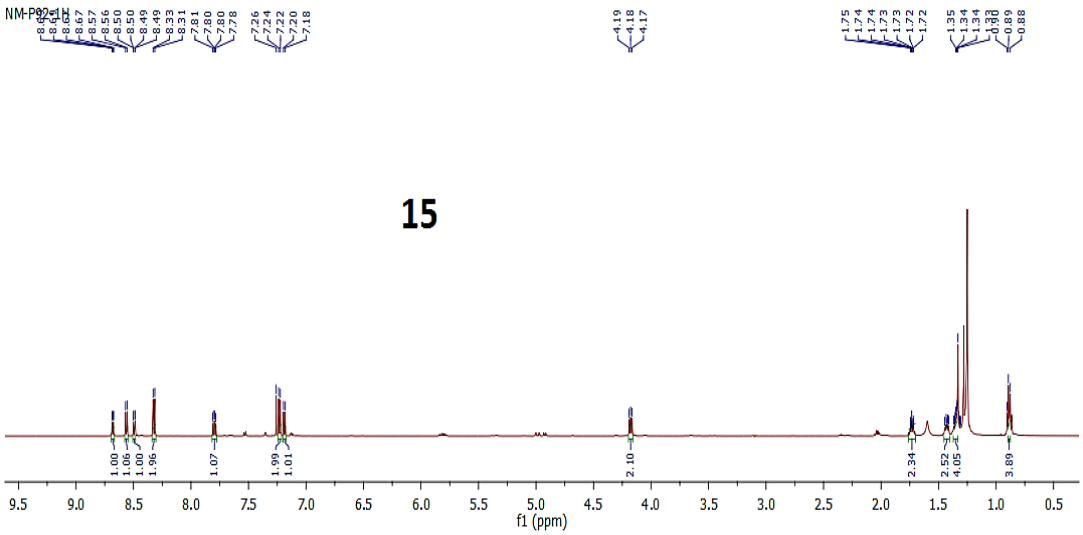

^{13}C NMR Spectra

HNIBr

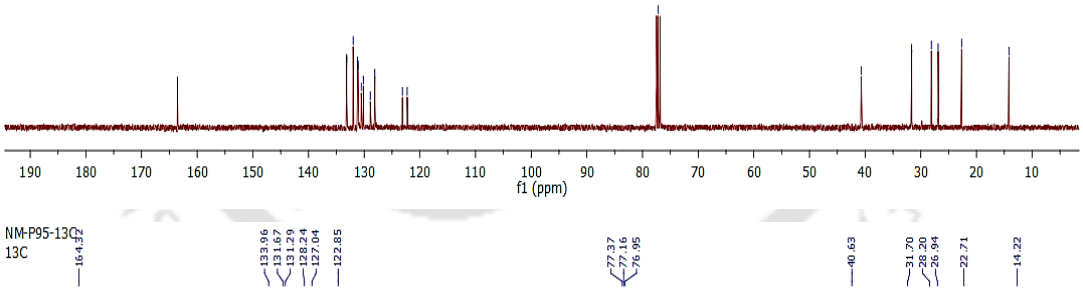

HNI

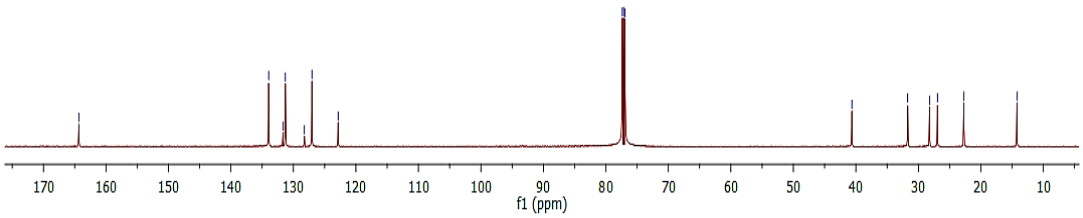


NM-P82-13C
NM-P82-13C
164.47
164.27
146.97
138.97
132.73
131.28
130.93
130.18
130.11
128.79
128.59
127.97
126.95
123.06
121.94
77.37
77.16
76.95
40.67
31.72
28.23
26.96
22.72
14.22

1

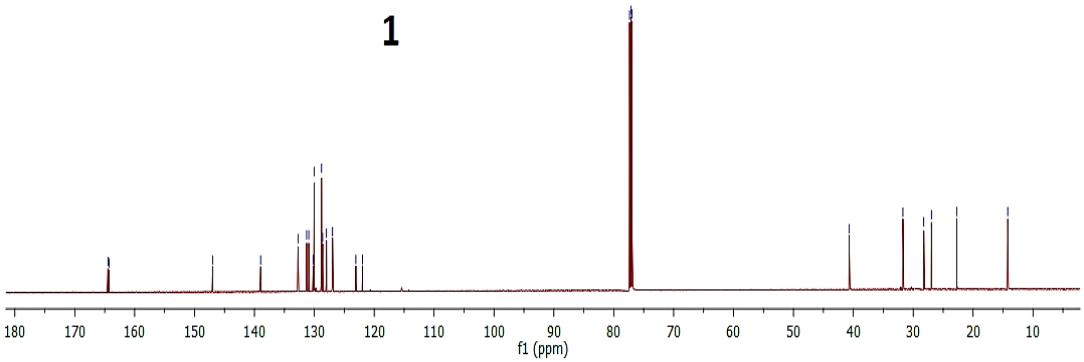
180
170
160
150
140
130
120
110
100
90
80
70
60
50
40
30
20
10
f1 (ppm)


NM-P83_13C
NM-P83_13C
160.04
146.80
132.84
131.27
131.00
130.30
128.80
127.89
126.82
123.06
121.54
116.15
114.92
114.29
77.37
77.16
76.95
55.59
40.66
31.72
28.23
26.96
22.73
14.22

2

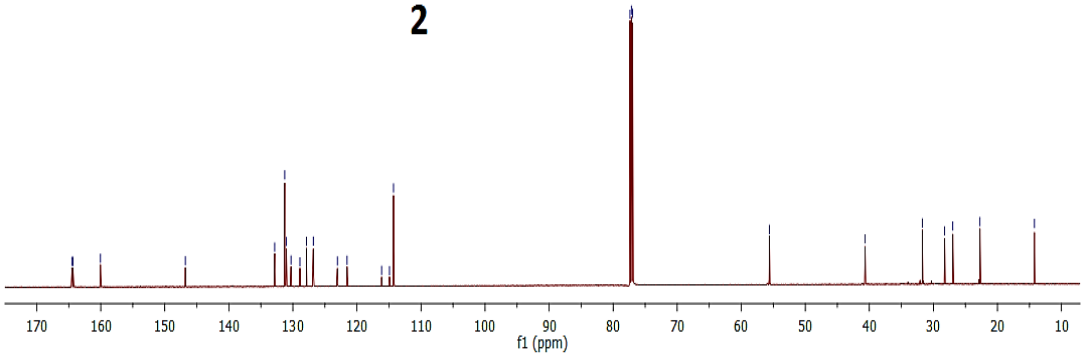
170
160
150
140
130
120
110
100
90
80
70
60
50
40
30
20
10
f1 (ppm)


NM-P74-13C
NM-P74-13C
191.76
164.18
163.97
145.17
145.04
136.22
132.09
131.57
131.32
130.86
130.60
130.16
129.97
128.71
127.92
127.37
123.19
122.71
77.16
40.69
31.66
28.17
26.91
22.68
14.10

3

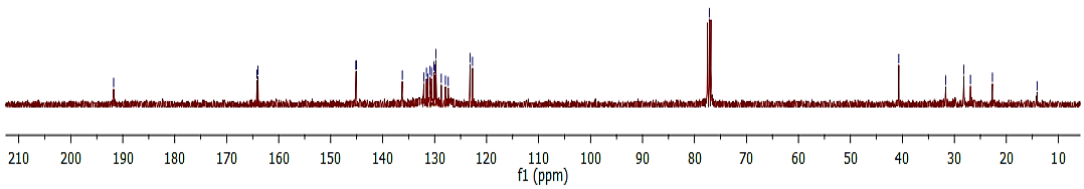
210
200
190
180
170
160
150
140
130
120
110
100
90
80
70
60
50
40
30
20
10
f1 (ppm)

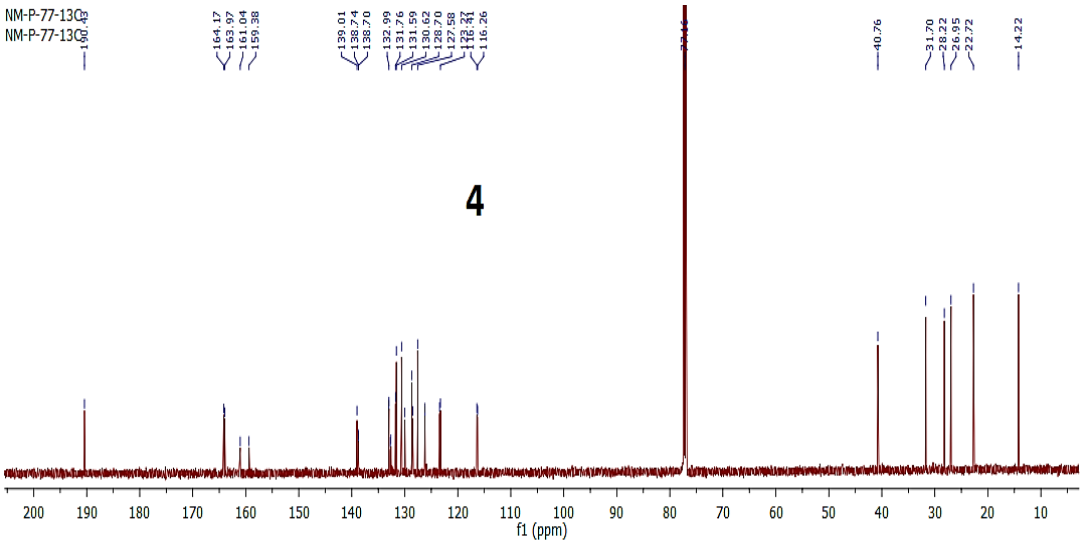

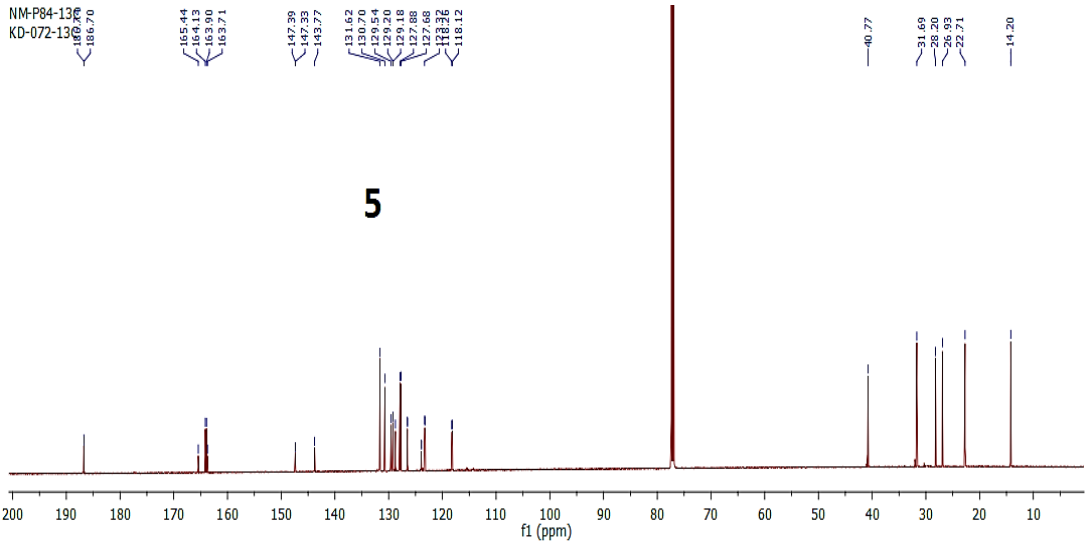

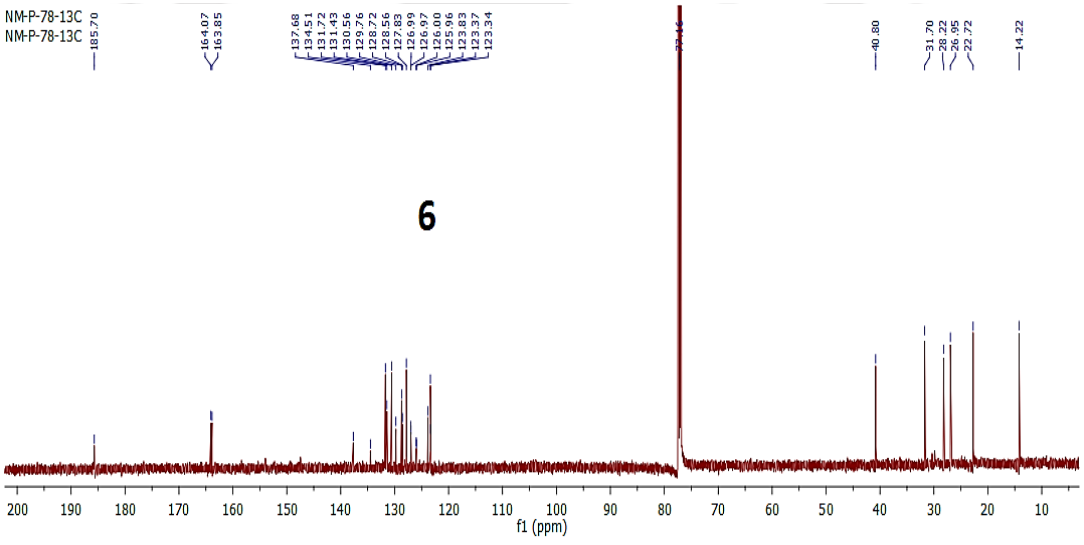

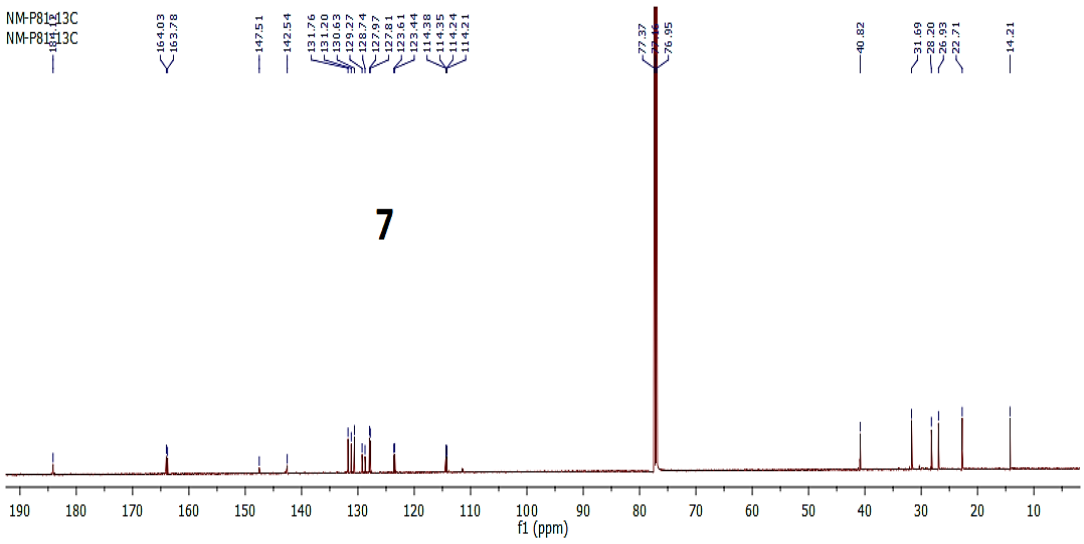
NM-P81-13C
NM-P81-13C
164.03
163.78
147.51
142.54
131.76
131.20
130.63
129.27
128.74
127.97
127.81
123.61
123.44
114.38
114.35
114.24
114.21
77.37
77.16
76.95
40.82
31.69
28.20
26.93
22.71
14.21
7
f1 (ppm)

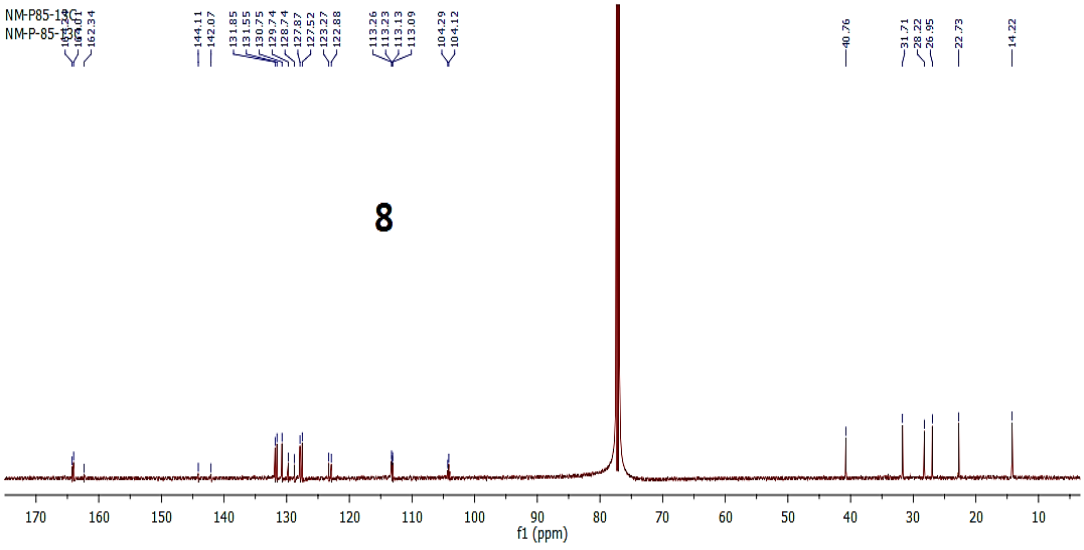
NM-P85-13C
144.11
142.07
131.85
131.55
130.75
129.74
128.74
127.87
123.52
123.27
122.88
113.26
113.23
113.13
113.09
104.29
104.12
40.76
31.71
28.22
26.95
22.73
14.22
8
f1 (ppm)

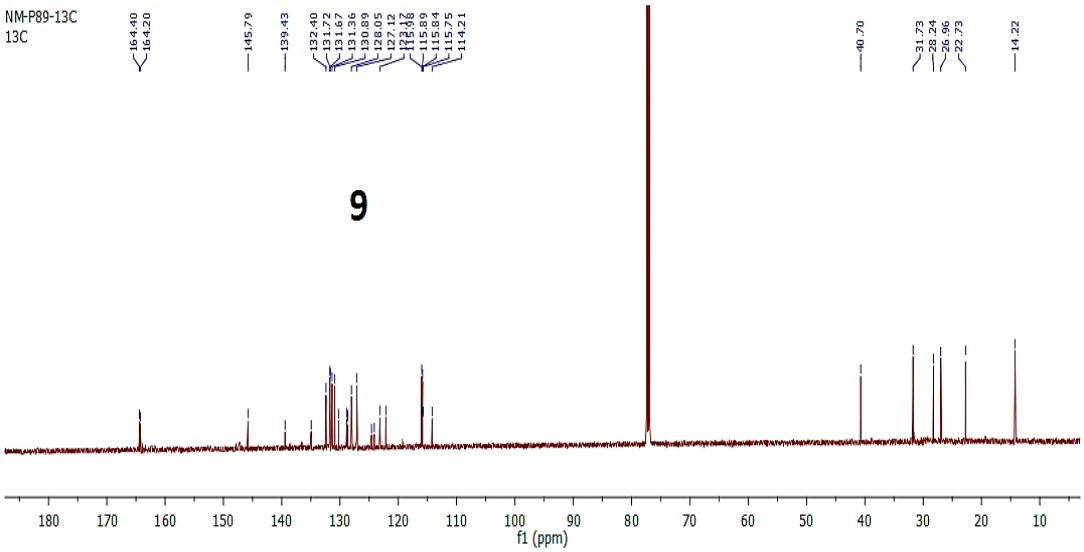
NM-P89-13C
13C
164.40
164.20
145.79
139.43
132.40
131.72
131.67
131.36
130.89
128.05
127.12
115.89
115.84
115.75
114.21
40.70
31.73
28.24
26.96
22.73
14.22
9
f1 (ppm)

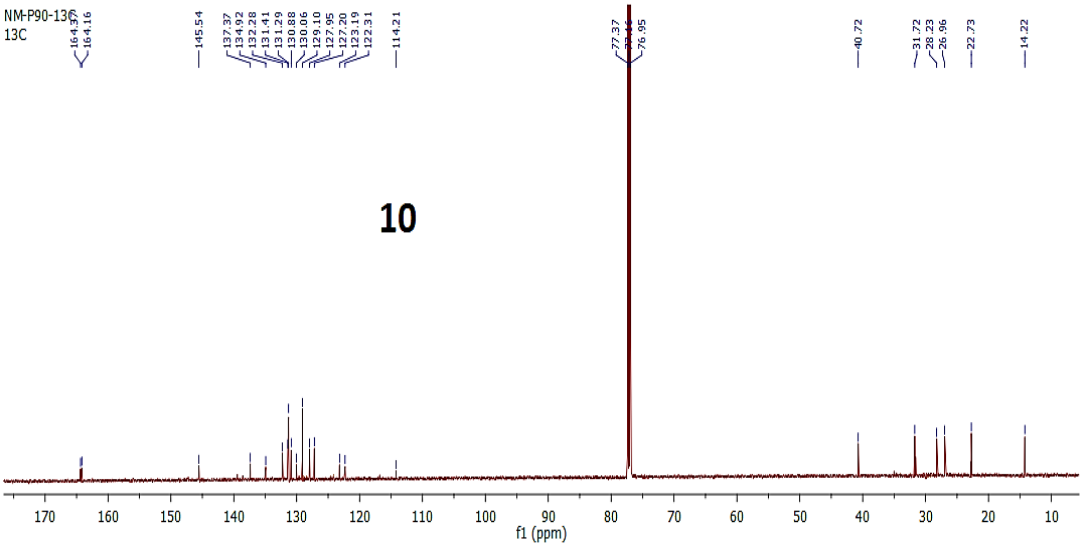
NM-P90-13C
13C
164.37
164.16
145.54
137.37
134.92
132.28
131.41
131.29
130.88
130.06
129.10
127.95
127.20
123.19
122.31
114.21
77.37
77.16
76.95
40.72
31.72
28.23
26.96
22.73
14.22
10
170 160 150 140 130 120 110 100 90 80 70 60 50 40 30 20 10
f1 (ppm)

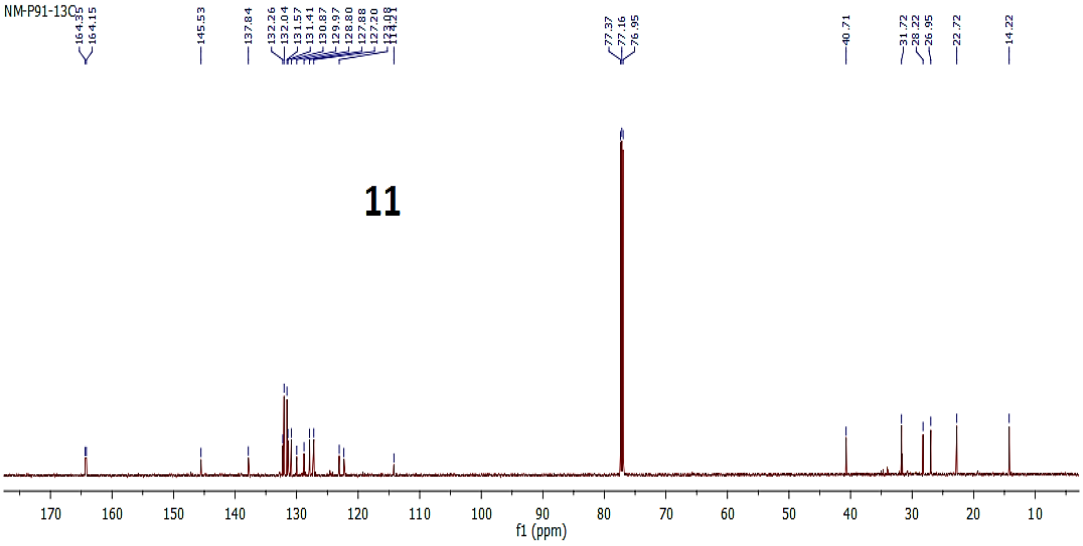
NM-P91-13C
164.35
164.15
145.53
137.84
132.26
132.04
131.57
131.41
130.87
129.97
128.80
127.88
127.20
114.01
77.37
77.16
76.95
40.71
31.72
28.22
26.95
22.72
14.22
11
170 160 150 140 130 120 110 100 90 80 70 60 50 40 30 20 10
f1 (ppm)

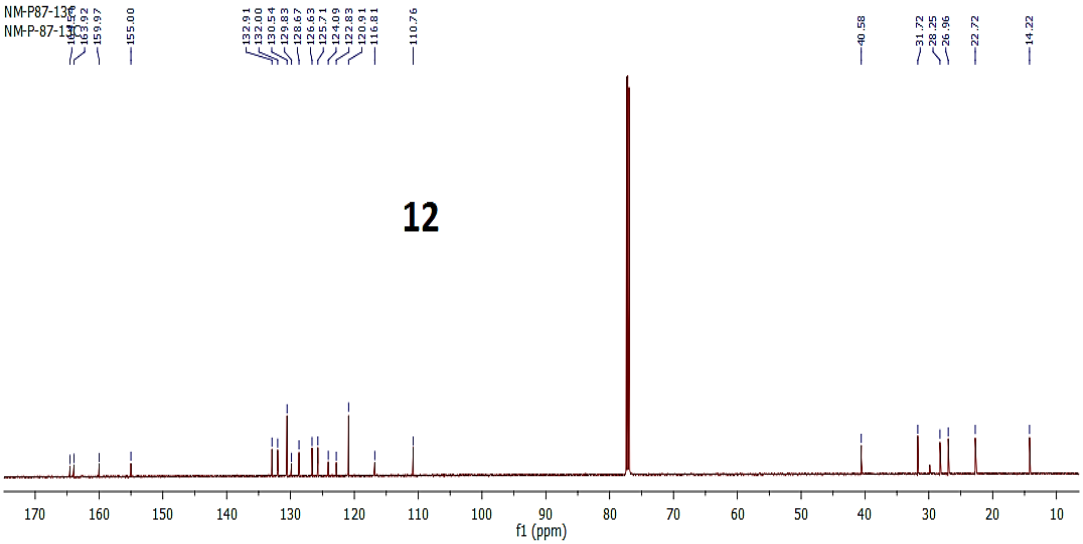
NM-P87-13C
NM-P-87-13C
164.56
163.92
159.97
155.00
132.91
132.00
130.54
129.83
128.67
126.63
125.71
124.09
122.83
120.91
116.81
110.76
40.58
31.72
28.25
26.96
22.72
14.22
12
170 160 150 140 130 120 110 100 90 80 70 60 50 40 30 20 10
f1 (ppm)

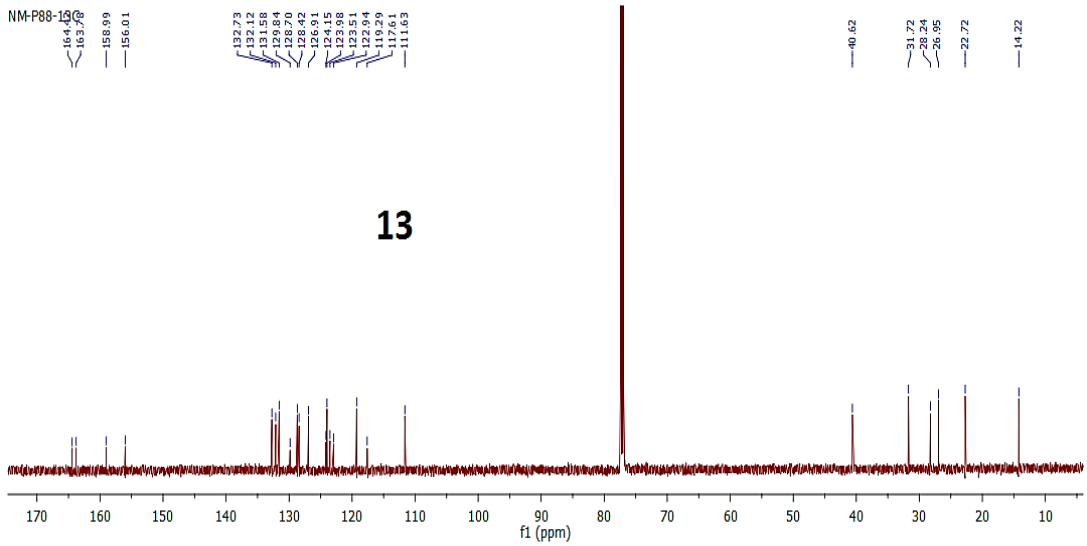

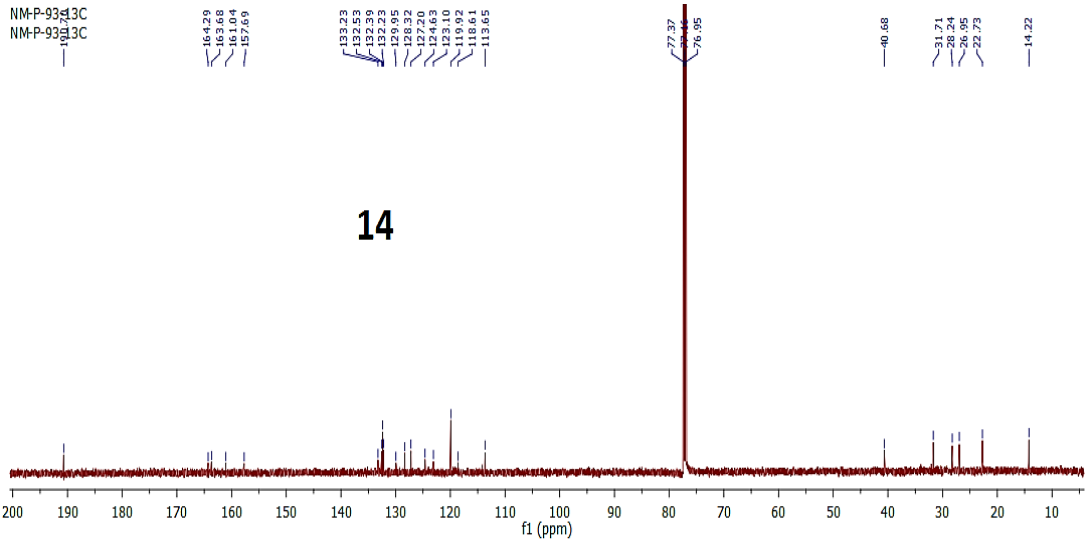

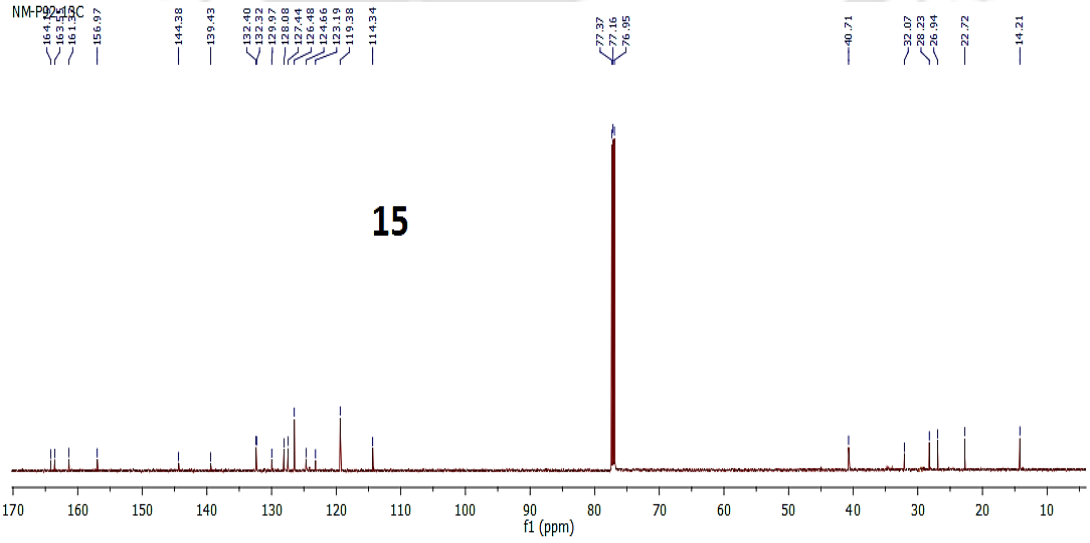

^{19}F NMR Spectra

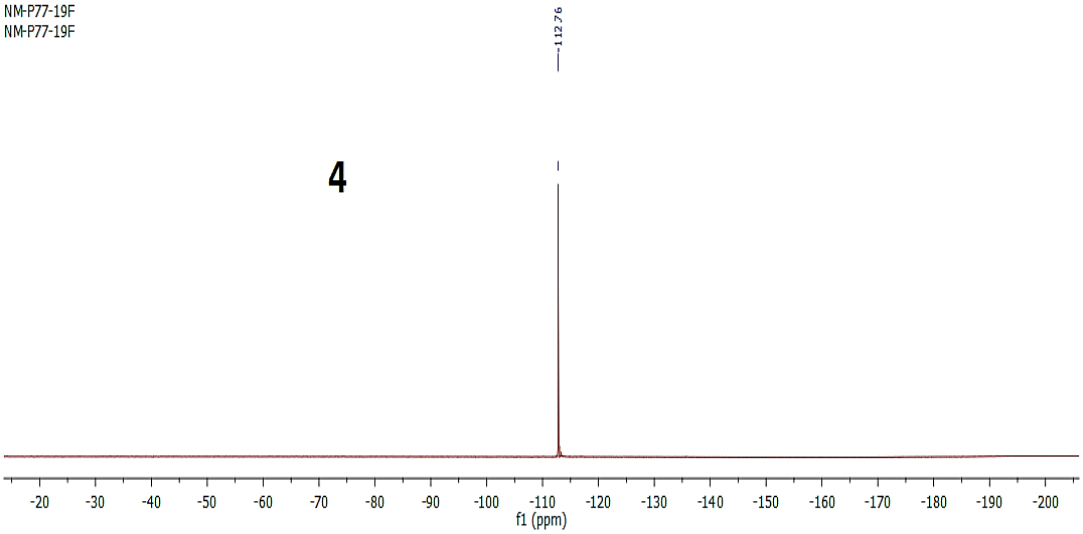

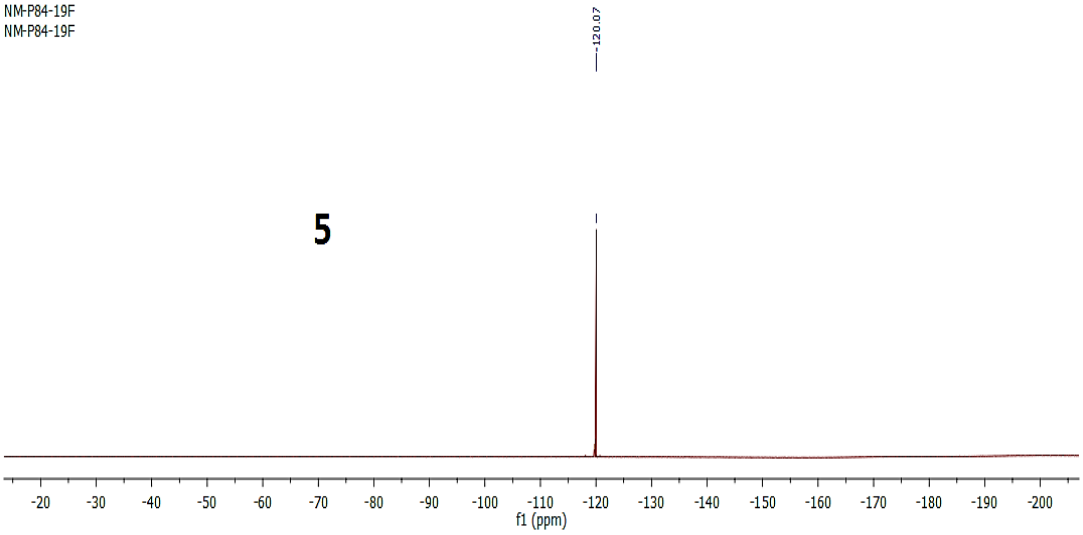

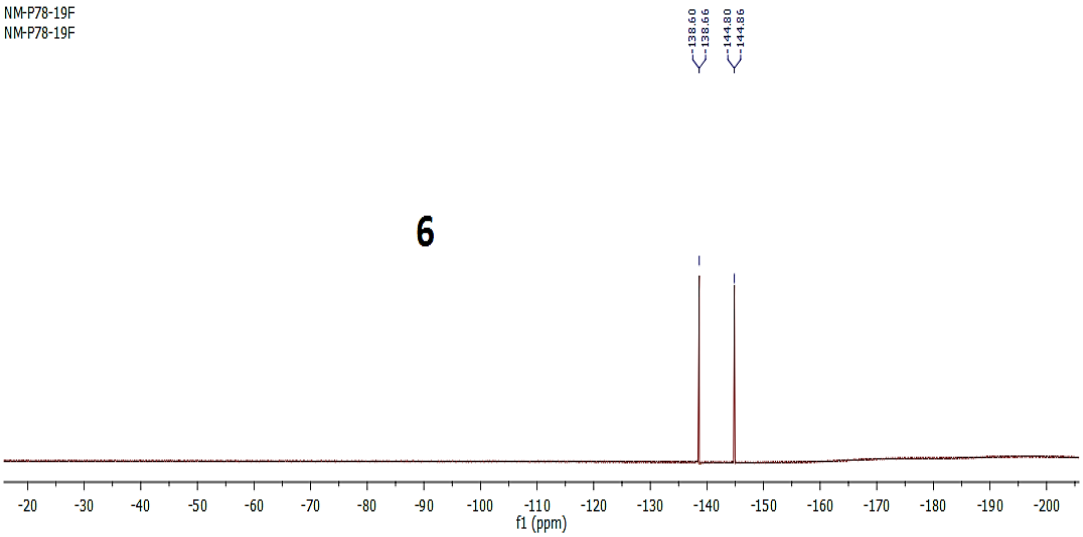

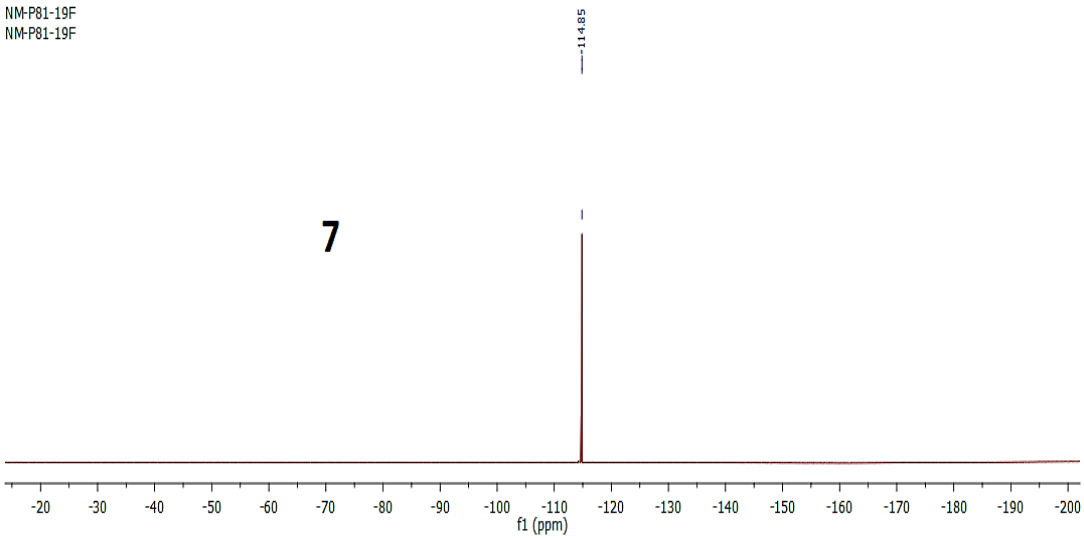

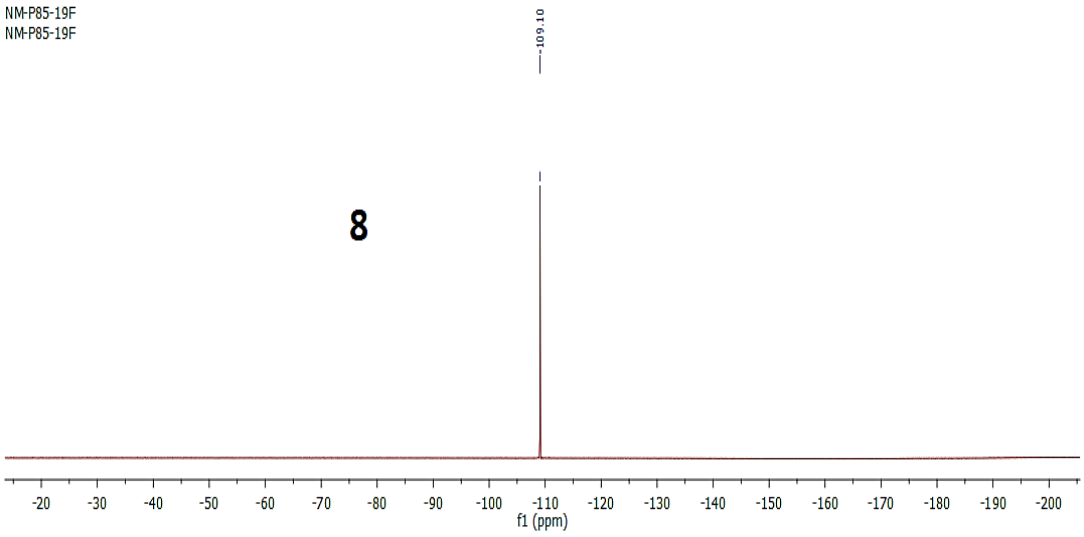

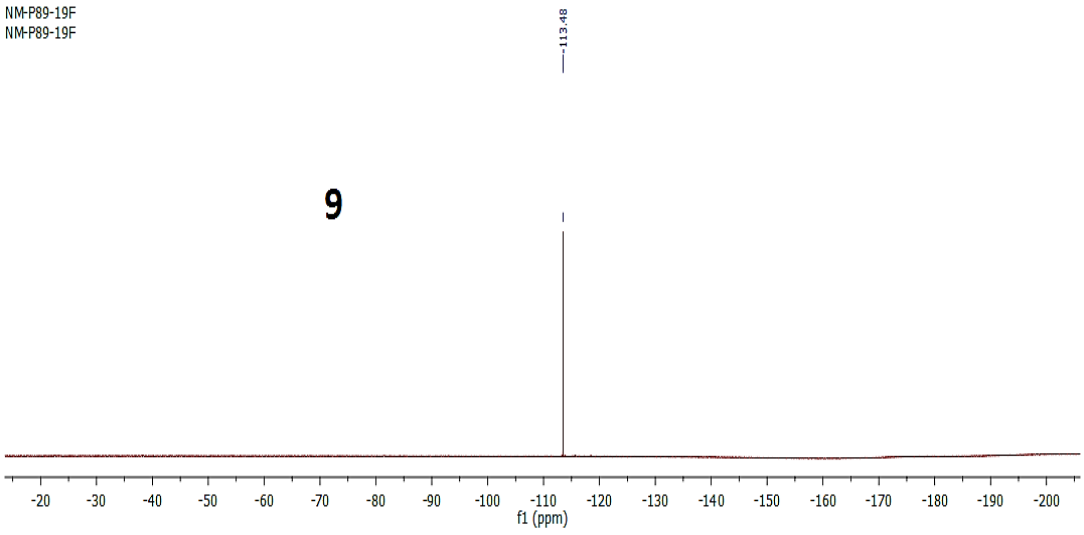

Mass Spectra

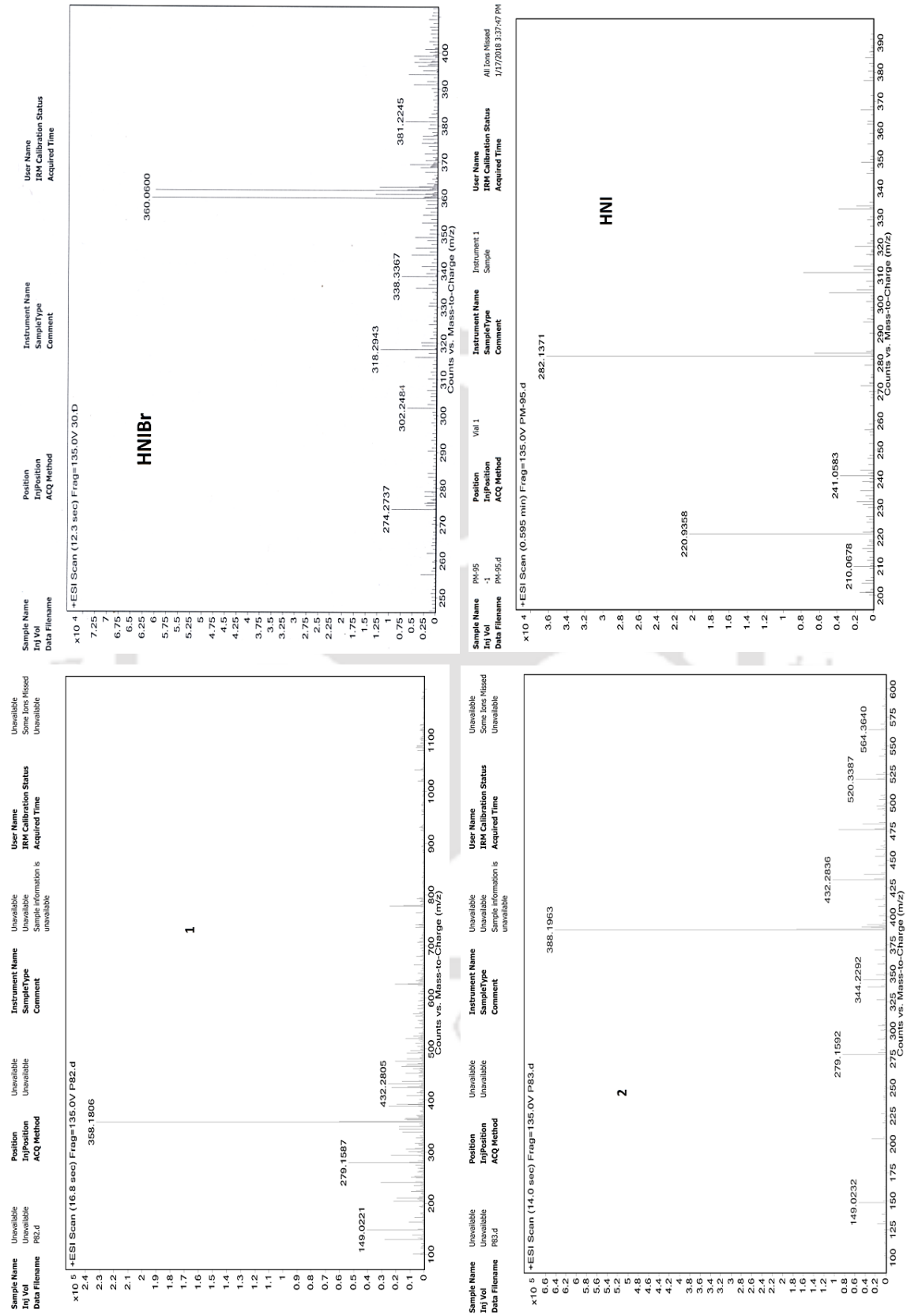

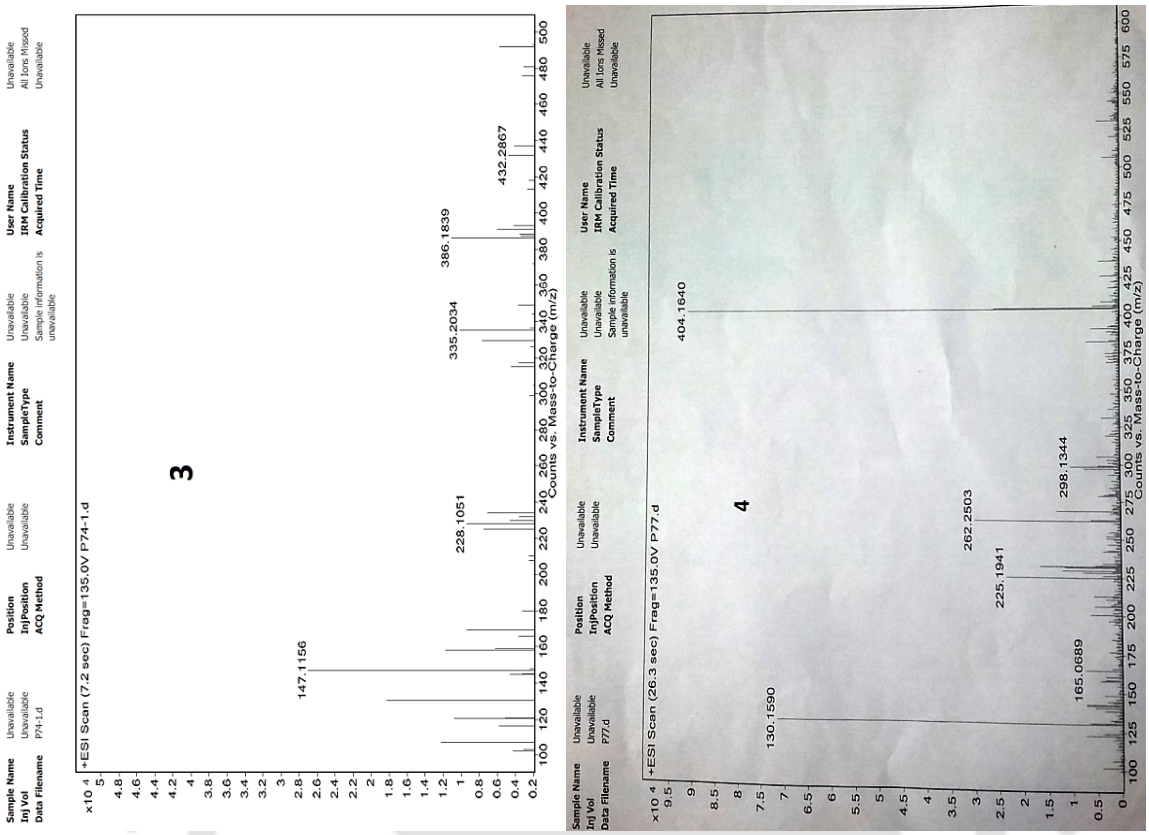

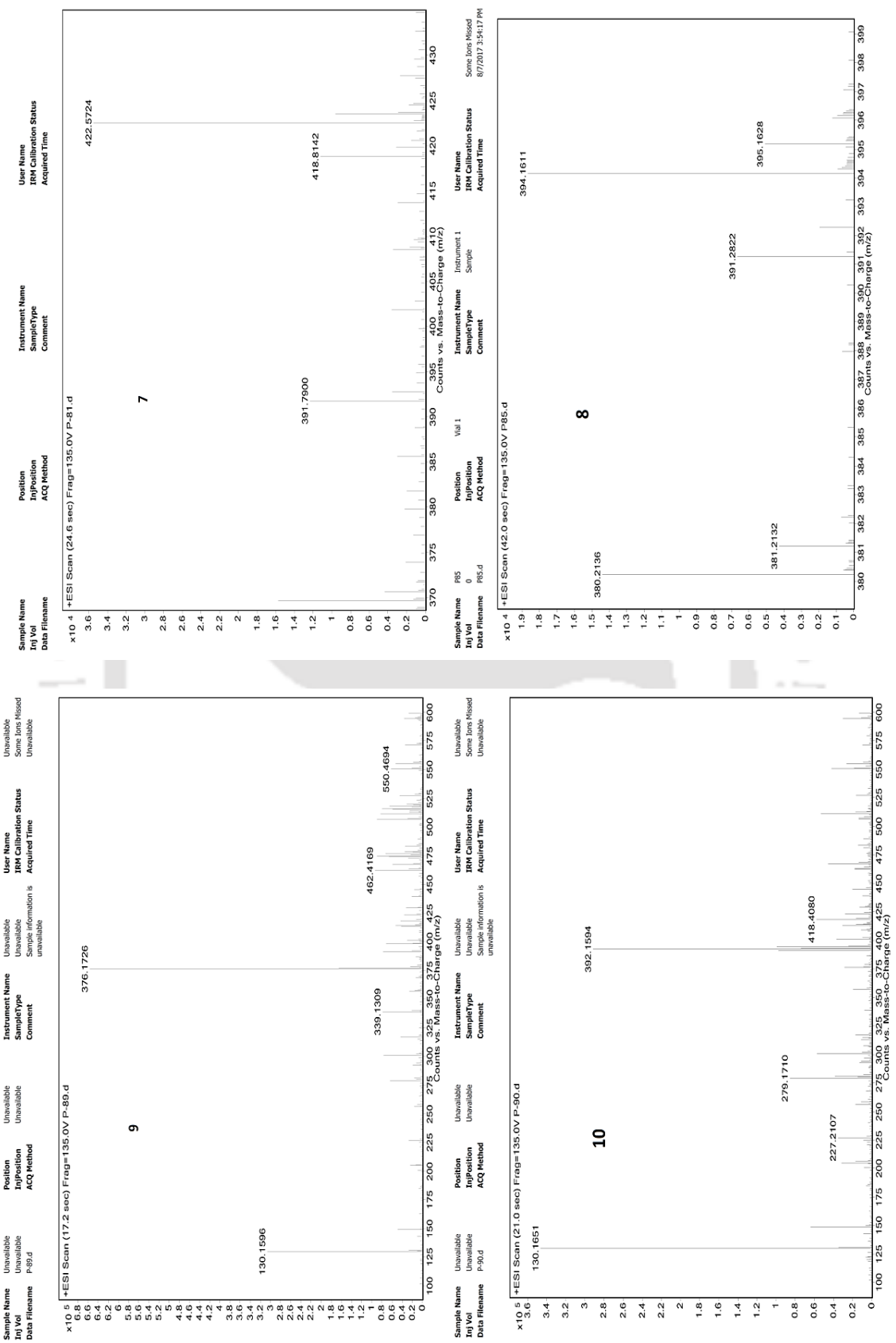

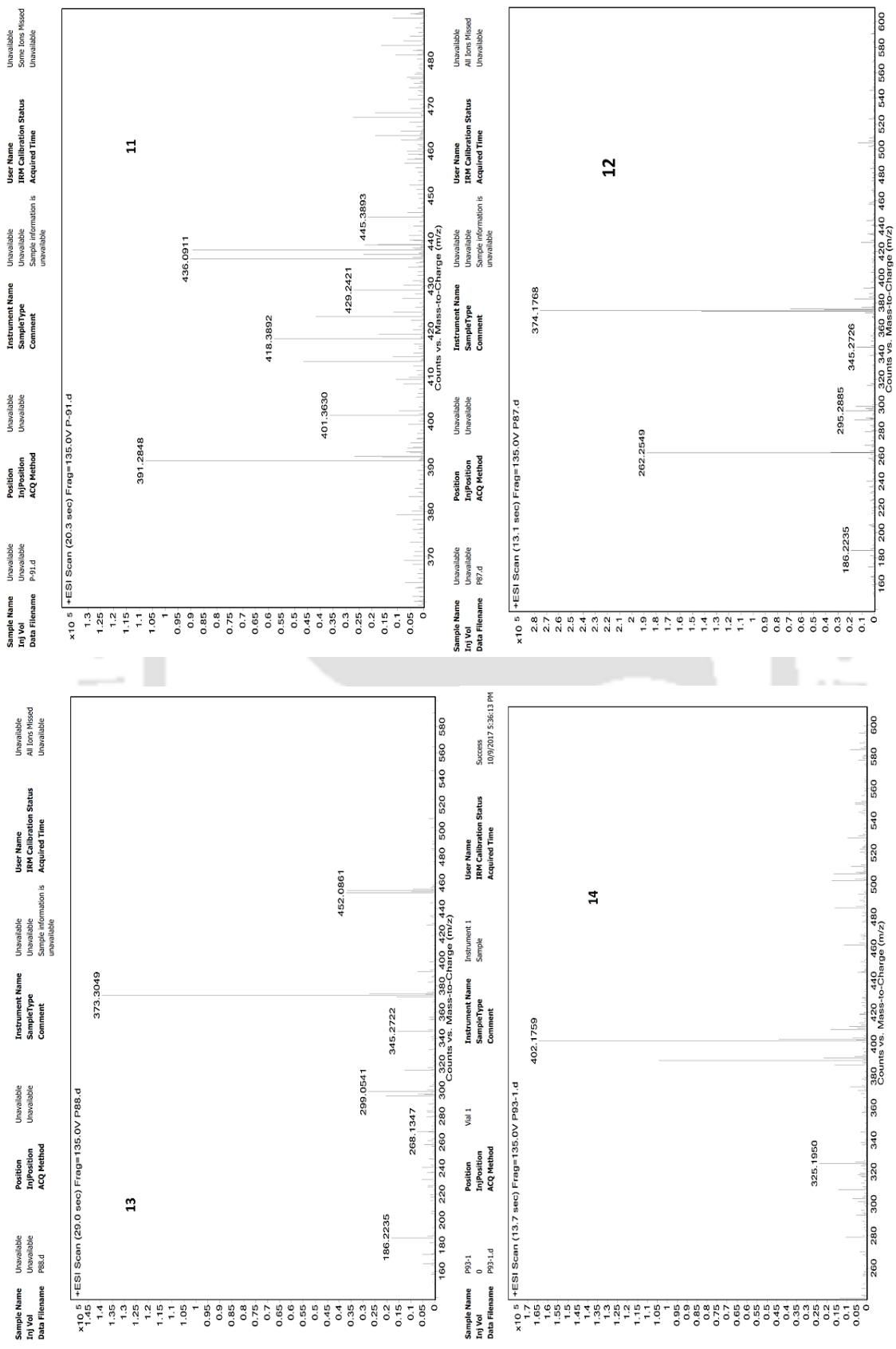

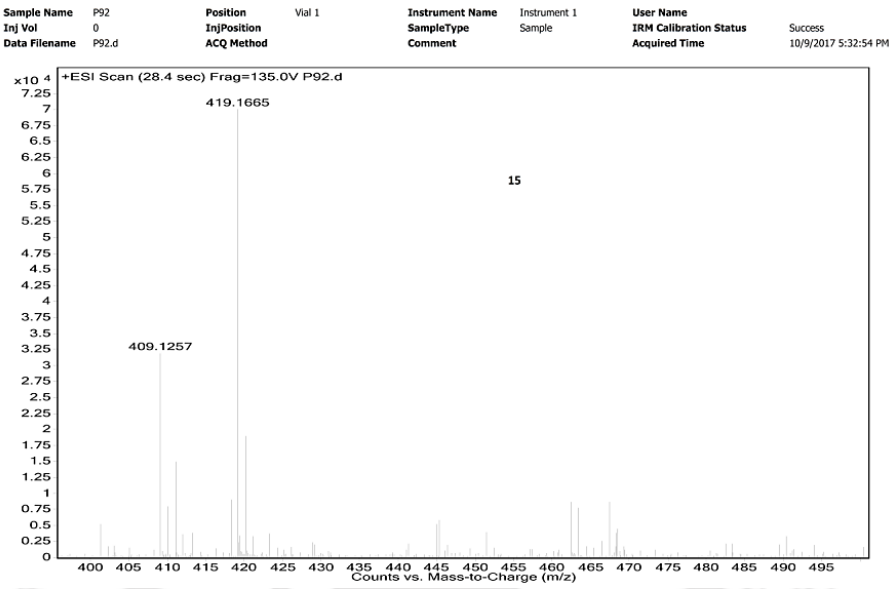

References

(1) Becke, A. D. *J. Chem. Phys.* **1993**, *98*, 5648.

(2) Frisch, M. J.; Trucks, G. W.; Schlegel, H. B.; Scuseria, G. E.; Robb, M. A.; Cheeseman, J. R.; Scalmani, G.; Barone, V.; Mennucci, B.; Petersson, G. A.; Nakatsuji, H.; Caricato, M.; Li, X.; Hratchian, H. P.; Izmaylov, A. F.; Bloino, J.; Zheng, G.; Sonnenberg, J. L.; Hada, M.; Ehara, M.; Toyota, K.; Fukuda, R.; Hasegawa, J.; Ishida, M.; Nakajima, T.; Honda, Y.; Kitao, O.; Nakai, H.; Vreven, T.; Montgomery, J. A.; Jr., Peralta, J. E.; Ogliaro, F.; Bearpark, M.; Heyd, J. J.; Brothers, E.; Kudin, K. N.; Staroverov, V. N.; Kobayashi, R.; Normand, J.; Raghavachari, K.; Rendell, A.; Burant, J. C.; Iyengar, S. S.; Tomasi, J.; Cossi, M.; Rega, N.; Millam, J. M.; Klene, M.; Knox, J. E.; Cross, J. B.; Bakken, V.; Adamo, C.; Jaramillo, J.; Gomperts, R.; Stratmann, R. E.; Yazyev, O.; Austin, A. J.; Cammi, R.; Pomelli, C.; Ochterski, J. W.; Martin, R. L.; Morokuma, K.; Zakrzewski, V. G.; Voth, G. A.; Salvador, P.; Dannenberg, J. J.; Dapprich, S.; Daniels, A. D.; Farkas, O.; Foresman, J. B.; Ortiz, J. V.; Cioslowski, J.; Fox, D. J. *Gaussian 09, Revision A.02, Gaussian, Inc., Wallingford CT*, **2009**.

(3) (a) Z. Chen, D. Wu, X. Han, Y. Nie, J. Yin, G.-A. Yu, S. H. Liu. (**2014**), CCDC 1014214: Experimental Crystal Structure Determination, Cambridge Crystallographic Data Centre. *http://dx.doi.org/10.5517/cc131cl3*. (b) Z. Chen, D. Wu, X. Han, Y. Nie, J. Yin, G.-A. Yu, S. H. Liu. *RSC Adv.* **2014**, *4*, 63985-63988.

(4) Sheldrick, G. M. SAINT and XPREP, 5.1 edn, Siemens Industrial Automation Inc., Madison, WI, **1995**.

(5) Sheldrick, G. M. SHELX97. Program for X-ray Crystal Structure Solution and Refinement, University of Göttingen, Germany, **1997**.

Chapter 4

Formyl Group Driven Ultra-Detection of Hydrazine on Multiple Platforms

Meher, N.; Panda, S.; Kumar, S.; Iyer, P. K. *Chem. Sci.* **2018**, *9*, 3978–3985.

Meher, N.; Iyer, P. K. Hydrazine Detector Device Comprising of Fluorescent Organic Molecular Probe, Ref. No 201831017337, App. Number: TEMP/E-1/18338/2018-KOL, (08/05/2018).

Abstract

Naphthalimide AIEEgen (NIBD) designed with formyl group as receptor site accomplished ultrasensitive detection of hydrazine at parts per trillion level (LOD/81 ppt) in aqueous media with high selectivity and enormous improvement over the existing state of the art. An exceptional sensitivity is also achieved in the vapor phase (LOD/0.003%) using a Whatman paper strip based portable device for simple and cost-effective on-site detection. The detection mechanism involved a reaction-based spontaneous formation of a non-fluorescent hydrazone Schiff base derivative (NIBDH). The in vitro potential of the AIEEgenic probe was also demonstrated in two mammalian cell lines i.e. HeLa (human cervical cancer cell line) and HEK293T (Human embryonic kidney cell line that expresses a mutant version of the SV40 large T antigen). Owing to the highly selective formation of the hydrazone Schiff base complex with hydrazine, NIBD responds to the existence of hydrazine in both these cell lines without any interference from other biologically rich metal ions and amino acids. These outcomes could initiate a much wider use of formyl group triggered hydrazone Schiff base complexation for probing and manipulating hydrazine biology associated with several metabolic activities.

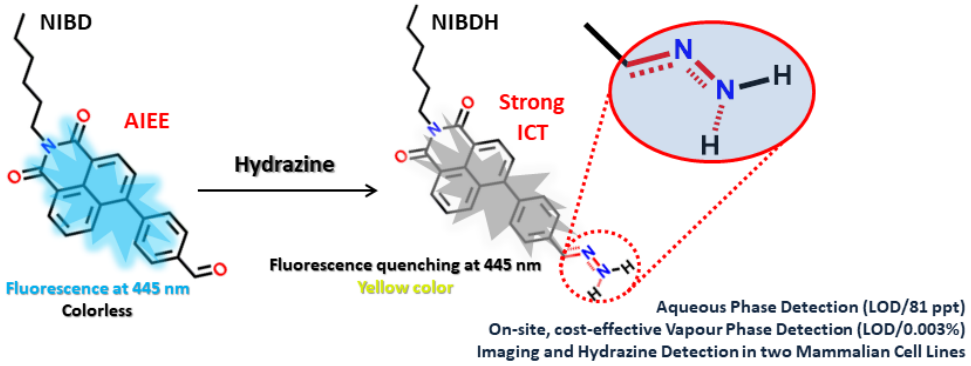

4.1. Introduction

Regardless of being a strong human carcinogen and having a threshold limit value (TLV) of 10 ppb as identified by the USEPA, hydrazine is extensively used in several industrial applications as a chief chemical reagent including pesticides, pharmaceuticals, textiles, dyes, and many more.[1-4] Hydrazine has mutagenic effects and can harm the human central nervous system, kidneys, lungs and liver.[5-9] It is also used as a propellant in projectile propulsion systems and gas precursor for air bags due to its greater enthalpy of burning.[10] Reports have witnessed that more than 120000 tons of approximately 64% hydrazine hydrate solution were produced globally per year.[11] Due to its high solubility in water, hydrazine readily contaminates the soil and ground water during manufacturing, usage, transport, disposal, etc., and could enter the food chain easily.

Among the detection methods developed for hydrazine, electrochemical and chromatographic techniques are time consuming and suffer primarily from portability and on-site application issues that make them very expensive, complex and impractical.[12-14] Fluorescence signaling based sensing of hydrazine is receiving increased attention owing to its high selectivity and sensitivity and because it can be applied in both liquid and solid state. In this respect, few molecular probes specific for hydrazine have been designed.[15-20] However, to the best of our knowledge, almost all the classical fluorometry based detections were executed in mixed solvent systems (organic and aqueous), which could be the primary reason for their poor detection limit (Table A4.1). Again, sensitive detection of hydrazine vapor using a solid support is another crucial hurdle associated with the existing fluorophores.[17-20] Herein, the designed naphthalimides AIEEgens (NIBD) exhibited highly selective ultra-detection of hydrazine at the ppt level in aqueous medium (Figure 4.1). More

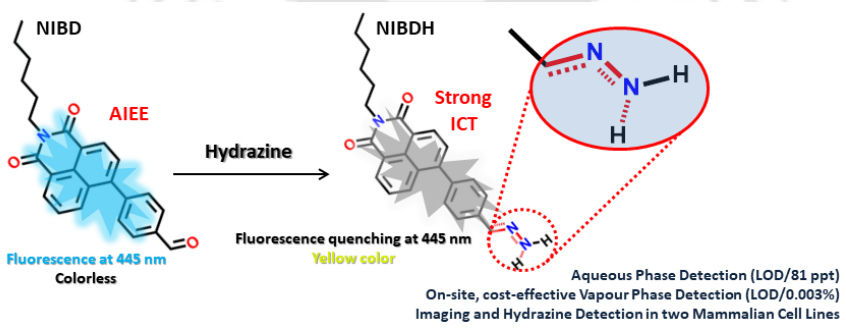

Figure 4.1. Graphical presentation of the AIEgenic ODNI-NS and their application for OVCs detection via the a-PET mechanism in water.

importantly, the formation of the non-fluorescent hydrazone Schiff base derivative appears to be highly effective in the vapor phase with huge advancement from the existing state of the art and could be applied for instant on-site testing (Table A4.1). The in vitro potential of the probe was also demonstrated in two different mammalian cell lines with a high signal-to-noise ratio. The formation and non-fluorescent nature of the hydrazone Schiff base complex was investigated by various experimental and theoretical studies (Figure 4.1).

4.2. Experimental Section

4.2.1. Materials and Instrumentations

All starting materials and reagents (viz: 4-bromo-1,8-naphthalene anhydride, 4-formylphenylboronic acid, metal salt, amines, amino acids) were purchased from Sigma Aldrich (INDIA) and were of reagent grade. HPLC grade solvents were purchased from Zenith India and Northeast Chemicals. NMR (^{1}H, ^{13}C) spectra were recorded with a Varian-AS400 NMR spectrometer or Bruker Avance 600 MHz spectrometer. Electrospray ionization mass (ESIMS) spectra were recorded on a Waters (Micro mass MS-Technologies) Q-Tof MS Analyzer spectrometer. Microbalance (± 0.1mg) and volumetric glassware were used for the preparation of solutions. UV/vis and PL spectra were recorded on a Perkin-Elmer Model Lambda-750 spectrophotometer and a Horiba Fluoromax-4 spectrofluorometer respectively using 4 mm quartz cuvettes at 298 K. Malvern Zetasizer instrument was used to measure the hydrodynamic diameter of the compounds. Lifetime measurements were performed using a MicroTime-200 instrument. FE-SEM samples were made using the drop-cast method from Water and were left for drying at room temperature. FE-SEM-images were obtained on Sigma Carl ZEISS field emission scanning electron microscope.

4.2.2. Cell Culture and Imaging

Both HeLa and HEK293T cell were seeded in a 24-well cell culture dish for 18 h in Dulbecco's modified Eagle's medium (DMEM) supplemented with 10% fetal bovine serum (FBS), penicillin (1 unit/mL), and streptomycin (1 μg/mL) maintained at humidified atmosphere of 37 ^{o}C under 5% CO_2 flow in an incubator. The cells were treated and incubated with 1 μM of NIBD at 37 °C under 5% CO_2 for 2 h. To remove the remaining extracellular dye, the cells were washed two times with PBS and then cell images were recorded before and after the treatment of hydrazine directly into the medium using a

fluorescence microscope from ThermoFisher Scientific, USA. Blue emission was collected with a 446 nm window.

4.2.3. Sensing Studies

The monomer NIBD (3.8 mg) stock solution was prepared at a concentration of 10 mM in 1 mL DMF. This was diluted to 10 μM for each titration in a 1 mL cuvette. The stock solutions of various analytes were (1 mM) were introduced in portions and the fluorescence intensity changes were recorded at pH 7.4 at room temperature (excitation wavelength: 355 nm) in PBS-buffer.

4.2.4. Calculation of Detection Limit

For calculating detection limit, different samples of NIBD (10 μM) each containing hydrazine (0 μM, 0.1 μM, 0.2 μM, 0.3 μM, 0.4 μM and 0.5 μM) were prepared separately and fluorescence spectrum was then recorded for each sample by exciting at 355 nm. The detection limit plot for hydrazine was obtained by plotting change in the fluorescence intensity versus concentration of hydrazine. The curve shows a linear relationship and the correlation coefficient (R^2) via linear regression analysis was calculated to be 0.9843. The limit of detection (LOD) was then calculated using the equation $3\sigma/K$, where σ represents the standard deviation in the intensity of NIBD in the absence of hydrazine and K symbolizes slope of the equation.

4.2.5. Synthesis of Compounds

The synthetic procedures and respective characterization data for the naphthalimide derivative (NIBD) hava been provided in the previous chapters where it corresponds to compound 2 (Scheme A4.1).

4.2.6. Theoretical Studies

To evaluate the fluorescence quenching of NIBD after the formation of the complex with hydrazine, the electronic distribution of both NIBD and NIBDH (hydrazone Schiff base complex of NIBD) were calculated using time-dependent density functional theory (TDDFT). The excited state optimized geometries along with HOMO/LUMO energy were calculated using B3LYP hybrid functional incorporated in the Gaussian 09 package. The 6-31G basis set for all the atoms has been used in all calculations, which offers high-quality outcomes at a reasonable time.

4.2.7. Calculation of Stern–Völmer Quenching Constant (K_{sv}) and Limit of Detection (LOD)

The fluorescence response of the present probe was evaluated by fitting the obtained statistics to a Stern–Völmer equation linearly:

$$I_0/I = 1 + K_{sv}[Q] \quad (1)$$

Where 'I_0' represents the initial fluorescence intensity of probe before the addition of analytes, 'I' signifies the fluorescence response after the addition of sensing analytes, [Q] symbolizes the molar concentration of the analyte, and K_{sv} is the Stern–Volmer quenching constant.

The sensitivity of present probe towards these OVCs was calculated by performing the fluorescence titrations at very low concentrations of OVCs (0 to 5 ppm). The standard mathematical formula used for calculating the detection limit is:

$$\text{Detection limit} = 3\sigma/K \quad (2)$$

Where σ represents the standard deviation of the initial fluorescence intensity in the absence of sensing analytes while K represents slope of the linear calibration plot determined by plotting the changes in the emission intensity of probe as a function of sensing analyte concentrations.

4.3. Results and Discussion

4.3.1. Design, Synthesis and Characterization

The naphthalimide derivative (NIBD) was synthesized by alkylation of 4-bromo-1,8-naphthalicanhydride followed by Suzuki coupling with 4-formylphenylboronic acid in good yields (Scheme A4.1). The synthesized molecules were well characterized by multinuclear NMR spectroscopy and HRMS. The complete synthetic processes and associated spectra have been provided in the previous chapter where NIBD is presented as compound 2. The phenyl group was intentionally incorporated onto the naphthalimide ring to implement the restriction in intramolecular rotation (RIR) phenomenon in their condensed state to generate AIEgenic properties, whereas the formyl group was introduced to provide a specific recognition site for hydrazine through the favorable hydrazone Schiff base formation at room temperature. However, the exceptional effect of the functional groups (formyl group)

to regulate the condensed state emission properties has been explored in Chapter 3 through a comparative analysis of 16 naphthalimide derivatives.

4.3.2. Detection Hydrazine in Aqueous Medium

As demonstrated in Chapter 3, NIBD formed nanorod like structures in water with AIEEgenic properties and showed similar emission profile in PBS buffer (pH = 7.4). Thus the fluorescent aggregates of NIBD (10 μM) formed in the buffer medium were considered for sensing studies. To investigate the optical response, fluorescence quenching titrations were carried out by subjecting different portions of hydrazine to NIBD (Figure 4.2a). Each of the spectra was recorded after 15 min incubation at room temperature. Almost 90% fluorescence quenching was observed upon adding just 9 μM solution of hydrazine. The disappearance of the blue luminescence of NIBD in the presence of hydrazine was clearly visible under UV light (Figure 4.2b). The UV-visible spectrum of NIBD was recorded with and without hydrazine in aqueous media. The absorption band at 360 nm shifted towards the shorter wavelength region and a new band at 300 nm appeared corresponding to the hydrazone Schiff base derivative (Figure A4.1). The transparent solution of NIBD transformed into yellow with the addition of hydrazine, which was visible to the naked eye (Figure 4.2c). The quenching efficiency was obtained by fitting the Stern–Volmer equation linearly at lower concentration, and the Stern–Volmer constant (K_{sv}) was found to be 7.25×10^5 M^{-1} confirming the very high sensitivity of NIBD towards hydrazine (inset, Figure 4.2a). The limit of detection (LOD) for hydrazine was calculated to be 2.54×10^{-9} M (81 ppt) using the standard method ($n\sigma/K$, n = 3) which appeared to be the best value observed so far in the literature and much below the TLV (10 ppb) as identified by the US-EPA. (Figure A4.2 and Table A41).[1,21,22]

4.3.3. Selectivity Study

For achieving practicability of the probe along with sensitivity, the selectivity of NIBD towards hydrazine in an aquatic system was also tested. During this course, fluorescence titration experiments of NIBD with several amino acids (considering biological importance), amines, anionic and cationic analytes were executed to monitor the selectivity of NIBD for hydrazine under identical conditions (Figure 4.2d and Figure A4.3). It was observed that other amines, such as urea, thiourea and ethylenediamine, could not quench the fluorescence intensity of NIBD significantly (~7–11%). Almost negligible quenching in fluorescence intensity of NIBD was observed with various anions (NO_3^-, NO_2^-, $H_2PO_4^-$,

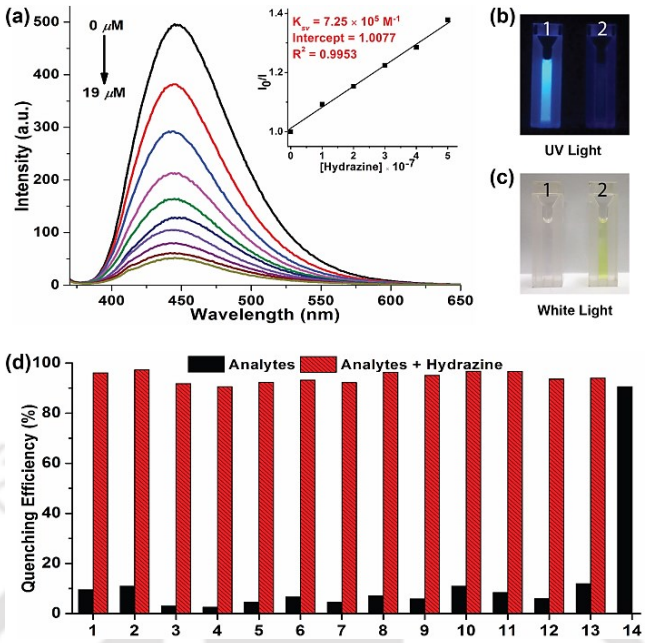

Figure 4.2. Aqueous phase detection of hydrazine. (a) Photo-luminescence spectra of NIBD (10 μM) with increasing concentration of hydrazine recorded after 15 min of incubation in PBS buffer at room temperature. Inset: Stern–Volmer plot of NIBD at different hydrazine concentrations. (b and c) Color change of NIBD nanoaggregates in PBS buffer before (1) and after (2) the addition of hydrazine under UV light (365 nm) and white light respectively. (d) Quenching efficiency of NIBD (10 μM) with several analytes (10 μM) in BPS buffer before and after the addition of hydrazine (10 μM): thiourea (1), urea (2), cysteine (3), homocysteine (4), glutathione (5), leucine (6), glycine (7), dimethylamine (8), diethylamine (9), ethylenediamine (10), triethylamine (11), ammonium hydroxide (12), hydroxylamine (13), and hydrazine (14).

$H_3PO_2^-$, F^-, Cl^-, Br^-, I^-, OAc^-, PPi^-, CN^-, and SCN^-) and cations (Cs^+, Mn^{2+}, Co^{2+}, Cr^{2+}, Al^{3+}, Cu^{2+}, Cd^{2+}, Pd^{2+}, Zn^{2+}, La^{3+}, Fe^{3+}, and Fe^{2+}). Thus, the NIBD AIEEgen responded to hydrazine with outstanding sensitivity and selectivity even in the presence of commonly interfering analytes in pure aqueous medium which is a very unique feature of this probe.

4.3.4. Elucidation of the Detection Mechanism

Several experimental analyses were performed to understand the mode of interaction between NIBD and hydrazine. ^{1}H NMR spectra of NIBD were recorded in DMSO-d_6 at different hydrazine concentrations (0, 0.5, 1.0, and 2.0 equiv.) after 15 min of incubation (Figure 4.3a and 4.3b). The addition of hydrazine causes a shift of the =CH (a) peak of the formyl group from δ = 10.15 ppm (^{1}H) to δ = 7.80 ppm, which matched well with the =CH (b) peak of the hydrazone Schiff base derivative (NIBDH). Besides, the chemical shifts of the phenyl protons towards the more shielded region along with the total integration value supported the complete formation of the hydrazone Schiff base derivative. ESI-HRMS

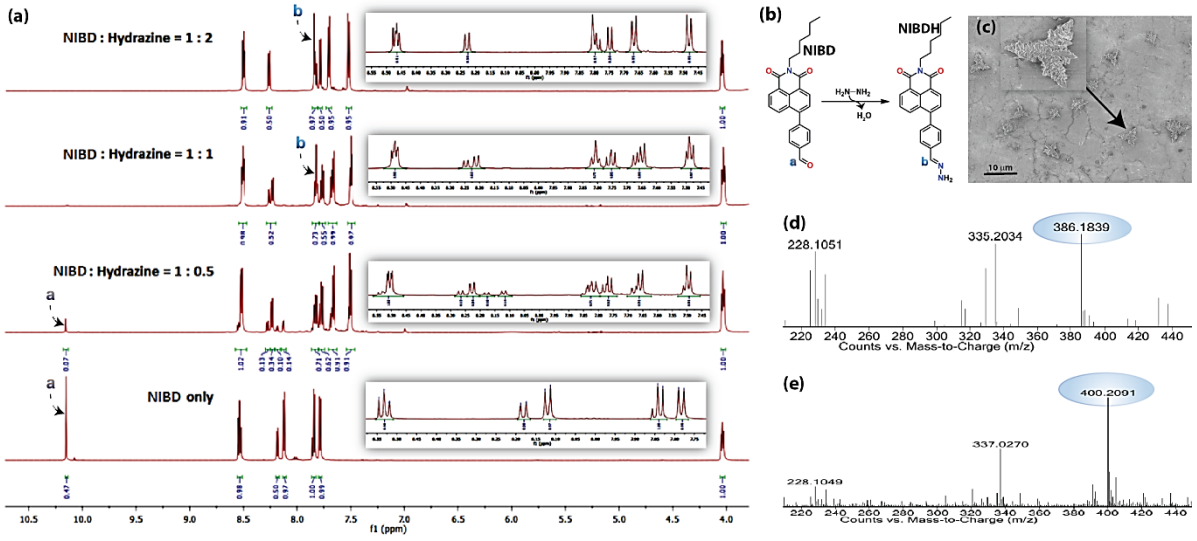

Figure 4.3. Elucidation of the sensing mechanism via formation of the hydrazone Schiff base complex. (a) ^{1}H NMR spectra of NIBD (50 mM) recorded in the absence and presence of hydrazine at different concentrations (0.5, 1.0 and 2.0 equiv.) after 15 min of incubation in DMSO-d_6. (b) Scheme representing the formation of the naphthalimide Schiff base derivative from NIBD at room temperature. (c) FESEM image of NIBD + hydrazine; the inset shows the corresponding magnified image. The FESEM images have been recorded by dropcasting the corresponding probe and analyte solution at 10 μM concentration from water on aluminium foil at room temperature. (d) ESI-HRMS of NIBD. (e) ESI-HRMS of NIBDH.

analysis of this hydrazone Schiff base derivative also revealed the formation of NIBDH with nearly 100% conversion and confirms the proposed mechanism (Figure 4.3d and 4.3e). Furthermore, DLS studies performed in aqueous media showed an increase in the particle size after the formation of the Schiff base derivative (NIBD, Z_{ave} = 367.8 nm; NIBDH, Z_{ave} = 550.2 nm) and was confirmed from FESEM images (Figure A4.4 and A4.5). Along with the size, a huge morphological transformation from nanorods to hastate shape microstructures (>10 μM) was witnessed after formation of NIBDH (Figure 4.3c and A4.6).

To better understand the spectral changes of NIBD responding to hydrazine, theoretical calculations were performed using time dependent density functional theory (TDDFT) with the B3LYP(d) exchange functional, employing 6-31G* basis sets in a suite of the Gaussian 09 program (Figure 4.4a and 4.4b).[23-28] Both NIBD and its hydrazone Schiff base adduct (NIBDH) showed highly distinct structural conformation and electronic distribution in their excited state (Figure 4.4b). In NIBD, electron densities over the HOMO and LUMO are dispersed all over the conjugated units without any significant charge separation. However, the π-electrons over the HOMO and LUMO are localized in the respective hydrazone and naphthalimide units in NIBDH with complete charge separation, suggesting that NIBDH is a

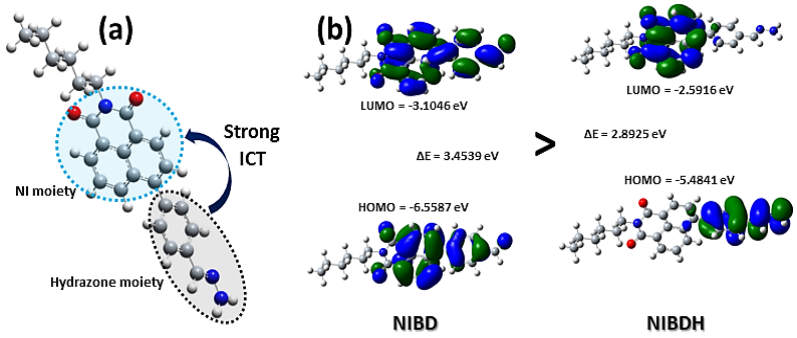

Figure 4.4. (a) Optimized structure of NIBDH and the co-regulation of response emission by the ICT mechanism. (b) Frontier molecular orbital energy of NIBD and NIBDH in the excited state. Computations were executed using time dependent density functional theory with the B3LYP exchange functional employing 6-31G* basis sets in the Gaussian 09 program.

typical ICT based fluorophore having strong donor (D) and accepter (A) units with push–pull interactions (Figure 4.4).[23-28] The hydrazone product NIBDH from the spontaneous reaction between NIBD and hydrazine retained a smaller energy difference between the LUMO and the HOMO (2.89 eV) than that of NIBD (3.45 eV) (Figure 4.4b), which can be ascribed to the high feasibility of the ICT process from the electron-donating hydrazone group (D) to the electron-withdrawing naphthalimide group (A). Additionally, the huge increase in dipole moment (6.91 to 34.29 in Debye) along with dihedral angle (43.31^{o} to 90.78^{o} angle between D and A units) after formation of the hydrazone Schiff base adduct also strongly supports the twisted ICT based fluorescence quenching in NIBDH.[23-28] The strong donating nature of the hydrazone adduct is due to the conjugated $-NH_2$ group with the aromatic ring. This was confirmed by the FTIR analysis of NIBDH, which showed a characteristic intense broad band at 3480 cm^{-1} assigned to the secondary amine (Figure 4.1 and A4.7).[20]

4.3.5. Detection of Hydrazine Vapour Cost-Effective Paper Strips

After gaining an unprecedented sensitivity by the fluorometric method, portable and simple paper strip based devices coated with the AIEEgen NIBD were fabricated to make these outcomes more practical for cost-effective on-site application. All of the fabrication steps are pictured in Figure 4.5a. Whatman filter paper was cut into pieces of 1 cm × 1 cm dimensions and dipped in 20 mM DMF solution of NIBD. The paper strips were then dried on a hot plate at 50 ^{o}C for rapid evaporation of solvent before exposing them to hydrazine vapor. As shown in Figure 4.5a(4), vials containing various concentrations of hydrazine hydrate solution (5% to 0.001%) were prepared and their mouths were covered with the dried probe-

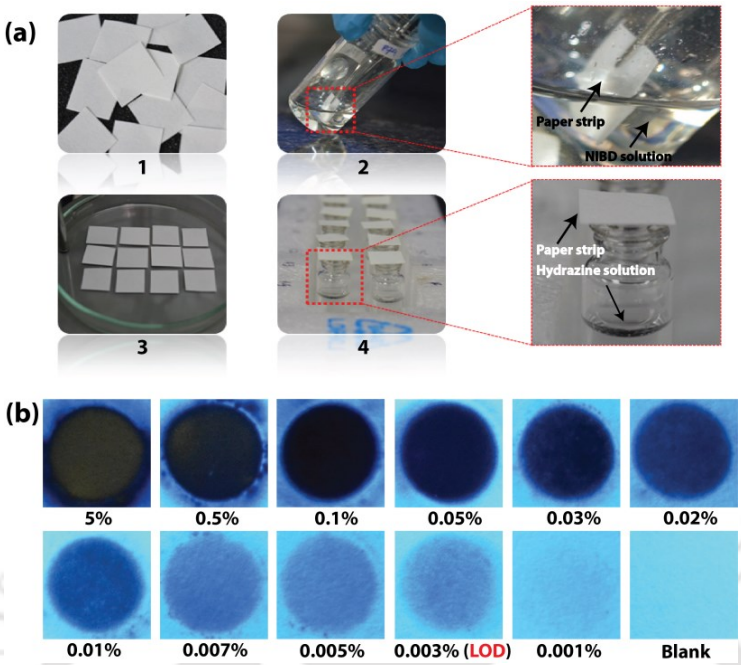

Figure 4.5. Fabrication of cost-effective paper strips for vapour phase onsite detection of hydrazine. (a) Representation of test strip fabrication for simple and cost-effective vapor phase detection of hydrazine using Whatman filter paper. (1) Whatman paper was cut into 1 cm × 1 cm pieces. (2) Dip-coating of Whatman paper strips in DMF solution of NIBD (20 mM) at room temperature for 10 seconds. (3) Drying of the paper strips on a hot-plate at 50 °C. (4) The mouth of the vials containing hydrazine hydrate solution of different concentrations was covered with the dried probe-loaded paper strips at room temperature. (b) Fluorescence color change of the probe-loaded test strips after exposing them to different hydrazine concentrations for 15 min. The fluorescence color variations were perceived by UV light illumination at 365 nm.

loaded paper strips for 15 min. A solvent blank was also taken as a control. Although hydrazine is highly volatile in nature, in previous reports, sophisticated special instruments that could work at low pressure for the effective vaporization of hydrazine have been used.[20] This clearly depicts the low sensitivity and challenges faced by the existing probes. All the above hurdles have been overcome completely owing to the very high sensitivity of the newly designed AIEEgen. The filter papers were then pictured under 365 nm UV light irradiation. Different strengths of dark spots were witnessed on these test strips, which vary with the concentration of hydrazine present inside the vials (Figure 4.5b).

The lowest amount of hydrazine vapor detectable (LOD) under UV-light irradiation was 0.003%, comprising the best result among the reported values (Table A4.1). In addition, vapor phase selectivity studies were also carried out with other competing vapor analytes such as ammonia, H_2O_2, triethylamine, butylamine, HCl and diethylamine, which confirmed the high selectivity of NIBD towards hydrazine (Figure A4.8). These observations with

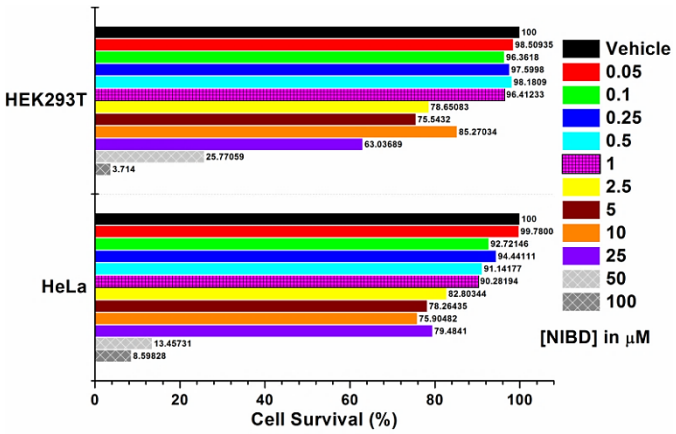

Figure 4.6. Cell cytotoxicity experiment for NIBD via MTT assay. Both HEK293T and HeLa cells were plated in a 96-well polystyrene culture plate and allowed to grow for 24 h in DMEM supplemented with 10% fetal bovine serum (FBS), penicillin (1 unit per mL), and streptomycin (1 mg mL^{-1}). The cells were maintained in a humidified atmosphere at 37 °C under 5% CO_2 flow in an incubator. After 24 h, the existing medium was replaced with fresh medium containing different NIBD concentrations (0–100 μM) and incubated for another 24 h. Following 24 h of incubation, the medium was treated with 10 mL of methylthiazolyldiphenyl-tetrazolium bromide (MTT) solution (5 mg mL^{-1} in PBS) and kept as such for 4 h. The MTT-formazan crystals were then solubilized in DMSO and absorbance at 570 nm was recorded. Each of the data points is the average of three individual readings.

extraordinary efficacy of the paper test strips endorse huge application potential for onsite, simple and cost-effective detection of hydrazine vapor.

4.3.6. In Vitro Detection of Hydrazine in Two Mammalian Cells

The applicability of this highly selective and novel naphthalimide AIEEgen (NIBD) was also examined in living cells for the detection of hydrazine. In this instant, two mammalian cell lines, i.e. HeLa (human cervical cancer cell line), and HEK293T (Human embryonic kidney cell line), procured from the repository of the National Centre for Cell Science (NCCS) Pune, India were employed to study the in vitro selectivity and potential of NIBD toward hydrazine. Before the hydrazine detection study, the effect of NIBD towards the cell lines was determined by treating both the cells with different concentrations (from 0.05 μM to 100 μM) of the same AIEEgen. MTT assay was performed to check the cytotoxicity of NIBD (Figure 4.6) and simultaneously fluorescence imaging was carried out for each of the concentrations. Considering these results, a lower but effective concentration (1 μM) was selected for further imaging and hydrazine detection study. Both the cell lines were treated independently with NIBD (1 μM) for 90 minutes and then hydrazine was subjected to the media. Images were acquired using a fluorescence microscope after 2 h of post-incubation. As revealed in Figure 4.7, the strong blue fluorescence of NIBD incubated cells disappeared

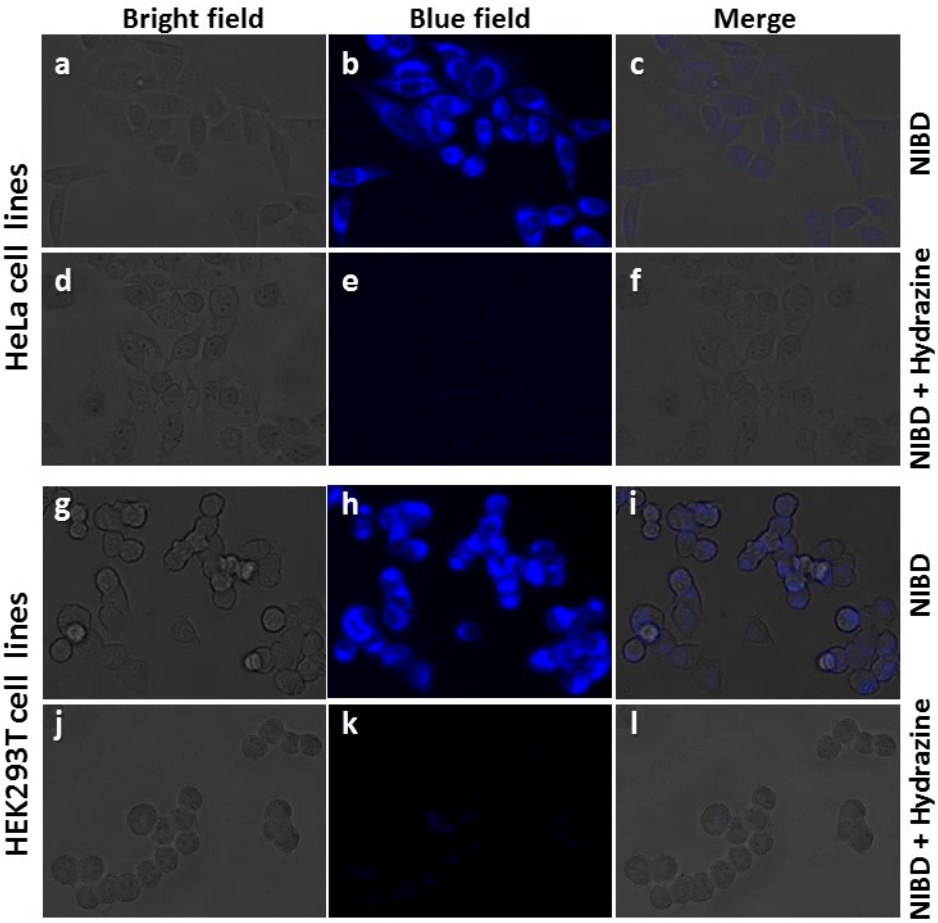

Figure 4.7. Fluorescence microscopy images of NIBD in response to hydrazine addition in two mammalian cell lines (HeLa and HEK293T). Both the cells were treated with 1 μM NIBD in a medium (DMEM supplemented with 10% fetal bovine serum (FBS), penicillin (1 unit per mL), and streptomycin (1 mg mL^{-1})) and were incubated in a humidified atmosphere at 37 ^{o}C under 5% CO_2 flow for 90 min, exchanged into fresh medium containing hydrazine and incubated for another 2 h. Bright, blue and merged field images of HeLa (a–c) with NIBD and (d–f) NIBD + hydrazine respectively. Bright, blue and merged field images of HEK293T (g–i) with NIBD and (j–l) NIBD + hydrazine respectively.

almost completely in the presence of hydrazine after 2 h due to the formation of the non-fluorescent hydrazone Schiff base derivative (NIBDH). This result lends further support to the high selectivity of the hydrazine induced in vitro complexation of NIBD to form NIBDH and shows no considerable interference from other biologically abundant metal ions and amino acids present in the medium.

It is also worth mentioning that NIBD could image the cells with high fluorescence in a wash-free medium owing to the application of a very low concentration of the AIEEgenic probe (Figure A4.9). These results led us to believe that almost all the probes were engulfed by the cells actively within 60 min of incubation, thereby resulting in almost no background

fluorescence in a wash-free medium. These results also confirm that the NIBD AIEEgen could efficiently detect and bind hydrazine in vitro to form hydrazone Schiff base derivative NIBDH, a non-fluorescent complex even in a physiological environment, thereby demonstrating the unique sensitivity and selectivity in multiple cell lines as well as providing avenues for cellular imaging, sensing, monitoring and clinical diagnosis.

4.4. Conclusion

In conclusion, the newly designed naphthalimide AIEEgen with the formyl group selectively detects hydrazine at parts per trillion level (81 ppt) in pure aqueous media. The probe could spontaneously react with hydrazine to form a hydrazone Schiff base derivative resulting in fluorescence quenching at room temperature. An extremely high detection limit was also accomplished in the vapor phase (0.003%) by fabricating Whatman paper strips which could provide a simple, portable and cost-effective method for on-site detection of hydrazine. The in vitro efficacy of the AIEEgenic probe towards hydrazine was also demonstrated in two mammalian cell lines (HeLa and HEK293T) with a high signal-to-noise response. Along with good imaging capability, the probe responds to hydrazine without any interference from biologically abundant metal ions and amino acids. This complexation could be potentially applicable to the hydrazine scaffold and can be envisioned for a broader utility of this chemistry in elucidating new targets of hydrazine metabolism in biological pathways.

References

(1) U.S. Environmental Protection Agency (EPA), Integrated Risk Information System (IRIS) on Hydrazine/Hydrazine Sulfate, National Center for Environmental Assessment, Office of Research and Development, *Washington, DC*, **1999**.

(2) Toth, B. *Cancer Res.* **1975**, *35*, 3693.

(3) Choudhary, G.; Hansen, H. *Chemosphere* **1998**, *37*, 801–843.

(4) Ragnarsson, U. *Chem. Soc. Rev.* **2001**, *30*, 205–213.

(5) Garrod, S.; Bollard, M. E.; Nicholls, A. W.; Connor, S. C.; Connelly, J.; Nicholson, J. K.; Holmes, E. *Chem. Res. Toxicol.* **2005**, *18*, 115–122.

(6) Zelnick, S. D.; Mattie, D. R.; Stepaniak, P. C. *Aviat., Space Environ. Med.* **2003**, *74*, 1285–1291.

(7) Reilly, C. A.; Aust, S. D. *Chem. Res. Toxicol.* **1997**, *10*, 328–334.

(8) Mo, J.-W.; Ogorevc, B.; Zhang, X.; Pihlar, B. *Electroanalysis* **2000**, *12*, 48–54.

(9) Moloney, S. J.; Prough, R. A. *in Biochemical Toxicology of Hydrazine, ed. E. Hodgson and R. M. Philpot, Elsevier Science, New York*, **1983**, p. 313.

(10) Wang, J.; Chen, L. *Anal. Chem.* **1995**, *67*, 3824–3827.

(11) Schirmann, J.-P.; Bourdauducq, P. *Ullmann's Encyclopedia of Industrial Chemistry, Wiley-VCH, Weinheim*, **2002**.

(12) Oh, J.-A.; Park, J.-H.; Shin, H.-S. *Anal. Chim. Acta* **2013**, *769*, 79–83.

(13) Umar, A.; Rahman, M. M.; Kim, S. H.; Hahn, Y.-B. *Chem. Commun.* **2008**, 166–168.

(14) Gu, X.; Camden, J. P. *Anal. Chem.* **2015**, *87*, 6460–6464.

(15) Zhang, J. F.; Zhou, Y.; Yoon, J.; Kim, J. S. *Chem. Soc. Rev.* **2011**, *40*, 3416–3429.

(16) Chen, X.; Tian, X.; Shin, I.; Yoon, J. *Chem. Soc. Rev.* **2011**, *40*, 4783–4804.

(17) Xiao, L.; Tu, J.; Sun, S.; Pei, Z.; Pei, Y.; Pangb, Y.; Xu, Y. *RSC Adv.* **2014**, *4*, 41807–41811.

(18) Cui, L.; Peng, Z.; Ji, C.; Huang, J.; Huang, D.; Ma, J.; Zhang, S.; Qian, X.; Xu, Y. *Chem. Commun.* **2014**, *50*, 1485–1487.

(19) Zhang, R.; Zhang, C.-J.; Song, Z.; Liang, J.; Kwok, R. T. K.; Tang, B. Z.; Liu, B. *J. Mater. Chem. C* **2016**, *4*, 2834–2842.

(20) Lee, M. H.; Yoon, B.; Kim, J. S.; Sessler, J. L. *Chem. Sci.* **2013**, *4*, 4121–4126.

(21) Meher, N.; Chowdhury, S. R.; Iyer, P. K. *J. Mater. Chem. B* **2016**, *4*, 6023–6031.

(22) Meher, N.; Iyer, P. K. *Nanoscale* **2017**, *9*, 7674–7685.

(23) Callan, J. F.; d. Silvaa, A. P.; Magri, D. C. *Tetrahedron* **2005**, *61*, 8551–8588.

(24) Duan, X.-H.; Li, X.-Y.; He, R.-X.; Cheng, X.-M. *J. Chem. Phys.* **2005**, *122*, 084314.

(25) Kathayat, R. S.; Finney, N. S. *J. Am. Chem. Soc.* **2013**, *135*, 12612–12614.

(26) Kathayat, R. S.; Yang, L.; Sattasathuchana, T.; Zoppi, L.; Baldridge, K. K.; Linden, A.; Finney, N. S. *J. Am. Chem. Soc.* **2016**, *138*, 15889–15895.

(27) He, L.; Yang, X.; Xu, K.; Kong, X.; Lin, W. *Chem. Sci.* **2017**, *8*, 6257–6265.

(28) Cidlina, A.; Miletin, M.; Fathi-Rasekh, M.; Nemykin, V. N.; Zimcik, P.; Novakova, V. *Chem.–Eur. J.* **2017**, *23*, 1795–1804.

Appendix

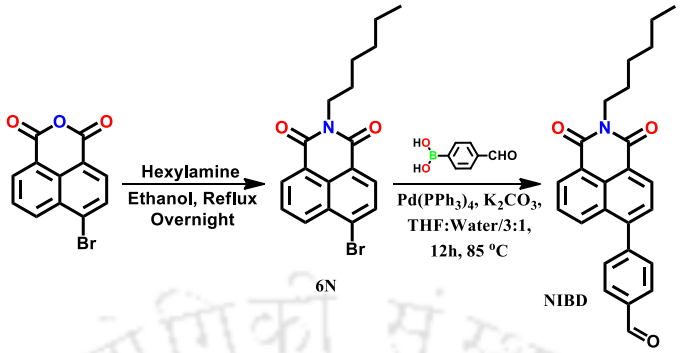

Scheme A4.1: Synthetic route to **NIBD**.

Table A4.1. A comparative study of the K_{sv} and the detection limit (both in solution and vapor phase) along with the material and medium used for hydrazine detection with the existing state of art.

Publication	Material Used	K_{sv} (M^{-1})	Detection Limit (Liquid Phase)	Medium Used	Detection Limit (Vapor Phase)
Present Work	**Naphthalimide AIEEgens**	**7.25×10^5**	**2.54 nM (81 ppt)**	**PBS Buffer**	**0.003%**
J. Mater. Chem. C, **2016**, *4*, 2834	Tetraphenylethylene moiety	--	143 ppb	DMSO–PBS buffer (9/1, v/v);	0.1%
Chem. Commun., **2016**, *52*, 6166	Pthalimide based probe	--	1.5 ppb	In HEPES buffer using Triton X 100 surfactant	--
Sensors and Actuators B, **2016**, *232*, 369–374	Coumarin/benzopyrylium based probe	--	47 nM (1.5 ppb)	DMSO:PBS (2:3, v/v)	1%
RSC Adv., **2016**, *6*, 70855	Thiadiazol based moiety	--	84 nM (2.9 ppb)	DMSO–H2O (6/4, v/v)	--
Anal. Chem. **2015**, *87*, 9101–9107	Hemicyanine based probe	--	0.17 μM (5.4 ppb)	HEPES buffer-DMSO (8/2, v/v)	--
Org. Biomol. Chem., **2015**, *13*, 5344–5348	ESIPT-based fluorescent	--	0.147 μM	PBS buffer-ethanol (99/1, v/v)	--
Chem. Commun., **2014**, *50*, 1485	Naphthalimide moiety	--	8.8 nM (0.3 ppb)	DMSO-H_2O (6/4, v/v).	10%
J. Mater. Chem. B, **2014**, 2, 7344	Dansyl-based	1.03×10^4	188 nM (6.01 ppb)	DMSO-HEPES buffer (9/1, v/v)	0.01%
Anal. Chem. **2014**, *86*, 4611–4617	Phthalimide based probe	--	0.1 μM (3.2 ppb)	H2O/DMSO (v/v, 3:7)	0.1%
J. Mater. Chem. B, **2014**, 2, 1846	ICT-based probe	--	12 nM	DMF–Tris HCl buffer (7/3, v/v)	--
RSC Adv., **2014**, *4*, 41807–41811	Benzo[*d*]oxazole	--	84 nM (2.7 ppb)	CH3CN–HEPES buffer (1/2, v/v)	10%
Chem. Sci., **2013**, *4*, 4121-4126	Naphthalimide moiety	--	100 nM (3.2 ppb)	CH_3CN	Excess

Org. Lett., **2013**, *15*, 5412–5415	Benzothiazole based probe	--	66 nM (2.2 ppb)	$CH_3CN:H_2O$ (2/3, v/v)	--
Org. Lett., **2013**, *15*, 4022–4025	Cyanine dye derivative	5.68×10^5	25 nM (0.81 ppb),	DMSO–Acetate buffer (9/1, v/v)	--
RSC Adv., **2013**, *3*, 18872–18877	Carbazole based probe	--	1.02 μM	CH3CN–H2O (8 : 2, v/v)	--
Org. Lett., **2011**, *13*, 5260–5263	Coumarin dye	--	2.46 μM (0.08 ppm)	DMSO–Acetate buffer (7/3, v/v)	--
Org. Biomol. Chem., **2013**, *11*, 2961	Dichlorofluorescein and resorufin acetates	--	90 nM (2.9 ppb)	DMSO-tris buffer (1 : 1, v/v)	--

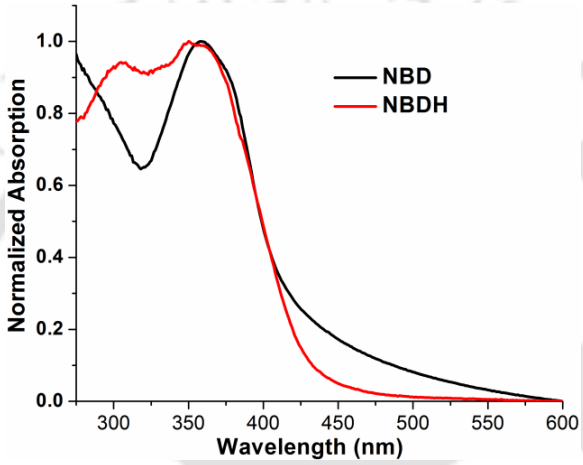

Figure A4.1. Normalized UV-Visible spectrum of **NIBD** and **NIBD**H in 99.9% aqueous media.

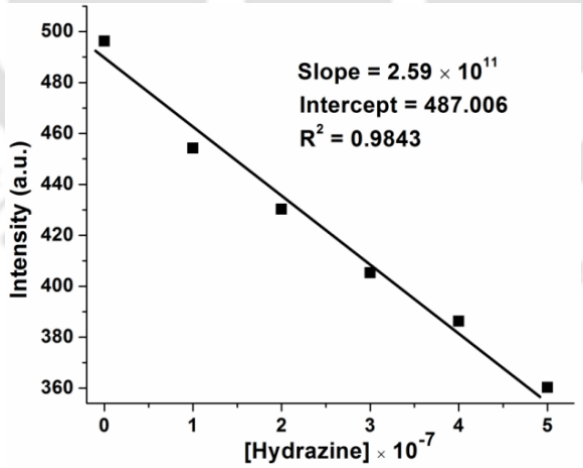

Figure A4.2. Fluorescence response of **NIBD** (10 μM) taken in aqueous buffer solution (pH 7.4) as a function of hydrazine concentration.

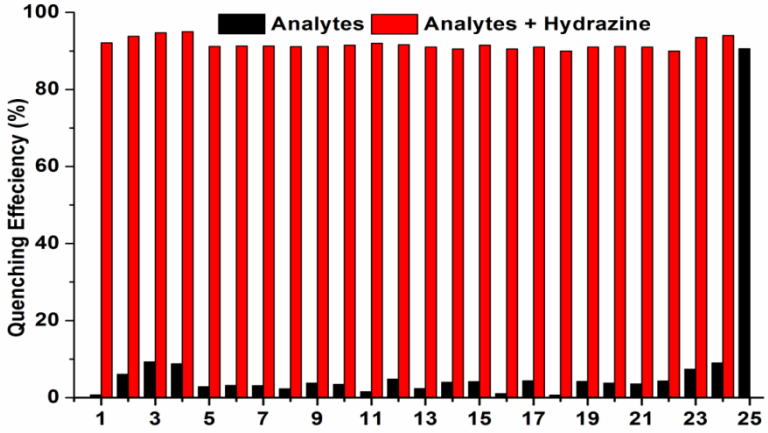

Figure A4.3. Quenching efficiency of **NIBD** (10 μM) with several anions and cations (10 μM) in BPS buffer before and after the addition of hydrazine (10 μM). NO_3^- (1), NO_2^- (2), $H_2PO_4^-$ (3), $H_3PO_2^-$ (4), F^- (5), Cl^- (6), Br^- (7), I^- (8), OAc^- (9), PPi (10), CN^- (11), SCN^- (12), Cs^+ (13), Mn^{2+} (14), Co^{2+} (15), Cr^{2+} (16), Al^{3+} (17), Cu^{2+} (18), Cd^{2+} (19), Pd^{2+} (20), Zn^{2+} (21), La^{3+} (22), Fe^{3+} (23), Fe^{2+} (24), Hydrazine (25).

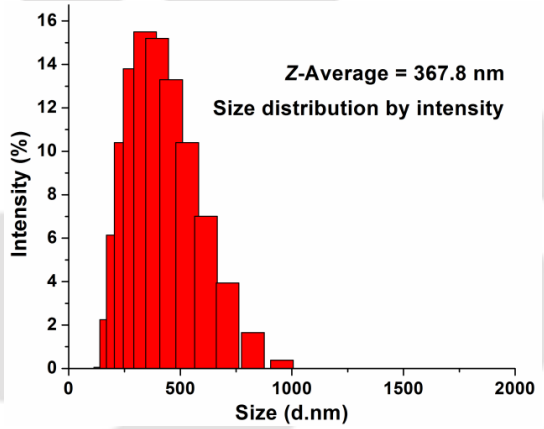

Figure A4.4. Size distribution by DLS of **NIBD** aggregate (10 μM) in water at 25 ^oC.

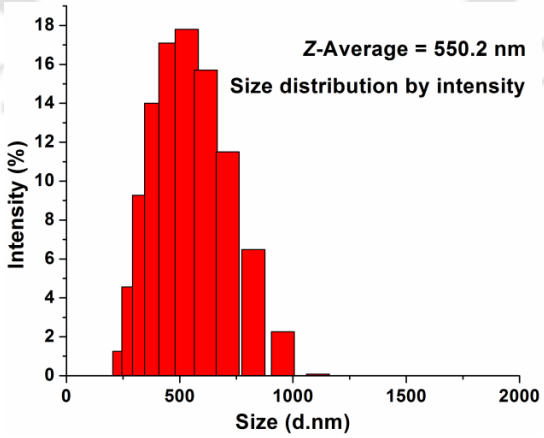

Figure A4.5. Size distribution by DLS of **NIBDH** aggregate (10 μM) in water at 25 ^oC.

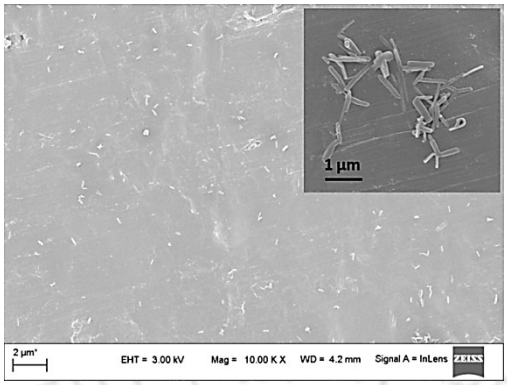

Figure A4.6. FE-SEM image of NIBD formed by the evaporation of its aggregates from at 99.9% water–0.1% DMF mixture on aluminium foil at room temperature (10 μM).

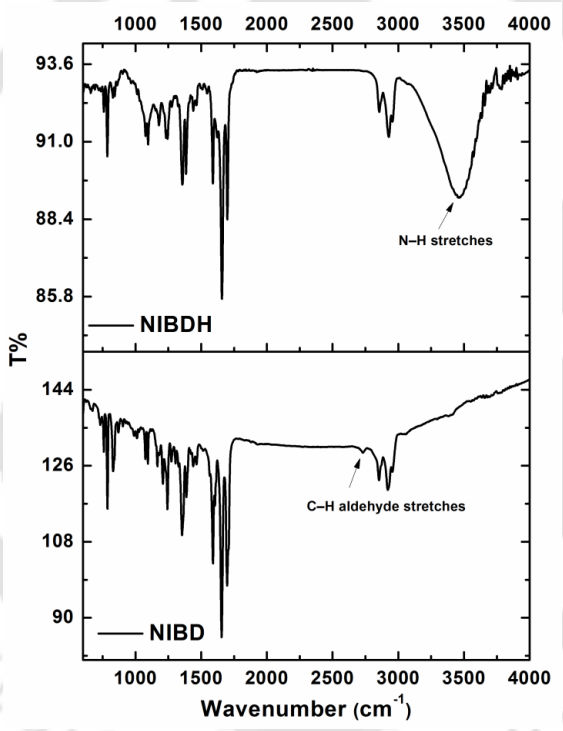

Figure A4.7. IR spectra of **NIBD** and **NIBD**H.

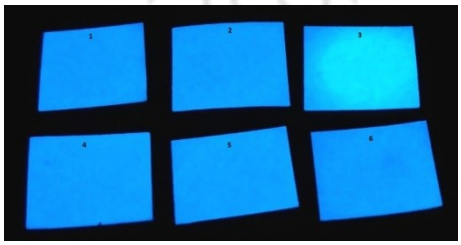

Figure A4.8. Digital photographs showing the fluorescence response of the **NIBD**-deep coated test strips after exposing to different vapor analytes for 15 min. (1) Diethylamine, (2) ammonia, (3) butylamine, (4) triethylamine, (5) HCl, (6) H_2O_2

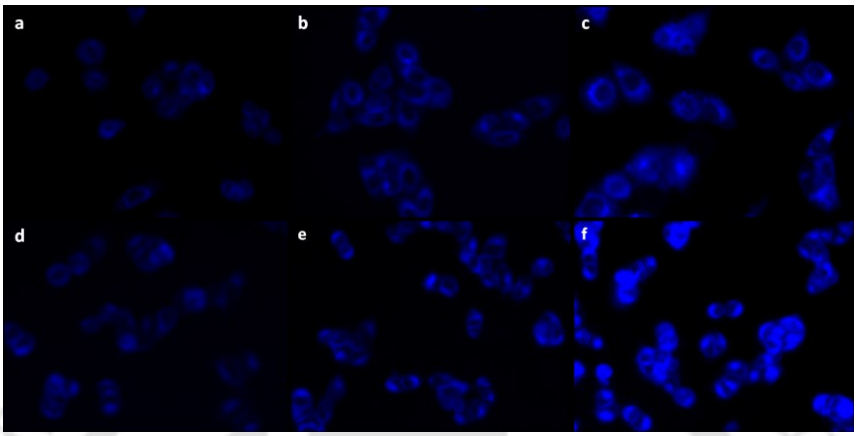

Figure A4.9. Fluorescence microscopy images of **NIBD** in a wash-free medium in HeLa and HEK293T cells at different concentrations. Fluorescence microscopy images of HeLa (a-c) and HEK293T (d-f) cells at 0.5 μM, 1 μM and 2.5 μM respectively. Images were recorded after 90 min of incubation at 37 °C under 5% CO_2 flow.

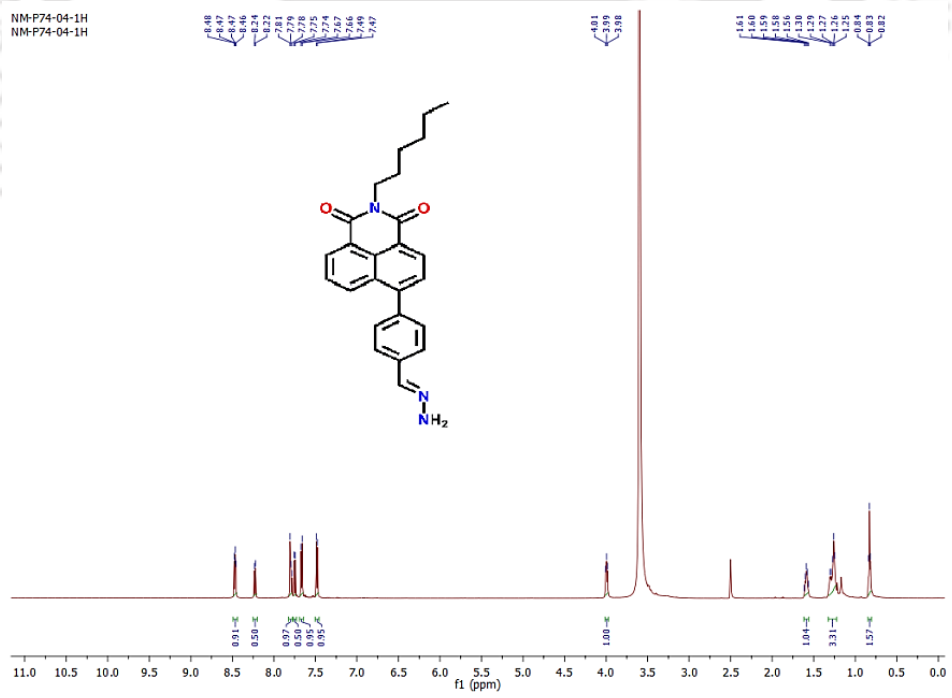

^{1}H NMR of **NIBDH**

Sample Name	Unavailable	**Position**	Unavailable	**Instrument Name**	Unavailable	**User Name**	Unavailable
Inj Vol	Unavailable	**InjPosition**	Unavailable	**SampleType**	Unavailable	**IRM Calibration Status**	All Ions Missed
Data Filename	P74-HZ.d	**ACQ Method**		**Comment**	Sample information is unavailable	**Acquired Time**	Unavailable

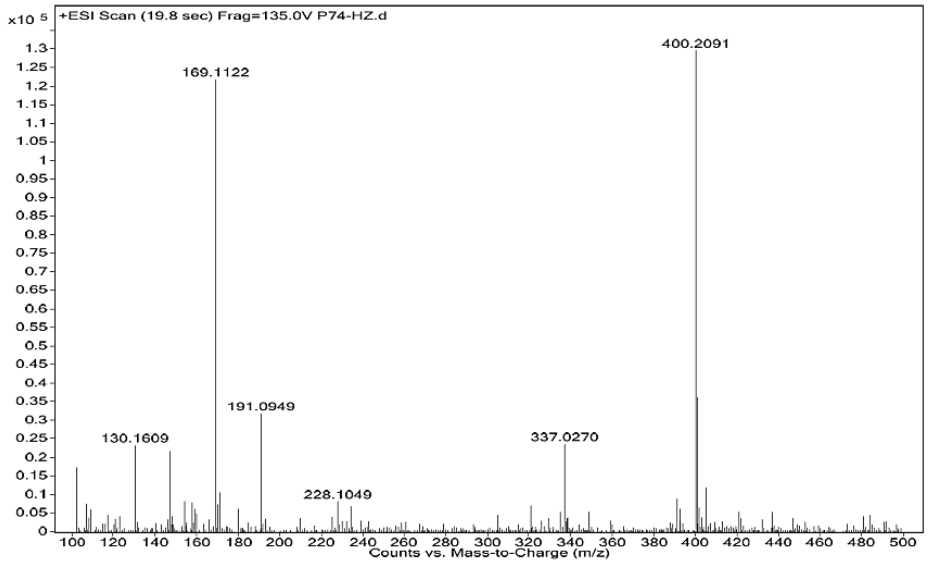

Mass Spectra of **NIBDH**

Chapter 5

Spontaneously Self-Assembled Naphthalimide Nanosheets: Condensed State Emission and Unveiling *a*-PET for Sensitive Detection of Organic Volatile Contaminants in Water

Meher, N.; Iyer, P. K. *Angew. Chem. Int. Ed.* **2018**, *57*, 8488 –8492.

Meher, N.; Iyer, P. K. Spontaneously Self-Assembled Nanosheets for the Detection of Organic Volatile Contaminants in Water, Ref No. 201831026896, App. Number: TEMP/E-1/29385/2018-KOL, (18/07/2018).

Abstract

A simple design strategy of long alkyl chain substitution was formulated to block the detrimental π–π interaction that potentially transforms the aggregation-caused quenching (ACQ) chromophores into aggregation-induced emission (AIE) active smart nanomaterials. The long octadecyl pendant chain substituted naphthalimide (NI) derivatives self-assembled into fluorescent nanosheets (NS)-like structures that spontaneously have surfaces coated with NI cores in water. The fluorescent NS were subsequently used to recognize the organic volatile contaminants (OVCs) at ppb levels via an acceptor-excited photoinduced electron transfer (*a*-PET) mechanism, unveiled as the first representative example. A new design strategy is thereby provided to detect toxic xylene derivatives in water using smart nanomaterials.

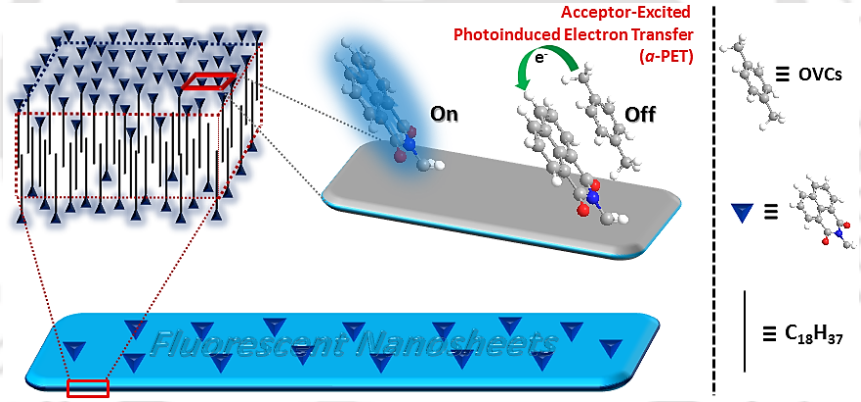

5.1. Introduction

The design of new molecular systems that can self-assemble spontaneously and reproducibly into multifunctional fluorescent micro- and nanostructures have gained unique research interest in recent years.[1–3] However, the traditional fluorophores habitually suffer from the notorious ACQ effect in aggregated state owing to the strong π–π interaction among the aromatic cores.[4,5] Recently, some luminogens have been reported to display AIE properties that are principally opposite to the ACQ effect.[6,7] These are named as AIEgens and are faintly fluorescent in solution but show bright emission in their condensed state, allowing them to find wide applications in optoelectronics, bioimaging, and sensory arrays.[8,9]

Since the discovery of the concept of AIE, research groups have explored several strategies to generate and manipulate new AIEgenic materials. Recently, few new strategies were formulated where, it was observed that, the condensed-state emission could be manipulated by space conjugation, ionization, or anion–π^+ interactions.[10–12] Besides, various types of organic-framework (OF)-based fluorescent materials were also developed by decorating them with inherent AIE active chromophores.[13–18] While recognizing the prominence of AIEgens, the task to develop new design strategy that can potentially generate AIEgenic system from well-known ACQphores is far from trivial. Herein, a simple design strategy of introducing a long alkyl chain substitution has been proposed to develop smart AIEgenic nanostructure from a conventional ACQ-prone moiety such as 1,8-naphthalic anhydride (NA). The long octadecyl units in **ODNI** undergo strong interchain hydrophobic interactions that effectively abolish the detrimental π–π interaction between the ACQ-prone NI cores in water and subsequently form NS-like self-assembly having the outer surface coated with the NI cores in an amorphous phase (Figure 5.1). Additionally, as another vital part of the design

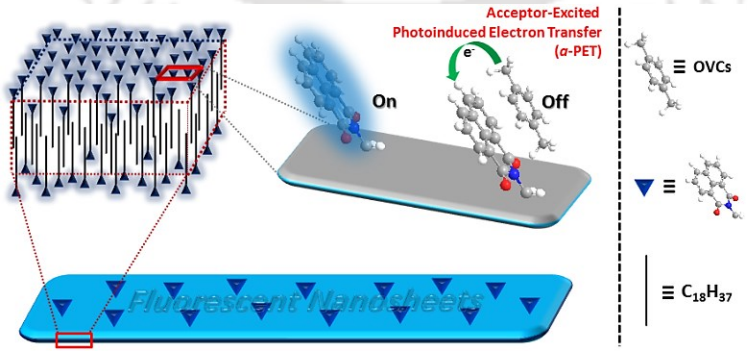

Figure 5.1. Graphical presentation of the AIEgenic **ODNI-NS** and their application for OVCs detection via the *a*-PET mechanism in water.

strategy, the small NI core was chosen owing to its electron deficit nature that could provide the driving force to detect the highly toxic OVCs.[17–19]

5.2. Experimental Section

5.2.1. Materials and Instrumentations

All starting materials and reagents (viz: 1,8-naphthalic anhydride, octadecylamine) were purchased from Sigma Aldrich (INDIA) and were of reagent grade. HPLC grade organic volatile compounds, such as p-xylene (p-xyl), mesitylene (Mes), mxylene (m-xyl), o-xylene (o-xyl), toluene (Tol), benzene (Ben), chlorobenzene (CB), dichlorobenzene (DCB), dimethyl sulfoxide (DMSO), carbon tetrachloride (CTC), dichloromethane (DCM), tetrahydrofuran (THF), methanol (MeOH), acetonitrile (MeCN), acetone (Ace), ethyl acetate (EA), diethyl ether (DEE), hexane (Hex), nitrobenzene (NB), dinitrobenzene (DNB) and p-nitrotoluene (p-NT) were purchased from Fisher Scientific Ltd. and RANKEM. NMR (^{1}H, ^{13}C) spectra were recorded with a Bruker Avance 600 MHz spectrometer. Electrospray ionization mass spectrometry (ESI-MS) was recorded on a Waters (Micro mass MS-Technologies) Q-Tof MS Analyzer spectrometer. Microbalance (± 0.1 mg) and volumetric glassware were used for the preparation of solutions. UV/vis and PL spectra were recorded on a Perkin-Elmer Model Lambda-750 spectrophotometer and a Horiba Fluoromax-4 spectrofluorometer respectively using 4 mm quartz cuvettes at 298 K. Lifetime measurements were performed using a time-correlated single photon counting set up from Horiba. The laser diode 375 (DeltaDiode-375) was used as a source with an excitation wavelength of 375 nm. Malvern Zetasizer instrument was used to measure the hydrodynamic diameter of the compounds. Field emission scanning electron microscopy (FESEM) images were obtained on Sigma Carl ZEISS field emission scanning electron microscope. The three-dimensional morphology of **ODNI** aggregate was investigated by atomic force microscopy (AFM) using a commercial atomic force microscope (Agilent 5500). X-ray diffraction (XRD) measurements were performed using Bruker D2 PHASER X-ray diffractometer (10 mA, 30 kV) equipped with Ni-filtered Cu Kα radiation, at a wavelength of 0.154 nm. The samples were scanned at a rate of 1.2^{o} min^{-1}. Single crystal data were obtained with a Bruker SMART APEX diffractometer equipped with a CCD area detector. The single crystal of the naphthalimide with hexyl chain was obtained from DMF which was found to be precisely similar to that of the reported single crystal generated by the slow diffusion of n-hexane into its dichloromethane solution.[20,21]

5.2.2. Synthetic Procedure of ODNI and HNI

1,8-naphthalic anhydride (396.4 mg, 2 mmol) was taken in ethanol (20 mL) and octadecylamine (592.92 mg, 2.2 m.mol) was added to it at room temperature. The suspension was heated at 85 ^{o}C with vigorous stirring for 8h. Then the mixture was cooled to room temperature and then kept at 5 ^{o}C for 1 h to recrystallize **ODNI**. The solvent was filtered out and the **ODNI** residue was washed with ethanol to get the pure white crystalline solid of **ODNI** (840 mg, 93% yield). Similar synthetic procedure was followed for **HNI** yielding a light brown color crystalline solid with 84% yield.

Characterization data of ODNI: ^{1}H NMR (600 MHz, $CDCl_3$, δ ppm) 0.88 (t, 3H), 1.26 (m, 26H), 1.35 (m, 2H), 1.42 (m, 2H), 4.18 (t, 3H) 7.76 (t, 2H), 8.21 (d, 2H), 8.61 (d, 2H). ^{13}C NMR (150.00 MHz, $CDCl_3$, δ ppm) 14.14, 22.70, 27.18, 28.16, 29.37, 29.41, 29.58, 29.63, 29.66, 29.67, 29.68, 29.71, 31.94, 40.54, 122.80, 126.92, 128.17, 131.17, 131.59, 133.82, 164.21. HRMS (+ESI): Calculated for $C_{30}H_{43}NO_2$ 449.3294 $[M]^+$, Found 450.3466 $[M+1]^+$.

Characterization data of HNI: ^{1}H NMR (600 MHz, $CDCl_3$, δ ppm) 0.88 (t, 3H), 1.33 (m, 4H), 1.42 (m, 2H), 1.72 (m, 2H), 4.17 (t, 2H), 7.74 (t, 2H), 8.19 (d, 2H), 8.58 (d, 2H). ^{13}C NMR (150.00 MHz, $CDCl_3$, δ ppm) 14.22, 22.71, 26.94, 28.20, 31.70, 40.63, 122.85, 127.04, 128.24, 131.29, 131.67, 133.96, 164.32. HRMS (+ESI): Calculated for $C_{18}H_{19}NO_2$ 281.1416 $[M]^+$, Found 282.1371 $[M+1]^+$.

5.2.3. Preparation of ODNI Nanosheets

The **ODNI** stock solution was prepared at a concentration of 20 mM in 1 mL DMF. Then, 0.04 mL of the solution was added to 19.96 mL of distilled water separately with vigorous stirring at room temperature. DMF was removed using dialysis tubes (20 mL × 2) and then sonicated for 30 minutes to obtain **ODNI** fluorescent nanosheets suspension in water. The same protocol was followed for **HNI** resulting in the formation of irregular fluorescent nanoaggregates. The fluorescent nanosheets can also be applied without dialysis, as the DMF contain is very low. It can also be recrystallized from ethanol or methanol with further sonication to get the naphthalimide nanosheets of **ODNI**.

5.2.4. Preparation of FESEM and AFM Samples

The dilute suspension of **ODNI** and **HNI** in water were drop-casted on aluminium foil or glass surface after sonicating properly and were dried in room temperature overnight before analysis.

5.2.5. Preparation of Samples for PXRD Study

Each of the monomers stock solutions was prepared at a concentration of 50 mM and were added dropwise to 50 mL distilled water separately with stirring at room temperature. The nanoaggregate suspensions were collected by centrifugation and dried in vacuum oven for overnight at 40 ^{o}C. The dried powders were taken for PXRD analysis.

5.2.6. Calculation of Detection Limit

For calculating detection limit, different samples of fluorophore (20 μM) suspension in water each containing different concentrations of OVCs were prepared separately and the fluorescence spectrum was recorded for each sample by exciting at 350 nm. The Stern-Volmer Quenching Constant (K_{sv}) was calculated by plotting Io/I verses OVCs concentration. The curve shows a linear relationship and the correlation coefficient (R^2) via linear regression analysis was calculated to be close to 1. The detection limit plot for various OVCs was obtained by plotting change in the fluorescence intensity versus concentration of OVCs. The limit of detection (LOD) was then calculated using the equation $3\sigma/K$, where σ represents the standard deviation in the intensity of fluorophores in the absence of OVCs and K symbolizes the slope of the equation.

5.2.7. Theoretical Studies

To evaluate the interactions between **ODNI**-nanosheets and OVC molecules, the electronic properties of **ODNI** and OVC molecules were calculated using DFT. The ground state optimized geometries along with HOMO/LUMO energy were calculated using B3LYP hybrid functional incorporated in the Gaussian 09 package.[22,23] The 6-31G basis set for all the atoms has been used in all calculations, which offers high-quality outcomes at a reasonable time.

5.2.8. Calculation of Stern–Völmer quenching constant (K_{sv}) and Limit of Detection (LOD)

The fluorescence response of the present probe was evaluated by fitting the obtained statistics to a Stern–Völmer equation linearly:

$$I_o/I = 1 + K_{sv}[Q] \qquad (1)$$

Where 'I_o' represents the initial fluorescence intensity of probe before the addition of analytes, 'I' signifies the fluorescence response after the addition of sensing analytes, [Q]

symbolizes the molar concentration of the analyte, and K_{sv} is the Stern–Volmer quenching constant.

The sensitivity of present probe towards these OVCs was calculated by performing the fluorescence titrations at very low concentrations of OVCs (0 to 5 ppm). The standard mathematical formula used for calculating the detection limit is:

$$\text{Detection limit} = 3\sigma/K \qquad (2)$$

Where σ represents the standard deviation of the initial fluorescence intensity in the absence of sensing analytes while K represents slope of the linear calibration plot determined by plotting the changes in the emission intensity of probe as a function of sensing analyte concentrations.

5.3. Results and Discussion

5.3.1. Design, Synthesis and Characterization

With an intention to achieve enhanced interchain hydrophobic interaction in water that could destroy the strong π-π interaction between the planar naphthalimide cores, the commercially available NA was functionalized with a long octadecyl chain via simple condensation reaction to obtain **ODNI** with more than 93% yield (Scheme 5.1 and A5.1).[24] Besides, the naphthalimide core was favored for its electron deficit nature that could bind with the electron rich OVCs via strong hydrophobic and π-π interactions. To gain more insight into the effect of chain length on the photophysical, aggregation, and sensing properties, **HNI** with a hexyl unit was also synthesized (Scheme 5.1 and A5.1). Both **HNI** and **ODNI** were characterized by multinuclear NMR spectroscopy (^{1}H and ^{13}C) and HRMS.

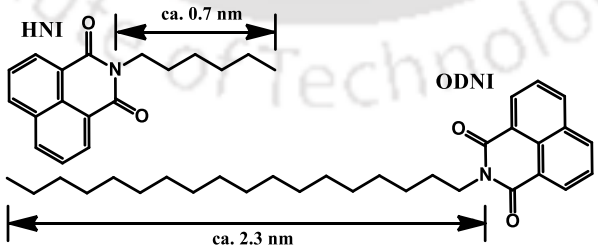

Scheme 5.1. Chemical structures of the alkylated naphthalimide derivatives. The length of alkyl chains are calculated values obtained from ground state optimized structures.

5.3.2. Aggregation Study

The planar NA moieties exhibit strong intermolecular π–π interaction in their condensed state that effectively suppresses their fluorescence emission.[4,5] In contrast to pristine NA; **HNI** and **ODNI** powders emit intensely under UV irradiation indicating their AIE properties (Figure A5.1). The aggregation properties of the **HNI** and **ODNI** were studied in DMF (good solvent) at different water fractions (f_w; poor solvent). Both **HNI** and **ODNI** showed similar UV/Vis spectra in pure DMF, whereas red-shifted (24–27 nm) absorption spectra with different extent of apparently grown-up baseline were observed in 99.8% f_w in DMF (Figure A5.2) suggesting their distinct aggregation behavior. Both the congeners were nearly non-fluorescent in pure DMF (in molecularly dissolved form) with two emission bands at 380 nm and 530–540 nm, which could be assigned to a π–π transition and excimer emission, respectively (λ_{ex}=350 nm; Figures A5.3). With increasing f_w, **ODNI** started aggregating at 40% f_w with red-shifted intense AIE emission (more than 5-fold to 8-fold higher than DMF solution). However, **HNI** remained in molecularly dispersed form up to 90% f_w, indicating its lower aggregation ability (Figure A5.3). This comparative AIE study confirmed the prime role of simple non-conjugated pendant chain-length on the AIEgenic properties of the congeners, which effectively enables the AIE phenomenon to be induced and controlled in an inherently ACQphoric moiety NA.

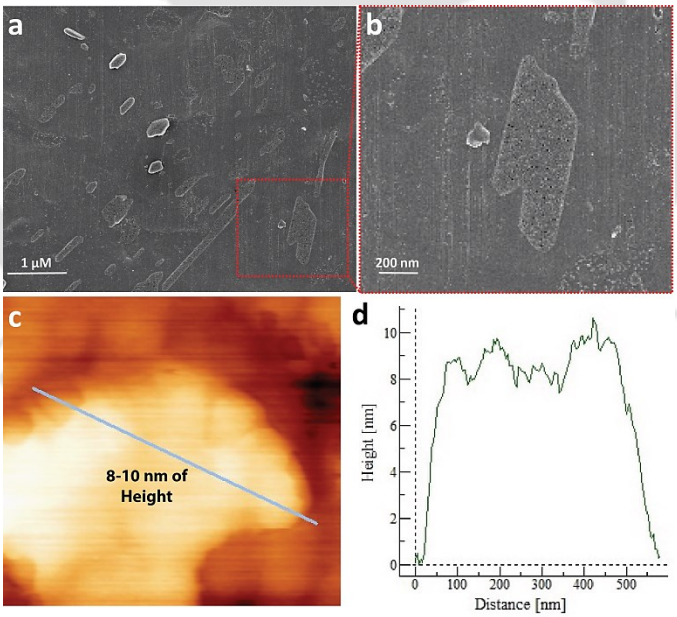

Figure 5.2. (a) Field emission scanning electron microscopy (FESEM) image of **ODNI-NS**. (b) Magnified FESEM image of (a) at the selected area. (c) Atomic force microscopy (AFM) image of **ODNI-NS**. (d) The height profile plot of (c) at the selected area.

5.3.3. Morphological Analysis

The morphology of the spontaneously self-assembled **ODNI-NS** in water was subjected to field emission scanning electron microscopy (FESEM) and atomic force microscopy (AFM) analysis (Figure 5.2). DMF solution of **ODNI** was added dropwise to water with vigorous stirring at room temperature and a trace amount of DMF was removed using dialysis to obtain the nanoaggregate suspension in water. The FESEM image showed a sheet-like structure with variable size and was in line with the hydrodynamic diameter obtained from dynamic light scattering (DLS) measurements (Z_{ave} = 369.7 nm; Figure A5.4). AFM images displayed that the **ODNI-NS** had a height of about 8–10 nm, corresponding to the fully stretched length of two **ODNI** molecules. A similar procedure was followed to obtain the self-assembled **HNI**-nanoaggregates (**HNI**na) in water (Z_{ave} =252.8 nm; Figure A5.4) that formed unsymmetrical nanoparticles (Figure A5.5). The formation of distinct self-assembly in **ODNI** and **HNI** suggested the prominent role of alkyl chain length in the aggregation behavior of the NI congeners, which subsequently tuned their photophysical behavior.

5.3.4. XRD Analysis

The intermolecular interaction and molecular packing within the nanostructures were further investigated by single-crystal X-ray diffraction (SCXRD) and powder X-ray diffraction (PXRD) studies. Along with the **ODNI-NS**, the PXRD patterns of commercially available octadecylamine (ODA) and NA were recorded to comprehend the intermolecular packing in spontaneously formed NS (Figure 5.3a–c). As the NA core is prone to strong π–π interaction, multiple Bragg's diffractions were observed between the 2θ values of 23–29 corresponding to the *d*-spacing of 3.9–3.0 Å (Figure 5.3b). All these interactions were almost abolished in **ODNI-NS** indicating the existence of NI cores in an amorphous phase in the NS. However, multiple distinct diffraction peaks in the range of 2θ value of 33–47 (corresponding to the *d*-spacing of 2.6–1.9 Å) were observed in **ODNI-NS** that could be assigned to the interchain hydrophobic interaction between long alkyl chains as observed in ODA (Figure 5.3c). Since most of the Bragg's diffractions observed in ODA are also active in **ODNI-NS**, the dominant role of long alkyl chain inside the self-assembly could be assumed. The interchain hydrophobic interactions among **ODNI** molecules in water were very strong that directed the formation of NS like structures by pushing the NI cores out on its surface. DFT optimized structure showed the linear conformation of **ODNI** with nearly 2.93 nm lengths (Figure 5.4a). Thus, the highly dominant interchain hydrophobic interaction could

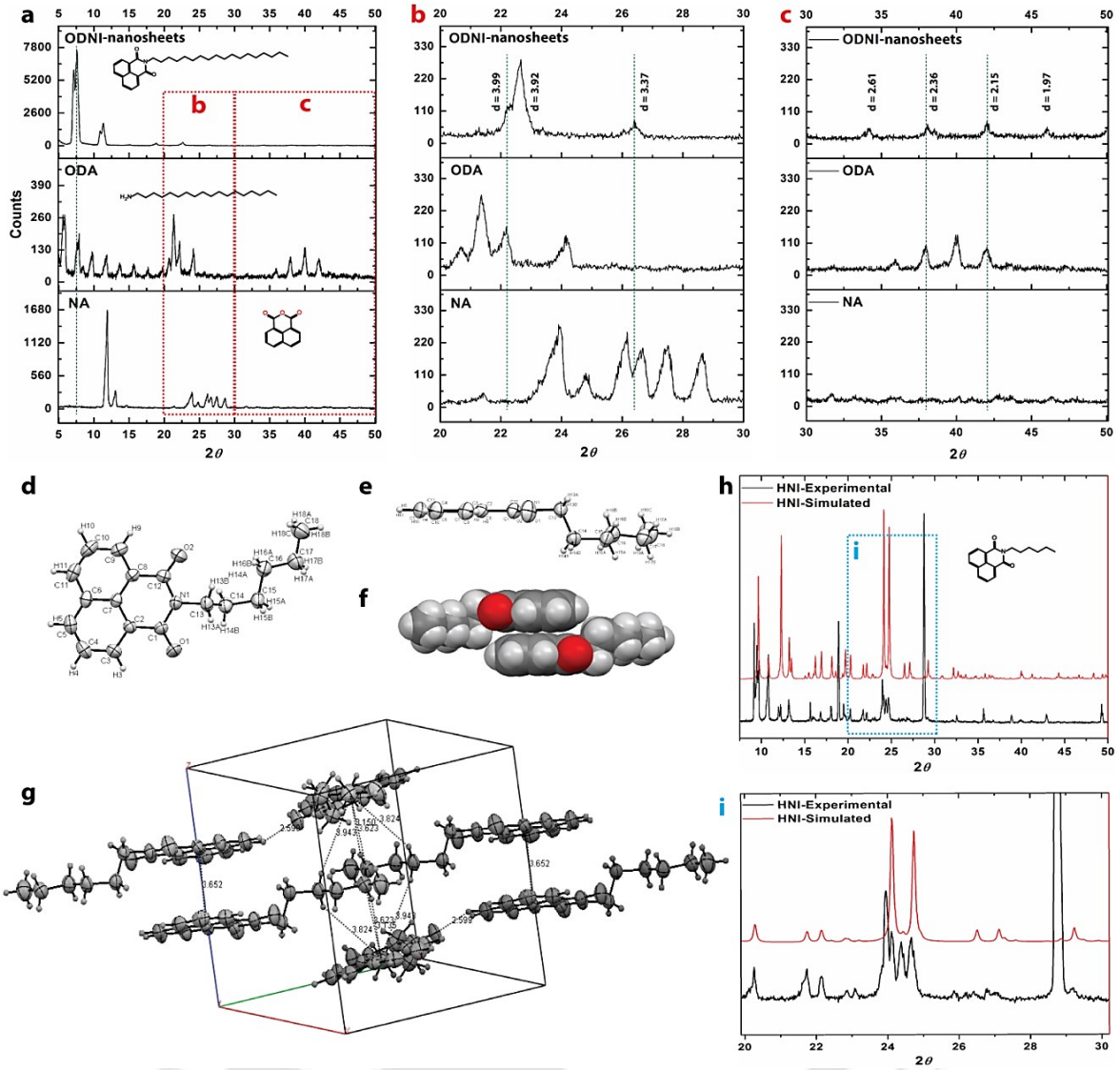

Figure 5.3. XRD analysis for the interpretation of the packing arrangement in **ODNI-NS** and **HNI**na. (a) PXRD pattern of **ODNI-NS** compared to pristine NA and ODA. (b,c) The magnified PXRD patterns of (a); d-spacings are in Å. (d) Top view and (e) side view ORTEP diagrams of **HNI** with the thermal ellipsoids set at 50% probability.[20,21] (f) π–π interaction between two NI cores in **HNI** drawn with space-filling model. (g) Crystal packing diagram of **HNI** showing multiple intermolecular π–π and CH–X (X = O, π) interactions, with values given in Å. (h) PXRD pattern of **HNI**na and (i) the corresponding magnified PXRD pattern of **HNI**na.

be a key feature in the formation of NS like structures in water with thickness ≤ 8–10 nm and having surfaces coated with NI moieties (Figure 5.4b).

In contrast to **ODNI**, the short alkyl chains allow **HNI** to exhibit multiple π–π and CH–π interactions within the range of 3.1–4.0 Å (Figure 5.3d–g, Figure A5.6 and Table A5.2). The simulated PXRD pattern from the SC-XRD data was found to be consistent with the

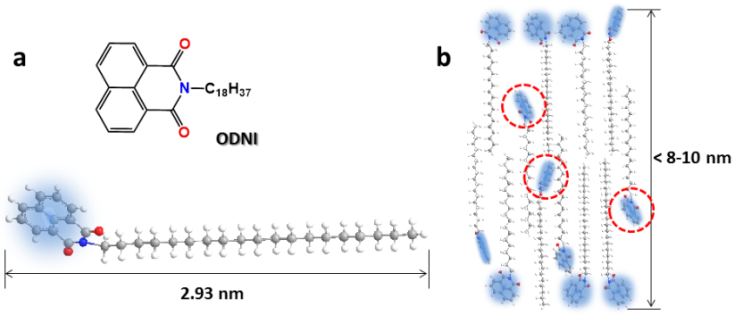

Figure 5.4. (a) Chemical structure and DFT optimized structure of **ODNI**. (b) The packing arrangements in **ODNI-NS**.

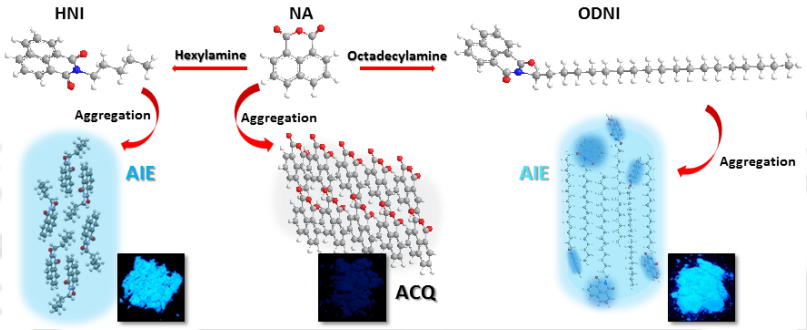

Figure 5.5. Representation of the aggregated-state packing of NA and its alkylated congeners that could be directly correlated with their condensed state fluorescence properties.

experimental PXRD pattern of **HNI**na (Figure 5.3h,i), which indicated that although the interchain hydrophobic interactions between the short hexyl units are not strong enough to direct the self-assembly (as in case of **ODNI**), they can partially weaken the intermolecular π–π interaction between NI cores (the Bragg's diffractions in NA and **HNI** within the 2θ range of 20–30 can be referred, Figures 5.3b and 5.3i) leading to the enhanced condensed state emission.[25] The simple non-conjugated pendant-chain-driven AIE properties in **HNI** and **ODNI** are depicted in Figure 5.5.

5.3.5. Detection of Organic Volatile Contaminants

The spontaneously self-assembled fluorescent **ODNI-NS** coated with NI cores were subjected to OVC detection in pure aqueous medium owing to their huge significance in environmental monitoring, chemical assays, and disease recognition.[17–19] The **ODNI-NS** suspension in water having strong and stable blue emission centered at 465 nm suffered a remarkable quenching in emission upon addition of trace quantity of *p*-xylene and mesitylene (Figure 5.6a,b). The hydrophobic interactions between the **ODNI-NS** and OVCs are highly prominent in water, thereby favoring strong intermolecular π–π interactions

between the electron-deficient NI core and electron-rich phenyl derivatives. Remarkably, about 75% of fluorescence quenching of **ODNI-NS** was witnessed after the addition of just 20 ppm of *p*-xylene or mesitylene. However, as depicted in Figure 5.4b, and highlighted by red dotted circles, few NI cores likely remain trapped within the NS and are unavailable to interact with the OVCs, thus preventing complete quenching of **ODNI-NS**. It also supports the idea that the longer alkyl chain length could be used to enhance the interchain hydrophobic interaction to enable formation of more defined AIEgenic functional nanoassembly.

The K_{sv} for *p*-xylene and mesitylene were calculated to be 2.3 × 10^4 L.mol^{-1} and 3.5 × 10^4 L.mol^{-1} (insets in Figure 5.6a,b) with limit of detection (LOD) as low as 12.7 ppb and 16.4 ppb in aqueous media that provided highly improved values from previous reports (Table A5.1, Figures A5.7). It should also be noted that, previously, well-known AIE-active cores were mostly used to develop luminescent materials for OVC detection (Table A5.1). Nevertheless, for the first time, AIEgenic nanostructures coated with classical electron-deficit ACQ moieties in an amorphous phase were successfully developed for the detection of OVCs in water. The significant role of the nanomorphology for the OVC detection was confirmed by evaluating the recognition efficacy of the random **HNI**na suspension where nearly 10-fold reduction in the sensitivity toward *p*-xylene was observed (K_{sv}=2.7 X 103 L.mol^{-1} and LOD=103 ppb for **HNI**na; Figures A5.8). This could be attributed to the quantity of exposed NI units which played a crucial role for the extraordinary fluorescence response of the **ODNI-NS** towards OVCs. Although, the random **HNI**na with comparatively small size may provide higher surface area for analyte interaction, the fraction of NI core exposed on the surface of random **HNI**na are lesser compared to that of the **ODNI-NS**. This led to the higher fluorescence response of **ODNI-NS** towards OVCs. Similarly, fluorescence titrations with various commonly used OVCs were performed under identical conditions that confirmed the high selectivity of **ODNI-NS** towards mesitylene and xylene derivatives over benzene and its chlorinated derivatives (Figure 5.6c; Figures A5.9).

5.3.6. Evaluation of Detection Mechanism

In this system, it was assumed that the strong hydrophobic and π–π interactions between the electron-deficit NI core and electron-rich toluene derivatives could enhance the rate of collision between the excited states leading to the fluorescence quenching in **ODNI-NS**. To confirm the speculation, excited state lifetime was measured, that showed a huge reduction

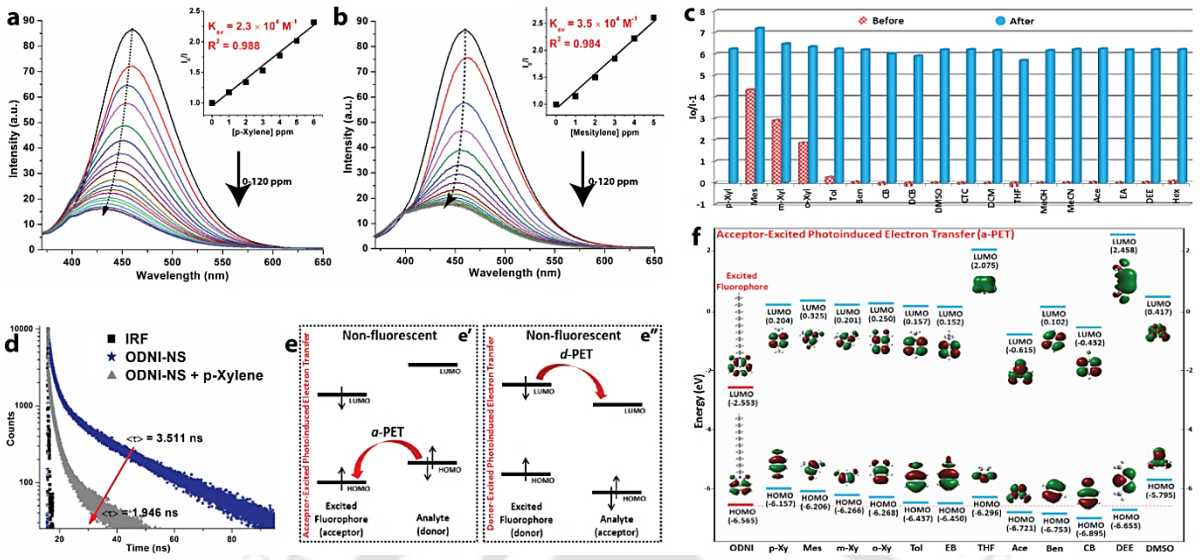

Figure 5.6. Fluorescence response of **ODNI-NS** (20 mm) upon addition of (a) *p*-xylene and (b) mesitylene at room temperature (insets are the corresponding Stern–Volmer plots; λ_{ex} = 350 nm). (c) Fluorescence response of **ODNI-NS** (20 mm) to various OVCs (120 ppm) before (red bars) and after (cyan bars) addition of *p*-xylene. (d) Time-resolved fluorescence spectra of **ODNI-NS** (20 mm) before and after addition of *p*-xylene (100 ppm) in water. (e) Representative band energy diagram for the feasibility of *a*-PET and *d*-PET based quenching mechanisms. (f) DFT calculated HOMO–LUMO energy profiles. HOMO–LUMO energy profiles of few other OVCs are not included in the presentation as they have HOMO energy below -7 eV (Table A5.3).

in the **ODNI-NS** lifetime from 3.511 ns to 1.946 ns on addition of 100 ppm *p*-xylene and strongly supported the probability of excited state charge/electron transfer mechanism (Figure 5.6d). In general, two types of excited-state charge/electron transfer mechanisms can occur in either direction (Figure 5.6e): donor-excited photoinduced electron transfer (*d*-PET) or *a*-PET.[26] As the **ODNI-NS** consists of the highly electron-deficit NI moieties, the process of *a*-PET from electron rich OVCs to **ODNI-NS** could be involved in the suppression of fluorescence emission.[26–29] To validate this mechanism, the HOMO and LUMO energy levels of **ODNI** and the OVCs were computed and summarized in Table A5.3 (Figure 5.6f). The obtained HOMO value for **ODNI** was -6.565 eV, offering a strong probability of *a*-PET from HOMO of *p*-xylene (-6.15 eV) and mesitylene (-6.26 eV).

Furthermore, despite the negligible response towards chlorobenzenes, the **ODNI-NS** were found to respond weakly towards the nitrobenzenes (Figure 5.6c, Figures A5.10). DFT calculations show that although the electron-deficit analytes rule out the probability of *a*-PET due to their deeper HOMO energy level, the comparatively lower LUMO energy level in nitrobenzenes to that of **ODNI** could facilitate *d*-PET (Figures A5.11 and A5.12).[26] The excited-state charge transfer was also confirmed by TCSPC experiment, where a significant

decrease in the excited state lifetime of **ODNI-NS** in presence of 1,3-dinitrobenzene was observed (Figure A5.13). The weak fluorescence response of **ODNI-NS** towards nitrobenzenes could be ascribed to the weak electron-donating nature of the NI moiety that limits the *d*-PET process. Furthermore, the hydrodynamic diameter of **ODNI-NS** was measured at different analyte concentrations, which ruled out the possibility of disaggregation of the NS (Figures A5.14 and A5.15). A steady enhancement in the hydrodynamic diameter of the NS with increasing analyte concentration confirmed the sensing process to be completely a surface phenomenon. While *d*-PET is a well-explored sensing mechanism, *a*-PET has been observed for the first time in the present system for the sensitive detection of xylene derivatives in water. In this regard, the size-selective detection of electron rich OVCs that have been employed as primary sensing mechanism are depicted in the Table A5.1.

5.4. Conclusion

In summary, a novel strategy to develop AIEgenic nanoassembly by employing non-conjugated long pendant chain to block the detrimental π–π interaction was proposed. ACQphoric cores (NI) are spontaneously arranged on the outer surface of the nanosheets in an amorphous phase owing to the strong interchain hydrophobic interaction that dominantly direct the self-assembly in water. The fluorescent **ODNI-NS** having surfaces coated with electron-deficit NI cores were applied to detect the toxic OVCs in pure aqueous media at ppb level via *a*-PET mechanism. Apart from the new design strategy of long-chain incited self-assembly and ACQ-to-AIE transformation, the present study unveils the first representative example of *a*-PET mechanism-based fluorophore/analyte system for the detection of xylene derivatives, which is very rare and provides important leads to develop inherent AIEgens and high-performance sensors with simple variations.

References

(1) Neel, A. J.; Hilton, M. J.; Sigman, M. S.; Toste, F. D. *Nature* **2017**, *543*, 637–646.

(2) Biedermann, F.; Schneider, H.-J. *Chem. Rev.* **2016**, *116*, 5216 –5300.

(3) Zhou, Z.; Yan, X.; Cook, T. R.; Saha, M. L.; Stang, P. J. *J. Am. Chem. Soc.* **2016**, *138*, 806–809.

(4) Jenekhe, S. A.; Osaheni, J. A. *Science* **1994**, *265*, 765–768.

(5) Klymchenko, A. S. *Acc. Chem. Res.* **2017**, *50*, 366–375.

(6) Luo, J.; Xie, Z.; Lam, J. W. Y.; Cheng, L.; Chen, H.; Qiu, C.; Kwok, H. S.; Zhan, X.; Liu, Y.; Zhu, D.; Tang, B. Z. *Chem. Commun.* *2001*, 1740–1741.

(7) An, B.; Kwon, S.; Jung, S.; Park, S. Y. *J. Am. Chem. Soc.* **2002**, *124*, 14410–14415.

(8) Mei, J.; Hong, Y.; Lam, J. W. Y.; Qin, A.; Tang, Y.; Tang, B. Z. *Adv. Mater.* **2014**, *26*, 5429–5479.

(9) Mei, J.; Leung, N. L. C.; Kwok, R. T. K.; Lam, J. W. Y.; Tang, B. Z. *Chem. Rev.* **2015**, *115*, 11718–11940.

(10) Zhang, H.; Zheng, X.; Xie, N.; He, Z.; Liu, J.; Leung, N. L. C.; Niu, Y.; Huang, X.; Wong, K. S.; Kwok, R. T. K.; Sung, H. H. Y.; Williams, I. D.; Qin, A.; Lam, J. W. Y.; Tang, B. Z. *J. Am. Chem. Soc.* **2017**, *139*, 16264–16272.

(11) Sturala, J.; Etherington, M. K.; Bismillah, A. N.; Higginbotham, H. F.; Trewby, W.; Aguilar, J. A.; Bromley, E. H. C.; Avestro, A.-J.; Monkman, A. P.; McGonigal, P. R. *J. Am. Chem. Soc.* **2017**, *139*, 17882–17889.

(12) Wang, J.; Gu, X.; Zhang, P.; Huang, X.; Zheng, X.; Chen, M.; Feng, H.; Kwok, R. T. K.; Lam, J. W. Y.; Tang, B. Z. *J. Am. Chem. Soc.* **2017**, *139*, 16974–16979.

(13) Moragues, M. E.; Toscani, A.; Sancenln, F.; Martínez-Máñez, R.; White, A. J. P.; Wilton-Ely, J. D. E. T. *J. Am. Chem. Soc.* **2014**, *136*, 11930–11933.

(14) Liu, X.; Xu, Y.; Jiang, D. *J. Am. Chem. Soc.* **2012**, *134*, 8738–8741.

(15) Campbell, M. G.; Liu, S. F.; Swager, T. M.; Dinca, M. *J. Am. Chem. Soc.* **2015**, *137*, 13780–13783.

(16) Shustova, N. B.; Cozzolino, A. F.; Reineke, S.; Baldo, M.; Dinca, M. *J. Am. Chem. Soc.* **2013**, *135*, 13326–13329.

(17) Zhang, M.; Feng, G.; Song, Z.; Zhou, Y.-P.; Chao, H.-Y.; Yuan, D.; Tan, T. T. Y.; Guo, Z.; Hu, Z.; Tang, B. Z.; Liu, B.; Zhao, D. *J. Am. Chem. Soc.* **2014**, *136*, 7241–7244.

(18) Dong, J.; Zhang, K.; Li, X.; Qian, Y.; Zhu, H.; Yuan, D.; Xu, Q.-H.; Jiang, J.; Zhao, D. *Nat. Commun.* **2017**, *8*, 1142.

(19) Konvalina, G.; Haick, H. *Acc. Chem. Res.* **2014**, *47*, 66– 76.

(20) Chen, Z.; Wu, D.; Han, X.; Nie, Y.; Yin, J.; Yu, G.-A.; Liu, S. H. **2014**, *CCDC 1014214*: Experimental Crystal Structure Determination, Cambridge Crystallographic Data Centre; https://doi.org/10.5517/cc131cl3.

(21) Chen, Z.; Wu, D.; Han, X.; Nie, Y.; Yin, J.; Yu, G.-A.; Liu, S. H. *RSC Adv.* **2014**, *4*, 63985–63988.

(22) Becke, A. D. *J. Chem. Phys.* **1993**, *98*, 5648.

(23) Frisch, M. J. et al. *Gaussian 09, Revision A.02, Gaussian, Inc., Wallingford CT,* **2009**.

(24) Meher, N.; Iyer, P. K. *Nanoscale* **2017**, *9*, 7674–7685.

(25) Wenger, O. S. *Chem. Rev.* **2013**, *113*, 3686–3733.

(26) Ueno, T.; Urano, Y.; Setsukinai, K.; Takakusa, H.; Kojima, H.; Kikuchi, K.; Ohkubo, K.; Fukuzumi, S.; Nagano, T. *J. Am. Chem. Soc.* **2004**, *126*, 14079–14085.

(27) Tanaka, K.; Miura, T.; Umezawa, N.; Urano, Y.; Kikuchi, K.; Higuchi, T.; Nagano, T. *J. Am. Chem. Soc.* **2001**, *123*, 2530–2536.

(28) Miura, T.; Urano, Y.; Tanaka, K.; Nagano, T.; Ohkubo, K.; Fukuzumi, S. *J. Am. Chem. Soc.* **2003**, *125*, 8666–8671.

(29) Urano, Y.; Kamiya, M.; Kanda, K.; Ueno, T.; Hirose, K.; Nagano, T. *J. Am. Chem. Soc.* **2005**, *127*, 4888–4894.

Appendix

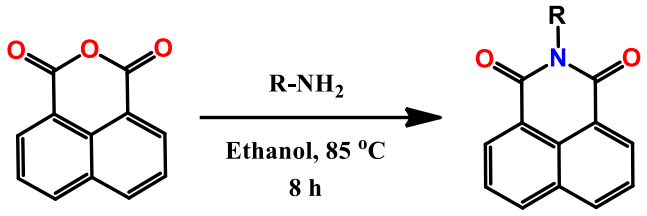

R = C_6H_{13}; HNI
= $C_{18}H_{37}$; ODNI

Scheme A5.1: Synthetic route to **ODNI** and **HNI**.

Table A5.1. A comparative study of the K_{sv} and the detection limit along with the materials and medium used for the detection of OVCs with the existing state of art.

Publication	Material Used	K_{sv} (M^{-1})	Detection Limit (Liquid)	Medium Used
Present Work	**Naphthalimide nanosheets**	**2.3×10^4**	**12.7 μg/L (12.7 ppb)**	**Water**
Chem. Sci. **2018**, DOI:10.1039/c7sc05243j	Organoboron Polymer	--	3.7 ppm	Vapor
Nat. Commun. **2017**, *8*, 1142	TPE Based 2D Materials	--	Excess	Vapor/Solution
Anal. Chem. **2017**, *89*, 3814	Perylene Derivatives	--	8 ppm	Vapor
J. Mater. Chem. A **2017**, *5*, 2115	TPE Based Polymer	1.6×10^4	7 ppb	Water
Molecules **2017** *22,* 1306	Polystyrene Films	--	150 ppm	Vapor
Chem. Mater. **2016**, *28*, 7889	TPE Based MOF	--	Excess	Solution
Adv. Funct. Mater. **2016,** *26*, 393	Anthracene Based MOF	--	Excess	Solution
Chem. Mater. **2015**, *27*, 1465	Coordination Polymer	--	500 ppm	Vapor/Solution
Chem. Commun. **2015,** *51*, 1677	TPE Based MOF	--	Excess	Vapor/Solution
Dyes and Pigments **2015,** *113*, 47	Julolidine Molecule	--	Excess	Vapor
Scientific Reports **2015**, *5*, 12462	Potentiometric Detection Using Polymer	--	3.5 ppm	Vapor
J. Am. Chem. Soc. **2014,** *136*, 7241	2D MOF	--	Excess	Solution
J. Mater. Chem. C **2014**, *2*, 9012	Calix[4]azacrown Films	--	Excess	Vapor
J. Mater. Chem. C **2014**, *2*, 9224	Molecular rotor Doped in Polymer	--	Excess	Vapor
Adv. Funct. Mater. **2013**, *23*, 6044–6050	Graphene Composite	---	0.01%	Vapor
J. Am. Chem. Soc. **2011**, *133*, 20126	TPE Based MOFs	--	Excess	Solution
J. Am. Chem. Soc. **2011**, *133*, 4153	MOFs	--	Excess	Vapor

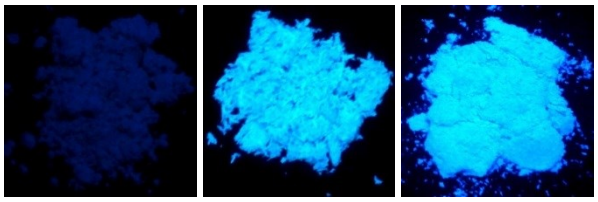

Figure A5.1. Digital photographs of (left) **NA**, (middle) **HNI** and (right) **ODNI** powders under UV-light illumination (365 nm).

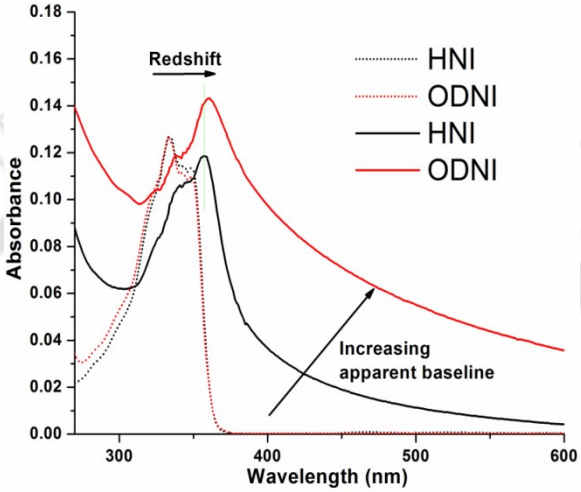

Figure A5.2. UV-Visible spectrum of **HNI** (Black) and **ODNI** (Red) in DMF (Dotted line) and 99.8% water in DMF (Dark line) respectively (20 μM).

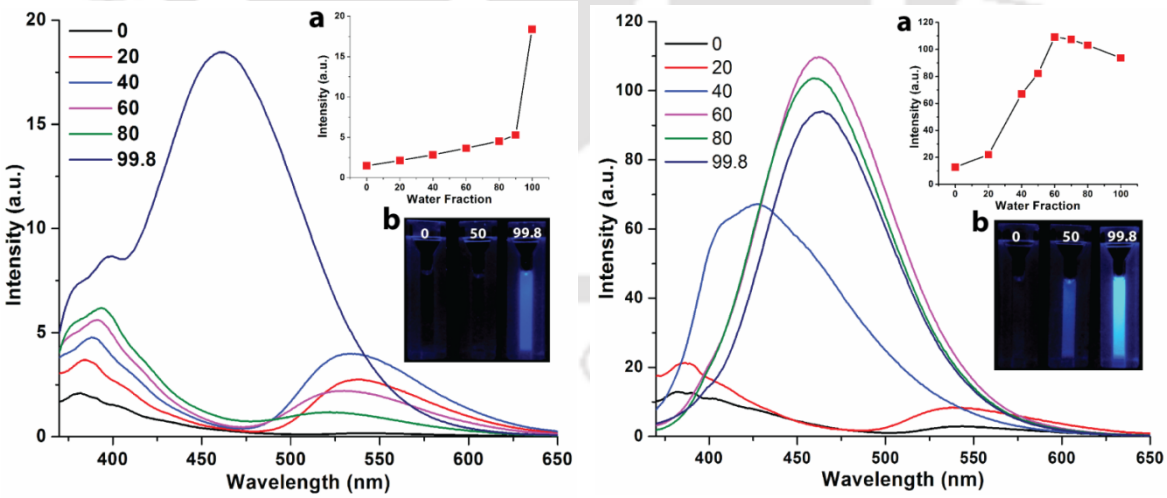

Figure A5.3. Emission spectra of (left) **HNI** and (right) **ODNI** at different water fraction in DMF (at 25 ^{o}C, 20 μM, λ_{ex} = 350 nm). Insets: the respective (a) plot of $\lambda_{emi.max}$ Vs water fraction and (b) digital photographs at different water fraction in DMF.

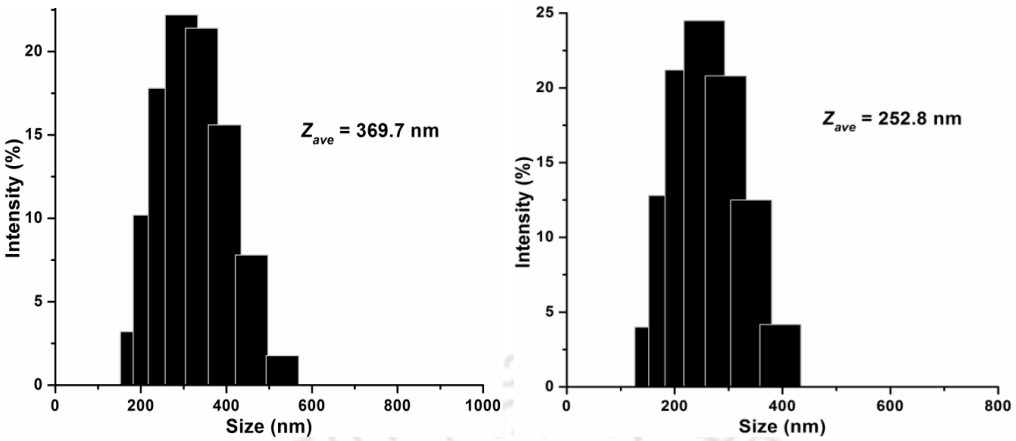

Figure A5.4. Size distribution of **ODNI-nanosheets** and **HNI-nanoaggregates** (20 μM) by DLS measurements in water at 25 °C.

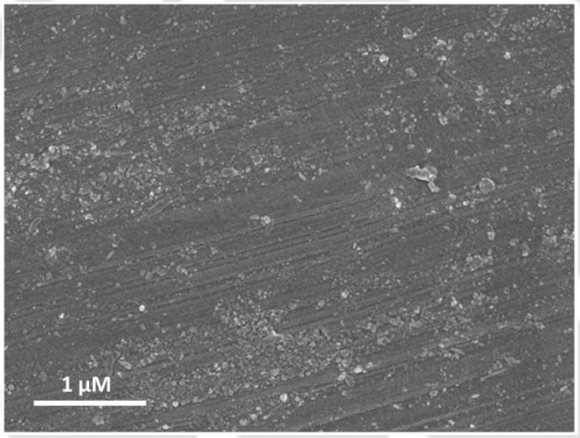

Figure A5.5. FESEM image of irregular **HNI-nanoaggregates** formed in water (10 μM).

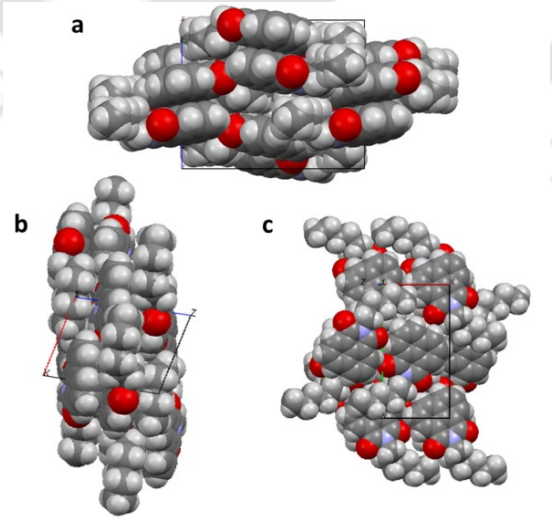

Figure A5.6. Space-filling crystal packing model of **HNI** viewed down crystallographic (a) 'a' axis, (b) 'b' axis and (c) 'c' axis respectively.

Table A5.2. Single Crystal Data and Parameters of **HNI** crystal.

Compound Code	**HNI**
CCDC	1014214
Empirical Formula	C_{18} H_{19} N O_2
Formula Weight	281.34
Temperature	298(2) K
Wavelength	0.71073 Å
Crystal System	Monoclinic
Space Group	P 21/n
Unit Cell Dimension	a = 8.2418(14) Å, α= 90°
	b = 16.336(3) Å, β = 103.266(3)°
	c = 11.3610(19) Å, γ = 90°
Volume	1488.8(4) A^3
Z	4
Absorption coefficient	0.082 mm^{-1}
F (000)	600
Theta range for data collection	2.22 to 25.99°
Index Range	-10<=h<=10, -20<=k<=20,
	-13<=l<=14
Reflections Collected/unique	11160/2930 (R_{int} = 0.0346)
Goodness-of-fit on F^2	1.036
Final R indices [I>2σ(I)]	R1 = 0.0569, ωR2 = 0.1592
R indices (all data)	R1 = 0.0689, ωR2 = 0.1744
Largest difference peak and hole(e $Å^{-3}$)	0.625, -0.295

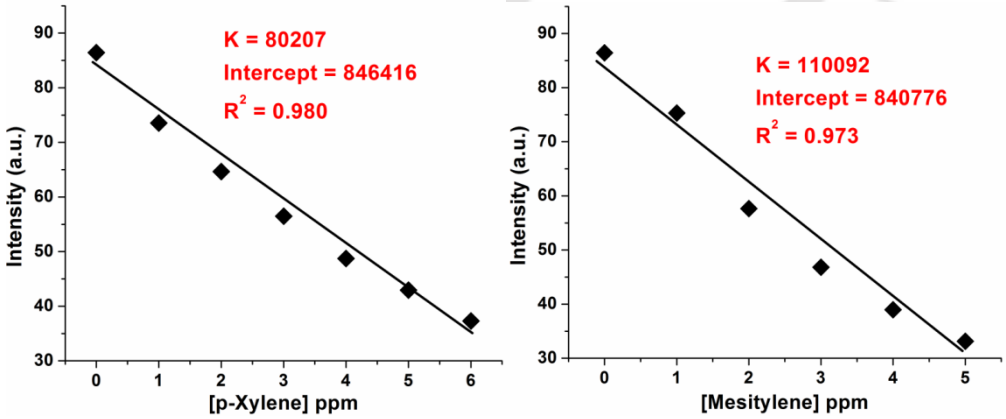

Figure A5.7. Change in fluorescence emission intensity of **ODNI-nanosheets** (20 μM) at different concentrations of p-xylene (**LOD = 12.7 μg/L; 12.7 ppb**) and of mesitylene (**LOD = 16.4 μg/L; 16.4 ppb**).

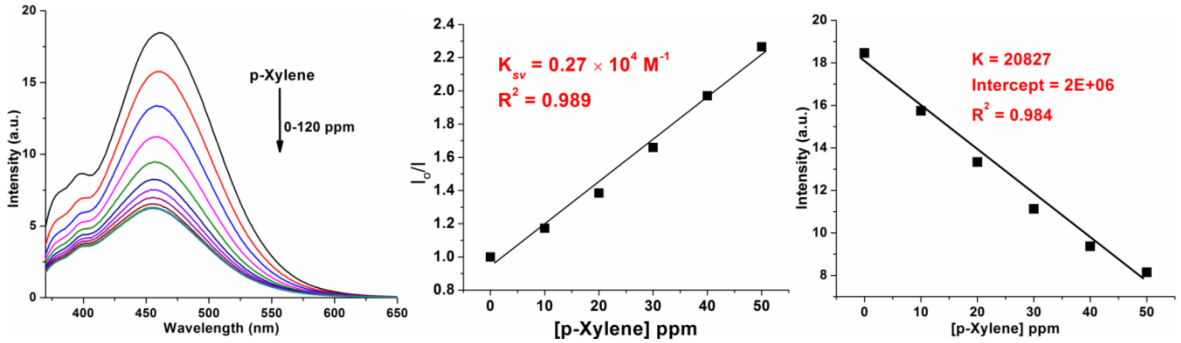

Figure A5.8. (left) Effect of increasing concentration of p-xylene on the fluorescence emission of **HNI-nanoaggregates** (20 μM) in water at room temperature. (middle) Stern–Volmer plots for the fluorescence quenching of **HNI-nanoaggregates** (20 μM) by p-xylene in water. (right) Linear fitting of change in fluorescence emission intensity of **HNI-nanoaggregates** (20 μM) by the addition of p-xylene in water at room temperature. **LOD = 103 μg/L (103 ppb)**

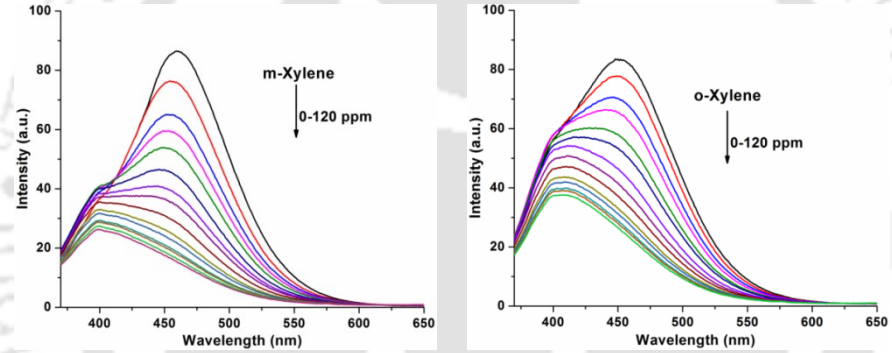

Figure A5.9. Effect of increasing concentration of m-xylene and o-xylene on the fluorescence emission of **ODNI-nanosheets** (20 μM) in water at room temperature respectively.

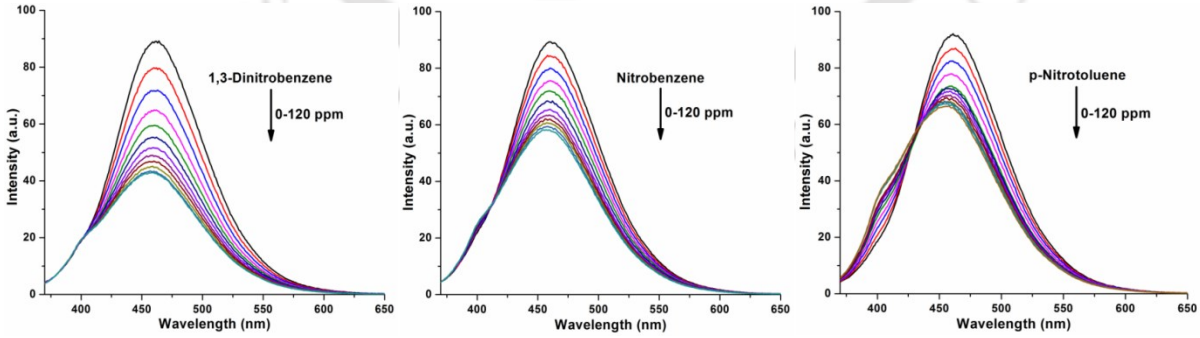

Figure A5.10. Effect of increasing concentration of 1,3-dinitrobenzene, nitrobenzene and p-nitrotoluene on the fluorescence emission of **ODNI-nanosheets** (20 μM) in water at room temperature respectively.

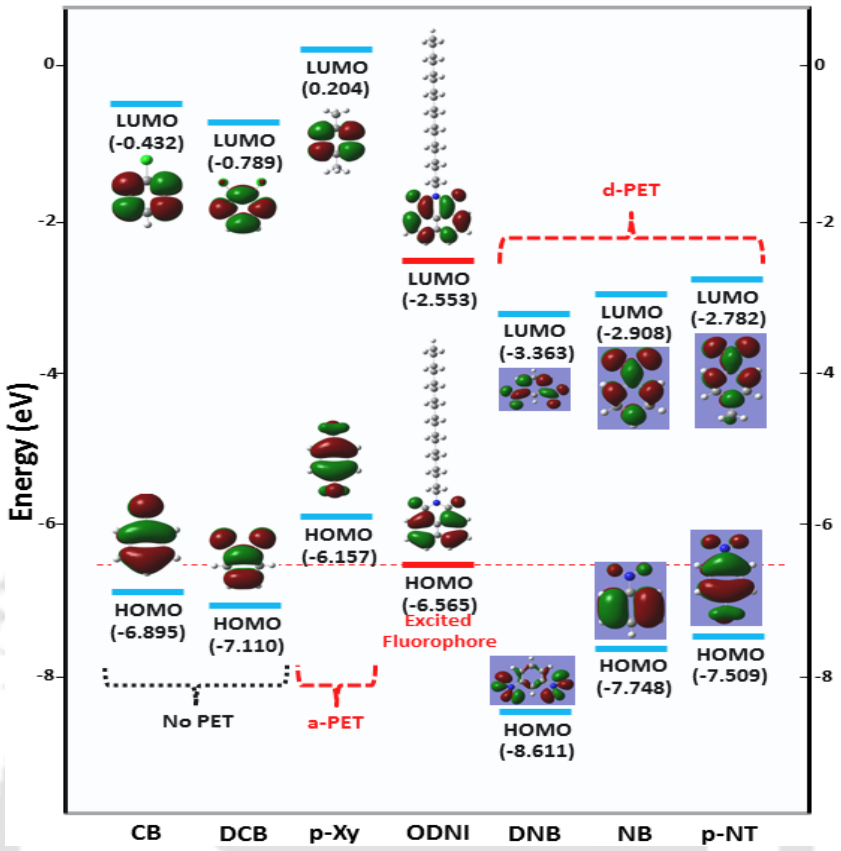

Figure A5.11. DFT-calculated HOMO–LUMO energy profiles **ODNI** to picturize the feasibility of *a*-PET and *d*-PET mechanisms in **ODNI** in presence of different analytes. (Left to right) chlorobenzene, dichlorobenzene, p-xylene, **ODNI**, dinitrobenzene, nitrobenzene and p-nitrotoluene.

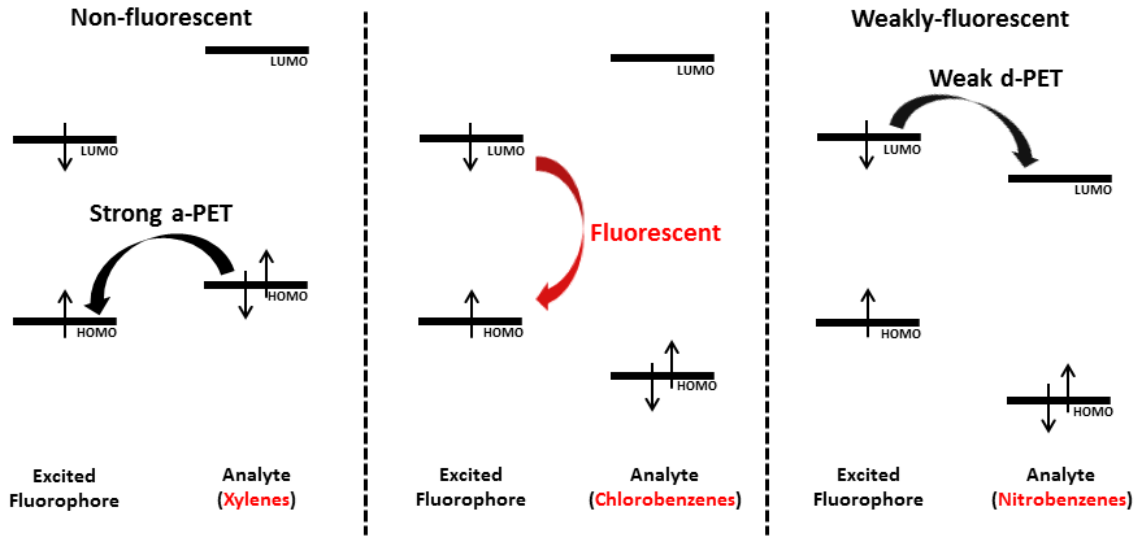

Figure A5.12. Schematic molecular orbital diagram of the fluorescence off/on switch in **ODNI** via PET process.

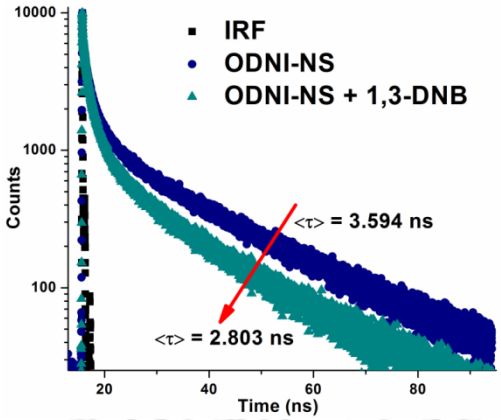

Figure A5.13. Time-resolved fluorescence spectra of **ODNI-nanosheets** (20 μM) before and after addition of 1,3-dinitrobenzene (100 ppm) in water.

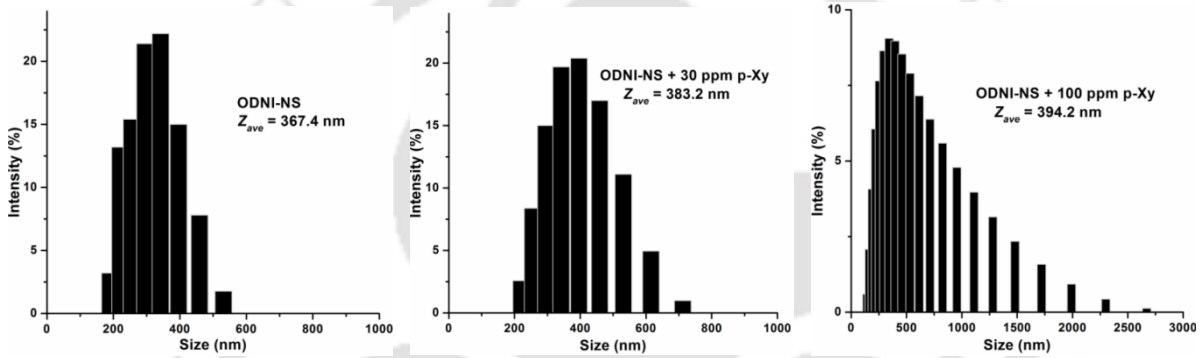

Figure A5.14. Size distribution of **ODNI-nanosheets** (20 μM) in the absence and presence of different concentration of p-xylene obtained by DLS measurements in water at 25 °C. Z_{ave} presented in the figures are the average of five concurrent readings.

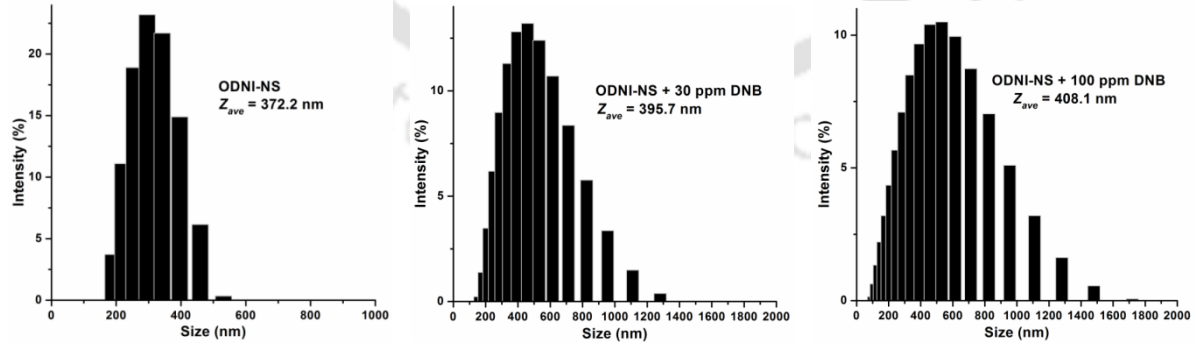

Figure A5.15. Size distribution of **ODNI-nanosheets** (20 μM) in the absence and presence of different concentration of Dinitrobenzene obtained by DLS measurements in water at 25 °C. Z_{ave} presented in the figures are the average of five concurrent readings.

Table A5.3. DFT calculated HOMO, LUMO energy and band gaps.

OVCs	HOMO (eV)	LUMO (eV)	Band Gap (eV)
p-Xylene	-6.15794	0.20463	6.36257
Mesitylene	-6.2061	0.32572	6.531824
m-Xylene	-6.26651	0.201636	6.46815
o-Xylene	-6.26815	0.250345	6.518491
Toluene	-6.4374	0.157554	6.594955
Ethylbenzene	-6.45046	0.152384	6.602846
Tetrahydrofuran	-6.29645	2.075686	8.372131
Acetone	-6.72149	-0.61579	6.105694
Benzene	-6.75387	0.102043	6.855912
Chlorobenzene	-6.8951	-0.43212	6.46298
Diethyl ether	-6.65373	2.458822	9.112554
DMSO	-5.79576	0.417151	6.212907
CCl_4	-9.12507	-3.04006	6.085013
$CHCl_3$	-8.83092	-2.11705	6.713869
DCM	-8.61976	-1.11131	7.508442
Dichlorobenzene	-7.11034	-0.78913	6.321208
Ethyl acetate	-7.32939	0.030749	7.360139
Hexane	-8.30193	2.494197	10.79612
CH_3CN	-9.02684	0.850356	9.877194
CH_3OH	-7.16476	1.825341	8.990102
Nitrobenzene	-7.74845	-2.9089	4.839547
1,3-Dinitrobenzene	-8.61186	-3.63626	4.975604
p-Nitrotoluene	-7.50953	-2.78264	4.726892
ODNI	-6.56532	-2.55341	4.01191

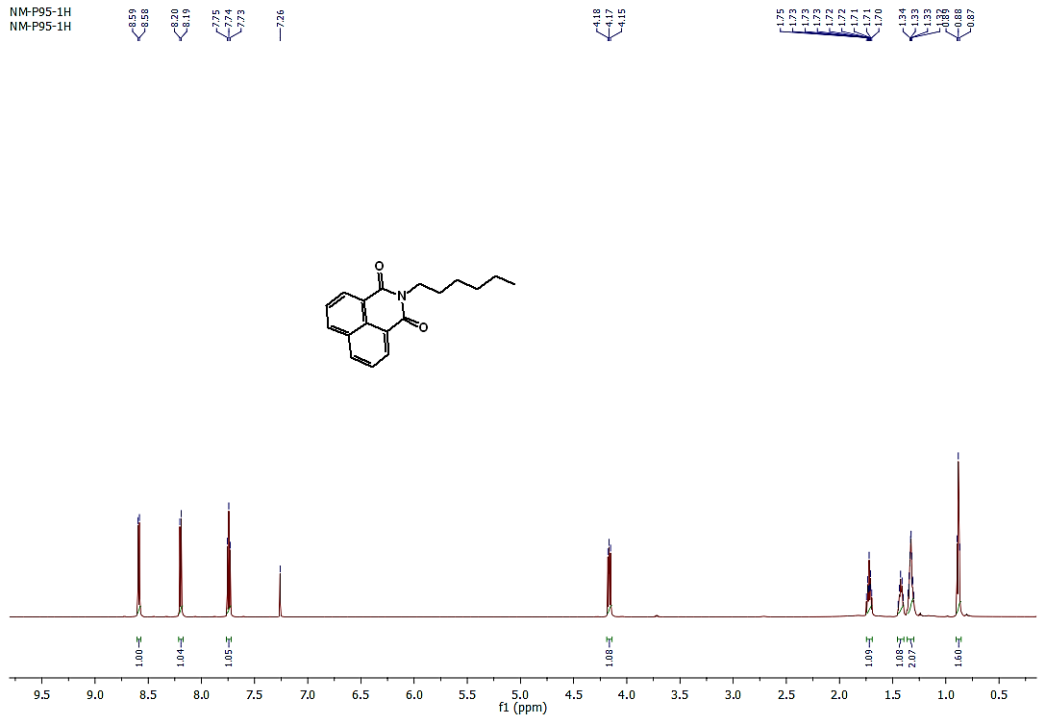

^{1}H NMR of **HNI**

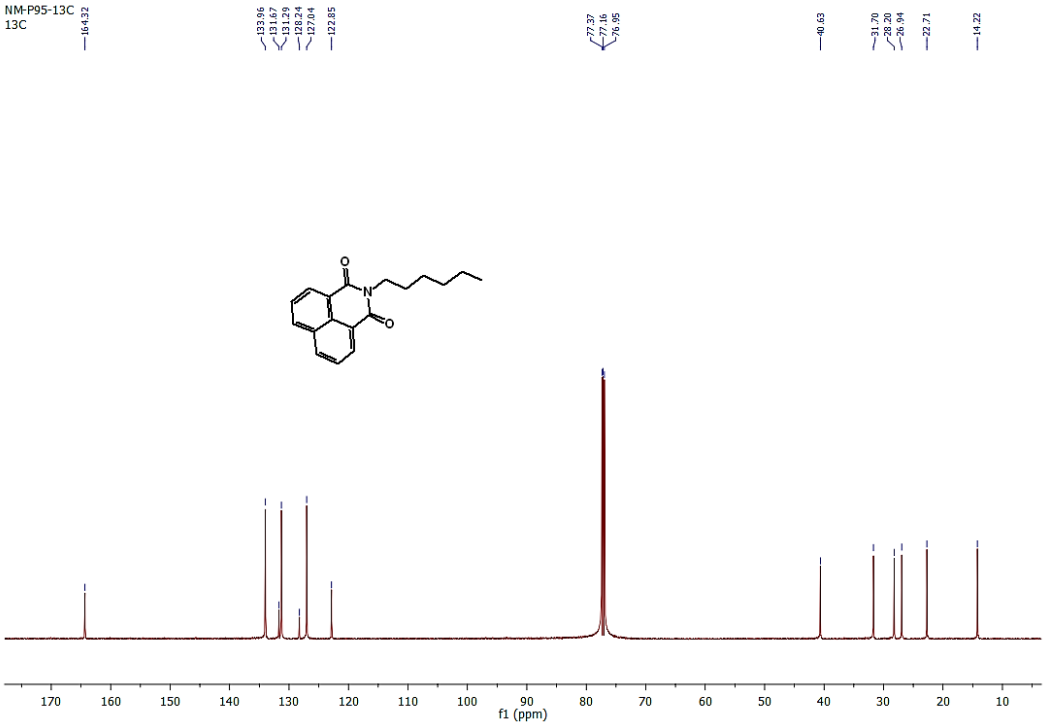

^{13}C NMR of **HNI**

Sample Name	PM-95	**Position**	Vial 1	**Instrument Name**	Instrument 1	**User Name**	
Inj Vol	-1	**InjPosition**		**SampleType**	Sample	**IRM Calibration Status**	All Ions Missed
Data Filename	PM-95.d	**ACQ Method**		**Comment**		**Acquired Time**	1/17/2018 3:37:47 PM

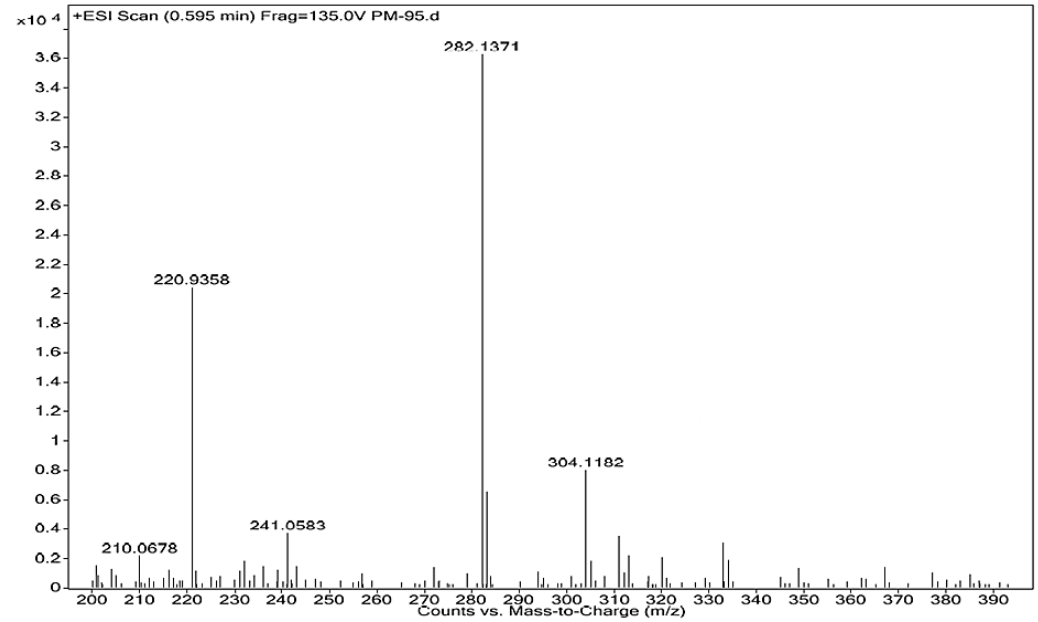

Mass Spectra of **HNI**

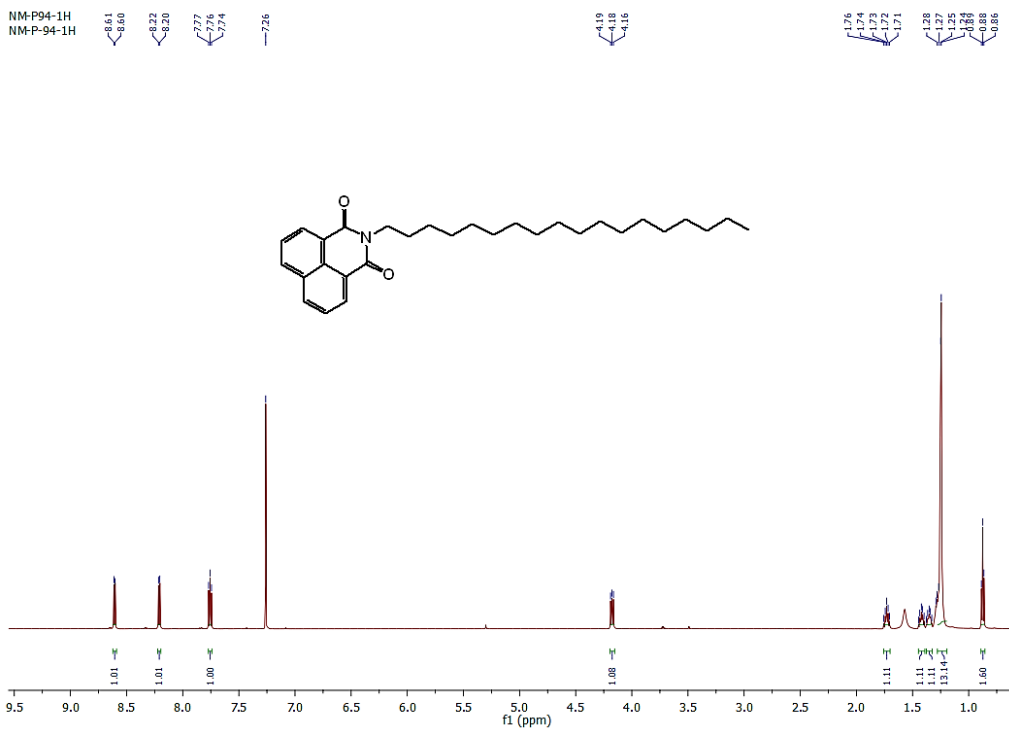

^{1}H NMR of **ODNI**

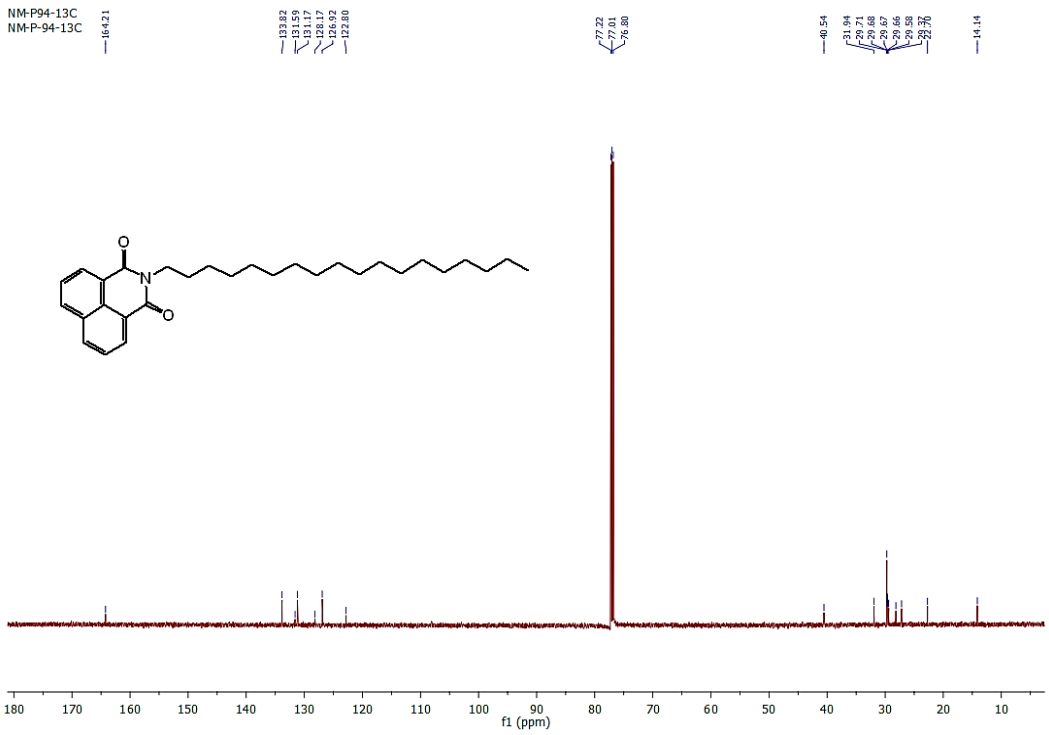

^{13}C NMR of **ODNI**

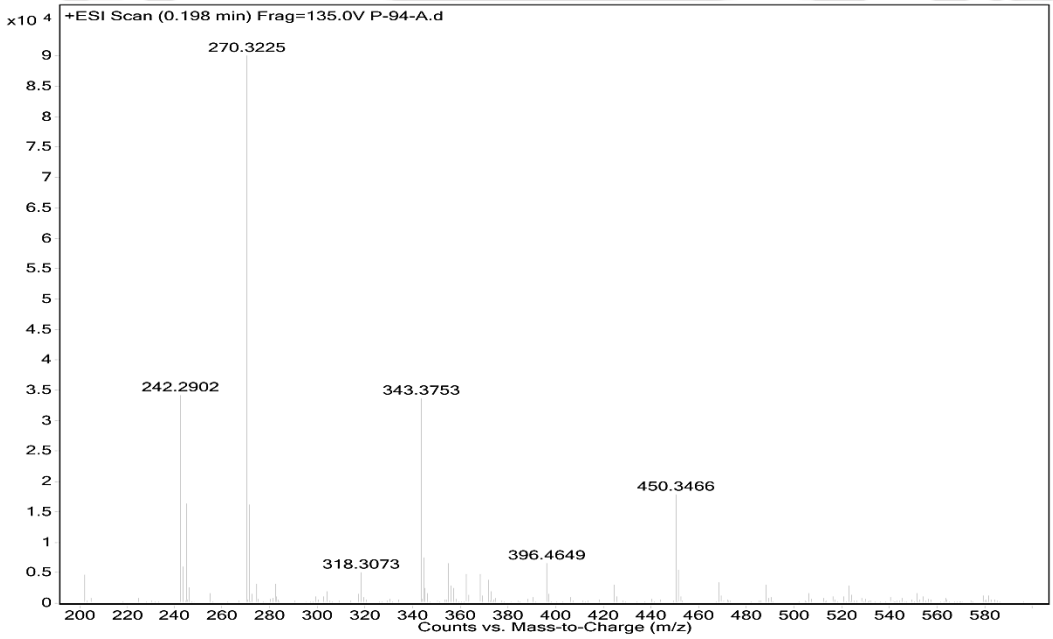

Mass Spectra of **ODNI**

Future Aspects and Thesis Overview

Naphthalimide (NI) compounds are imide-group-containing well-known acceptors and their derivatives have been developed to realize multiple applications over the past several decades. Because of their accepting capacity and high PL quantum yields, NIs have received considerable attention among the scientific community. The AIE activity in NIs opens a new class of AIE-active materials with immense possibilities for various real-world applications both in solution and condensed states. Although the propeller-shaped molecules like TPE and HPS derivatives have been established as an efficient and standard luminogenic core, a large number of research groups have been enthusiastically participating in this area and have designed many new AIE/AIEE-active derivatives with huge potential applications.

After the first report on NI luminogens, exploration of the aggregation properties of NIs owing to their easy synthetic route has increased over the years. The highly attractive applications of NI luminogens are in the areas of bio- and chemosensors and self-assembly studies. Apart from this, various groups are also exploring the NIs in the field of organic light-emitting diodes, stimuli response materials, in vitro and in vivo imaging, and as biogenic molecules. Because of the good biocompatibility, photostability, and high condensed-state emission behavior, NIs are promising for in-depth and long-term bioimaging and tracking applications. Multiple research groups have devoted careful efforts to expand the scope of this core as a possible alternative to existing systems. The highly electron withdrawing and asymmetric NI cores have been realized to have unique structure–property relationships. Because of the strong tendency of the NI cores toward intermolecular π-π stacking interactions, the structural conformation of the asymmetric NI core could be easily tweaked to extend their applications toward many unexplored possibilities.

In this context, this research work has been focused to develop new strategies to control the ACQ/AIE phenomenon in NI derivatives. In particular, these research projects included the construction and systematic tuning of condensed state properties of the NIs by simple structural perturbation. Different approaches have been unveiled to tune the supramolecular self-assembly in NIs by judicious simple structural manipulations. Since the intermolecular packing arrangement plays a significant role in the supramolecular self-assembly and photophysical properties of the NIs over the electronic influence of the attached motifs, it

could be of huge benefit to evaluate the biomedical applications of distinct supramolecular assembly spontaneously generated from electronically similar molecular species. Apart from the different strategies developed to generate and tailor the condensed state photophysical and self-assembly properties of the NIs, the spontaneously formed fluorescent supramolecular assembly of the NIs have been employed for the detection of various environmentally toxic and biologically active analytes in physiological conditions.

The content of this thesis report entitled "**Naphthalimide Luminogens: Structure-Property Relationships and Sensing Applications**" has been divided into five chapters as:

Chapter 1 commences with a brief essay on the need and discovery of condensed state emission. Guided by the mechanistic aspects of condensed state emission, this chapter summarizes the importance, applications and structural manipulation in naphthalimide luminogens along with a concluding remark on this thesis work.

Chapter 2 demonstrates the influence of non-conjugated pendant chains on the supramolecular self-assembly and solid-state emission of the quinolone substituted naphthalimide luminogens. This chapter also includes the detection and unfolding of multi-functional nonheme protein ferritin under physiological conditions, which serves as a well-known inflammatory marker for various diseases.

Chapter 3 provides a conceptual insight on functional group assisted fine-tuning of supramolecular self-assembly and condensed state luminescence in naphthalimides, where the intermolecular packing arrangements dominate their condensed state properties over the electronic influence of the attached functional groups at the molecular level.

Chapter 4 demonstrates the formyl group driven ultra-detection of hydrazine on multiple platforms, which includes the fabrication of simple and portable Whatman paper strips for the cost-effective on-site detection of hydrazine vapor. The detection mechanism involved a reaction-based spontaneous formation of a non-fluorescent hydrazone Schiff base derivative via intramolecular charge transfer process.

Chapter 5 demonstrates the spontaneous formation of long alkyl chain incited fluorescent naphthalimide nanosheets. Along with the mechanistic aspect of condensed state emission in these ACQphoric naphthalimide congeners, sensitive detection of organic volatile contaminants in water via acceptor excited photoinduced electron transfer (*a*-PET) has been unveiled.

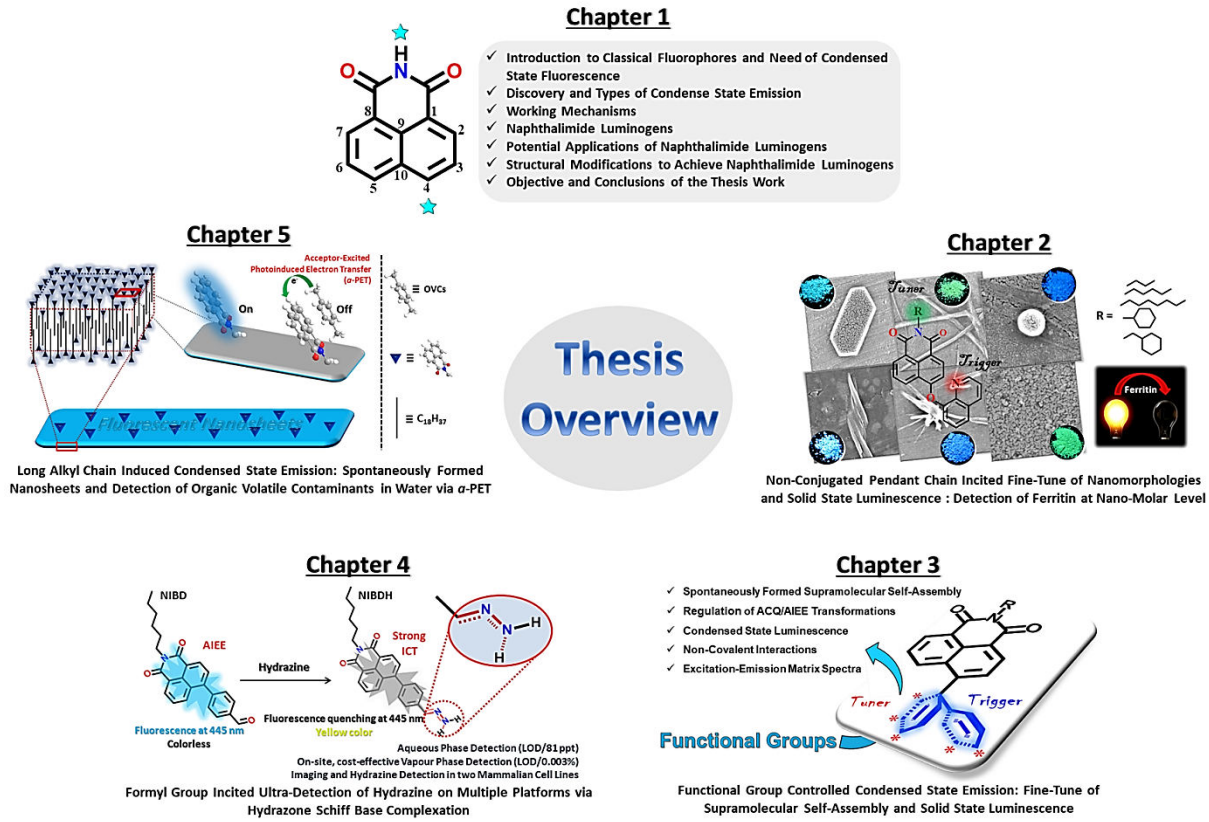

Thesis Overview: Development of new strategies to generate condensed state emission in classical fluorophores for systematic tuning of supramolecular self-assembly and solid state emission. Besides, the spontaneously formed fluorescent supramolecules were used to detect biologically active and environmentally active analytes in aqueous media.

Publications

1. Meher, N.; Paroi, R.; Iyer, P. K.* Alteration of Non-Conjugated Alkyl Chain Length as a Simple yet Potential Tool to Fine-Tailor Condensed State Properties. (Under Preparation)

2. **Meher, N.**; Bitkar, A. P.; Ghosh, S. S.; Iyer, P. K.* Naphthalimide Luminogens: Perturbation of Nano-Assembly for Enhanced Cellular Uptake and Imaging Efficacy. (Submitted)

3. Narasimhan. R. A.; Meher, N.; Barman, D.; Iyer P. K.* Self-assembled naphthalimide nanoparticles for non-volatile ReRAM devices: a new approach towards high performance solution-processed and all-organic two terminal resistive memory devices. (Submitted)

4. Tanwar, A. S.; **Meher, N.**; Adil, L. R.; Iyer, P. K.* Step-wise Elucidation of Fluorescence Based Sensing Mechanisms Taking Picric Acid as a Model Analyte. (Submitted)

5. Khatun, M. N.; Tanwar, A. S.; **Meher, N.**; Iyer, P. K.* An Unprecedented Blueshifted Naphthalimide AIEEgen for Ultrasensitive Detection of 4-Nitroaniline in Water via "Receptor-Free" IFE Mechanism. *Chem. Asian J.*, **2019**, DOI:10.1002/asia.201901065.

6. **Meher, N.**; Iyer, P. K.* Functional Group Engineering in Naphthalimides: A Conceptual Insight to Fine-Tune the Supramolecular Self-Assembly and Condensed State Luminescence. *Nanoscale*, **2019**, *11*, 13233-13242.

7. Maharana, M.; Baruah, N.; Nayak, S.;* **Meher, N.**; Iyer, P. K. Condition Assessment of Aged Ester based Nanofluid Through Physicochemical and Spectroscopic Measurement. *IEEE Trans. Instrum. Meas.* **2019**, DOI:10.1109/TIM.2019.2900883.

8. Dutta, P.; **Meher, N.**; Malik, A. H.; Choudhury, B.; Iyer, P. K.* Polyfluorene-Based Bioconjugates for Selective Detection of Ferritin in Normal and Cancer Human Blood Serums. *ACS Appl. Polym. Mater.* **2019**, *1*, 18-26.

9. Chowdhury, S. R.; Balaji, S. N.; Mondal, S.; **Meher, N.**; Trivedi, V.; Iyer, P. K.* Modulating Early Stage Oligomeric Amyloid Aggregates by Dipeptide Linked Perylenebisimides: Structure Activity Relationship, Inhibition of fibril formation in Human CSF and Aβ1-40. *ACS Appl. Bio. Mater.* **2018**, *1*, 403-413.

10. **Meher, N.**; Iyer, P. K.* Spontaneously Self-assembled Naphthalimide Nanosheets: Aggregation Induced Emission and Unveiling a-PET for Sensitive Detection of Organic Volatile Contaminants in Water. *Angew. Chem. Int. Ed.* **2018**, *57*, 8488–8492.

11. **Meher, N.**; Panda, S.; Kumar S.; Iyer, P. K.* Aldehyde Group Driven Aggregation-Induced Enhanced Emission in Naphthalimides and its Application for Ultradetection of Hydrazine on Multiple Platforms. *Chem. Sci.* **2018**, *9*, 3978–3985.

12. Gopikrishna, P.;¶ **Meher, N.**;¶ Iyer, P. K.* Functional 1,8-Naphthalimide AIE/AIEEgens: Recent Advances and Prospects. *ACS Appl. Mater. Interfaces* **2018**, *10*, 12081–12111. ("¶": Equal Contribution)

13. **Meher, N.**; Kalita, A.; Tanwar, A. S.; Adil, L. R.; Malik, A. H.; Hussain, S.; Iyer, P. K.* Conjugated Smart Materials for Sensing Application on Multiple Platform. *ISRAPS Bulletin* **2018**, *30*, 14-31.

14. **Meher, N.**; Iyer, P. K.* Pendant Chain Engineering to Fine-Tune the Nanomorphologies and Solid State Luminescence of Naphthalimide AIEEgens: Application to Phenolic Nitro-Explosive Detection in Water. *Nanoscale* **2017**, *9*, 7674–7685.

15. **Meher, N.**; Chowdhury, S. R.; Iyer, P. K.* Aggregation Induced Emission Enhancement and Growth of Naphthalimide Nanoribbons via J-aggregation: Insight into Disaggregation Induced Unfolding and Detection of Ferritin at the Nanomolar Level. *J. Mater. Chem. B* **2016**, *4*, 6023–6031.

16. Chowdhury, S. R.; Agarwal, M.; **Meher, N.**; Muthuraj, B.; Iyer, P. K.* Modulation of Amyloid Aggregates into Nontoxic Co-aggregates by Hydroxyquinoline Appended Polyfluorene. *ACS Appl. Mater. Interfaces* **2016**, *8*, 13309–13319.

Patents

1. **Meher, N.**; Iyer, P. K. (21/01/2019), Functional Group Engineering in Naphthalimides to Fine-Tune the Supramolecular Self-Assembly and Condensed State Luminescence. Ref No. 201931020811, App. Number: TEMP/E-1/21902/2019-KOL.

2. **Meher, N.**; Iyer, P. K. (18/07/2018), Spontaneously Self-Assembled Nanosheets for the Detection of Organic Volatile Contaminants in Water. Ref No. 201831026896, App. Number: TEMP/E-1/29385/2018-KOL.

3. **Meher, N.**; Iyer, P. K. (08/05/2018), Hydrazine Detector Device Comprising of Fluorescent Organic Molecular Probe. Ref. No 201831017337, App. Number: TEMP/E-1/18338/2018-KOL.

Awards

1. Received **BEST POSTER** Presentation award in the 20th CRSI National Symposiums in Chemistry (CRSI-NSC)-2017, during February 02-05, 2017 organized by Gauhati University, Guwahati.
2. Received **BEST POSTER** Presentation award in the Newton Bhabha Researcher Links Workshop held during December 14-16, 2017 organized by IISER Kolkata.
3. Received **BEST ORAL** Presentation award in the National Conference on Frontiers in Chemical Sciences (FICS)-2018, during December 06-08, 2018 organized by the Department of Chemistry, Indian Institute of Technology Guwahati.
4. Received **BEST POSTER** Presentation award in the 5th National Workshop on MEMS/NEMS and Theranostic Devices held during February 21-23, 2019 organized by Centre of Excellence in Nanoelectronics and Theranostic devices under the aegis of Centre for Nanotechnology, Indian Institute of Technology Guwahati.

Conferences

1. Attended the National Conference on Recent Advances in Cancer Biology and Therapeutics held in December 5, 2014 organized by Department of Biotechnology, Indian Institute of Technology Guwahati.
2. Attended the 4th International Conference on Advance Nanomaterials and Nanotechnology held during December 08-11, 2015 organized by Centre for Nanotechnology, Indian Institute of Technology Guwahati.
3. Attended the 2nd National Workshop on MEMS/NEMS and Theranostic Devices held during March 21-22, 2016 organized by Centre of Excellence in Nanoelectronics and Theranostic devices under the aegis of Centre for Nanotechnology, Indian Institute of Technology Guwahati.
4. Presented **POSTER** in the National Conference on Frontiers in Chemical Sciences (FICS)-2016, during December 08-10, 2016 organized by the Department of Chemistry, Indian Institute of Technology Guwahati.
5. Presented **POSTER** in the International Conference on Functional Materials (ICFM)-2016, during December 12-14, 2016 organized by the Material Science Centre, Indian Institute of Technology Kharagpur.
6. Attended the full agenda of ACS on Campus at IIT Guwahati on January 16, 2017.
7. Presented **POSTER** in the 20th CRSI National Symposiums in Chemistry (CRSI-NSC)-2017, during February 02-05, 2017 organized by Gauhati University, Guwahati.
8. Presented **POSTER** in the Newton Bhabha Researcher Links Workshop held during December 14-16, 2017 organized by IISER Kolkata.
9. Presented **POSTER** in the 5th International Conference on Advance Nanomaterials and Nanotechnology held during December 18-21, 2017 organized by Centre for Nanotechnology, Indian Institute of Technology Guwahati.
10. Presented **POSTER** in the Young Scientists' Colloquium-2018, Materials Research Society of India (MRSI), Kolkata Chapter held on September 20, 2018 organized by Indian Association for the Cultivation of Science (IACS), Kolkata.
11. Delivered an **ORAL TALK** in in the National Conference on Frontiers in Chemical Sciences (FICS)-2018, during December 06-08, 2018 organized by the Department of Chemistry, Indian Institute of Technology Guwahati.
12. Presented **POSTER** in the 5th National Workshop on MEMS/NEMS and Theranostic Devices held during February 21-23, 2019 organized by Centre of Excellence in Nanoelectronics and Theranostic devices under the aegis of Centre for Nanotechnology, Indian Institute of Technology Guwahati.
13. Presented **POSTER** in the Research Conclave organized by Indian Institute of Technology Guwahati, during March 14-17, 2019.
14. Presented **POSTER** in the 14th International Symposium on Functional ?-Electron Systems (Fπ14) held at Humboldt University in Berlin, Germany, during June 2-7, 2019.

Vitae

Niranjan Meher was born in Odisha, India. He obtained his Bachelor of Science in Chemistry (Hons.) from Anchal College, Padampur and completed his Master of Science in Organic Chemistry from Sambalpur University, India in 2012 and 2014 respectively. In 2014, he joined as a PhD student in the Department of Chemistry; Indian Institute of Technology Guwahati under the supervision of Prof. Parameswar K. Iyer. He started his research career on the development of new naphthalimide based condensed state emitting materials for sensing applications with an in-depth study of their intermolecular interaction, which principally controls the condensed state photophysical and supramolecular self-assembly properties. Besides, he is interested in working on small molecule, conjugated polymer and covalent organic framework based luminogenic materials for biological and theranostic applications.